Single W measurement at DELPHI

Single W measurement at DELPHI

ACADEMISCH PROEFSCHRIFT

ter verkrijging van de graad van doctor
aan de Universiteit van Amsterdam
op gezag van de Rector Magnificus
prof. mr P.F. van der Heijden
ten overstaan van een door het college voor promoties
ingestelde commissie, in het openbaar te verdedigen
in de Aula der Universiteit
op dinsdag 22 april 2003, te 12:00 uur

door

Herman Martin Blom

geboren te Hattem

promotor: prof. dr J.J. Engelen
co-promotores: dr J.J.M. Timmermans
dr P.M. Kluit

Faculteit der Natuurwetenschappen, Wiskunde en Informatica

The work described in this thesis is part of the research programme of 'het Nationaal Instituut voor Kernfysica en Hoge-Energie Fysica' (NIKHEF) in Amsterdam, the Netherlands.

Contents

Introduction

Throughout its history, mankind has been searching for explanations of the phenomena that surround it. The ancient Greeks already tried to find these explanations both in an intellectual and a spiritual way: they searched for a mathematical understanding of the universe and they consulted priestesses at oracles, the sanctuary at Delphi being one of the most famous ones.
The study of the universe and its fundamental structure has evolved enormously since then and has resulted in the rise of a field of science that is called “particle physics”.
During the last century, particle physicists have constructed a theory, now called “Standard Model”, that describes our current understanding of fundamental matter and its interactions.
This model has been extensively verified since its formulation, notably by experiments at accelerators probing the internal structure of matter. The higher the energy that can be achieved with an accelerator, the deeper the level at which the structure can be probed.

For the analyses presented in this thesis, the data recorded by the DELPHI detector resulting from collisions between electrons and positrons at the Large Electron Positron collider (LEP) at the European Organisation for Nuclear Research (CERN) near Geneva have been used.
The DELPHI detector revealed “explanations” like from the priestesses in the ancient Greek days.

In this thesis, the single W final state, $We\nu_e$, is analysed in order to test the Standard Model. Firstly, the cross section of this process is measured and secondly, the self-couplings between three gauge bosons, “trilinear gauge boson couplings” (TGCs) at the $WW\gamma$ and WWZ vertices, are studied by extracting from the data the couplings $\Delta\kappa_\gamma$, λ_γ and Δg_1^Z. These TGC parameters are defined in such a way that they are all equal to zero in the Standard Model. A measurement of non-zero values would therefore reveal deviations from the Standard Model predictions.

This thesis is organised as follows. Chapter 1 presents the necessary theoretical ingredients for the analysis of the single W final state. The first part of this chapter gives an introduction to the Standard Model. The electroweak part of this model, describing the electromagnetic and weak interactions, shows the existence of specific interactions between the gauge bosons (the “force particles” W, γ and Z). If three of these “mediating” particles interact, the corresponding couplings are called TGCs. The Standard Model can be interpreted as an effective low-energy limit of any new physics theory beyond this model. This new physics might give rise to additional TGCs or to deviations from the Standard Model couplings. The second part of chapter 1 is devoted to the theory corresponding to the production of the single W final state. This final state can be obtained by involving three mediating particles that couple. The analyses of the cross section and the TGCs of the single W final state are described in chapters 4 and 5 respectively.

Chapter 2 gives an overview of the experimental setup, which includes the LEP collider and the DELPHI detector. Out of the many recorded reaction products, the single W final state has to be selected for the analyses. The selection of events is explained in chapter 3. Finally in chapter 6, both a comparison with the results from other experiments and an outlook is presented.

CHAPTER 1

Theoretical Overview

This chapter gives an overview of the theoretical framework that is underlying the analysis presented in this thesis. The first section gives a short historical overview of the theory of weak interactions that serves as starting point for the description of the Standard Model, the model that describes our current understanding of fundamental matter and its interactions. The introduction to this model is based on reference [1]. The part of the model that describes specific interactions, called "trilinear gauge boson couplings", is elaborated after this introduction. The chapter ends with theory concerning the so-called "single W" final state which can be correlated to these trilinear gauge boson couplings.

1.1 Weak interactions

Weak interactions have been described in a theoretical model for the first time by Fermi in 1934 [2]. He assumed that the interaction between leptons was a point interaction between two currents of the form:

$$\mathcal{L}_F = -\frac{G_F}{\sqrt{2}} j^{\lambda\dagger} j_\lambda, \tag{1.1}$$

where the Fermi constant G_F is approximately equal to $10^{-5}/m_p^2$ GeV^{-2} if m_p represents the proton mass in GeV/c^2.
The form of the current j^λ has been changed in the course of years due to altering views, finally resulting in [3]:

$$j^\lambda = \bar{\psi}_e \gamma^\lambda (1-\gamma_5)\psi_{\nu_e} + \bar{\psi}_\mu \gamma^\lambda (1-\gamma_5)\psi_{\nu_\mu}, \tag{1.2}$$

where $\gamma_5 = i\gamma_0\gamma_1\gamma_2\gamma_3$ and γ_i ($i = 0, 1, 2, 3$) are the Dirac γ-matrices.
The matrix γ_5 has to be included, because of the discovery of parity[1] violation for weak decays in 1956 [4, 5]: $\bar{\psi}\gamma^\lambda\psi$ is a vector and $\bar{\psi}\gamma^\lambda\gamma_5\psi$ is an axial vector, therefore calling the model corresponding to equation (1.2) the "V-A model".
This V-A model for the weak current (1.2) is not satisfactory at high energies as can be seen by looking at the following process:

$$\bar{\nu}_\mu \mu^- \;\rightarrow\; \bar{\nu}_e e^-. \tag{1.3}$$

[1]The parity operator P reflects the spatial components of a 4-vector x_μ: P$x_\mu = (x_0, -\vec{x})$.

The cross section for this process behaves like:

$$\sigma \sim G_F^2 k^2, \tag{1.4}$$

where k^2 is the squared 4-momentum of the muon. This cross section violates ultimately the conservation of probability (unitarity limit).
An alternative way to describe weak interactions is to make use of the exchange of vector particles, similar to electromagnetism, which means that for the beforementioned process the diagram with the 4-fermion interaction is replaced by a diagram with the exchange of a charged vector particle with interaction strength proportional to the dimensionless constant g (see figure 1.1).

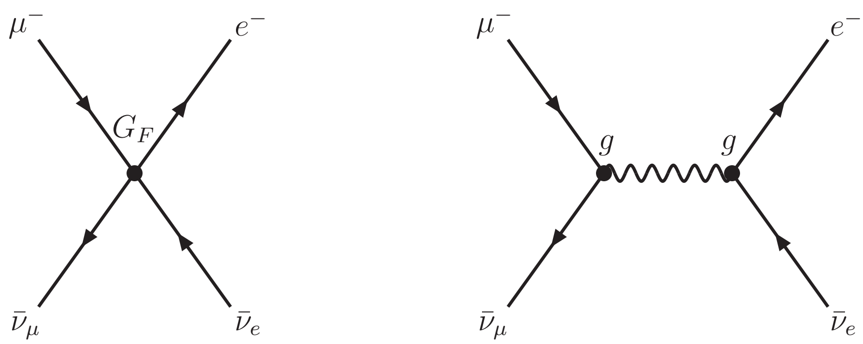

Figure 1.1: *Diagrams for the process $\bar{\nu}_\mu \mu^- \rightarrow \bar{\nu}_e e^-$ in the V-A model (left) and in a model with exchange of a vector particle (right).*

In this way, the factor G_F is replaced by g^2 multiplied by the propagator of the field:

$$G_F \rightarrow \frac{g^2}{k^2 - M^2}, \tag{1.5}$$

where M is the mass of the vector particle.
At low energies, the momentum k can be neglected with respect to M, resulting in:

$$G_F^2 \rightarrow \frac{g^4}{M^4}, \tag{1.6}$$

which gives the same result as the V-A model calculation for the decay in equation (1.3), where low momenta are involved.
At energies much higher than M, the cross section behaves like:

$$\sigma \sim \frac{g^4}{k^2}, \tag{1.7}$$

thereby solving the problems for the V-A model at high energies.

Using the matrix γ_5, one can construct two projection operators:

$$P_\pm = \frac{1}{2}(1 \pm \gamma_5), \tag{1.8}$$

which can be used to form the left-chiral and right-chiral fermions ψ_L and ψ_R:

$$\psi_L = P_-\psi \; ; \quad \psi_R = P_+\psi. \tag{1.9}$$

The electron part of the current (1.2) can thus be written as:

$$j^\lambda = 2\bar{\psi}_{e,L}\gamma^\lambda\psi_{\nu_e,L}. \tag{1.10}$$

The weak current thus only contains the left-handed part of the electron and neutrino. For the electron, there must exist a right-handed part, since both parts contribute to the electromagnetic current. The neutrino is only involved in weak interactions, which means that the right-handed part does not manifest itself at microscopic scale.

1.2 The Standard Model

The present understanding of the fundamental building blocks of nature and their interactions is based on the Standard Model (SM), describing the unification of electroweak and strong interactions. Gravity, the fourth fundamental force, although being the most important force at macroscopic scale, is not taken into account by the SM. This force is much weaker than the other three forces at current energy scales and is therefore not discussed in this thesis.
The SM is a non-Abelian gauge theory with underlying symmetry group $SU(3)_C \otimes SU(2)_I \otimes U(1)_Y$. The theory of strong interactions, called "Quantum Chromo Dynamics" (QCD), is based on the interaction between coloured quarks, mediated by eight gluons, and is invariant under local $SU(3)_C$ transformations. QCD is outside the scope of this thesis and is therefore not discussed in more detail.
The electroweak part of the Standard Model, describing electromagnetic and weak interactions, has been constructed in the 1960s by Glashow, Weinberg and Salam [6, 7, 8], which resulted in a theory called "GSW model". $SU(2)_I \otimes U(1)_Y$ is the symmetry group associated with the GSW model, where the indices I and Y refer to the quantum numbers weak isospin I and hypercharge Y. The third component of I, I_3, being the third generator of the group $SU(2)_I$, is related to the hypercharge Y and electric charge Q via:

$$Q = I_3 + \frac{1}{2}Y. \tag{1.11}$$

The GSW model is discussed in more detail in section 1.2.1.

The fundamental constituents of matter are fermions (spin-$\frac{1}{2}$ particles), including quarks and leptons. These fermions can be grouped into three generations of increasing mass and are listed in table 1.1. Left-handed fermions appear in doublets in the SM, while right-handed fermions show up as singlets. As already explained in the previous section, only left-handed neutrinos exist.
The fermions can interact with each other by means of the exchange of gauge bosons (spin-1 particles) that are shown in table 1.2. Both quarks and leptons are involved in electroweak interactions, but only quarks interact via strong interactions.

Table 1.1: *The fermions in the Standard Model.*

fermions	generations			I_3	Y	Q
leptons	$\begin{pmatrix} \nu_e \\ e \end{pmatrix}_L$	$\begin{pmatrix} \nu_\mu \\ \mu \end{pmatrix}_L$	$\begin{pmatrix} \nu_\tau \\ \tau \end{pmatrix}_L$	+1/2 -1/2	-1 -1	0 -1
	e_R	μ_R	τ_R	0	-2	-1
quarks	$\begin{pmatrix} u \\ d \end{pmatrix}_L$	$\begin{pmatrix} c \\ s \end{pmatrix}_L$	$\begin{pmatrix} t \\ b \end{pmatrix}_L$	+1/2 -1/2	+1/3 +1/3	+2/3 -1/3
	u_R	c_R	t_R	0	+4/3	+2/3
	d_R	s_R	b_R	0	-2/3	-1/3

Table 1.2: *The gauge bosons in the Standard Model.*

interaction	bosons	mass (GeV/c^2)
electromagnetic	γ	0
weak	W^+, W^-	80.4
weak	Z	91.2
strong	gluon	0

Interactions between fermions occur in the SM, because of the fact that this theory is invariant under local gauge transformations. The SM has the property that calculations of physically observable quantities yield finite results, which means that this theory is "renormalisable". In the beginning of the 1970s, 't Hooft and Veltman have shown that every gauge theory with local gauge invariance is renormalisable [9, 10].

1.2.1 The Electroweak Theory

The electroweak theory describes the electromagnetic and weak interactions in the SM and is invariant under local $SU(2)_I \otimes U(1)_Y$ transformations, resulting in the introduction of three gauge fields for the group $SU(2)_I$, A^a_μ ($a = 1, 2, 3$), and one gauge field for the group $U(1)_Y$, B_μ. The first set of gauge fields couple with strength g and the field B_μ couples with strength g'. To facilitate the introduction of the electroweak theory, only the first lepton generation is considered. The contribution of the kinetic terms for the electron, the electron neutrino and gauge fields and their mutual interactions to the total electroweak Lagrangian density $\mathcal{L}_{\text{GSW}}$ can be expressed as:

$$\mathcal{L}_{\text{kin.+int.}} = \bar{l}_L i\gamma^\mu \mathcal{D}_\mu l_L + \bar{e}_R i\gamma^\mu \mathcal{D}_\mu e_R - \frac{1}{4} F^a_{\mu\nu} F^{\mu\nu}_a - \frac{1}{4} G_{\mu\nu} G^{\mu\nu} \; (a = 1, 2, 3), \tag{1.12}$$

where the following notations are used:

$$l_L = \begin{pmatrix} \nu_e \\ e \end{pmatrix}_L \; , \quad \mathcal{D}_\mu l_L = (\partial_\mu - \tfrac{1}{2} i g A^a_\mu \sigma_a + \tfrac{1}{2} i g' B_\mu) l_L \; , \quad \mathcal{D}_\mu e_R = (\partial_\mu + i g' B_\mu) e_R \; ,$$
$$F^a_{\mu\nu} = \partial_\mu A^a_\nu - \partial_\nu A^a_\mu + g \epsilon_{abc} A^b_\mu A^c_\nu \; , \quad G_{\mu\nu} = \partial_\mu B_\nu - \partial_\nu B_\mu . \tag{1.13}$$

σ_a and ϵ_{abc} are the Pauli matrices and Levi-Civita tensor respectively.
These four gauge fields have to be transformed into the four gauge bosons of the electroweak part of the SM: W^+, W^-, Z and γ. In section 1.1 it has already been shown that it is inevitable to incorporate massive vector particles in the theory of weak interactions to describe correctly these interactions at low and high energies. The particle that is exchanged in the right diagram of figure 1.1 is, of course, the W^--boson.
The fields A_μ^3 and B_μ are linked to the photon field A_μ and the weak neutral vector boson field Z_μ. The neutrino does not couple to the photon, so the interaction between the fermions and photon field has to result in: $-eA_\mu\bar{e}\gamma^\mu e = -eA_\mu\bar{e}_L\gamma^\mu e_L - eA_\mu\bar{e}_R\gamma^\mu e_R$, with e being the electric charge. From the kinetic terms for the gauge fields in equation (1.12) a pure kinetic term for the photon field ($-\frac{1}{4}F_{\mu\nu}F^{\mu\nu}$ with $F_{\mu\nu} = \partial_\mu A_\nu - \partial_\nu A_\mu$) and for the Z field ($-\frac{1}{4}Z_{\mu\nu}Z^{\mu\nu}$ with $Z_{\mu\nu} = \partial_\mu Z_\nu - \partial_\nu Z_\mu$) must be constructed without any coupling between these fields, since photons do not couple to neutral particles. In this case, the fields A_μ^3 and B_μ and the fields A_μ and Z_μ have to be related by a rotation:

$$\begin{aligned} B_\mu &= \cos\theta_W A_\mu - \sin\theta_W Z_\mu, \\ A_\mu^3 &= \sin\theta_W A_\mu + \cos\theta_W Z_\mu, \end{aligned} \tag{1.14}$$

where θ_W is the Weinberg angle. From the abovementioned information, the following relations between g, g' and e and θ_W can be deduced:

$$g\,\sin\theta_W = g'\cos\theta_W = e. \tag{1.15}$$

The physical fields describing the $W^\pm$-bosons are obtained from the fields A_μ^1 and A_μ^2 by:

$$W_\mu^\pm = \frac{1}{\sqrt{2}}(A_\mu^1 \mp iA_\mu^2). \tag{1.16}$$

Substituting equations (1.14) and (1.16) in the kinetic terms for the gauge fields in equation (1.12) gives rise to pure kinetic terms for the gauge fields A_μ, Z_μ and $W_\mu^\pm$ and to interactions between these gauge fields, resulting in couplings between three gauge fields and between four gauge fields. These self-couplings are discussed in more detail in the next section, with emphasis on the first type of couplings, since these couplings are the subject of this thesis.
At this stage, all particles in the GSW model have no mass, although experiments have shown the contrary. This means that the $SU(2)_I \otimes U(1)_Y$ symmetry has to be broken in order to give mass to the W- and Z-bosons. However, the $U(1)_Q$ symmetry must be respected, since photons are massless. Electroweak symmetry breaking can be achieved in two ways: either by adding explicitly mass terms to the total Lagrangian density $\mathcal{L}_{\text{GSW}}$ for the W- and Z-bosons or by making use of so-called local spontaneous symmetry breaking. The problem of the first method is that it makes the model non-renormalisable. The second method, that does not violate renormalisability, is more elegant and is known as the "Higgs mechanism" [11, 12, 13]. The idea of this mechanism is to add the following term to the total Lagrangian density corresponding to the complex doublet $\Phi = \begin{pmatrix} \phi^+ \\ \phi^0 \end{pmatrix}$ with hypercharge $Y(\Phi) = 1$:

$$\mathcal{L}_{\text{Higgs}} = (\mathcal{D}_\mu\Phi)^\dagger(\mathcal{D}^\mu\Phi) - V(\Phi), \tag{1.17}$$

where the covariant derivative $\mathcal{D}_\mu$ and the potential $V(\Phi)$ are given by:

$$\mathcal{D}_\mu\Phi = (\partial_\mu - \frac{1}{2}igA^a_\mu\sigma_a - \frac{1}{2}ig'B_\mu)\Phi \; ; \quad V(\Phi) = -\mu^2\Phi^\dagger\Phi + \lambda(\Phi^\dagger\Phi)^2 \text{ with } \lambda > 0. \quad (1.18)$$

To break the $SU(2)_I \otimes U(1)_Y$ symmetry, μ^2 in the potential has to be positive, giving rise to the following minima (ground states) of the potential:

$$\Phi_0^\dagger\Phi_0 = \frac{\mu^2}{2\lambda} \equiv \frac{1}{2}v^2, \quad (1.19)$$

where v is the vacuum expectation value. By choosing a specific solution out of the infinite solutions that satisfy equation (1.19), the $SU(2)_I \otimes U(1)_Y$ symmetry is broken. One can take as solution $\Phi_0 = \frac{1}{\sqrt{2}}\begin{pmatrix} 0 \\ v \end{pmatrix}$ that does not break the $U(1)_Q$ symmetry.
Instead of parametrising Φ with the complex fields ϕ^+ and ϕ^0, one can make use of the "polar" coordinates η and $\vec{\xi}$ and define Φ by:

$$\Phi = \frac{1}{\sqrt{2}}H\begin{pmatrix} 0 \\ \eta + v \end{pmatrix} \text{ with } H = e^{i\vec{\xi}\cdot\vec{\sigma}/v}. \quad (1.20)$$

The idea is to redefine the field Φ and the gauge fields $\vec{A}_\mu$ in such a way by making use of the matrix H, thus of the fields $\vec{\xi}$, that their redefinitions Φ' and $\vec{A}'_\mu$ are invariant under local $SU(2)_I$ transformations, which is called the "unitary gauge". Substituting these redefinitions in equation (1.17) results in the disappearance of the fields $\vec{\xi}$ and the appearance of three massive vector fields for the Z- and W-bosons, which is the consequence of the Goldstone theorem, stating that for every spontaneously broken local symmetry a massive vector field appears [14]. The masses of the weak gauge bosons are given by:

$$M_W = \frac{1}{2}v\frac{e}{\sin\theta_W} \; ; \quad M_Z = \frac{1}{2}v\frac{e}{\sin\theta_W\cos\theta_W}. \quad (1.21)$$

The values of the Weinberg angle θ_W and v can thus be expressed in terms of the masses M_W and M_Z and are known to high precision.
The abovementioned substitution also results in the appearance of a real scalar field, the Higgs field η, with mass $M_{\text{Higgs}} = \sqrt{2}\mu$. Since the value of λ is not fixed, the Higgs mass is a free parameter in the SM.
The Higgs particle does not only couple to the Z- and W-bosons, but also to the first generation leptons via the Yukawa coupling with coupling strength g_e:

$$\mathcal{L}_{\text{Yukawa}} = g_e\bar{l}_L\Phi e_R + h.c.. \quad (1.22)$$

Applying the abovementioned redefinitions results in the following electron mass:

$$m_e = -\frac{1}{\sqrt{2}}g_e v. \quad (1.23)$$

The extension of the first lepton generation to the first fermion generation and to three fermion generations is rather straightforward: for example, the number of kinetic and mass terms for the leptons and quarks enhances. Equation (1.23) generalises to:

$$m_f = -\frac{1}{\sqrt{2}} g_f v, \tag{1.24}$$

where f represents all the massive fermions in table 1.1. There also appear interactions between the W-bosons and quarks. The down type quarks (d, s and b) in table 1.1 are the eigenstates of these quarks under weak interactions. These eigenstates are not the same as the mass eigenstates of these quarks that are observed in bound-state in hadrons in nature. These eigenstates are related via the unitary Cabibbo-Kobayashi-Maskawa (CKM) matrix V_{CKM} as [15, 16]:

$$\begin{pmatrix} d \\ s \\ b \end{pmatrix}_{\mathrm{weak}} = \begin{pmatrix} V_{ud} & V_{us} & V_{ub} \\ V_{cd} & V_{cs} & V_{cb} \\ V_{td} & V_{ts} & V_{tb} \end{pmatrix} \begin{pmatrix} d \\ s \\ b \end{pmatrix}_{\mathrm{mass}}, \tag{1.25}$$

making possible transitions between quarks of different generations. The current values of the magnitudes of the elements of the complex matrix V_{CKM} are [17]:

$$|V_{\mathrm{CKM}}| \sim \begin{pmatrix} 0.975 & 0.223 & 0.004 \\ 0.222 & 0.974 & 0.040 \\ 0.009 & 0.039 & 0.999 \end{pmatrix}. \tag{1.26}$$

1.3 Trilinear Gauge Boson Couplings

The fact that the GSW model is a non-Abelian theory results in the existence of interactions between the gauge fields as has been explained in section 1.2.1. The contribution of these self-couplings to the total Lagrangian density $\mathcal{L}_{\mathrm{GSW}}$ is expressed as:

$$\begin{aligned} \mathcal{L}_{\mathrm{TGC+QGC}} = \; & ie(A^\mu + \cot\theta_W Z^\mu)(W^+_{\mu\nu} W^{-\nu} - W^-_{\mu\nu} W^{+\nu}) \\ & + \frac{ie}{2}(F^{\mu\nu} + \cot\theta_W Z^{\mu\nu})(W^+_\mu W^-_\nu - W^-_\mu W^+_\nu) \\ & + e^2 A_\mu (A_\nu W^{+\mu} W^{-\nu} - A^\mu W^+_\nu W^{-\nu}) \\ & + e^2 \cot^2\theta_W Z_\mu (Z_\nu W^{+\mu} W^{-\nu} - Z^\mu W^+_\nu W^{-\nu}) \\ & + e^2 \cot\theta_W [W^{+\mu} W^{-\nu}(Z_\mu A_\nu + Z_\nu A_\mu) - 2W^+_\mu W^{-\mu} Z_\nu A^\nu] \\ & + \frac{e^2}{2\sin^2\theta_W} W^+_\mu W^-_\nu (W^{+\mu} W^{-\nu} - W^{-\mu} W^{+\nu}), \end{aligned} \tag{1.27}$$

containing couplings between three gauge bosons, "trilinear gauge boson couplings" (TGCs), at the $WW\gamma$ and WWZ vertices and between four gauge bosons, "quartic gauge boson couplings" (QGCs), at the $WWWW$, $WWZZ$, $WW\gamma\gamma$ and $WWZ\gamma$ vertices. The following relation between field tensors and vectors has been used in equation (1.27):

$$T_{\mu\nu} \; (\equiv F_{\mu\nu}, Z_{\mu\nu}, W^\pm_{\mu\nu}) = \partial_\mu V_\nu - \partial_\nu V_\mu \quad (V_\mu \equiv A_\mu, Z_\mu, W^\pm_\mu \text{ resp.}). \tag{1.28}$$

Since TGCs are the subject of this thesis, the rest of this section is devoted to these couplings. The TGC part of equation (1.27) can be written as:

$$\mathcal{L}_{WWV} = -ig_{WWV}[g_1^V V^\mu (W^-_{\mu\nu}W^{+\nu} - W^+_{\mu\nu}W^{-\nu}) + \kappa_V V^{\mu\nu}W^+_\mu W^-_\nu], \tag{1.29}$$

where the following notations have been used:

$$V = \gamma \text{ or } Z,\ \ V^\mu = A^\mu \text{ or } Z^\mu \ \text{ and } \ V^{\mu\nu} = F^{\mu\nu} \text{ or } Z^{\mu\nu}. \tag{1.30}$$

The overall couplings g_{WWV} are defined as:

$$g_{WW\gamma} = e \ \text{ and } \ g_{WWZ} = e\cot\theta_W, \tag{1.31}$$

while the couplings g_1^V and κ_V are given by:

$$g_1^\gamma = g_1^Z = \kappa_\gamma = \kappa_Z = 1. \tag{1.32}$$

The Lagrangian of equation (1.29) can be considered as an effective low-energy limit of any new physics theory beyond the SM at higher energy scale Λ. At this scale Λ, the new physics will reveal itself in the form of new TGC vertices, leading to additional couplings, or as deviations from the SM couplings in equation (1.32). To look for these possible new phenomena, an expansion of the SM Lagrangian of equation (1.29) to a more general description of the WWV vertex is required by adding all further possible Lorentz invariant terms [18, 19]:

$$\begin{aligned}
\mathcal{L}^{\text{eff}}_{WWV} \;=\; & -ig_{WWV}[g_1^V V^\mu (W^-_{\mu\nu}W^{+\nu} - W^+_{\mu\nu}W^{-\nu}) + \kappa_V V^{\mu\nu}W^+_\mu W^-_\nu \\
& + \frac{\lambda_V}{M_W^2} V^{\mu\nu} W^{+\rho}_\nu W^-_{\rho\mu} \\
& + ig_5^V \epsilon_{\mu\nu\rho\sigma}((\partial^\rho W^{-\mu})W^{+\nu} - W^{-\mu}(\partial^\rho W^{+\nu}))V^\sigma \\
& + ig_4^V W^-_\mu W^+_\nu (\partial^\mu V^\nu + \partial^\nu V^\mu) \\
& - \frac{\tilde{\kappa}_V}{2} W^-_\mu W^+_\nu \epsilon^{\mu\nu\rho\sigma} V_{\rho\sigma} - \frac{\tilde{\lambda}_V}{2M_W^2} W^-_{\rho\mu} W^{+\mu}_\nu \epsilon^{\nu\rho\alpha\beta} V_{\alpha\beta}],
\end{aligned} \tag{1.33}$$

where the anti-symmetric tensor $\epsilon_{\mu\nu\rho\sigma}$ equals +1 (-1) if the indices are an even (odd) number of permutations of 0, 1, 2 and 3 and is 0 otherwise. The couplings g_1^V and κ_V satisfy equation (1.32) at tree level in the SM, while the additional couplings vanish in this case. The couplings g_1^V, κ_V and λ_V conserve the operations of charge conjugation[2] C and parity P separately, g_5^V conserves CP, but violates C and P separately and the couplings g_4^V, $\tilde{\kappa}_V$ and $\tilde{\lambda}_V$ are CP violating. Since fourteen couplings are too many to be determined from the available data, this number has to be reduced. A good choice is to ignore the C, P and CP violating couplings, since it is not likely that these couplings have large impact at LEP2, the period of data-taking at the LEP collider that will be discussed in the next chapter. From electromagnetic gauge invariance, the condition $g_1^\gamma = 1$ can be imposed, leading to five couplings. It is convenient to make use of the following set of parameters, since we would like to study possible deviations from the SM:

$$\Delta g_1^Z \equiv g_1^Z - 1,\ \ \Delta\kappa_\gamma \equiv \kappa_\gamma - 1,\ \ \Delta\kappa_Z \equiv \kappa_Z - 1,\ \ \lambda_Z \ \text{ and } \ \lambda_\gamma. \tag{1.34}$$

[2]The charge conjugation operator C changes a particle into its anti-particle.

The number of parameters can be reduced even further if one takes into account the fact that the $SU(2) \otimes U(1)$ symmetry has turned out to be a good symmetry at current energy scales, which leads to the following relations between the parameters of the set in equation (1.34):

$$\begin{aligned} \Delta\kappa_Z &= \Delta g_1^Z - \Delta\kappa_\gamma \tan^2\theta_W, \\ \lambda_Z &= \lambda_\gamma. \end{aligned} \tag{1.35}$$

If one knows the couplings $\Delta\kappa_\gamma$, λ_γ and Δg_1^Z , the other two parameters can easily be determined using equation (1.35). This set ($\Delta\kappa_\gamma$, λ_γ and Δg_1^Z) is called the "Baur set" and is the set that is used in the rest of this thesis.

The couplings g_1^γ, κ_γ and λ_γ, related to the $WW\gamma$ vertex, correspond to the lowest order terms in a multipole expansion of the $W\gamma$ interaction and can therefore be used in expressions for the electric charge Q_W, the magnetic dipole moment μ_W and the electric quadrupole moment q_W of the W-boson:

$$\begin{aligned} Q_W &= e g_1^\gamma \;=\; e, \\ \mu_W &= \frac{e}{2M_W}(g_1^\gamma + \kappa_\gamma + \lambda_\gamma) \;=\; \frac{e}{2M_W}(1 + \kappa_\gamma + \lambda_\gamma), \\ q_W &= -\frac{e}{M_W^2}(\kappa_\gamma - \lambda_\gamma). \end{aligned} \tag{1.36}$$

In general, the magnetic moment μ of a particle is related to its spin s through the gyromagnetic ratio g via:

$$\mu = gs\frac{Q}{2m}, \tag{1.37}$$

where Q and m are the charge and mass of the particle respectively. Hence, a simultaneous measurement of $\Delta\kappa_\gamma$ and λ_γ can be interpreted as a "$g-2$" measurement of the W-boson.

1.4 Single *W* production at LEP2

In this thesis, part of the $We\nu_e$ final state is analysed. The decay modes of the W and their corresponding theoretical branching ratios are summarised in table 1.3. Throughout the text, generic symbols are used for the fundamental particles in order to comprise a particle and its anti-particle in one symbol: e.g. $We\nu_e$ includes $W^-e^+\nu_e$ and $W^+e^-\bar{\nu}_e$.
Most attention is given to the 4-fermion final states $q\bar{q}e\nu_e$, $e\nu_e e\nu_e$ and $\mu\nu_\mu e\nu_e$ in the rest of this thesis.

1.4.1 Trilinear Gauge Boson Couplings

At LEP2 centre-of-mass energies between 161 and 209 GeV, 4-fermion final states are produced with large cross sections. All the possible classes of 4-fermion production diagrams at tree level at LEP2, with exception of Higgs graphs, are shown in figure 1.2, including the non-Abelian classes that involve trilinear gauge boson couplings.

Table 1.3: *Decay modes and corresponding theoretical branching ratios (BRs) of the W-boson.*

decay mode	BR (%)
$q\bar{q}$	67.51
$e\nu_e$	10.83
$\mu\nu_\mu$	10.83
$\tau\nu_\tau$	10.82

Table 1.4: *Contribution of each 4-fermion production class to the final states $e^-\bar{\nu}_e e^+\nu_e$, $\mu^-\bar{\nu}_\mu e^+\nu_e$ and $q\bar{q}e^+\nu_e$ (with $q\bar{q} = d\bar{u}$ or $s\bar{c}$).*

class of diagram	type of channel	$e^-\bar{\nu}_e e^+\nu_e$	$\mu^-\bar{\nu}_\mu e^+\nu_e$	$q\bar{q}e^+\nu_e$
bremsstrahlung	t-channel	22	4	4
multiperipheral	t-channel	9	3	4
fusion	t-channel	6	2	2
conversion	s-channel	5	1	1
Abelian annihilation	s-channel	12	6	7
non-Abelian annihilation	s-channel	2	2	2
total		56	18	20

The contribution of each 4-fermion production class to the final states $e^-\bar{\nu}_e e^+\nu_e$, $\mu^-\bar{\nu}_\mu e^+\nu_e$ and $q\bar{q}e^+\nu_e$ (with $q\bar{q} = d\bar{u}$ or $s\bar{c}$) are listed in table 1.4.
Twelve diagrams contribute to the $We\nu_e$ final state: nine single-resonant diagrams and three double-resonant diagrams. One can argue that the latter group, containing one conversion and two non-Abelian annihilation diagrams, the so-called "CC03 family", does not really give rise to a $We\nu_e$ final state, since for this family the e and ν_e are not coming from the incoming e^+ and e^-, but from the second W. The nine single-resonant diagrams contain three Abelian annihilation diagrams, four bremsstrahlung diagrams and two fusion diagrams. These last six diagrams are part of the so-called "single W" final state, thus only containing contributions from t-channel diagrams. These single W diagrams are shown in figure 1.3 for the $W^-e^+\nu_e$ final state.
Both the t-channel and s-channel diagrams are TGC dependent via the fusion and the non-Abelian annihilation diagrams. Figures 1.4, 1.5 and 1.6 show the dependence of the total cross section on the couplings $\Delta\kappa_\gamma$, λ_γ and Δg_1^Z at $\sqrt{s}$ = 189 GeV, including the contributions from the t-channel, the s-channel and the interference between them, for the three decay channels $e\nu_e e\nu_e$, $\mu\nu_\mu e\nu_e$ and $q\bar{q}e\nu_e$ respectively. Since the dominant contribution to the fusion diagrams in figure 1.3 arises from the γ-exchange part at LEP2 energies, the single W cross section is quite insensitive to anomalous WWZ couplings at these energies, which explains the weak dependence of the t-channel cross sections in figures 1.4 - 1.6 on the coupling Δg_1^Z.
These figures have been obtained using the generator GRC4F [20, 21]. Some features of it will be discussed in chapter 3.
The interference does not play a role for the $\mu\nu_\mu e\nu_e$ and $q\bar{q}e\nu_e$ final states, but influences the cross section of the $e\nu_e e\nu_e$ final state.

One can clearly see from these plots that the dependence of the total cross sections on $\Delta\kappa_\gamma$ is weaker than on λ_γ and Δg_1^Z, while the dependence of the t-channel cross sections, thus the single W cross sections, on $\Delta\kappa_\gamma$ is stronger than on the other two couplings, which makes it interesting to analyse the single W channel.

1.4.2 Cross section

Besides determining the anomalous couplings $\Delta\kappa_\gamma$, λ_γ and Δg_1^Z from the single W diagrams, one can measure its cross section. During the Crete LEP WW99 Workshop a proposal has been made to reach a common signal definition for this cross section [22]. Single W production is defined by the complete t-channel subset of diagrams contributing to $e^+e^- \rightarrow We\nu_e;\;\; W \rightarrow f\bar{f}'$, with additional cuts on kinematical variables at generator level. These cuts exclude regions of phase space dominated by multiperipheral diagrams, where the cross section calculation is affected by large uncertainties. In this way, a gauge invariant set of diagrams is obtained that has small interference with the s-channel diagrams. The kinematical cuts used in the common signal definition are the following:

- $l\nu_l e\nu_e$: $E_l >$ 20 GeV with $l = \mu$ or τ,
- $e\nu_e e\nu_e$:
  - $W^-e^+\nu_e; W^- \rightarrow e^-\bar{\nu}_e$: $|\cos\theta_{e^-}| <$ 0.95 ; $E_{e^-} >$ 20 GeV ; $|\cos\theta_{e^+}| >$ 0.95,
  - $W^+e^-\bar{\nu}_e; W^+ \rightarrow e^+\nu_e$: $|\cos\theta_{e^+}| <$ 0.95 ; $E_{e^+} >$ 20 GeV ; $|\cos\theta_{e^-}| >$ 0.95,
- $q\bar{q}e\nu_e$: $M_{q\bar{q}} >$ 45 GeV/c^2.

The $e\nu_e e\nu_e$ final state is more complicated than the $\mu\nu_\mu e\nu_e$ and $q\bar{q}e\nu_e$ final states due to the presence of two charged fermions from the same generation. The generic name $e\nu_e e\nu_e$ only comprises one final state, while both $\mu\nu_\mu e\nu_e$ and $q\bar{q}e\nu_e$ contain two final states. Therefore, there are twice as many $e^-\bar{\nu}_e e^+\nu_e$ final states contributing to single W production as $\mu^-\bar{\nu}_\mu e^+\nu_e$ and $q\bar{q}e^+\nu_e$ (with $q\bar{q} = d\bar{u}$ or $s\bar{c}$) final states, which means that eight bremsstrahlung and four fusion diagrams have to contribute to single W production for the $e^-\bar{\nu}_e e^+\nu_e$ final state as can be concluded from table 1.4 and figure 1.3. It is not sufficient to apply only an energy cut for the $e\nu_e e\nu_e$ final state, since this cut does not get rid of the fourteen bremsstrahlung and two fusion diagrams (see table 1.4) that still would fit in the signal definition. The angular cuts are necessary to remove these sixteen diagrams and get a clean signal.
The choice of the kinematical cuts is made plausible by means of the plots at generator level, using the generator GRC4F, in figure 1.7 for the $\mu\nu_\mu e\nu_e$ channel, in figure 1.8 for the $e\nu_e e\nu_e$ channel and in figure 1.9 for the $q\bar{q}e\nu_e$ final state.

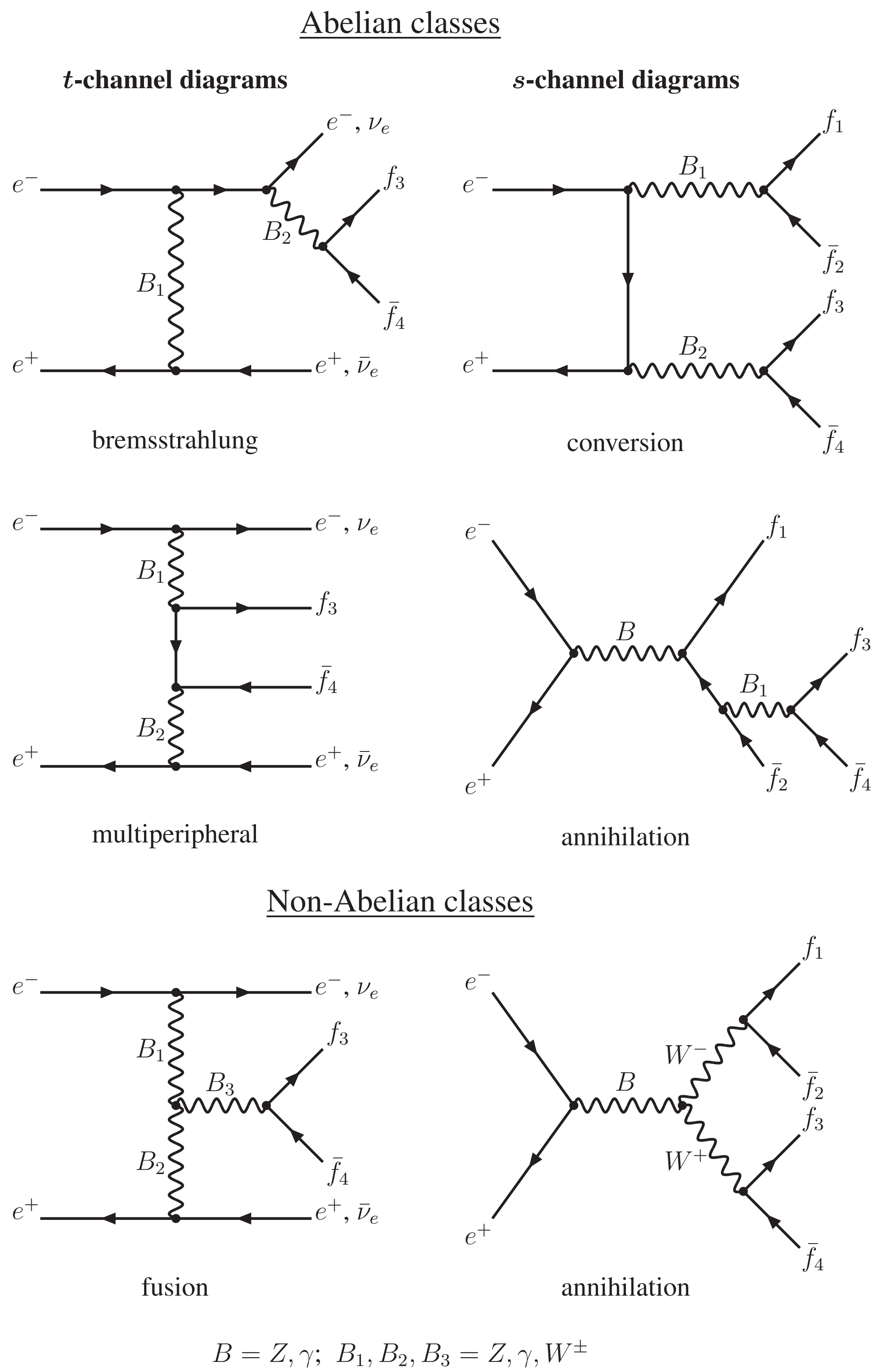

Figure 1.2: *4-fermion production classes of diagrams, excluding Higgs graphs. The left column shows t-channel diagrams and the right column presents s-channel diagrams.*

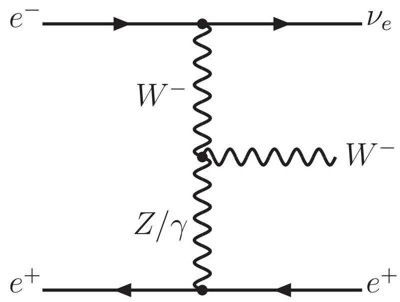

fusion: two diagrams

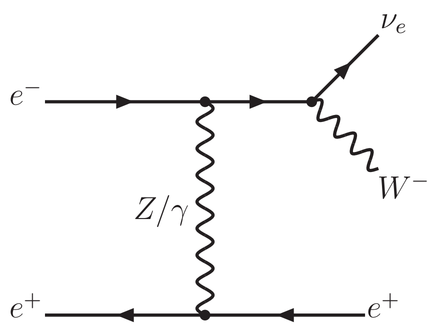

bremsstrahlung 1: two diagrams

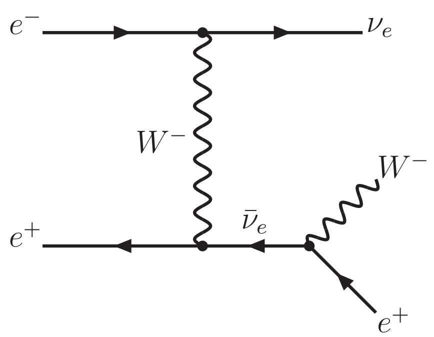

bremsstrahlung 2: one diagram

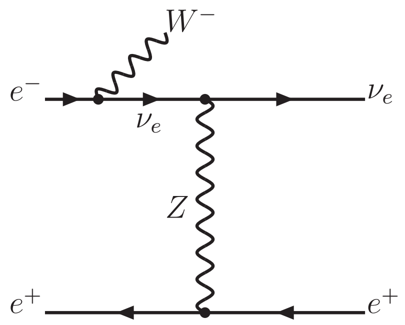

bremsstrahlung 3: one diagram

Figure 1.3: *Single W diagrams for the $W^-e^+\nu_e$ final state.*

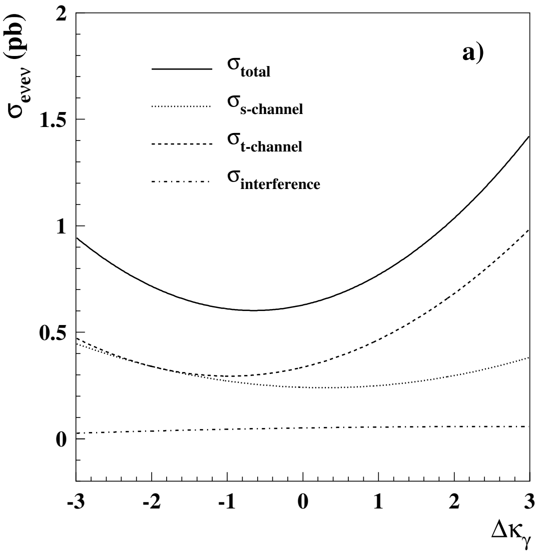

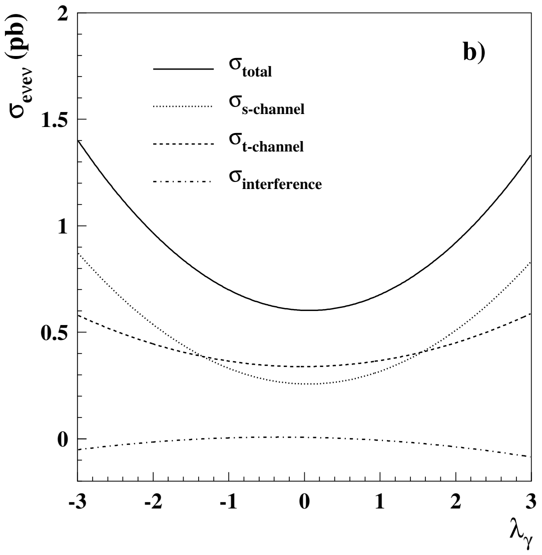

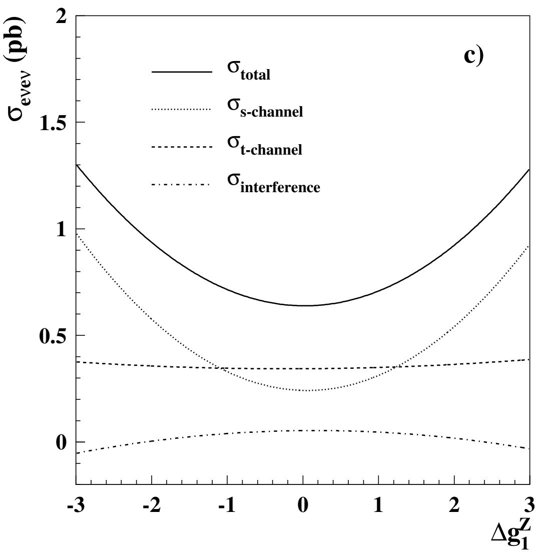

Figure 1.4: *The cross section of the $e\nu_e e\nu_e$ final state at $\sqrt{s}$ = 189 GeV as a function of $\Delta\kappa_\gamma$ (a)), λ_γ (b)) and Δg_1^Z (c)). The solid line indicates the total cross section, the dotted line represents the s-channel contribution, the dashed line shows the t-channel contribution and the dashed-dotted line gives the effect coming from the interference between the s-channel and t-channel contributions.*

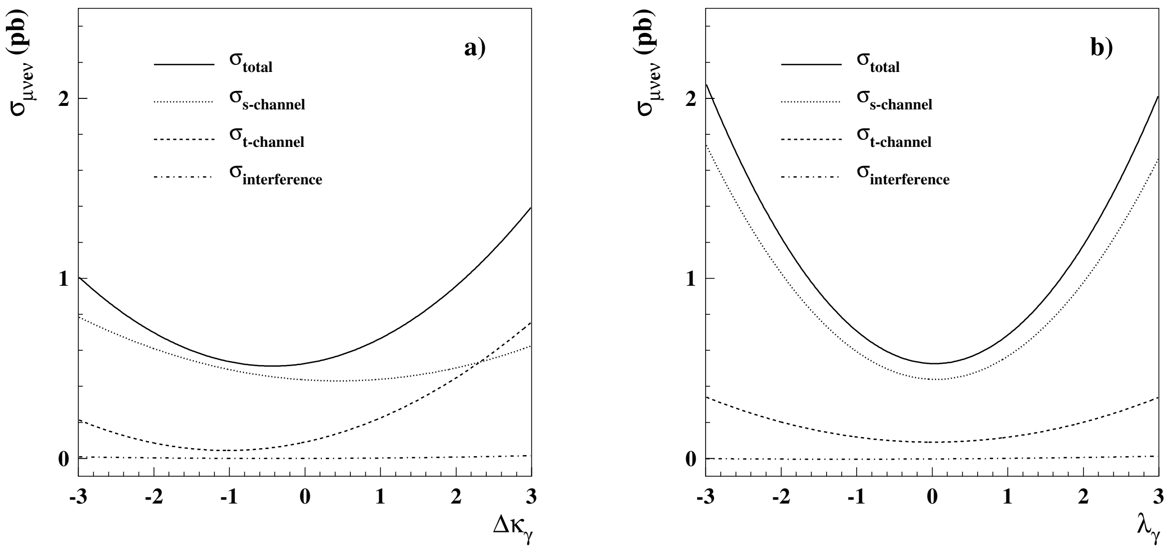

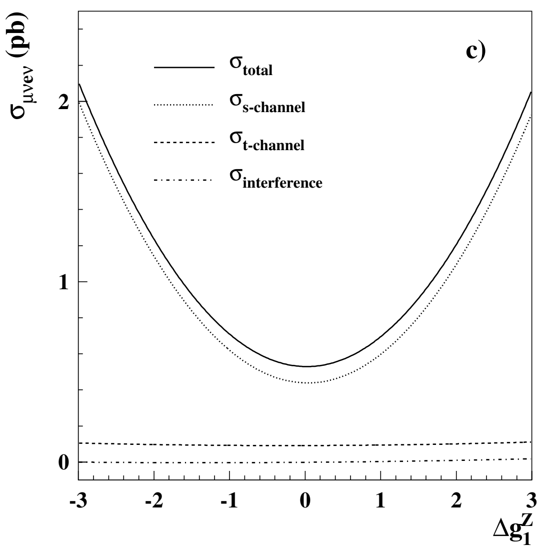

Figure 1.5: *The cross section of the $\mu\nu_\mu e\nu_e$ final state at $\sqrt{s}$ = 189 GeV as a function of $\Delta\kappa_\gamma$ (a)), λ_γ (b)) and Δg_1^Z (c)). The solid line indicates the total cross section, the dotted line represents the s-channel contribution and the dashed line shows the t-channel contribution and the dashed-dotted line gives the effect coming from the interference between the s-channel and t-channel contributions.*

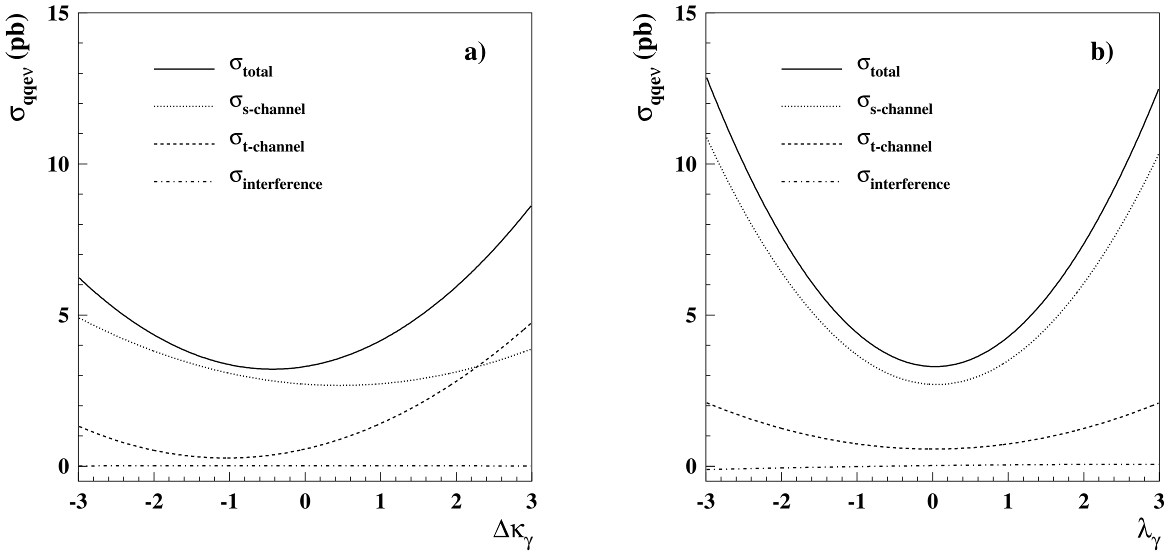

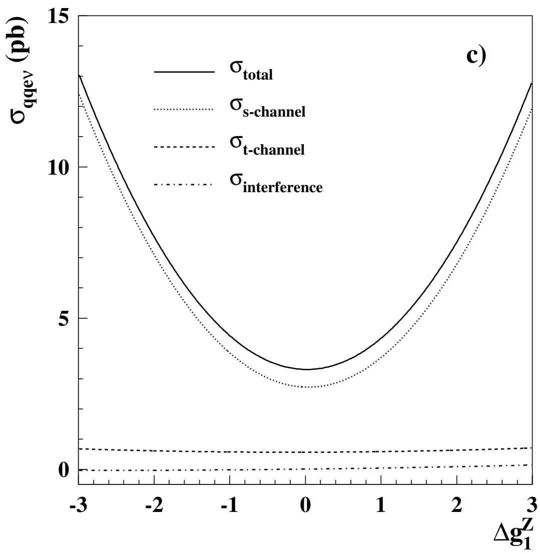

Figure 1.6: *The cross section of the $q\bar{q}e\nu_e$ final state at $\sqrt{s}$ = 189 GeV as a function of $\Delta\kappa_\gamma$ (a)), λ_γ (b)) and Δg_1^Z (c)). The solid line indicates the total cross section, the dotted line represents the s-channel contribution and the dashed line shows the t-channel contribution and the dashed-dotted line gives the effect coming from the interference between the s-channel and t-channel contributions.*

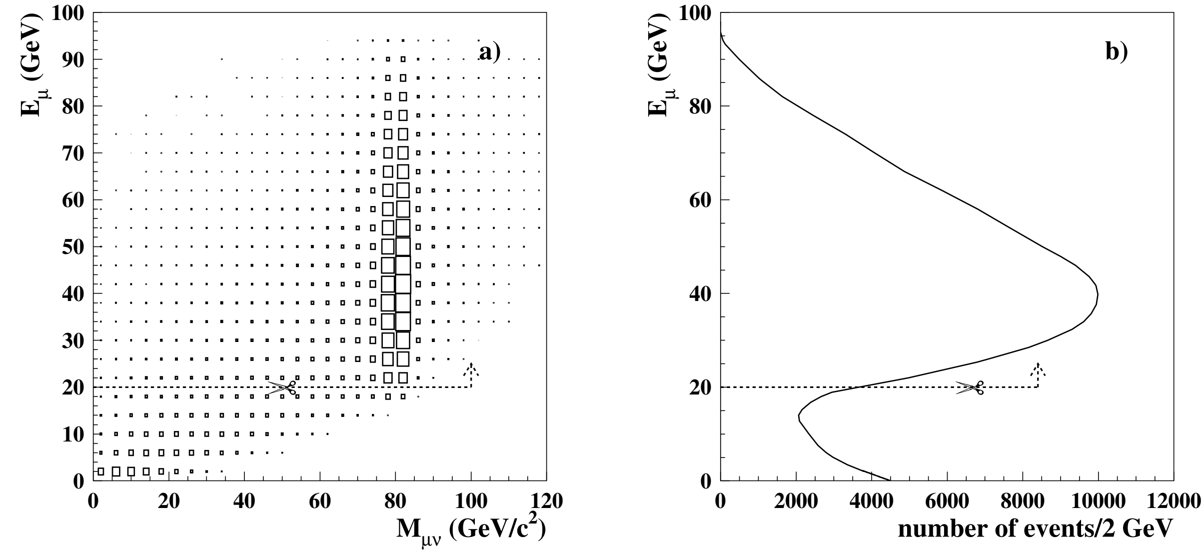

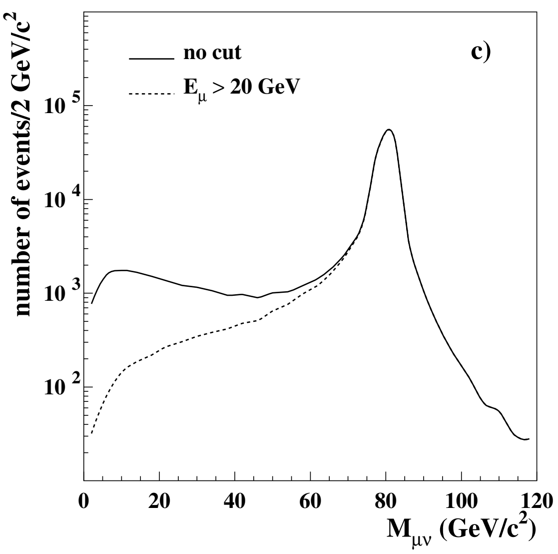

Figure 1.7: *Distributions for muons from the t-channel $\mu\nu_\mu e\nu_e$ final state at $\sqrt{s}$ = 189 GeV. Figure a) shows the muon energy E_μ versus the invariant mass of the muon and its corresponding neutrino $M_{\mu\nu_\mu}$. The activity in the bottom left corner of this plot comes from the non-resonant multiperipheral diagrams. Figure b) shows the energy distribution of the muons and figure c) indicates the invariant mass $M_{\mu\nu_\mu}$ on a logarithmic scale, where the solid line includes all t-channel diagrams and the dashed line represents the muons with $E_\mu > 20$ GeV. The dashed line with arrow in figures a) and b) indicates the Crete definition cut for this channel: $E_\mu > 20$ GeV.*

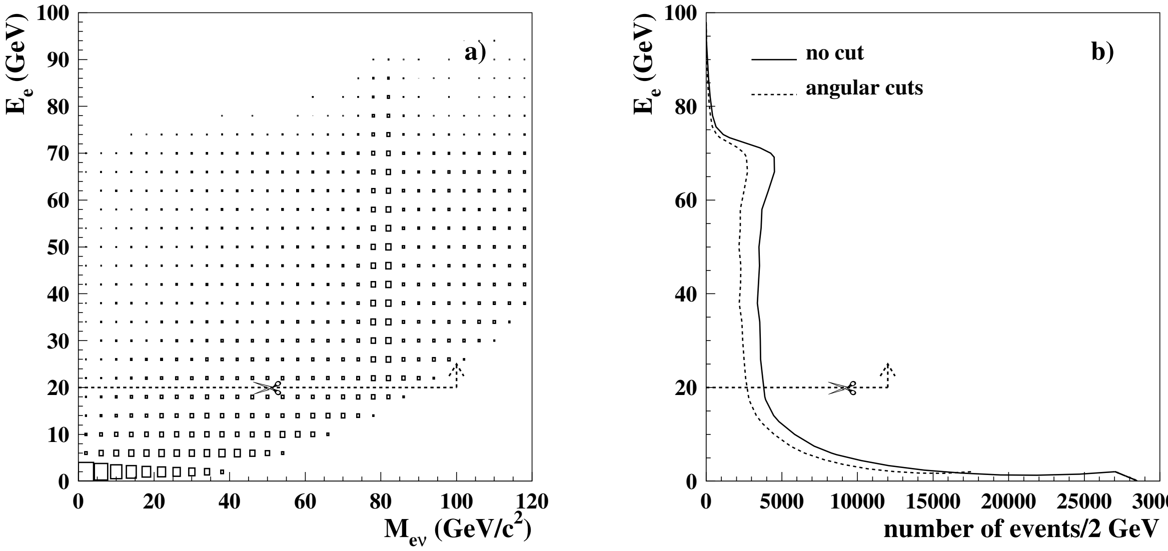

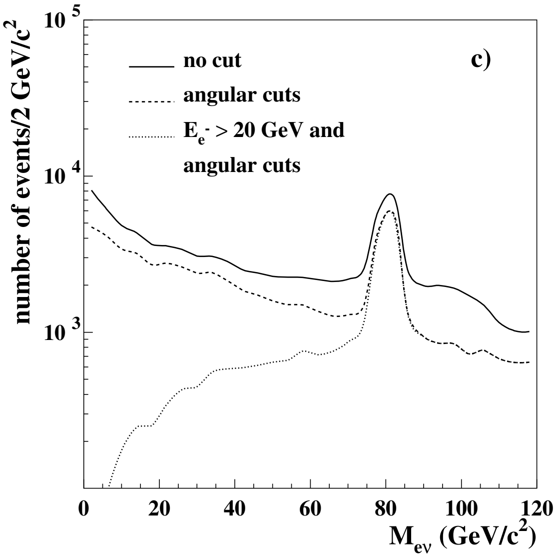

Figure 1.8: *Distributions for electrons from the t-channel $e^-\bar{\nu}_e e^+\nu_e$ ($W^-e^+\nu_e$; $W^- \rightarrow e^-\bar{\nu}_e$) final state at $\sqrt{s}$ = 189 GeV. Figure a) shows the electron energy E_{e^-} versus the invariant mass of the electron and its corresponding neutrino $M_{e^-\bar{\nu}_e}$. The sample satisfies the angular cuts $|cos\theta_{e^-}|$ < 0.95 and $|cos\theta_{e^+}|$ > 0.95. The activity in the bottom left corner of this plot mainly comes from the non-resonant multiperipheral diagrams. Figure b) shows the energy distribution of the electrons E_{e^-} and figure c) indicates the invariant mass $M_{e^-\bar{\nu}_e}$ on a logarithmic scale, where the solid lines include all t-channel diagrams and the dashed lines take only the events into account that satisfy the abovementioned angular cuts. The dotted line in figure c) represents the electrons that also fulfill the kinematical cut E_{e^-} > 20 GeV. The dashed line with arrow in figures a) and b) indicates the energy cut in the Crete definition for this channel: E_{e^-} > 20 GeV.*

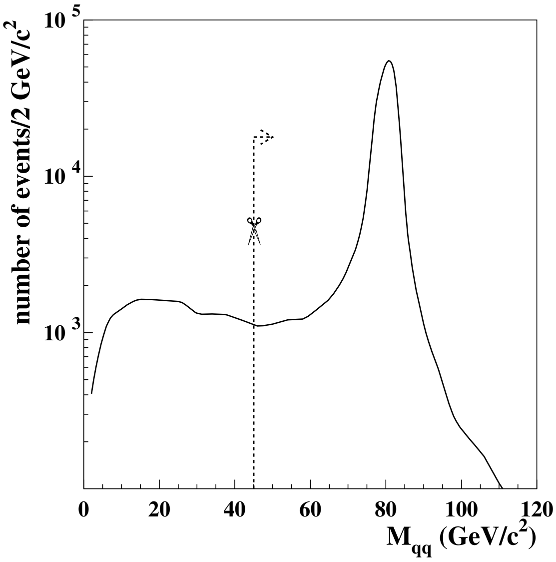

Figure 1.9: *Invariant mass distribution of the two quarks from the* t*-channel* $q\bar{q}e\nu_e$ *final state at* $\sqrt{s}$ *= 189 GeV on a logarithmic scale. The dashed line with arrow indicates the Crete definition cut for this channel:* $M_{q\bar{q}} > 45$ *GeV/c*^{2}*.*

CHAPTER 2

Experimental Setup

The first part of this chapter will give an overview of the hardware that has been used for the production, storage and acceleration of electrons and positrons. The second part will be devoted to the detector that has been used for the reconstruction of the reaction products from the collisions between these electrons and positrons: the DELPHI detector.

2.1 The LEP collider

The Large Electron-Positron collider (LEP) [23] is[1] the world's largest e^+e^- storage ring and part of the accelerator complex of CERN, the European Organisation for Nuclear Research, near the city of Geneva. The ring is about 26.7 km in circumference and is located in a tunnel between 50 and 150 meters below the surface. The LEP ring is not circular, but consists of eight short straight sections (about 500 m long) connected by curved ones. In the middle of four of these straight sections the e^+ and e^- beams are focused and collided head-on. Around these points detectors are located: ALEPH [24], DELPHI [25], L3 [26] and OPAL [27].
LEP is the last step in the process of producing, storing and accelerating the electrons and positrons for which other accelerators at CERN serve as an injector system.

Injector chain

Electrons are produced using an electron gun and accelerated by a linear accelerator (LINAC; LIL-I) to an energy of 200 MeV, while the positrons are produced by bombarding a tungsten target with this electron beam. Subsequently, both the electron and positron beam are accelerated by a second LINAC (LIL-II) to 600 MeV and stored (in bunches) in the Electron-Positron-Accumulator ring (EPA). Finally, two further acceleration steps are applied in the Proton Synchrotron (PS) and the Super Proton Synchrotron (SPS), where the bunches are accelerated to energies of 3.5 and 22 GeV respectively before being injected into the LEP ring. (As a proton anti-proton collider in the 1980s, the SPS provided CERN with the first observations of the W- and Z-bosons [28, 29, 30, 31].) An overview of the full accelerator chain is given in figure 2.1.

[1] It is better to use "was", since LEP and its detectors are not active anymore since the end of 2000. LEP will be replaced by LHC (Large Hadron Collider) in which protons will be accelerated to 7.0 TeV, starting in 2007.

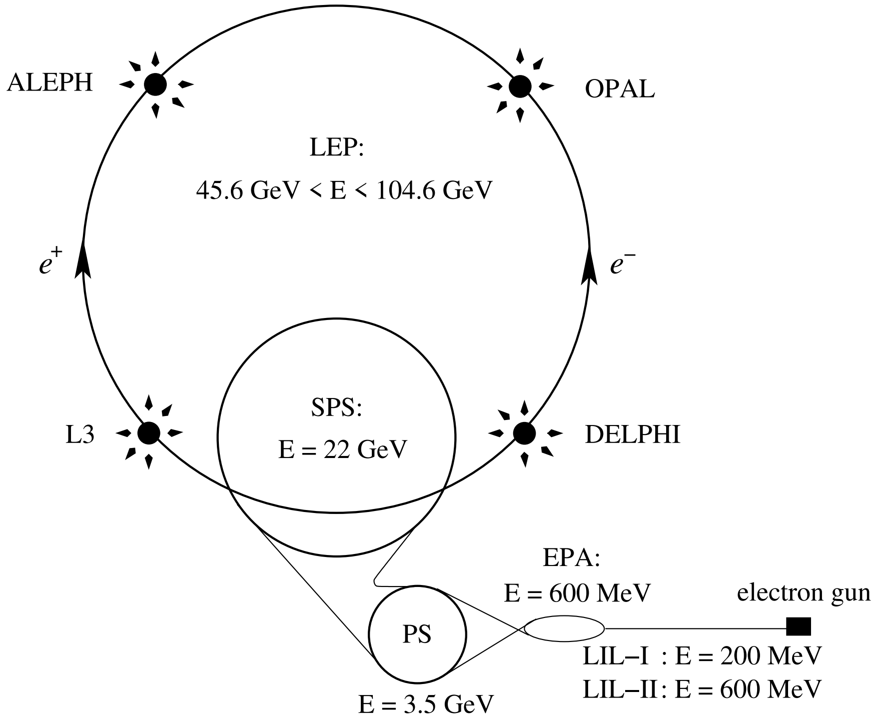

Figure 2.1: *An overview of the full CERN acceleration chain for the electrons and positrons.*

LEP as storage ring and accelerator

Guiding the beams through the vacuum pipe of LEP requires a complex electromagnetic field configuration consisting of dipoles, quadrupoles, sextupoles and both horizontal and vertical dipole correctors. The dipole magnets bend the electrons and positrons along a circular trajectory. The quadrupoles act as magnetic lenses and focus the beam to contain it within the vacuum chamber, while the sextupoles compensate for the dependence of the focusing strength on the beam energy. The dipole correctors steer the beam through the centre of the vacuum pipe.
Electrostatic separators separate the e^- from the e^+ beam, thereby avoiding collisions between them when they are still being accelerated. The acceleration of the electrons and positrons is performed by (super-conducting) Radio-Frequency (RF) cavities located in the straight sections. In addition, these cavities compensate for the energy loss of the electrons and positrons after every revolution, since a charged particle of energy E moving along a circle with radius r radiates energy proportional to E^4/r (synchrotron radiation). For an electron following a circular trajectory the size of LEP this energy loss is given by:

$$\Delta E = 2.1 \times 10^{-8}\ E^4_{\mathrm{beam}}\ \mathrm{GeV\ per\ revolution}, \tag{2.1}$$

where the beam energy E_{beam} is given in GeV, indicating that it looses more than 2% of its energy per revolution if $E_{\mathrm{beam}} = 100$ GeV.
Positioning the four detectors in straight sections of the LEP ring protects them from this radiation.

The operation of LEP can be divided into two periods: during the first one (LEP1; 1989 - 1995), LEP operated at centre-of-mass energies close to 91.2 GeV in order to study accurately the properties of the Z-boson. In that period about four million Z-events were collected by each of the four experiments. The second period (LEP2; 1996 - 2000) is characterised by centre-of-mass energies above the threshold for W-boson pair production with centre-of-mass energies from 161 up to 209 GeV.

Luminosity

Each e^- and e^+ beam consists of four bunches each containing about 3×10^{11} particles that collide head-on at the four points where the detectors are located. The interaction rate $\frac{\mathrm{d}N_{\mathrm{proc}}}{\mathrm{d}t}$ for a specific process depends on its cross section σ_{proc} and the instantaneous luminosity $\mathrm{L}(t)$, which is the number of particles that traverse the interaction region per second per unit area:

$$\frac{\mathrm{d}N_{\mathrm{proc}}}{\mathrm{d}t} = \mathrm{L}(t)\sigma_{\mathrm{proc}} = \frac{N_{e^-}N_{e^+}n_{\mathrm{b}}f_{\mathrm{b}}}{A}\,\sigma_{\mathrm{proc}}, \tag{2.2}$$

where N_{e^-} and N_{e^+} are the number of e^- and e^+ particles per bunch, n_{b} is the number of bunches, f_{b} is the bunch revolution frequency in LEP and A is the area of the interaction region. This region is elliptically shaped and has typical values of 150 μm and 10 μm in the horizontal and vertical plane respectively.

The total number of events from a specific process can be calculated by integrating the collected instantaneous luminosity over a certain period of data-taking with constant energy and multiplying it with the cross section of the corresponding process:

$$N_{\mathrm{proc}} = \sigma_{\mathrm{proc}} \int \mathrm{L}(t)\mathrm{d}t = \sigma_{\mathrm{proc}}\,\mathcal{L}. \tag{2.3}$$

This integrated luminosity $\mathcal{L}$ is obtained by measuring the rate of small angle Bhabha scattering ($e^+e^- \rightarrow e^+e^-$), since this is a process with a clear experimental signature and a large and accurately known cross section.
In this thesis, the data from the years 1998 - 2000 have been analysed. The integrated luminosities collected by the DELPHI detector at the various centre-of-mass energies during these years are given in table 2.1.
After September 1st 2000, DELPHI had to be operated without one twelfth of the main central tracking detector TPC (see section 2.2.1) which was no longer working properly. The period that the complete TPC was operational is referred to as “C-period”, while the period that one twelfth of the TPC was not operational is labelled as “S-period”.

Table 2.1: *Integrated luminosities collected by the DELPHI detector at various centre-of-mass energies during the period 1998 - 2000. The "C" and "S" indicate the periods that the complete TPC was and one twelfth of the TPC was not operational respectively. (note: 1 pb $\equiv 10^{-40}$ m^2)*

year	1998	1999				2000			
$\sqrt{s}$ (GeV)	189	192	196	200	202	<205.5		≥205.5	
$\mathcal{L}$ (pb^{-1})	158	25.8	76.9	84.3	41.1	76.7(C)	6.6(S)	87.8(C)	54.3(S)

2.2 The DELPHI detector

The DELPHI detector (DEtector with Lepton, Photon and Hadron Identification) is one of the four detectors at LEP. It is designed as a general purpose detector for e^+e^- physics with coverage of almost the full solid angle.

In the standard DELPHI coordinate system the origin coincides with the nominal centre of the detector. The z-axis points along the electron direction, the x-axis points towards the centre of LEP and the y-axis points upwards. These Cartesian coordinates are related to the cylindrical coordinates (R, θ, ϕ) in the following way: the polar angle θ defines the angle from the z-axis, the azimuthal angle ϕ defines the angle from the x-axis in the xy-plane and $R = \sqrt{x^2 + y^2}$ as can be seen in figure 2.2.

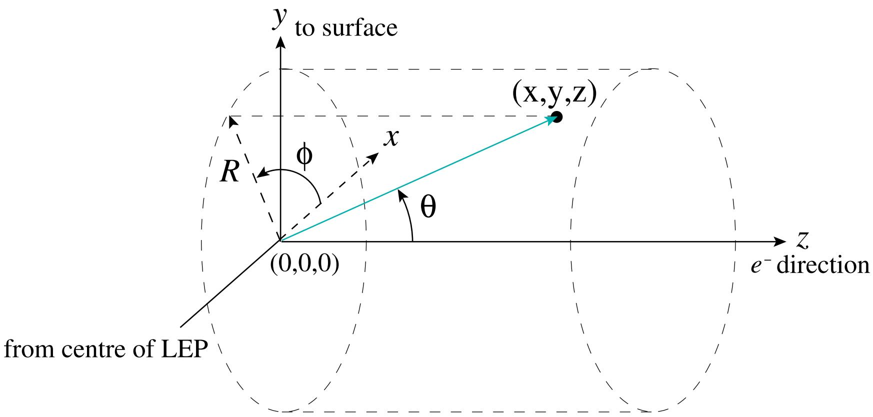

Figure 2.2: *The DELPHI coordinate system in Cartesian and spherical coordinates.*

The centre-of-mass system of the electrons and positrons coincides with the laboratory system of LEP, resulting in an optimal detector design that is symmetric in the interaction point. Both the diameter and the total length of the detector are about 10 m. It consists of a cylindrical central part ("barrel") covering polar angles between 40° and 140° and two parts ("endcaps") that cover the regions between 2° and 40° ("forward" region) and between 140° and 178° ("backward" region) respectively. All three parts consist of various subdetectors as can be seen in the layout of the detector in figure 2.3.

The subdetectors can be divided into two types: tracking detectors and calorimeters. The first

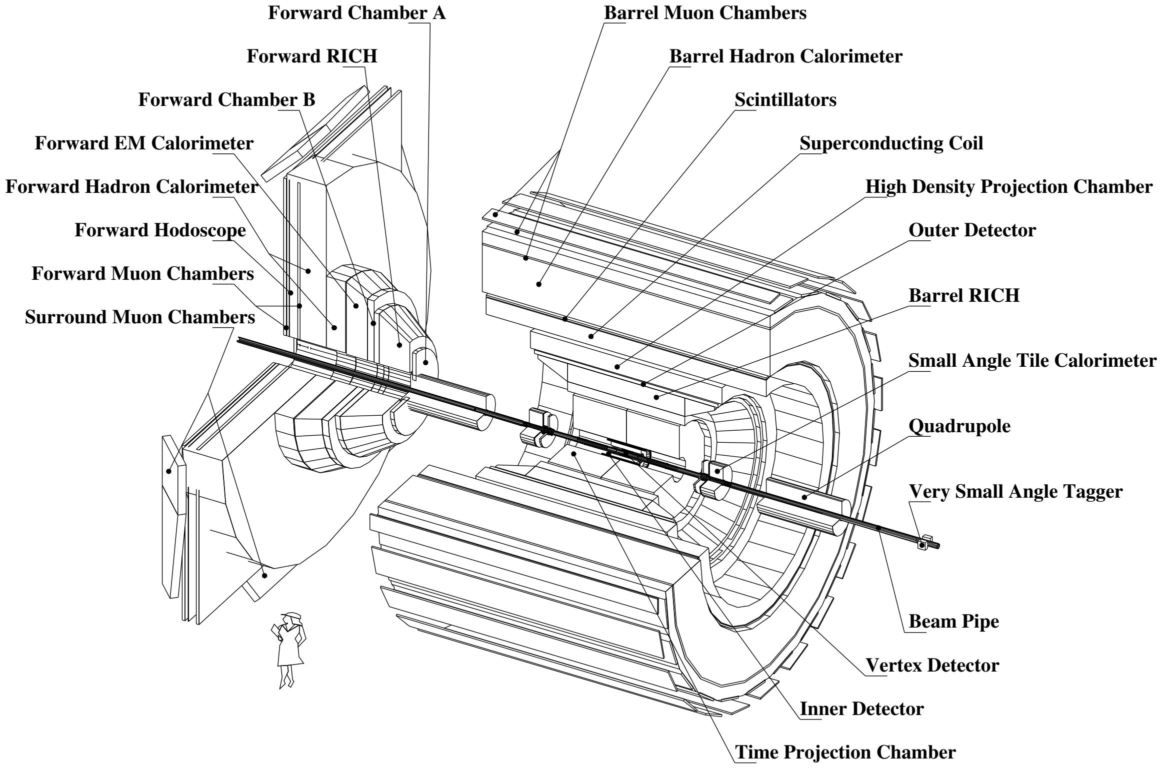

Figure 2.3: *Layout of the DELPHI detector. The barrel and one endcap are shown.*

class of detectors reconstructs the three-dimensional trajectories and momenta of charged particles, while the second type measures the energy deposit in its system. In the next sections both classes and their characteristics will be discussed briefly. A more detailed description of the performance of the DELPHI detector and its subdetectors can be found in [25] and [32].

2.2.1 Tracking detectors

Most of the tracking system is located inside a uniform magnetic field of 1.23 T parallel to the z-axis that bends the trajectory of each charged particle into a spiral with a radius proportional to the momentum of the particle. The field is provided by a large superconducting solenoid with a radius of 2.6 m. The muon chambers are farthest from the interaction point, located outside this magnetic field, since muons are the only charged particles that can traverse the detector completely. The specifications and performance of the tracking detectors described below are summarised in table 2.2.

- Micro-vertex Detector
  The micro-vertex detector is the detector that is located closest to the interaction point. It contains a barrel part and endcap parts, called Silicon Barrel (VD) and Very Forward Trackers (VFTs) respectively.
  The VD consists of three coaxial cylindrical layers of micro-strip silicon detectors located at average radii of 6.6, 9.2 and 10.6 cm. Each layer provides $R\phi$ measurements and covers

Table 2.2: *Specifications and performance of the tracking detectors.*

detector	acceptance R (cm)	$\|z\|$ (cm)	θ (°)	max. no. points along track	resolution per point (mm)
VD	6.6/9.2/10.6	≤ 24	25 - 155	$R\phi$: 3	$R\phi$: 0.008
				z: 2	z: 0.010
VFT			11 - 25; 155 - 169	4	x, y: 0.1
ID jet	11.8 - 22.3	≤ 60	15 - 165	24	$R\phi$: 0.085
ID straws	23 - 28	≤ 105	15 - 165	5	$R\phi$: ~ 0.3
TPC	35 - 111	≤ 134	20 - 160	$R\phi$, z: 16	$R\phi$: 0.25
				$R\phi$: 192	z: 0.88
OD	197 - 206	≤ 232	42 - 138	$R\phi$: 5	$R\phi$: 0.11
				z: 3	z: 35
FCA	30 - 103	155 - 165	11 - 32; 148 - 169	6	x: 0.29
					y: 0.24
FCB	53 - 195	267 - 283	11 - 36; 144 - 169	12	x, y: 0.15
MUB	~ 445	≤ 385	52 - 128	6	$R\phi$: 1.5
					z: 10
MUF	70 - 460	463/500	9 - 43; 137 - 171	x, y: 4	x, y: 1.0
MUS	~ 550	~ 487	42 - 53; 127 - 138	2	10×10

the full azimuthal angle in 24 sectors with overlaps between adjacent sectors. The inner and outer layers are equipped with double-sided silicon detectors, having strips orthogonal to each other, giving also measurements in the z-direction. The VFTs were fully operational from 1997 onwards, extending track reconstruction to polar angles in the ranges 11° - 25° and 155° - 169°. Each of the VFTs consists of two layers of silicon pixel detectors and two layers of micro-strip detectors.

- Inner Detector (ID)
  The ID consists of two parts: an inner drift chamber, surrounded by five concentric layers of straw tubes. The drift chamber has a jet chamber geometry with 24 azimuthal sectors, each providing up to 24 $R\phi$ points per track. The straw tubes provide additional $R\phi$ measurements, mainly used in triggering, and are used to resolve the left-right ambiguities inherent in the jet chamber.

- Time Projection Chamber (TPC)
  The TPC is the principal tracking device of DELPHI. The detector consists of two drift volumes separated by a high voltage (20 kV) plane at $z = 0$, producing an electric field parallel to the beam axis. A charged particle, crossing the TPC, produces by ionisation electrons that drift under influence of the electric field in the direction of the endplates of the TPC. Both endplates are divided into six azimuthal sectors, each with 192 sense wires and sixteen circular pad rows with constant spacing, thus resulting in up to sixteen space points per particle trajectory. The sense wires also provide up to 192 ionisation measurements per track in order to help in charged particle identification by measuring the dE/dx, the specific ionisation energy loss per unit length.

The inclusion of the Ring Imaging Cherenkov detectors (see section 2.2.3) has limited the size of the TPC. To improve the momentum resolution, the following three track chambers (OD, FCA and FCB) have been added.

- Outer Detector (OD)
  The OD consists of five layers of drift tubes subdivided in 24 sectors. All layers provide $R\phi$ measurements and three also give information about the z-coordinate. This detector is important for fast triggering and clearly improves the momentum resolution as can be seen in table 2.3.
- Forward Chambers (FCA and FCB)
  The forward chambers provide powerful tracking and triggering down to $11°$.
  Chambers A are mounted on either end of the TPC. Both sides consist of three modules, each with two staggered layers and split into half-discs with an outer radius of 103 cm. The modules are rotated by $120°$ with respect to each other, thus providing six coordinates.
  Chambers B are drift chambers, consisting of four independent modules, two on each end-cap. Each module contains twelve readout wire planes, four for each of the three wire orientations, rotated by $120°$ with respect to each other.

The momentum resolution of a track is determined by the resolutions of the detectors that have been traversed by the particle. The momentum precision of the tracking system can be illustrated by the resolution of muons produced by $Z \rightarrow \mu^+\mu^-$. Table 2.3 summarises the momentum precision for these dimuons in different polar angle regions and with different detector configurations. As can be seen from the table, the precision deteriorates when less detectors are included and when regions with smaller polar angle are traversed. The latter is caused by the fact that the influence of multiple scattering increases and the number of hits and detectors that provide tracking information decreases.

Table 2.3: *Momentum resolution for 45.6 GeV/c muons in different detector configurations.*

θ (°)	configuration	$\sigma(1/p)$ (GeV/c)$^{-1}$
42 - 138	VD+ID+TPC+OD	0.6×10^{-3}
	ID+TPC+OD	1.1×10^{-3}
	VD+ID+TPC	1.7×10^{-3}
≤ 36; ≥ 144	VD+FCB included	1.3×10^{-3}
25 - 30; 150 - 155	FCB included	1.5×10^{-3}
< 25; > 155	FCB included	2.7×10^{-3}

- Muon Chambers (MUC)
  - Barrel Muon Chambers (MUB)
    The MUB consists of three layers of modules and is divided into 24 azimuthal sectors. The inner layer is embedded 20 cm inside the iron of the barrel hadron calorimeter and the two outer layers lie outside the iron. The modules in the outermost layer cover the holes in the coverage of the other modules in adjoining sectors. Each module is

built up of a number of drift chambers arranged in two active planes. The inner layer contains a third plane that is regarded as spare. The chambers within each plane are staggered, thus resolving the left-right ambiguities of the drift chambers.

- Forward Muon Chambers (MUF)
  The MUF consists of two sets of planes of chambers for each endcap. The first is located 20 cm inside the iron of the forward hadron calorimeter, while the second lies outside this calorimeter. Each plane is composed of four quadrants, each measuring 4.4×4.4 m^2. A quadrant consists of two orthogonal layers of 22 drift chambers.
- Surround Muon Chambers (MUS)
  The MUS covers the gap between the MUB and MUF at polar angles of around 45° and 135°. The eight chambers are installed on the top and sides of the endcaps and are inclined at 45° in order to obtain maximum angular coverage. Each chamber is comprised of two staggered layers of streamer tubes.

2.2.2 Calorimetry

Calorimeters measure the energy that has been deposited by interacting neutral and charged particles by using layers of high density material such as lead or iron. Subsequent interactions of an incoming particle with these layers give rise to a typical "shower", specific for every particle. Different showering characteristics of electrons and photons with respect to hadrons have resulted in a separate electromagnetic and hadronic calorimeter system in order to optimally reconstruct the energy deposit.

Electromagnetic calorimeters

Electromagnetic calorimeters measure the energies of incident electrons and photons. These particles develop electromagnetic showers mainly through bremsstrahlung and e^+e^- pair production respectively, resulting in secondary particles that are again mainly electrons, positrons and photons. This process continues and can be characterised by the material dependent radiation length X_0, which is a measure of the length of material that is needed to reduce by bremsstrahlung the energy of an electron by a factor of e. To contain the cascade completely, calorimeters consist of several radiation lengths. Hadrons traverse the electromagnetic calorimeters hardly affected. The DELPHI electromagnetic calorimeter system covers almost the full solid angle using detectors of which the main characteristics are given table 2.4. A short description of each of them follows hereafter.

- High density Projection Chamber (HPC)
  The HPC is mounted on the inside of the solenoid. It consists of 144 independent modules, arranged in six rings of 24 modules each. Each module is a trapezoidal box with a width ranging from 52 to 64 cm, a height of 47 cm and a length of 90 cm, except for modules in the first and last rings that are smaller. The box is filled with 41 layers of lead of total thickness of $18X_0$ separated by gas gaps of 8 mm. An electromagnetic particle that passes the HPC showers in the lead and ionises the gas. The charge drifts to one end of the box, where it is collected by a proportional chamber with pad readout.

Table 2.4: *Characteristics of the DELPHI electromagnetic calorimeter system.*

detector	acceptance R (cm)	$\|z\|$ (cm)	θ (°)	depth	resolution σ_E/E (E in GeV)
HPC	208 - 260	$\leq$ 254	43 - 137	$18X_0$	0.043 $\oplus$ 0.32/$\sqrt{E}$
FEMC	46 - 240	284 - 340	10.0 - 36.5; 143.5 - 170.0	$20X_0$	0.03 $\oplus$ 0.12/$\sqrt{E}$ $\oplus$ 0.11/E
STIC	6.4 - 41	218 - 249	1.7 - 10.6 ; 169.4 - 178.3	$27X_0$	0.0152 $\oplus$ 0.135/$\sqrt{E}$
VSAT	6 - 9	770	5 - 7 mrad; 3.135 - 3.137 rad	$24X_0$	5% at 45.6 GeV

- Forward Electromagnetic Calorimeter (FEMC)
  The FEMC consists of two arrays, one in each endcap. Each array is made of 4532 Cherenkov lead glass blocks that are truncated pyramids with depths of 40 cm, corresponding to $20X_0$. Each block points to the interaction region with a tilt angle of about $1°$ in order to avoid any particle escaping undetected in the insensitive regions between the blocks. Charged particles inside the electromagnetic shower emit Cherenkov photons that are detected by a photomultiplier at the end of each block.
- Small Angle Tile Calorimeter (STIC) and Very Small Angle Taggers (VSAT)
  The STIC and VSAT are important in the measurement of the luminosity for which small angle Bhabha scattering is used.
  The STIC is a sampling lead-scintillator calorimeter, formed by two cylindrical detectors placed on either side of the interaction region, and covers polar angles below those of the FEMC.
  The VSAT is a calorimeter that is active at even smaller polar angles, between 5 and 7 mrad.

Hadron calorimeters

The hadronic showering process is dominated by a succession of inelastic hadronic interactions, characterised by multiparticle production. The produced charged particles in the shower are detected using scintillators or gaseous detectors inside the converting material. The interaction length λ in a material is defined as the mean free path of a particle between inelastic interactions. The main characteristics of the hadron calorimeters are given in table 2.5.

Table 2.5: *Characteristics of the DELPHI hadron calorimeter system.*

detector	acceptance R (cm)	$\|z\|$ (cm)	θ (°)	depth	resolution σ_E/E (E in GeV)
HCAL barrel	320 - 479	$<$ 380	} 10 - 170	6λ	0.21 $\oplus$ 1.12/$\sqrt{E}$
HCAL forward	65 - 460	340 - 489			

- Hadron Calorimeter (HCAL)
  The hadron calorimeter is a sampling gas detector incorporated in the magnet yoke. It is

made of two endcaps, each consisting of twelve sectors, and a barrel section that consists of 24 modules. 19,032 limited streamer tubes are installed in the 18 mm wide slots between the 50 mm thick iron plates. These tubes are connected to readout boards covering a fixed angular region of $\Delta\theta = 2.96°$ and $\Delta\phi = 3.75°$ consisting of up to 64 pads.

Scintillators

The HPC consists of modules arranged in six rings as has been described before. The gaps between the modules are about 1 cm in ϕ and z, except at $z = 0$, between the third and fourth rings, where there is a gap of 7.5 cm. This central z-gap and all the ϕ-cracks point straight back to the interaction point and make it possible for particles to escape without being detected. There are also large holes in the coverage of the HPC and the FEMC around $\theta = 40°$ and $\theta = 140°$ that also point towards the interaction region. In order to achieve complete hermeticity for high energy photon detection, lead scintillators have been installed in these “blind” regions: the 90°-taggers, the 40°-taggers and the ϕ-taggers. Part of a shower that is produced by a photon in the 40°-taggers can be detected by the FCB, which is called the “Smoking Gun”.

In addition, the DELPHI detector contains in the barrel part, between the solenoid and its return yoke, a cylinder of scintillator counters, the Time of Flight counter (TOF), that provides a fast event triggering. In the forward part, in between the two detection planes of the MUF, the Forward Hodoscope (HOF) serves the same purpose.

2.2.3 Particle identification

Adequate particle identification is crucial, especially when only one muon or electron can be detected as is the case for the leptonic analysis that will be discussed in the next chapter. The Ring Imaging Cherenkov detectors (see next page) and muon chambers have mainly been included in the DELPHI detector for this purpose, while other detectors perform particle identification as a secondary task.

Electron identification

Electron identification in DELPHI is performed using two independent and complementary measurements: the dE/dx measurement of the TPC and the energy deposition in the HPC and FEMC. The dE/dx information is used in the barrel part to a larger extent than in the forward part. The comparison of the energy E in the calorimeters with the independently measured momentum p from the tracking devices provides a powerful tool for electron identification. The distribution of the ratio E/p, which is expected to be close to unity independent of the electron energy, is parametrised and converted into a probability for the electron hypothesis. Two different levels of tagging are provided that classify electrons above a momentum of 2 GeV/c. Their typical efficiencies and misidentification probabilities (measured with $K^0_S \rightarrow \pi^+\pi^-$) are shown in table 2.6.
The efficiencies for electrons above a momentum of 20 GeV/c are almost independent of the momentum and the polar angle θ.

Table 2.6: *Efficiencies and misidentification probabilities for electrons ($p > 3$ GeV/c) in multi-hadronic events.*

tag	efficiency (%)	misident. prob. (%)
loose	80	$\simeq 1.6$
tight	45	$\simeq 0.2$

Muon identification

The iron of the HCAL provides a filter that gives a first level of separation between muons and hadrons. Most hadrons are stopped by the iron, whereas most of the muons of momenta above 2 GeV/c are expected to reach the muon chambers. But there remains a residual activity in the MUC arising from hadronic tracks: punch-throughs from hadronic showers, decays in flight and particles traversing the HCAL contribute to this background. The information about charged particle tracks, reconstructed in the central detectors, is combined with the hits in the MUC. Four different levels of tagging are defined that classify muons above a momentum of 3 GeV/c. Their typical efficiencies and misidentification probabilities (measured with $Z \to \tau^+\tau^-$; $\tau \to 3\pi\nu_\tau$) are shown in table 2.7.

Table 2.7: *Efficiencies and misidentification probabilities for 45.6 GeV/c muons as determined from $Z \to \mu^+\mu^-$.*

tag	efficiency (%)	misident. prob. (%)
very loose	95.9 ± 0.1	5.4 ± 0.2
loose	94.8 ± 0.1	1.5 ± 0.1
standard	86.1 ± 0.2	0.7 ± 0.1
tight	76.0 ± 0.2	0.4 ± 0.1

The efficiencies are depending on the muon momentum and the polar angle θ.

Ring Imaging Cherenkov (RICH) detectors

The RICH detectors provide charged particle identification (mainly pions, kaons and protons) in both the barrel and forward regions using liquid and gas radiators. The liquid radiators are used for particle identification in the momentum range from 0.7 to 8 GeV/c, while the gas radiators are used from 2.5 to 25 GeV/c. The RICH technique is based on the reconstruction of the Cherenkov photons emitted by charged particles. The RICH is not used in the analyses presented in this thesis.

2.2.4 Trigger system and off-line processing

Trigger system

To cope with high luminosities and large background rates, a trigger system has been designed of four successive levels of increasing selectivity. A detailed description of this system can be found in [33, 34]. The first two levels (T1 and T2) are hardware triggers synchronous with the beam crossings (BCOs) (beams cross every 22 μs), making their decisions to either select or reject the event after 3.5 μs and 39 μs respectively. For these decisions, signals from different detectors and combinations of them are used. The last two levels (T3 and T4) are software filters performed asynchronously with respect to the BCO. T3 halves the background passing T2, while T4 rejects about half of the background events remaining after T3.

DELANA

Events that pass the trigger system are collected and stored on magnetic tapes by the Data Acquisition System (DAS). This raw information is not directly useful for physics analyses and has to be processed by the DELPHI off-line system which is done by the DELPHI reconstruction programme DELANA [35]. This programme reconstructs particles by applying pattern recognition and track fitting by combining information from different subdetectors. The output from DELANA is stored on magnetic Data Summary Tapes (DSTs) that are accessible for users for physics analyses that can rely on software packages like SKELANA [36].

DELSIM

To compare the data with expectations, the response of the DELPHI detector is simulated using the DELPHI simulation programme DELSIM [37]. This programme simulates very precisely the response of the DELPHI detector for all particles traversing the detector. The output from DELSIM is subsequently analysed by DELANA and finally written to a DST, analogously to the data.

CHAPTER 3

Event Selection

In this chapter, the selection criteria for the leptonic and hadronic analyses are explained. Before applying such criteria, it is important that the behaviour of the signal, background and data are well-understood. The first part of this chapter shows how this is achieved, while the second part is devoted to the selection of the different single W final states.

3.1 Run quality selection

The data are stored on the DSTs if at least a minimum number of relevant detectors is performing well. To be sure that only data pass the event selections that have been reconstructed with well-operating subdetectors that are indispensable for the analyses described in this thesis, a run quality selection is applied. The following criteria are imposed for the final state $We\nu_e$; $W \to q\bar{q}$:

- the TPC data-taking efficiency must be, together with the data-taking efficiency from the VD, ID or OD, larger than 90%.
- the DELANA status flags for the TPC are checked every event to be sure that the high voltages were on and the TPC was fully operational for the DAS.
- the FCA, FCB or VFT data-taking efficiency must be larger than 90%.
- the HCAL, HPC and FEMC data-taking efficiencies must be larger than 80%.
- the STIC and hermeticity data-taking efficiencies must be larger than 95%.

During the data-taking period in 2000 when one twelfth of the TPC was not working properly, the S-period, the TPC data-taking efficiency is required to be larger than 80%.
For the final state $We\nu_e$; $W \to l\nu_l$ with $l = e$ or μ, the following additional criteria are applied:

- the HPC and FEMC data-taking efficiencies must be larger than 90%.
- the MUC data-taking efficiency must be larger than 80% and the HCAL data-taking efficiency must be larger than 90%.

Imposing this run quality selection reduces the integrated luminosities that are listed in table 2.1 and gives rise to the integrated luminosities that are presented in table 3.1. These luminosities have typical uncertainties of 6‰. Besides these luminosities, the corresponding luminosity weighted centre-of-mass energies during the period 1998 - 2000 are also indicated in table 3.1. In this thesis only the data are analysed that include a fully operational TPC, the C-period.

The energies in the second and fourth column of the table, corresponding to a fully operational TPC, are referred to as 189, 192, 196, 200, 202, 205 and 206.7 GeV respectively throughout the rest of this thesis.

Table 3.1: *Luminosity weighted centre-of-mass energies and corresponding integrated luminosities collected by the DELPHI detector during the period 1998 - 2000 after the run quality selection for the final states $We\nu_e; W \to q\bar{q}$ and $W \to l\nu_l$ with $l = e$ or μ has been applied. The "C" and "S" indicate the periods that the complete TPC was and one twelfth of the TPC was not operational respectively.*

	$We\nu_e; W \to q\bar{q}$		$We\nu_e; W \to l\nu_l$	
year	$\sqrt{s}$ (GeV)	$\mathcal{L}$ (pb^{-1})	$\sqrt{s}$ (GeV)	$\mathcal{L}$ (pb^{-1})
1998	188.63	154.35	188.63	153.81
1999	191.58	25.16	191.58	24.51
	195.51	76.08	195.51	71.99
	199.51	82.79	199.51	81.82
	201.64	40.31	201.63	39.70
2000	204.78(C)	76.25(C)	204.84(C)	69.09(C)
	205.14(S)	6.51(S)	205.14(S)	5.97(S)
	206.61(C)	84.62(C)	206.60(C)	79.82(C)
	206.45(S)	51.46(S)	206.46(S)	44.07(S)

3.2 Event simulation

In order to comprehend well the behaviour of a certain final state, one has to simulate it using a suitable event generator that is capable producing it. In this way, this final state can be studied with a luminosity many orders of magnitude higher than can be observed in the full LEP2 data set. The next two subsections give an overview of the generators that are used to study the selection of the single W final states out of the data set for the years 1998 - 2000.

3.2.1 DELPHI simulation

The most recent event simulations performed by the DELPHI collaboration at LEP2 energies, relevant for the analyses presented in this thesis, can be classified in three main categories:

(a) 4-fermion final states

(b) 2-fermion final states

(c) 2/3-photon final states

For the simulation of events in category (a), DELPHI has chosen WPHACT 2.0 [38] as general 4-fermion generator. One of its features is that it calculates fully massive matrix elements over the whole phase space for all the 4-fermion processes. In general, all these final states can be

divided into three classes: the charged current (CC) final states that are produced via W-pairs, the neutral current (NC) final states that are produced via a pair of neutral vector bosons and the mixed current (MIX) final states that can be produced by both possibilities.
DELPHI has created simulation sets that include both CC and MIX final states ("wphactcc sets") and files that contain both NC and MIX final states ("wphactnc sets").
4-fermion final states can overlap with the $\gamma\gamma$ processes as is the case for $e\bar{e}f\bar{f}$. The simulation of these $e\bar{e}f\bar{f}$ final states by DELPHI depends on the phase space one is dealing with:

- "4-fermion like" region: the multiperipheral contribution (see figure 1.2) is not dominant; wphactcc sets and wphactnc sets are used.
- "$\gamma\gamma$ like" region: the multiperipheral contribution starts to be dominant;
  WPHACT with constituent masses for light quarks are used ("wphactncgg sets").
- pure $\gamma\gamma$ region: the resolved photon component starts to be important.
  - BDK [39] is used for the $e\bar{e}e\bar{e}$ final state.
  - BDKRC [40] is used for the $e\bar{e}\mu\bar{\mu}$ and $e\bar{e}\tau\bar{\tau}$ final states.
  - PYTHIA [41] is used for the $e\bar{e}q\bar{q}$ final state.

The simulation of events belonging to category (b) is split in the following way:

- BHWIDE [42] is used for Bhabha events ($e^+e^-(\gamma)$)
- TEEGG [43] is used for Compton events ($e\gamma(e)$)
- KK2F [44] is used for $\mu^+\mu^-(\gamma)$ and $q\bar{q}(\gamma)$
- KORALZ [45] is used for $\tau^+\tau^-(\gamma)$ and $\nu\bar{\nu}(\gamma)$

The 2/3-photon final states, thus category (c) events, are simulated using the generator QEDBK [46].

Table 3.2 gives an overview of the cross sections of the final states that have just been described, while table 3.3 shows the corresponding luminosities that are used for the analyses.

Table 3.2: *Contributing MC generators for the analyses and their cross sections (in pb) for the various centre-of-mass energies. The cross sections have statistical uncertainties of the order of 0.1 - 0.3%.*

MC generator	$\sqrt{s}$ (GeV) 189	192	196	200	202	205	206.7
wphactcc	18.74	19.16	19.57	19.85	19.97	20.10	20.14
wphactnc	8.15	8.14	8.08	8.03	8.01	7.93	7.90
wphactncgg	58.50	57.21	55.84	55.07	55.31	55.50	55.26
BDK	1826	1834	1838	1848	1856	1857	1867
BDKRC ($e\bar{e}\mu\bar{\mu}$)	1709	1714	1724	1731	1740	1748	1749
BDKRC ($e\bar{e}\tau\bar{\tau}$)	436.7	441.3	445.9	451.8	454.0	457.7	459.9
PYTHIA	13240	13382	13571	13760	13856	13999	14080
BHWIDE	1205	1169	1121	1080	1056	1022	1008
TEEGG	53.4	51.8	49.6	47.7	46.9	45.5	44.7
KK2F ($\mu^+\mu^-(\gamma)$)	9.2	8.9	8.5	8.2	8.0	7.7	7.6
KK2F ($q\bar{q}(\gamma)$)	100.1	96.1	91.3	86.7	84.6	81.2	79.8
KORALZ ($\tau^+\tau^-(\gamma)$)	8.2	7.9	7.6	7.2	7.0	6.8	6.7
KORALZ ($\nu\bar{\nu}(\gamma)$)	11.1	10.9	10.5	10.1	9.9	9.8	9.7
QEDBK	10.7	10.3	9.7	9.4	9.3	8.9	8.7

Table 3.3: *Contributing MC generators for the analyses and their luminosities (in fb^{-1}) for the various centre-of-mass energies. At some places in the table, two numbers are quoted: the first number corresponds with the luminosity for the hadronic analysis, while the second indicates the luminosity for the leptonic analysis.*

MC generator	$\sqrt{s}$ (GeV) 189	192	196	200	202	205	206.7
wphactcc	26.60	26.01	25.42	25.10	9.13	24.73	23.61
wphactnc	58.06	57.45	67.49	37.12	60.51	62.91	59.94
wphactncgg	16.82	17.07	17.53	17.59	17.39	18.20	17.86
BDK	0.27	0.27	0.10	0.11	0.11	0.54/0.27	0.53/0.27
BDKRC ($e\bar{e}\mu\bar{\mu}$)	0.29	0.29	0.11	0.11	0.11	0.57/0.29	0.57/0.29
BDKRC ($e\bar{e}\tau\bar{\tau}$)	1.14	1.15	1.15	4.44/2.52	1.10	2.18	2.20
PYTHIA	0.06	0.06	0.13/0.35	0.13/0.34	0.13/0.34	0.11/0.28	0.11/0.28
BHWIDE	0.83	0.85	0.89	0.93	0.95	0.97	0.50
TEEGG	2.05	0.51	2.06	2.15	1.04	1.11	2.64
KK2F ($\mu^+\mu^-(\gamma)$)	5.42	11.24	11.74	12.26	13.85	13.02	13.21
KK2F ($q\bar{q}(\gamma)$)	5.00	5.19	5.47	5.73	5.90	6.13	6.26
KORALZ ($\tau^+\tau^-(\gamma)$)	4.62	6.28	2.15	5.21	5.02	9.11	10.95
KORALZ ($\nu\bar{\nu}(\gamma)$)	2.26	1.29	6.17	3.40	1.76	3.72	3.14
QEDBK	5.85	6.10	2.42	3.60	1.26	1.34	1.38

3.2.2 GRC4F simulation

Besides the simulations performed centrally by the DELPHI collaboration, simulations are also executed with the generator GRC4F [20, 21]. These simulations include the final states $\mu\nu_\mu e\nu_e$, $e\nu_e e\nu_e$ and $q\bar{q}e\nu_e$ that satisfy their respective Crete definitions and the final states $\mu\nu_\mu e\nu_e$, $e\nu_e e\nu_e$ and $q\bar{q}e\nu_e$ that take into account all contributing diagrams. These latter simulations are not only performed at the SM value of the TGCs, but also at the values α = -2.0, -1.0, 1.0 and 2.0 with α = $\Delta\kappa_\gamma$, λ_γ or Δg_1^Z. Comparable non-SM simulations are also completed for the TGC dependent background processes for the three abovementioned final states. In this chapter, only the SM samples are used, while the non-SM ones are included in the TGC analysis that is described in chapter 5.
GRC4F is used to execute all these simulations, because it covers the full phase space and one can perform non-SM simulations rather easily. One can include the effect of initial and final state radiation for the signal final states and choose a running $\alpha_{\rm QED}$ for this case.
Table 3.4 and table 3.5 show the cross sections and corresponding luminosities of the final states that have been simulated using GRC4F for the leptonic analysis. The l in the final states $l\nu_l\bar{l}\bar{\nu}_l$ and $e\bar{e}\nu_l\bar{\nu}_l$ comprises all three leptons.

Table 3.4: *Simulated final states using GRC4F for the leptonic analysis and their cross sections (in pb) for the various centre-of-mass energies.*

	$\sqrt{s}$ (GeV)						
final state	189	192	196	200	202	205	206.7
$\mu\nu_\mu e\nu_e$ (Crete)	0.078	0.081	0.088	0.093	0.096	0.101	0.104
$\mu\nu_\mu e\nu_e$ (all)	0.526	0.538	0.550	0.566	0.571	0.578	0.581
$e\nu_e e\nu_e$ (Crete)	0.078	0.078	0.086	0.092	0.094	0.097	0.102
$e\nu_e e\nu_e$ (all)	0.637	0.643	0.658	0.680	0.698	0.683	0.658
$\tau\nu_\tau e\nu_e$ (all)	0.472	0.483	0.494	0.504	0.510	0.519	0.525
$l\nu_l\bar{l}\bar{\nu}_l$	0.899	0.913	0.928	0.936	0.939	0.941	0.941
$e\bar{e}\nu_l\bar{\nu}_l$	1.153	1.169	1.178	1.210	1.231	1.220	1.194

Table 3.6 and table 3.7 indicate the cross sections and corresponding luminosities of the final states that have been simulated using GRC4F for the hadronic analysis.

Table 3.5: *Simulated final states using GRC4F for the leptonic analysis and their luminosities (in fb^{-1}) for the various centre-of-mass energies.*

	$\sqrt{s}$ (GeV)						
final state	189	192	196	200	202	205	206.7
$\mu\nu_\mu e\nu_e$ (Crete)	77.29	73.94	68.31	64.82	62.22	59.39	57.74
$\mu\nu_\mu e\nu_e$ (all)	9.68	9.30	8.86	8.55	8.49	8.20	8.12
$e\nu_e e\nu_e$ (Crete)	62.02	60.50	55.55	51.54	49.85	47.74	45.37
$e\nu_e e\nu_e$ (all)	7.84	7.77	7.54	7.16	6.82	7.05	7.13
$\tau\nu_\tau e\nu_e$ (all)	8.86	8.50	8.06	7.79	7.57	7.38	7.21
$l\nu_l\bar{l}\bar{\nu}_l$	6.67	6.57	6.46	6.37	6.36	6.28	6.22
$e\bar{e}\nu_l\bar{\nu}_l$	5.07	4.88	4.75	4.57	4.46	4.54	4.49

Table 3.6: *Simulated final states using GRC4F for the hadronic analysis and their cross sections (in pb) for the various centre-of-mass energies.*

	$\sqrt{s}$ (GeV)						
final state	189	192	196	200	202	205	206.7
$q\bar{q}e\nu_e$ (Crete)	0.487	0.512	0.552	0.589	0.609	0.638	0.655
$q\bar{q}e\nu_e$ (all)	3.311	3.367	3.469	3.533	3.566	3.662	3.626
$q\bar{q}l\nu_l$ ($l \neq e$)	4.795	4.880	4.967	5.016	5.041	5.055	5.060

Table 3.7: *Simulated final states using GRC4F for the hadronic analysis and their luminosities (in fb^{-1}) for the various centre-of-mass energies.*

	$\sqrt{s}$ (GeV)						
final state	189	192	196	200	202	205	206.7
$q\bar{q}e\nu_e$ (Crete)	9.45	8.97	8.38	7.78	7.52	7.19	7.02
$q\bar{q}e\nu_e$ (all)	1.32	1.29	1.25	1.23	1.19	1.15	1.16
$q\bar{q}l\nu_l$ ($l \neq e$)	0.91	0.89	0.87	0.86	0.85	0.85	0.85

3.3 Leptonic event selection

The electron and the anti-electron neutrino or the positron and the electron neutrino coming from the incoming electron and positron are not detected due to the fact that the outgoing electron or positron escapes along the beam pipe and neutrinos cannot be detected at all. Hence, the final state $e^+e^- \rightarrow We\nu_e$; $W \rightarrow l\nu_l$ with $l = e$ or μ is characterised by the presence of only one highly energetic charged lepton accompanied by a large missing momentum without the appearance of another significant energy deposition in the detector. To satisfy the Crete definition for the cross section of this process, the energy of this charged lepton must be larger than 20 GeV as is explained in section 1.4.2. Figures 1.7b) and 1.8b) show that the energy of the charged lepton does not exceed a value of 100 GeV. It is therefore a logical step to include the following preselection for the momentum of the charged track $p_{\rm char}$ besides the condition that the number of charged particles $n_{\rm char} = 1$: $0.10\sqrt{s} \leq p_{\rm char} \leq 0.50\sqrt{s}$.
In order to be sure that a charged particle with small polar angle is detected by one of the tracking detectors in the endcaps, its transverse momentum is required to satisfy: $p_{\rm T,char} \geq 0.10\sqrt{s}$.
The following selection criteria are applied as preselection to optimise the quality of the charged track:

- the relative error on the momentum $\Delta p_{\rm char}/p_{\rm char} < 1$
- the absolute value of the impact parameter along the z-direction $|\mathrm{IP}_z| \leq 2.0$ cm
- the absolute value of the impact parameter in the $R\phi$-plane $|\mathrm{IP}_{R\phi}| \leq 0.04$ cm

The impact parameter is defined for each charged track as being the closest distance between the extrapolated track and the primary vertex, which is the position where the electron and positron have collided. These cuts on the impact parameter are incorporated to remove cosmic events. Figure 3.1 represents these impact parameter distributions for the data and all possible $l\nu_l e\nu_e$ final states and for the subset satisfying the Crete definitions for the electrons and muons for the years 1998 - 2000, weighted to the corresponding integrated luminosities, in case there is only one charged track detected. The data distributions clearly show long tails. Note that in the two lower figures the hatched area is superimposed on top of the white area. Therefore, the white area above the hatched area contains the part of all possible $l\nu_l e\nu_e$ final states that does not satisfy the Crete definitions for the electrons and muons. The hatched area is considered as signal throughout this chapter. The efficiencies and purities, quoted at the end of this section, are determined from these Crete samples. This procedure will be repeated for the hadronic analysis in the next section. In general, selection criteria are obtained by determining the value in a certain distribution where the ratio signal/background clearly starts to decrease.
Since it is assumed that one electron or positron escapes along the beam pipe, it is expected that this particle does not deposit any energy in one of the STICs. Bhabha events are potential background events in case the charged track is an electron or positron. Bhabha events with small polar angles deposit a large amount of energy in one of the STICs. Therefore, events with one charged track that is not identified as a muon and that has deposited energy in one of the STICs are not accepted.

Besides the energy deposition of the charged track, there should be no other significant energy deposition by the possible neutral tracks. As is depicted in figure 3.2, the energy deposition in the electromagnetic calorimeters (EMF and HPC) not related to the charged track is required not to

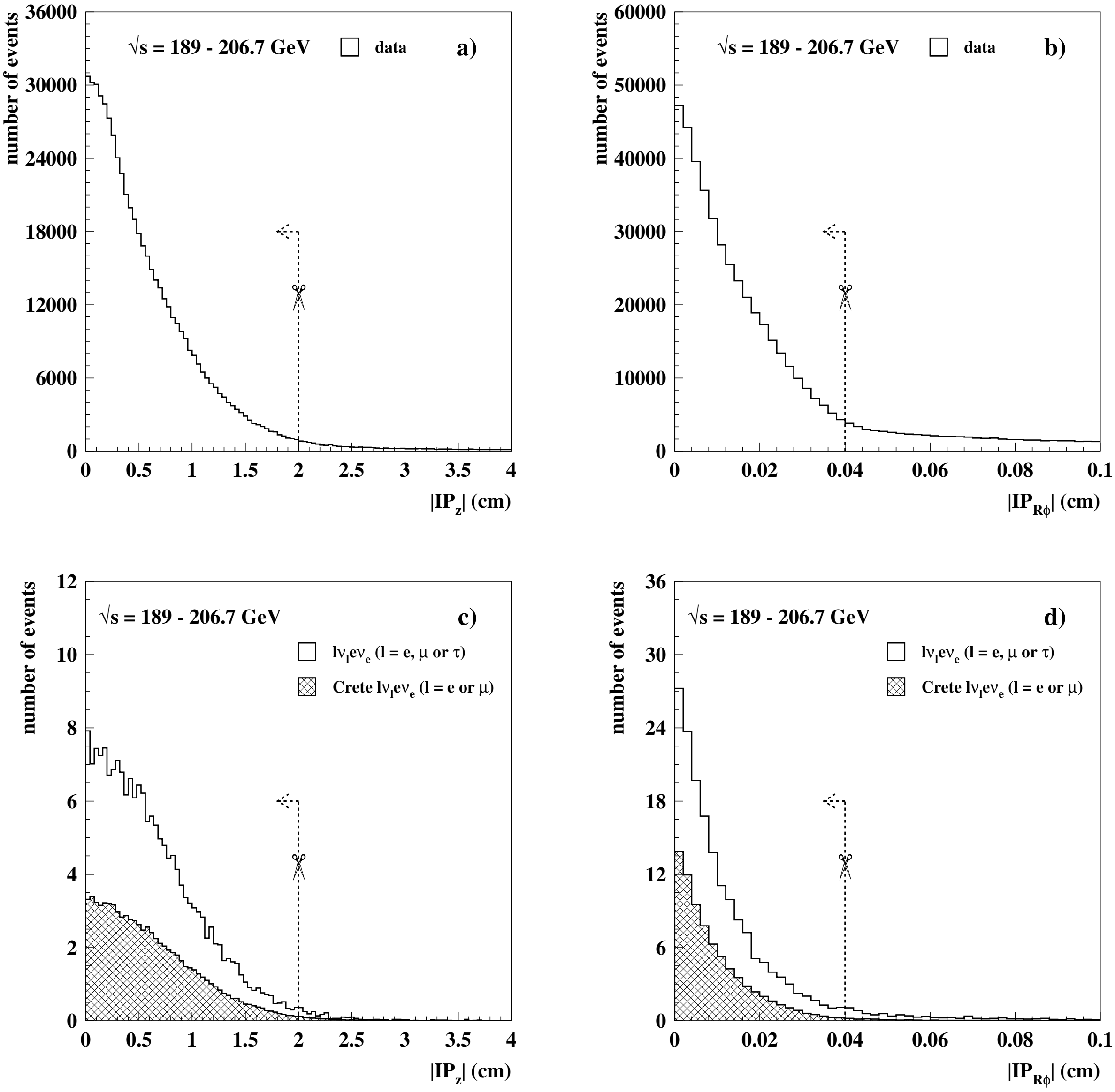

Figure 3.1: *Absolute value of the impact parameter along the z-direction and in the $R\phi$-plane for the data (figures a) and b)) and for all possible $l\nu_l e\nu_e$ final states and the subset satisfying the Crete definitions for the electrons and muons (figures c) and d)) for the energies $\sqrt{s}$ = 189 - 206.7 GeV, weighted to their integrated luminosities, in case there is only one charged track detected. The dashed lines with arrows in the figures show the corresponding cuts.*

exceed 2 GeV: $E_{\mathrm{EMC}} \leq 2$ GeV. Note that the hatched area in the figure is superimposed on top of the white area again and that it corresponds with the Crete $l\nu_l e\nu_e$ final state with $l = e$ or μ and that the white area indicates the $l\nu_l e\nu_e$ final state with $l = e, \mu$ or τ as in figure 3.1. These indications are also used in the figures of the remainder of this section.

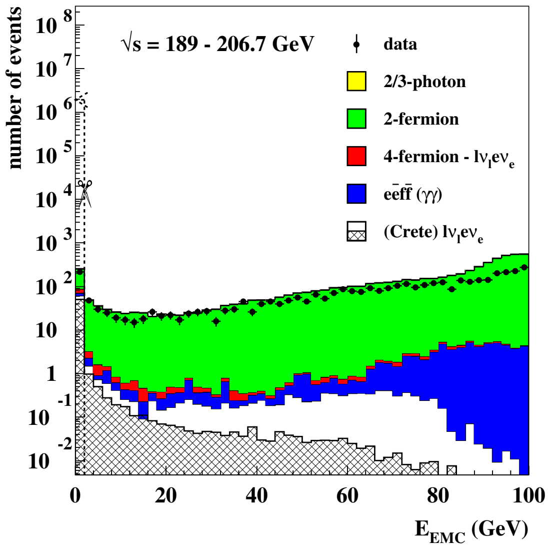

Figure 3.2: *Total energy deposition in the electromagnetic calorimeters (EMF and HPC) not associated to the charged track for the energies $\sqrt{s}$ = 189 - 206.7 GeV. The selection criteria previously defined in the text have already been applied. The dashed line with arrow in the figure shows the corresponding cut.*

$l\bar{l}\gamma$ events with $l = e, \mu$ or τ act also as background to the leptonic single W channel. One of the leptons of this 2-fermion background must escape along the beam pipe and the other lepton and the photon must counterbalance each other with their azimuthal angles: for a "perfect" $l\bar{l}\gamma$ event, their difference in the azimuthal angle $\Delta\phi = 180°$. The photon might give rise to some activity in one of the hermeticity counters. The following cut is applied to reject the contribution from this 2-fermion background as is shown in figure 3.3, showing only the events for which at least one of the counters is active.
Events are *rejected* if:

- the absolute value of the difference in the azimuthal angle between the charged track and the hermeticity tagger with the largest activity $|\phi_{\rm char} - \phi_{\rm tagger}| \geq 160°$.

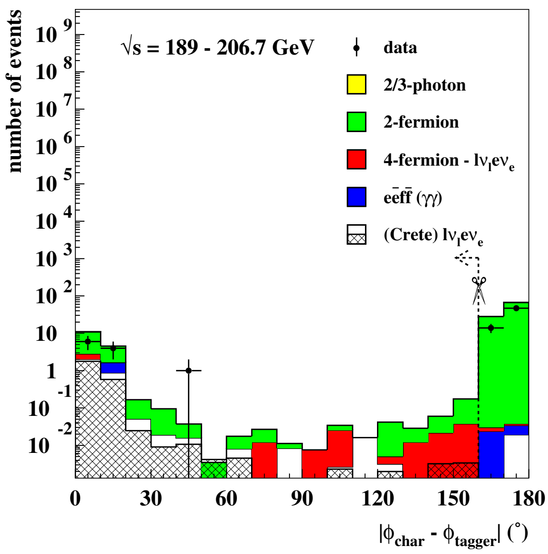

Figure 3.3: *Absolute value of the difference in the azimuthal angle $|\phi_{\rm char} - \phi_{\rm tagger}|$ between the charged track and the hermeticity tagger with the largest activity for the energies $\sqrt{s}$ = 189 - 206.7 GeV. The selection criteria previously defined in the text have already been applied. The dashed line with arrow in the figure shows the corresponding cut.*

$l\bar{l}$ events with $l = e, \mu$ or τ form also potential background events if one of the leptons has not been reconstructed well and the other lepton can be found in the acceptance region of the detector. The topology of this type of events is that the leptons are back-to-back: $\Delta\phi = 180°$. The lepton that has not been reconstructed as a track must have deposited some energy in the direction where it has gone. Therefore, the following cut is applied to *reject* these $l\bar{l}$ events as is shown in figure 3.4, showing only the events that contain a non-zero energy deposition not related to the track.
Events are *rejected* if:

- the absolute value of the difference in the azimuthal angle between the charged track and the largest energy deposition not related to the track $|\phi_{\mathrm{char}} - \phi_{\mathrm{neutral}}| \geq 160°$.

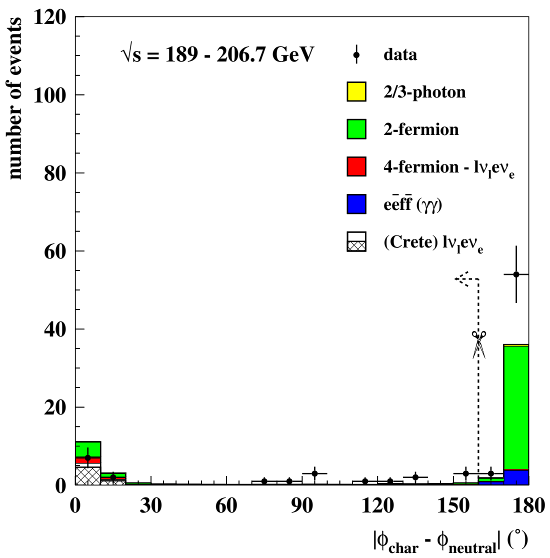

Figure 3.4: *Absolute value of the difference in the azimuthal angle $|\phi_{\mathrm{char}} - \phi_{\mathrm{neutral}}|$ between the charged track and the largest energy deposition not related to the track for the energies $\sqrt{s}$ = 189 - 206.7 GeV. The selection criteria previously defined in the text have already been applied. The dashed line with arrow in the figure shows the corresponding cut.*

The Compton background and $\mu^+\mu^-(\gamma)$ background are restricted by demanding that events that show a maximum energy deposition in the HCAL, not related to the charged track, larger than 2 GeV with $|\phi_{\mathrm{char}} - \phi_{\mathrm{HCAL}}| \geq 160°$ must be discarded. The condition that the total energy deposition in the EMF, not related to the charged track, should not exceed 2 GeV is applied to eliminate $ee(\gamma)$ events.
To reduce the contribution of the 2-fermion background further, the following cut concerning the number of tracks n_{track} is taken into account: $n_{\mathrm{track}} \leq 2$. The impact of this selection criterium is depicted in figure 3.5.
At this stage, it is not known yet what type of particle the charged track is: the charged lepton can be a muon or an electron or even a tau. It is therefore important to form an unambiguous statement about the nature of this charged track, which implies that selections are needed for the particle identification that only allow muons or electrons with a standard or tight tag. The different levels of tagging are explained in section 2.2.3.

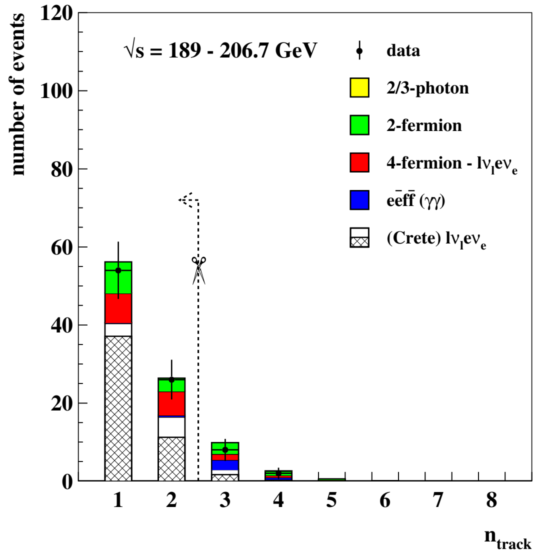

Figure 3.5: *Total number of tracks in the detector for the energies* $\sqrt{s}$ *= 189 - 206.7 GeV. The selection criteria previously defined in the text have already been applied. The dashed line with arrow in the figure indicates the corresponding cut.*

3.3.1 Muon selection

The charged lepton is considered as a muon if the muon tag for this lepton is standard or tight, hence rejecting particles that are tagged as being very loose or loose. Figure 3.6 shows this final cut for the muon event selection.

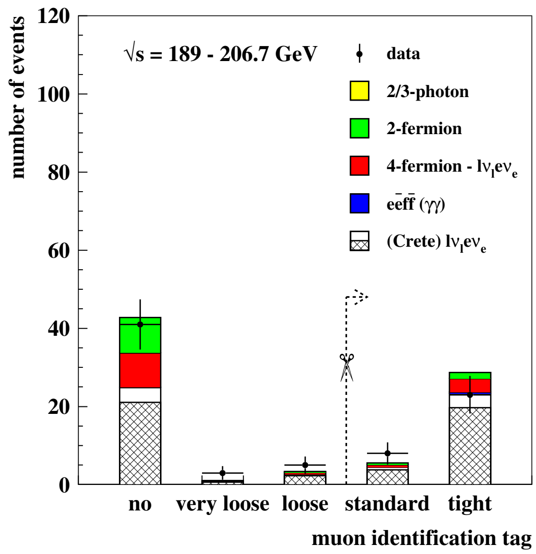

Figure 3.6: *Muon identification tag for the energies* $\sqrt{s}$ *= 189 - 206.7 GeV applied to the sample that remains after the general leptonic event selection. The dashed line with arrow in the figure shows the corresponding cut.*

In figure 3.7 a candidate muon event at $\sqrt{s} = 189$ GeV is presented, clearly showing only one track that has traversed the barrel part of the HCAL and the MUB.
Table 3.8 gives an overview of the different stages of the muon analysis for the years 1998 - 2000, showing how the efficiency ε drops, while the product of the efficiency and the purity $\varepsilon \cdot p$ increases. The disagreement between data and MC is large during the first three steps, which is partly due to the fact that not all possible final states have been simulated centrally by DELPHI

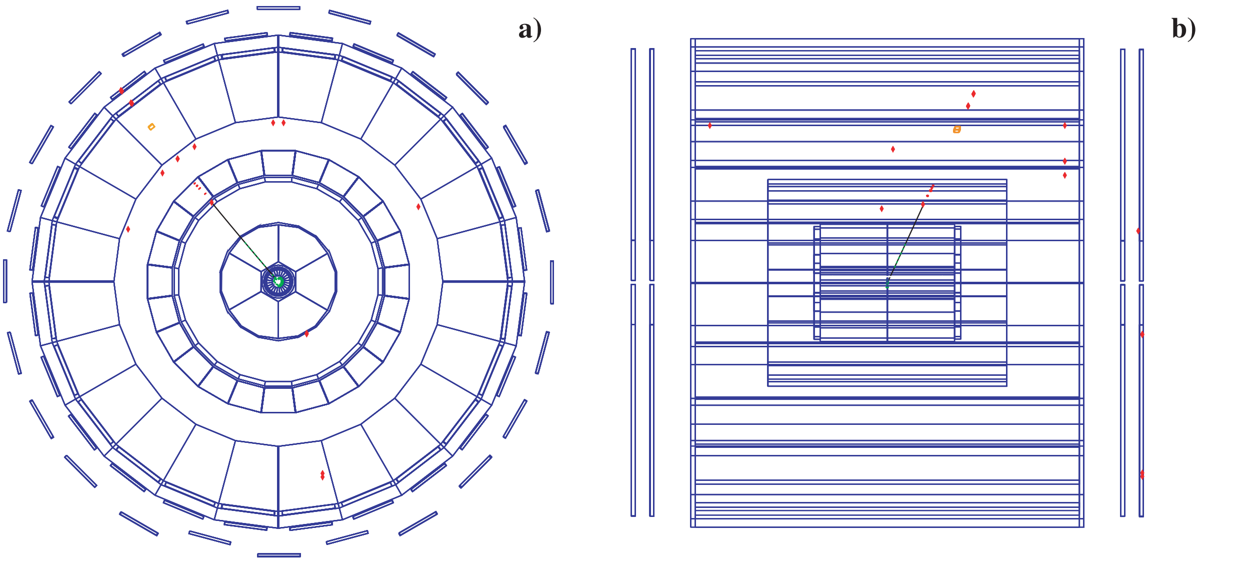

Figure 3.7: *Candidate event for $e^+e^- \to We\nu_e$; $W \to \mu\nu_\mu$ viewed in the xy-plane (a)) and zy-plane (b)) of the DELPHI detector at $\sqrt{s}$ = 189 GeV.*

most recently. From step 4 onwards there is reasonable agreement between data and MC.

Table 3.8: *Number of signal events, background events and data and the corresponding values of the efficiency ε and the product of the efficiency and the purity $\varepsilon \cdot p$ at different stages of the muon analysis for the years 1998 - 2000. The different step numbers correspond with the following sequential selection criteria: step #1: n_{char} = 1; step #2: 0.10$\sqrt{s} \leq p_{\mathrm{char}} \leq$ 0.50$\sqrt{s}$, $p_{\mathrm{T,char}} \geq$ 0.10$\sqrt{s}$, $\Delta p_{\mathrm{char}}/p_{\mathrm{char}} <$ 1; step #3: $|IP_z| \leq$ 2.0 cm and $|IP_{R\phi}| \leq$ 0.04 cm; step #4: Bhabha rejection and $E_{\mathrm{EMC}} \leq$ 2 GeV; step #5: $|\phi_{\mathrm{char}} - \phi_{\mathrm{tagger}}| \geq$ 160°; step #6: $|\phi_{\mathrm{char}} - \phi_{\mathrm{neutral}}| \geq$ 160°, Compton, $\mu^+\mu^-(\gamma)$ and $ee(\gamma)$ rejection; step #7: $n_{\mathrm{track}} \leq$ 2; step #8: cut on muon tag. See the text and figures in this section for more details.*

step	$N_{\mu\nu_\mu e\nu_e,\mathrm{Crete}}$	$N_{\mathrm{background}}$	N_{expected}	N_{observed}	ε (%)	$\varepsilon \cdot p$
#1	37.96	1100662.04	1100700.00	599852	80.9	2.79×10^{-5}
#2	31.86	13429.24	13461.10	17435	67.9	1.61×10^{-3}
#3	31.40	12121.50	12152.90	7868	66.9	1.73×10^{-3}
#4	29.47	224.89	254.37	217	62.8	7.27×10^{-2}
#5	29.47	129.06	158.53	156	62.8	1.17×10^{-1}
#6	29.26	66.35	95.61	90	62.4	1.91×10^{-1}
#7	28.37	54.08	82.45	80	60.5	2.08×10^{-1}
#8	23.48	10.81	34.29	31	50.0	3.43×10^{-1}

3.3.2 Electron selection

For the electron identification, the package REMCLU [47] is applied in both the barrel and the endcaps. Only events with a tight tag are accepted and in the endcaps only events are selected if they lack any energy deposition in the STICs and if they satisfy $|\cos\theta_e| \leq 0.92$.
The cut on the polar angle of the identified electron is needed, since the relative tracking efficiency for electrons at smaller polar angles is too low as is shown in figure 3.8b). This tracking efficiency $\varepsilon_{\mathrm{track},e}$ has been deduced from events that have passed the complete track selection, which includes all sequential selection criteria up to the Bhabha rejection cut as previously described, with a single charged track that has deposited more than 10 GeV in the HPC or EMF and with a total energy deposition in the electromagnetic calorimeters not related to the charged track smaller than 5 GeV. Imposing these conditions results in the $|\cos\theta_e|$-distributions for the barrel and endcaps for the data and Compton and Bhabha events (mainly Compton) as shown in figure 3.8.

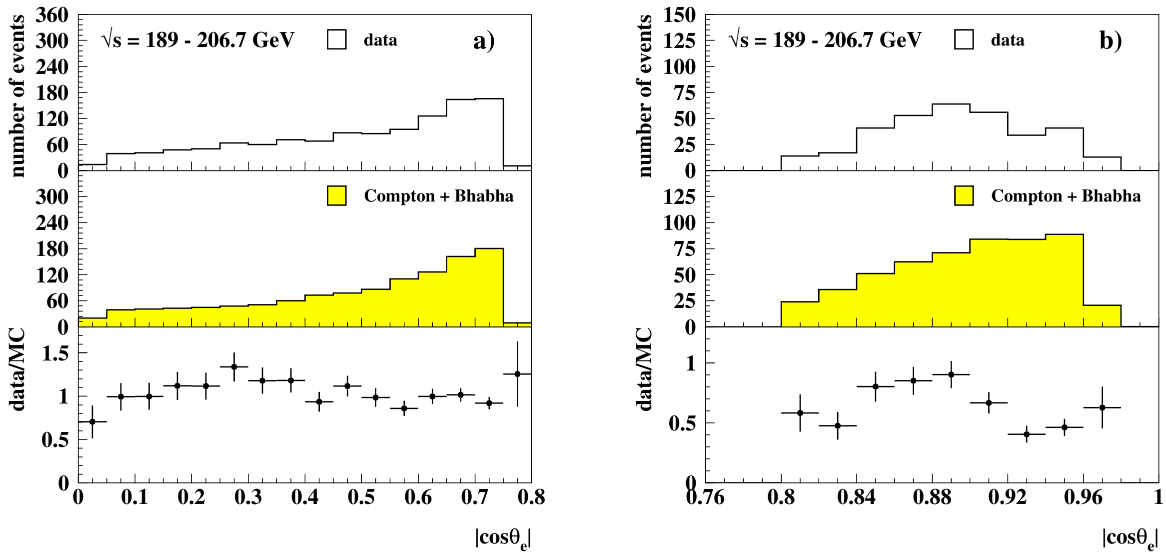

Figure 3.8: $|\cos\theta_e|$*-distributions for the barrel (a)) and endcaps (b)) for the data and Compton and Bhabha events and their ratio for the years 1998 - 2000 combined. Events in these distributions have passed the complete track selection, which includes all sequential selection criteria up to the Bhabha rejection cut as described in the text, with a single charged track that has deposited more than 10 GeV in the HPC or EMF and with a total energy deposition in the electromagnetic calorimeters not related to the charged track smaller than 5 GeV.*

The $|\cos\theta_e|$-distribution for data/MC for the barrel is rather flat with an average value of data/MC = 1.00 $\pm$ 0.03, while this distribution for the endcaps shows more irregularities. The discrepancy between data and MC in the region $|\cos\theta_e| > 0.92$ is too large to be included in the event selection. The value of data/MC for the region $0.80 \leq |\cos\theta_e| \leq 0.92$ gives an average value of 0.72 ± 0.10. Both errors indicate the statistical and systematic error and take into account the difference in

$\cos\theta_e$-dependence of the data and MC. In the endcaps, the MC will be scaled with this factor to obtain a better description of the data. Figure 3.9 shows the final selection criteria for the electron event selection.

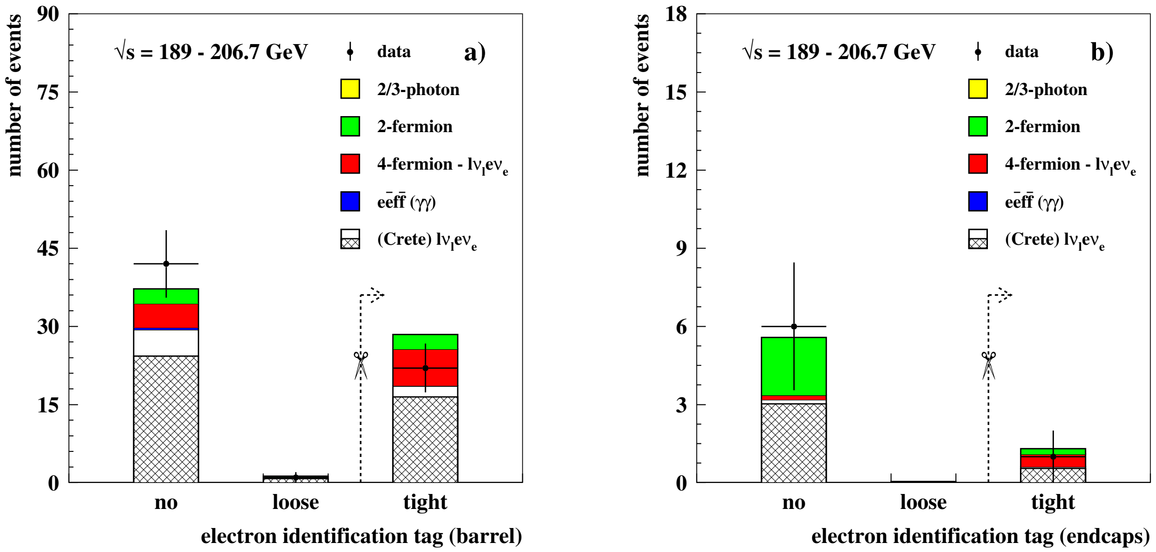

Figure 3.9: *Electron identification tag for the barrel (a)) and the endcaps (b)) for the energies* $\sqrt{s}$ = *189 - 206.7 GeV applied to the sample that remains after the general leptonic event selection. The events in the right plot lack any energy deposition in one of the STICs and satisfy* $|\cos\theta_e| \leq$ *0.92. The dashed lines with arrows in the figures show the corresponding cuts.*

Figure 3.10 presents a candidate electron event at $\sqrt{s} = 202$ GeV with a large energy deposition in the HPC.
Table 3.9 shows the different stages of the electron analysis for the years 1998 - 2000 combined, showing how the efficiency ε drops, while the product of the efficiency and the purity $\varepsilon \cdot p$ increases. Note that the quoted efficiencies, like all efficiencies in this chapter, are determined with respect to the full phase space.
Figure 3.11 shows the distribution of $|\cos\theta_e|$ at $\sqrt{s}$ = 189 GeV, where the "e" represents the electron or positron with energy larger than 20 GeV in the Crete definition for the $e\nu_e e\nu_e$ final state. The typical percentages for the three regions indicated in the figure are:
barrel: $|\cos\theta_e| \leq 0.766$: 74.7 $\pm$ 0.1%, endcaps 1: $0.766 < |\cos\theta_e| \leq 0.92$: 20.4 $\pm$ 0.1% and endcaps 2: $|\cos\theta_e| > 0.92$: 4.9 $\pm$ 0.1%

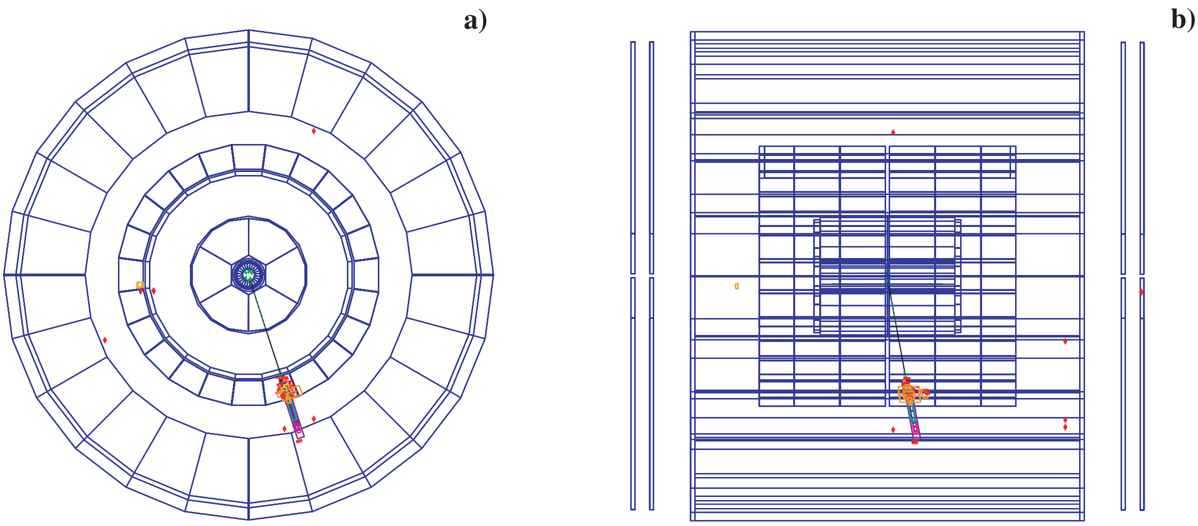

Figure 3.10: *Candidate event for $e^+e^- \rightarrow We\nu_e$; $W \rightarrow e\nu_e$ viewed in the xy-plane (a)) and zy-plane (b)) of the DELPHI detector at $\sqrt{s}$ = 202 GeV.*

Table 3.9: *Number of signal events, background events and data and the corresponding values of the efficiency ε and the product of the efficiency and the purity $\varepsilon \cdot p$ at different stages of the electron analysis for the years 1998 - 2000 combined. Steps #1 - #7 are the same as the ones listed in the caption of table 3.8. Steps #9a and #9b correspond with the cuts on the electron tags for the barrel and endcaps respectively.*

step	$N_{e\nu_e e\nu_e,\mathrm{Crete}}$	$N_{\mathrm{background}}$	N_{expected}	N_{observed}	ε (%)	$\varepsilon \cdot p$
#1	40.89	1100659.11	1100700.00	599852	88.3	3.28×10^{-5}
#2	31.05	13430.05	13461.10	17435	67.1	1.55×10^{-3}
#3	30.51	12122.39	12152.90	7868	65.9	1.65×10^{-3}
#4	21.44	232.93	254.37	217	46.3	3.90×10^{-2}
#5	21.44	137.09	158.53	156	46.3	6.26×10^{-2}
#6	21.04	74.57	95.61	90	45.4	1.00×10^{-1}
#7	19.95	62.50	82.45	80	43.1	1.04×10^{-1}
#9a	16.45	11.92	28.36	22	} 36.7	} 2.11×10^{-1}
#9b	0.54	0.75	1.29	1		

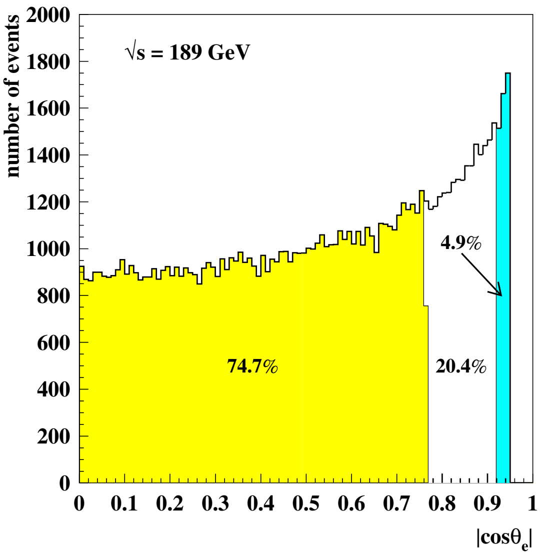

Figure 3.11: *Typical distribution of* $|\cos\theta_e|$ *at* $\sqrt{s}$ *= 189 GeV, where the "*e*" represents the electron or positron with energy larger than 20 GeV in the Crete definition for the* $e\nu_e e\nu_e$ *final state. Three regions are considered from left to right: barrel:* $|\cos\theta_e| \leq$ *0.766, endcaps 1: 0.766* $<$ $|\cos\theta_e| \leq$ *0.92 and endcaps 2:* $|\cos\theta_e| >$ *0.92.*

3.4 Hadronic event selection

The experimental signature of the final state $e^+e^- \to We\nu_e; W \to q\bar{q}$ consists of two acoplanar[1] jets with a large amount of missing energy due to the undetected electron and anti-electron neutrino (or positron and electron neutrino). Requiring that the number of charged tracks $n_{\mathrm{char}} \geq 7$ significantly reduces the number of observed events and hardly decreases the signal as can be seen from figure 3.12. This cut especially diminishes the contribution from lepton pairs and $\gamma\gamma$ events.

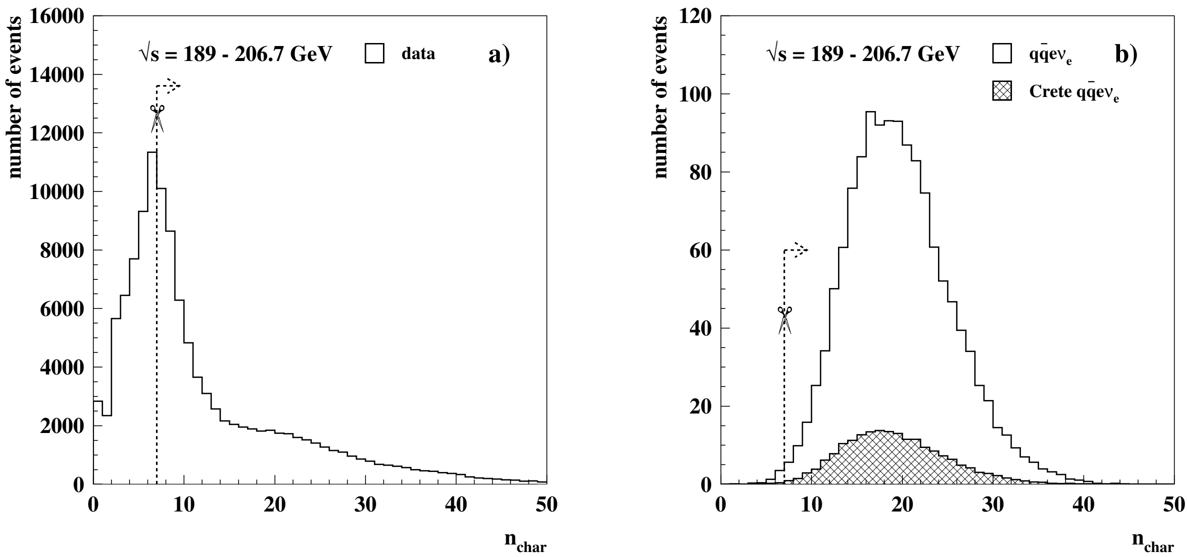

Figure 3.12: *Number of charged tracks for the data (a)) and for all possible $q\bar{q}e\nu_e$ final states and for the subset satisfying the Crete definitions for the hadrons (b)) for the energies $\sqrt{s}$ = 189 - 206.7 GeV. The dashed lines with arrows in the figures show the corresponding cut.*

For this analysis, events are forced into a 2-jet topology. For the reconstruction of jets, the DURHAM clustering algorithm [48] is used. This algorithm starts from a list of particles that is considered as the initial set of clusters. The two clusters with the smallest relative "distance" d_{ij} are merged into one, provided their distance is below some predefined minimum separation d_{cut}. The 4-momentum of the new cluster k is obtained from its constituents i and j by adding their 4-momenta: $p_k = p_i + p_j$. This joining procedure is repeated until all clusters exceed d_{cut}. These final clusters are called "jets".
In the DURHAM algorithm, the distance d_{ij} is defined by:

$$d_{ij}^2 = 2\min(E_i^2, E_j^2)(1 - \cos\theta_{ij}), \tag{3.1}$$

where θ_{ij} is the opening angle between the momentum vectors of the two clusters i and j.

[1]The acoplanarity between two vectors is defined as $|180° - |\phi_1 - \phi_2||$, where ϕ_1 and ϕ_2 are the azimuthal angles of the two vectors in degrees.

The dimensionless variables

$$y_{ij} = \frac{d_{ij}^2}{E_{\mathrm{vis}}^2} = \frac{2\min(E_i^2, E_j^2)(1 - \cos\theta_{ij})}{E_{\mathrm{vis}}^2} \quad (3.2)$$

and

$$y_{\mathrm{cut}} = \frac{d_{\mathrm{cut}}^2}{E_{\mathrm{vis}}^2} \quad (3.3)$$

are more often quoted in literature.
In order to reduce significantly the contribution from the background, it is required that the reconstructed jets satisfy: $|\cos\theta_{\mathrm{jet}}| \leq 0.85$. The reason why these cuts are applied is that it is desirable to have particles clustered in a jet that are well-reconstructed. The influence of these cuts for the data and signal is depicted in figure 3.13.

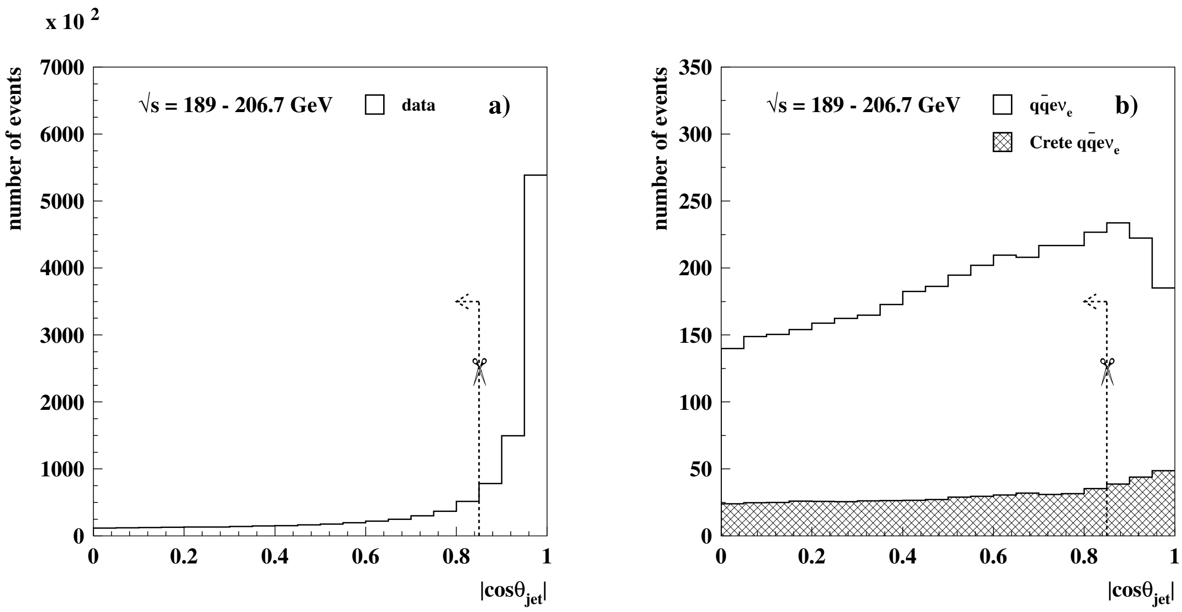

Figure 3.13: *Absolute value of the cosine of the polar angle of the two reconstructed jets for the data (a)) and for all possible $q\bar{q}e\nu_e$ final states and for the subset satisfying the Crete definitions for the hadrons (b)) for the energies $\sqrt{s}$ = 189 - 206.7 GeV. The dashed lines with arrows in the figures show the corresponding cut.*

Since the electron or positron escapes along the beam pipe, the total charged energy E_{char} or the dimensionless variable $E_{\mathrm{char}}/\sqrt{s}$ must be bounded. Figure 3.14 shows that the following cut is applied: $0.16\sqrt{s} \leq E_{\mathrm{char}} \leq 0.56\sqrt{s}$.
The specific signature of the signal gives rise to a small amount of energy in one of the FEMCs, contrary to Bhabha events. Therefore, a firm cut in the distribution of $\sqrt{E_{\mathrm{F}}^2 + E_{\mathrm{B}}^2}/E_{\mathrm{beam}}$, where E_{F} and E_{B} are the total deposited energy in the forward EMC and backward EMC respectively, strongly reduces the background. The exact value of this selection criterium can be read from figure 3.15: $\sqrt{E_{\mathrm{F}}^2 + E_{\mathrm{B}}^2} \leq 0.18E_{\mathrm{beam}}$.

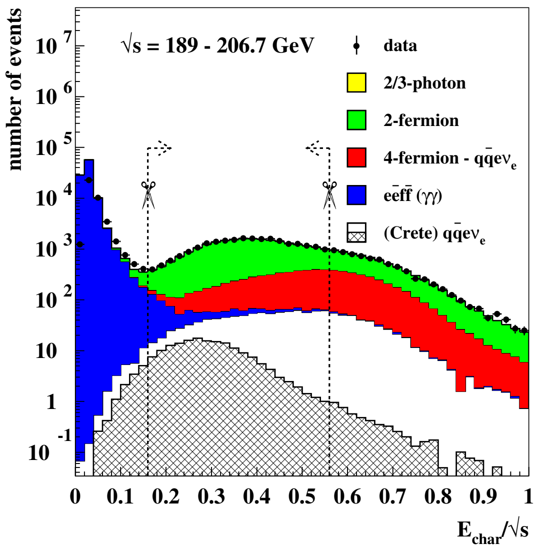

Figure 3.14: *Total charged energy divided by the corresponding centre-of-mass energy $E_{\rm char}/\sqrt{s}$ for the energies $\sqrt{s}$ = 189 - 206.7 GeV. The selection criteria previously defined in the text have already been applied. The dashed lines with arrows in the figure show the corresponding cuts.*

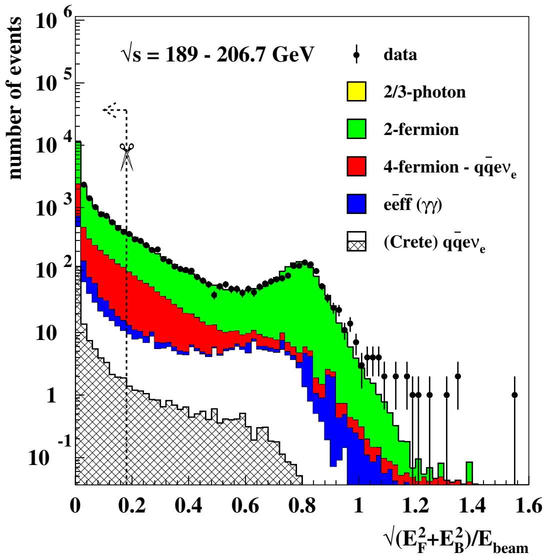

Figure 3.15: *Energy deposited in the forward and backward EMC, $E_{\rm F}$ and $E_{\rm B}$, divided by the corresponding beam energy $\sqrt{E_{\rm F}^2+E_{\rm B}^2}/E_{\rm beam}$ for the energies $\sqrt{s}$ = 189 - 206.7 GeV. The selection criteria previously defined in the text have already been applied. The dashed line with arrow in the figure shows the corresponding cut.*

The total transverse neutral energy $E_{\rm T,neutral}$ is also bounded, because of the characteristics of the signal. Figure 3.16 shows that the cut $E_{\rm T,neutral} \leq 0.30\sqrt{s}$ significantly reduces the background.

Cuts on the related variables $E_{\rm vis}/\sqrt{s}$ and $p_{\rm T,miss}/\sqrt{s}$ are also taken into account for the selection. After having applied the cut $0.28\sqrt{s} \leq E_{\rm vis} \leq 0.68\sqrt{s}$ on the former variable as depicted in figure 3.17, the background is further reduced by constraining the latter variable by $0.04\sqrt{s} \leq p_{\rm T,miss} \leq 0.36\sqrt{s}$ as shown in figure 3.18.

Another variable related to the missing momentum that clearly differentiates the signal and the background is the absolute value of the cosine of this vector, $|\cos\theta_{\rm miss}|$. Figure 3.19 indicates that the corresponding cut to this variable satisfies: $|\cos\theta_{\rm miss}| \leq 0.90$.

A photon that is radiated by the incoming electron or positron, an initial state radiation (ISR) photon, gives rise to a reduction of the centre-of-mass energy $\sqrt{s}$, leading to an effective centre-

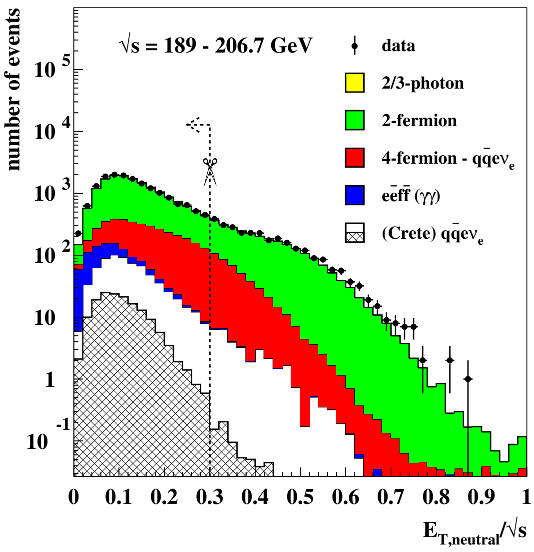

Figure 3.16: *Total transverse neutral energy divided by the corresponding centre-of-mass energy $E_{\mathrm{T,neutral}}/\sqrt{s}$ for the energies $\sqrt{s}$ = 189 - 206.7 GeV. The selection criteria previously defined in the text have already been applied. The dashed line with arrow in the figure shows the corresponding cut.*

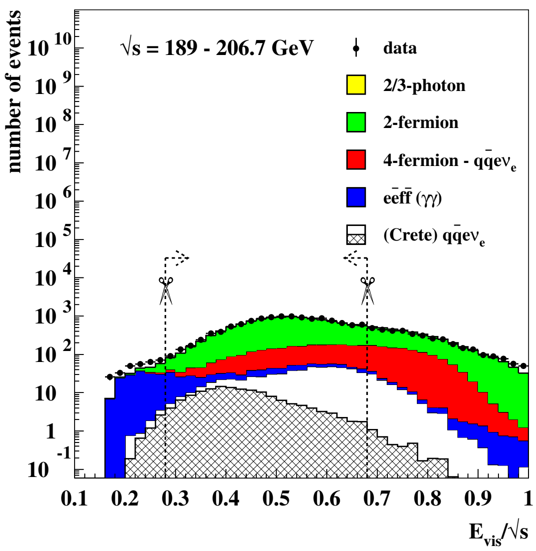

Figure 3.17: *Total visible energy divided by the corresponding centre-of-mass energy $E_{\mathrm{vis}}/\sqrt{s}$ for the energies $\sqrt{s}$ = 189 - 206.7 GeV. The selection criteria previously defined in the text have already been applied. The dashed lines with arrows in the figure show the corresponding cuts.*

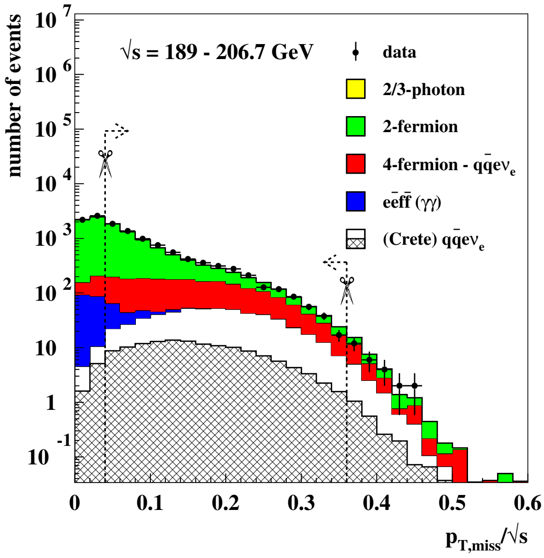

Figure 3.18: *Total transverse missing momentum divided by the corresponding centre-of-mass energy $p_{\mathrm{T,miss}}/\sqrt{s}$ for the energies $\sqrt{s}$ = 189 - 206.7 GeV. The selection criteria previously defined in the text have already been applied. The dashed lines with arrows in the figure show the corresponding cuts.*

of-mass energy $\sqrt{s'}$. This reduction can, of course, also be the result of a number of ISR photons. As shown in figure 3.20, $\sqrt{s'}$, being calculated using the updated DELPHI SPRIME package [49], has to satisfy: $0.38\sqrt{s} \leq \sqrt{s'} \leq 0.92\sqrt{s}$.

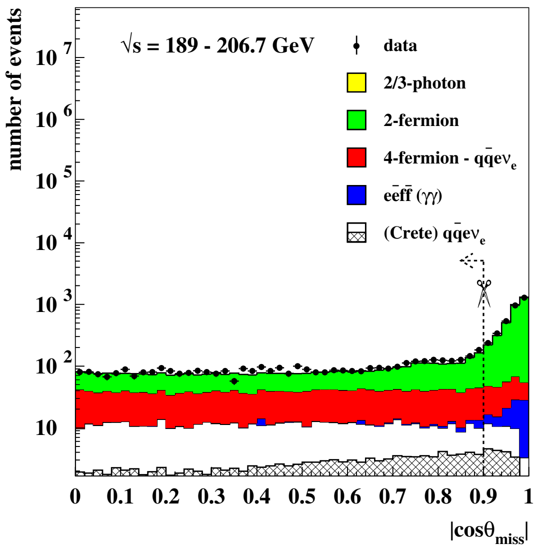

Figure 3.19: *Absolute value of the cosine of the polar angle of the missing momentum* $|\cos\theta_{\text{miss}}|$ *for the energies* $\sqrt{s}$ *= 189 - 206.7 GeV. The selection criteria previously defined in the text have already been applied. The dashed line with arrow in the figure shows the corresponding cut.*

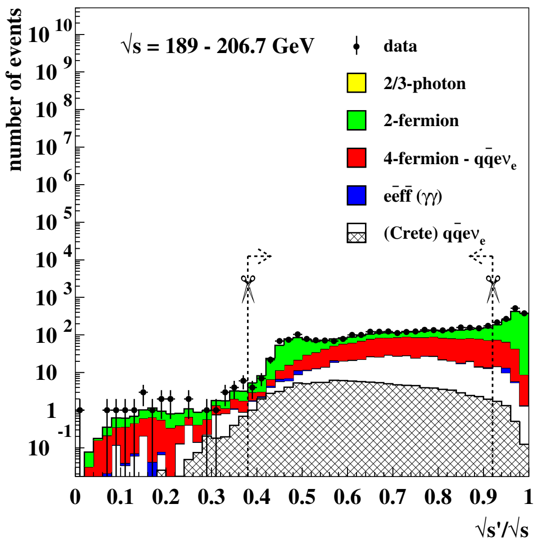

Figure 3.20: *Effective centre-of-mass energy divided by the corresponding centre-of-mass energy* $\sqrt{s'}/\sqrt{s}$ *for the energies* $\sqrt{s}$ *= 189 - 206.7 GeV. The selection criteria previously defined in the text have already been applied. The dashed lines with arrows in the figure show the corresponding cuts.*

As can be seen from figure 3.21, the invariant mass of the two reconstructed jets $M_{j\bar{j}}$ for the signal does not always exceed the Crete definition value of 45 GeV/c^2 and its distribution does not peak at 80 GeV/c^2, which is caused by the fact that there has not been applied a constrained fit. Requiring the invariant mass of the two reconstructed jets to satisfy 30 GeV/c^2 $\leq M_{j\bar{j}} \leq$ 90 GeV/c^2 introduces a large reduction of the background.

Since it is expected that the two reconstructed jets of the signal are not completely back-to-back like the 2-fermion background, the acoplanarity serves as a good discriminating variable. Figure 3.22 indicates the imposed cut for this variable: $10^\circ \leq$ acoplanarity $\leq 100^\circ$.

Figure 3.22 shows that at this level the most important contribution to the background is coming from 4-fermion events, mainly from WW events. In case this W-pair decays fully hadronically, a 4-jet topology should be observed, while in case of a semi-leptonic decay of this pair two jets

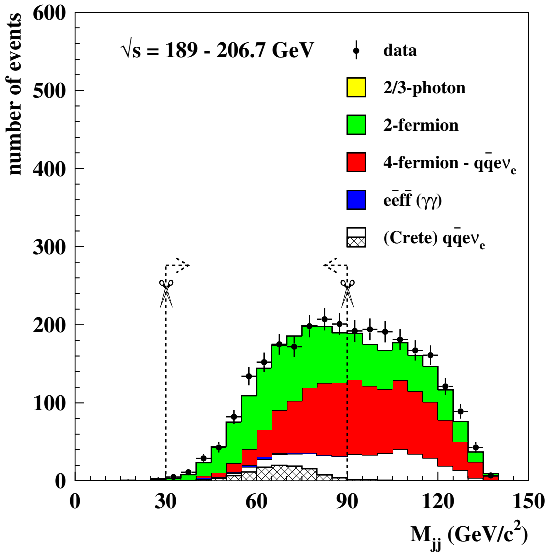

Figure 3.21: *Invariant mass of the two reconstructed jets $M_{j\bar{j}}$ for the energies $\sqrt{s}$ = 189 - 206.7 GeV. The selection criteria previously defined in the text have already been applied. The dashed lines with arrows in the figure show the corresponding cuts.*

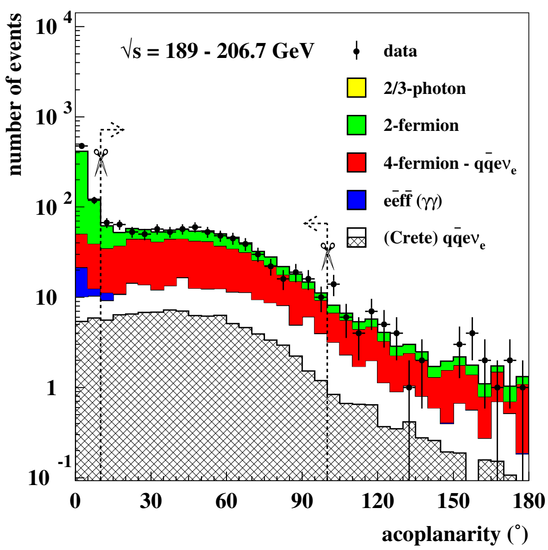

Figure 3.22: *Acoplanarity of the two reconstructed jets for the energies $\sqrt{s}$ = 189 - 206.7 GeV. The selection criteria previously defined in the text have already been applied. The dashed lines with arrows in the figure show the corresponding cuts.*

and an isolated lepton with high energy should be seen. In order to reduce the contribution from these decay modes of the W-pair, cuts on the variables $y_{\mathrm{cut},34}$ and $y_{\mathrm{cut},23}$ (see equation (3.3)) are applied. For clarity, these variables determine the values of the y_{cut} in case the event is merged from 4 to 3 jets and from 3 to 2 jets respectively. Figure 3.23 represents the distributions of these variables of the data and MC after having applied the previously defined selection criteria. After having reduced the background via $y_{\mathrm{cut},34} \leq 0.007$, it is further diminished by $y_{\mathrm{cut},23} \leq 0.03$.

The contribution from the semi-leptonically decaying W-pair is decreased by setting an upper bound to the value of the maximum transverse momentum of any charged track with respect to the closest jet $p_{\mathrm{T}}^{\mathrm{max}}$. The value of this variable is set to $p_{\mathrm{T}}^{\mathrm{max}} \leq 8$ GeV/c as can be seen from figure 3.24.

Determining the transverse momentum of every track with respect to the closest jet and taking

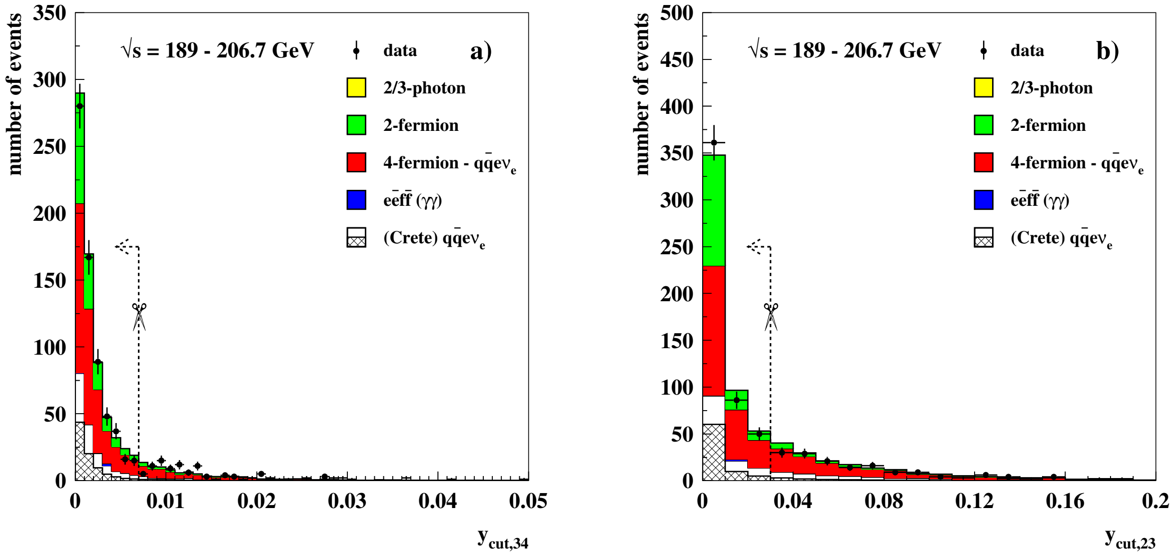

Figure 3.23: *Distributions of the scaled Durham variables $y_{\mathrm{cut},34}$ (a)) and $y_{\mathrm{cut},23}$ (b)) for the energies $\sqrt{s}$ = 189 - 206.7 GeV. The distribution of $y_{\mathrm{cut},23}$ is obtained after the cut on the distribution of $y_{\mathrm{cut},34}$. The dashed lines with arrows in the figures show the corresponding cuts.*

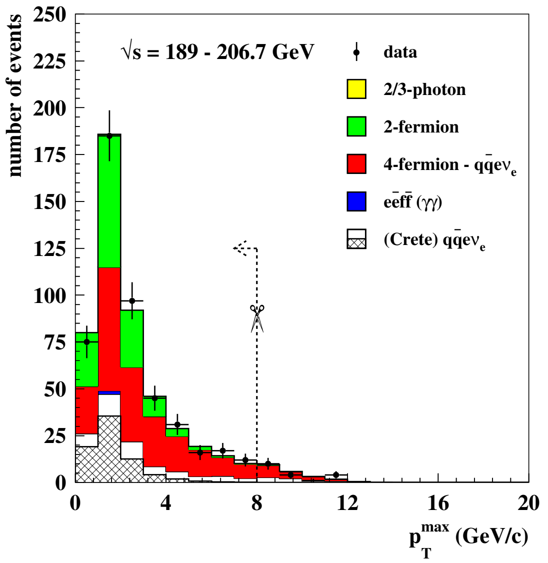

Figure 3.24: *Maximum transverse momentum of any charged track with respect to the closest jet $p_{\mathrm{T}}^{\mathrm{max}}$ for the energies $\sqrt{s}$ = 189 - 206.7 GeV. The selection criteria previously defined in the text have already been applied. The dashed line with arrow in the figure shows the corresponding cut.*

into account the nature of the track, the background can be further reduced. Events are *rejected* if a standard or tight muon is found with a transverse momentum with respect to the closest jet that satisfies: $p_{\mathrm{T},\mu} \geq 2$ GeV/c. Events are also *rejected* if a tight electron is found in the barrel or in the endcaps with a transverse momentum with respect to the closest jet that satisfies: $p_{\mathrm{T},e} \geq 2$ GeV/c. The same muon and electron identification tags and packages are used as for the leptonic analysis. The results of these last two selection criteria are depicted in figure 3.25.

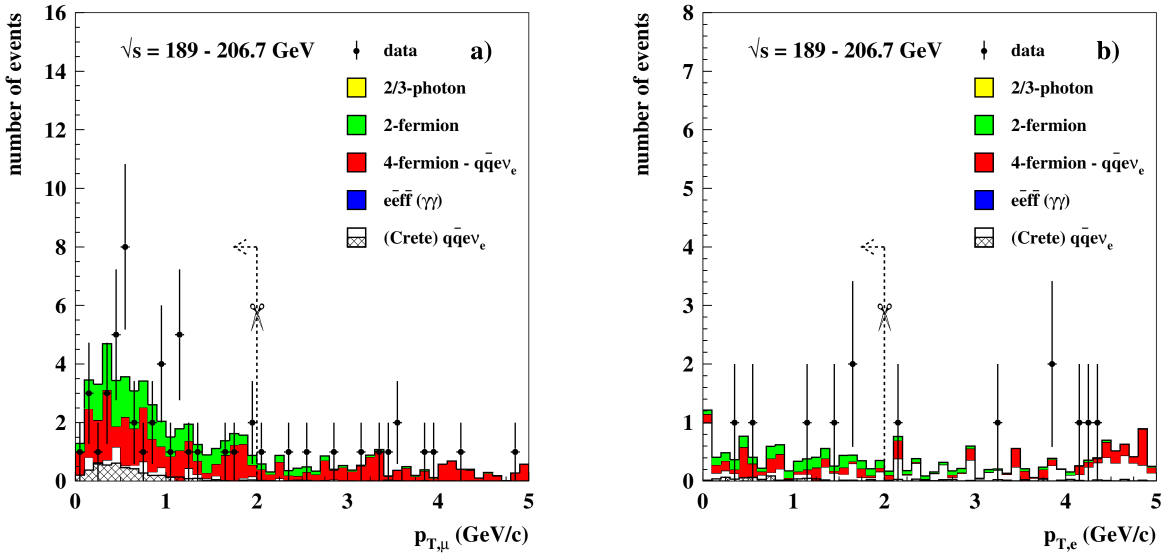

Figure 3.25: *Maximum transverse momentum with respect to the closest jet for a standard or tight muon (a)) and for a tight electron in the barrel or in the endcaps (b)) for the energies* $\sqrt{s}$ *= 189 - 206.7 GeV. The distribution in figure b) is obtained after the cut on the distribution of figure a). The dashed lines with arrows in the figures show the corresponding cuts.*

The 2-fermion background, that still gives rise to a large contribution, is reduced in the following way if there is a γ involved:
Firstly, the maximum transverse energy in the electromagnetic calorimeters (EMC) of any neutral track with respect to the closest jet $E^{\rm max}_{\rm T,EMC}$ can give rise to large values for this type of events. Requiring that $E^{\rm max}_{\rm T,EMC} \leq 3$ GeV reduces the 2-fermion background as can be seen from figure 3.26.
Secondly, $f\bar{f}\gamma$ events are suppressed by *rejecting* events that show activity within a cone of 30° around the direction of the missing momentum, since the γ can be misinterpreted as missing momentum that should come from the undetected electron or positron and the corresponding neutrino.

There is still room for improvement of the event selection. Plotting all previously depicted variables again after having applied all selection criteria, one can clearly see that in some of these distributions the ratio signal/background significantly changes going through the domain of the corresponding variable. As an example, figure 3.27 shows that the maxima of $M_{j\bar{j}}$ of the signal and background do not coincide. The shaded area corresponds with what is left from the backgrounds 2/3-photon, 2-fermion, 4-fermion - $q\bar{q}e\nu_e$ and $e\bar{e}f\bar{f}(\gamma\gamma)$.

Besides this distribution of $M_{j\bar{j}}$, the distributions of $E_{\rm T,neutral}/\sqrt{s}$, $p_{\rm T,miss}/\sqrt{s}$, $|\cos\theta_{\rm miss}|$, the acoplanarity, $y_{\rm cut,34}$, $y_{\rm cut,23}$ and $p^{\rm max}_{\rm T}$ are most sensitive to changes in the ratio signal/background. For all these eight variables, fits are performed to the distributions of signal/background, making use of polynomials, exponentials and/or Gaussians, after having scaled the signal with such a factor that the total number of signal events equals the total number of background events.

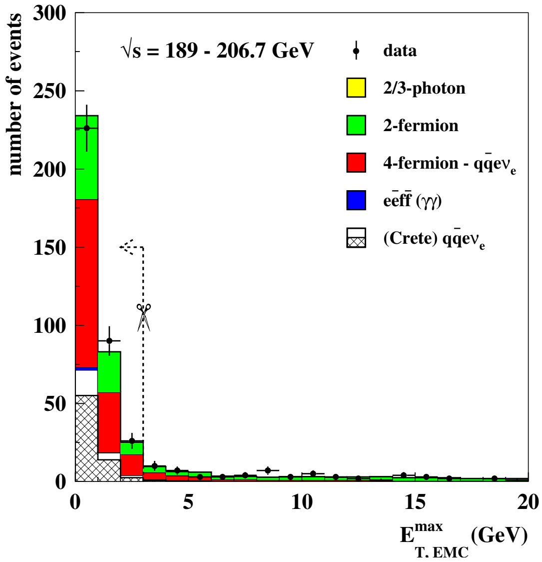

Figure 3.26: *Maximum transverse energy in the electromagnetic calorimeters (EMC) of any neutral track with respect to the closest jet $E^{\max}_{\mathrm{T,EMC}}$ for the energies $\sqrt{s}$ = 189 - 206.7 GeV. The selection criteria previously defined in the text have already been applied. The dashed line with arrow in the figure shows the corresponding cut.*

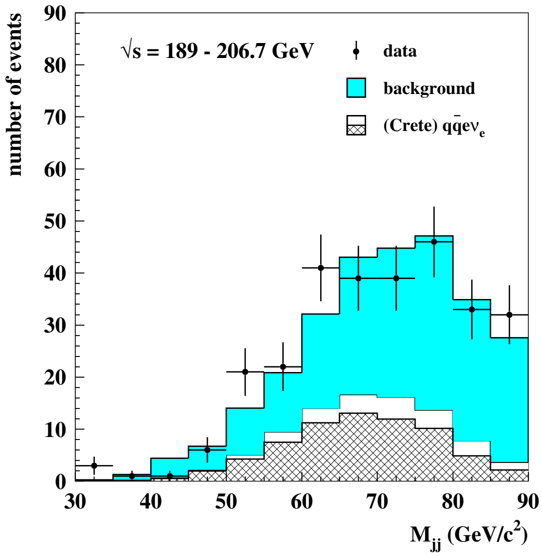

Figure 3.27: *Invariant mass of the two reconstructed jets $M_{j\bar{j}}$ for the energies $\sqrt{s}$ = 189 - 206.7 GeV after having applied all selection criteria previously defined in the text. The shaded area corresponds with the sum of the shaded areas as shown in the previous figures of this section.*

For clarity, the contribution of the background is obtained from the sum of the shaded area and the non-Crete $q\bar{q}e\nu_e$ final states in figure 3.27. The result of such a fit for the distribution of $M_{j\bar{j}}$ is shown in figure 3.28.

These eight fits give rise to the parametrisations $R_i, i = 1, 8$, which are multiplied to result in one 8-dimensional parametrisation $R = \prod_i R_i$ for the signal/background. From this total parametrisation, the rejection probabilities $P_{\mathrm{rej}} = \frac{R}{1+R}$ can be constructed for the signal and background. The distributions of the rejection probabilities for the signal and background are depicted in figure 3.29.

By reversing the bin order and making cumulative distributions, acceptance probabilities P_{acc} can be obtained for the signal and background. These two cumulative distributions serve as input for the distributions of the efficiency, the purity and their product. Figure 3.30 shows these

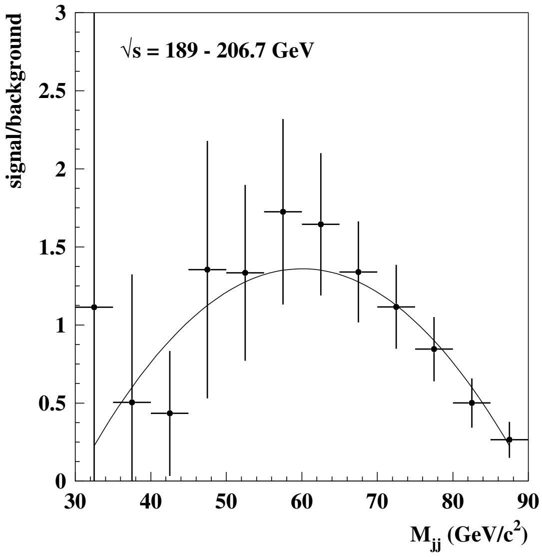

Figure 3.28: *Fit on the distribution of the signal/background ratio as a function of the invariant mass of the two reconstructed jets $M_{j\bar{j}}$ for the energies $\sqrt{s}$ = 189 - 206.7 GeV.*

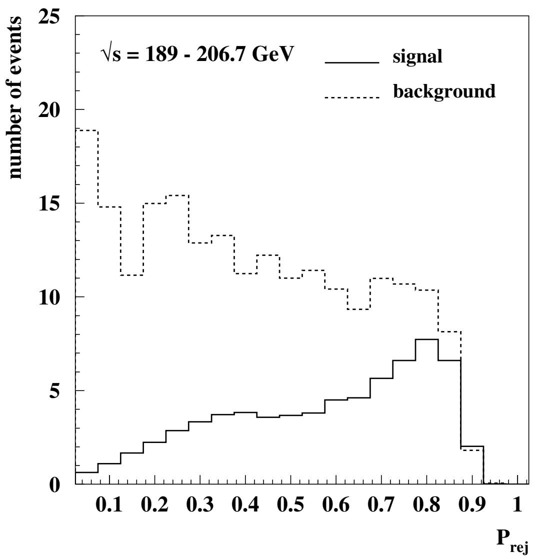

Figure 3.29: *Distributions of the rejection probability $P_{\rm rej} = \frac{R}{1+R}$ for the signal and background for the energies $\sqrt{s}$ = 189 - 206.7 GeV.*

distributions, where the maximum of the distribution of the product of efficiency and purity, located at $P_{\rm acc} = 0.80$, determines the working point.
Figure 3.31 shows a candidate event at $\sqrt{s} = 200$ GeV, in which two jets can be distinguished.
Table 3.10 indicates the different stages of the hadronic analysis for the years 1998 - 2000 combined, showing how the efficiency ε and the product of the efficiency and the purity $\varepsilon \cdot p$ evolve.

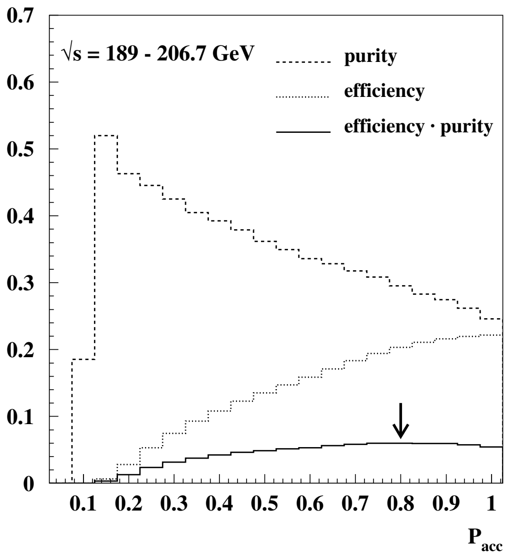

Figure 3.30: *Distributions of the efficiency, the purity and their product for the energies* $\sqrt{s}$ *= 189 - 206.7 GeV after having applied all selection criteria previously defined in the text. The arrow indicates the bin where the distribution of the product of efficiency and purity reaches its maximum.*

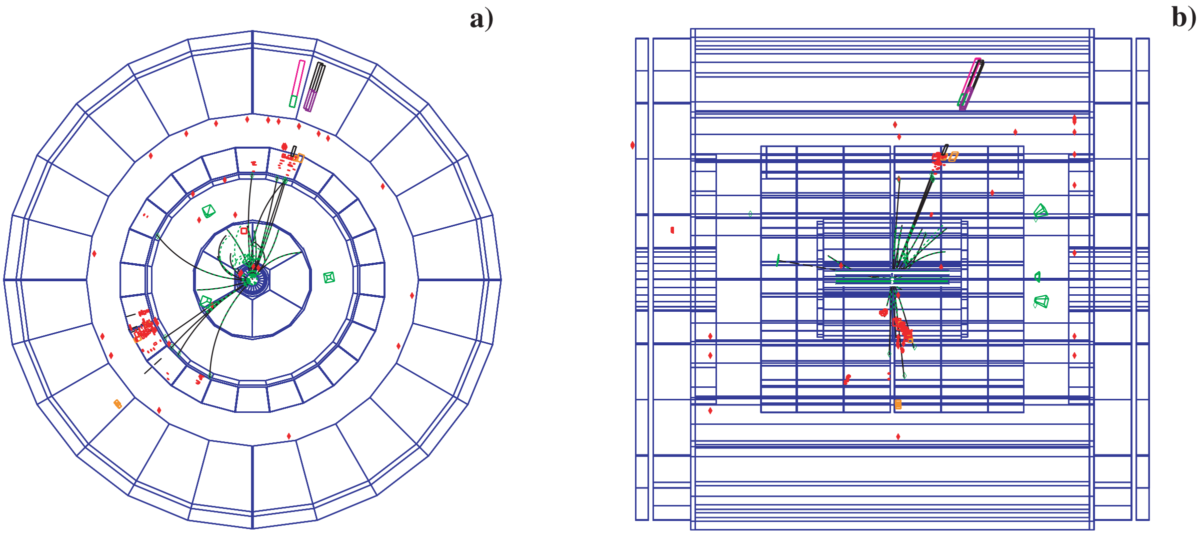

Figure 3.31: *Candidate event for* $e^+e^- \to We\nu_e$*;* $W \to q\bar{q}$ *viewed in the* xy*-plane (a)) and* zy*-plane (b)) of the DELPHI detector at* $\sqrt{s} = 200$ *GeV.*

Table 3.10: *Number of signal events, background events and data and the corresponding values of the efficiency ε and the product of the efficiency and the purity $\varepsilon \cdot p$ at different stages of the hadronic analysis for the years 1998 - 2000 combined. The different step numbers correspond with the following sequential selection criteria: step #1: $n_{\rm char} \geq 7$, $|\cos\theta_{\rm jet}| \leq 0.85$; step #2: $0.16\sqrt{s} \leq E_{\rm char} \leq 0.56\sqrt{s}$ and $\sqrt{E_{\rm F}^2 + E_{\rm B}^2} \leq 0.18 E_{\rm beam}$; step #3: $E_{\rm T,neutral} \leq 0.30\sqrt{s}$; step #4: $0.28\sqrt{s} \leq E_{\rm vis} \leq 0.68\sqrt{s}$; step #5: $0.04\sqrt{s} \leq p_{\rm T,miss} \leq 0.36\sqrt{s}$; step #6: $|\cos\theta_{\rm miss}| \leq 0.90$; step #7: $0.38\sqrt{s} \leq \sqrt{s'} \leq 0.92\sqrt{s}$; step #8: 30 GeV/c^2 $\leq M_{j\bar{j}} \leq$ 90 GeV/c^2; step #9: 10° $\leq$ acoplanarity $\leq$ 100°; step #10: $y_{\rm cut,34} \leq 0.007$ and $y_{\rm cut,23} \leq 0.03$; step #11: $p_{\rm T}^{\rm max} \leq 8$ GeV/c, $p_{{\rm T},\mu} \leq 2$ GeV/c and $p_{{\rm T},e} \leq 2$ GeV/c; step #12: $E_{\rm T,EMC}^{\rm max} \leq 3$ GeV and "30° cone cut"; step #13: acceptance probability $P_{\rm acc} = 0.80$. See the text and figures in this section for more details.*

step	$N_{q\bar{q}e\nu_e,\rm Crete}$	$N_{\rm background}$	$N_{\rm expected}$	$N_{\rm observed}$	ε (%)	$\varepsilon \cdot p$
#1	188.44	130905.56	131094.00	71840	61.3	8.81×10^{-4}
#2	154.33	18734.27	18888.60	19306	50.2	4.10×10^{-3}
#3	153.66	16011.84	16165.50	16448	50.0	4.75×10^{-3}
#4	145.13	11787.67	11932.80	12312	47.2	5.74×10^{-3}
#5	136.18	7068.48	7204.65	7519	44.3	8.38×10^{-3}
#6	118.29	3744.83	3863.11	4160	38.5	1.18×10^{-2}
#7	112.76	2495.94	2608.70	2759	36.7	1.59×10^{-2}
#8	106.77	1245.89	1352.66	1409	34.7	2.74×10^{-2}
#9	90.04	674.68	764.72	759	29.3	3.45×10^{-2}
#10	74.75	422.58	497.33	497	24.3	3.66×10^{-2}
#11	73.53	353.29	426.81	433	23.9	4.12×10^{-2}
#12	68.16	209.09	277.25	284	22.2	5.45×10^{-2}
#13	62.52	149.26	211.78	207	20.3	6.01×10^{-2}

3.5 Results

The following sections show the final number of selected events for the three analyses for the various centre-of-mass energies.

3.5.1 Selected muon sample

The contribution from cosmics is estimated by applying to the data all muon selection criteria except the cuts on the impact parameters $|\mathrm{IP}_z|$ and $|\mathrm{IP}_{R\phi}|$. Determining the values of $|\mathrm{IP}_z|_{\mathrm{cosmic}}$ and $|\mathrm{IP}_{R\phi}|_{\mathrm{cosmic}}$ within which all selected data are found, the number of cosmics N_{cosmic} is calculated via:

$$N_{\mathrm{cosmic}} = \frac{A_{\mathrm{muon}}}{A_{\mathrm{cosmic}} - A_{\mathrm{muon}}} \cdot (N_{\mathrm{obs,cosmic}} - N_{\mathrm{obs,muon}}), \tag{3.4}$$

where A_{muon} is the "area" within which all data satisfying all muon selection criteria $N_{\mathrm{obs,muon}}$ are found, i.e. A_{muon} = $|\mathrm{IP}_z|_{\mathrm{muon}} \cdot |\mathrm{IP}_{R\phi}|_{\mathrm{muon}}$ = 2.0×0.04 cm^2. A_{cosmic} is the "area" within which all data satisfying the cosmic selection criteria $N_{\mathrm{obs,cosmic}}$ are found. The data that pass the cosmic cuts fulfill the conditions: $|\mathrm{IP}_z|_{\mathrm{cosmic}} \leq$ 8.0 cm and $|\mathrm{IP}_{R\phi}|_{\mathrm{cosmic}} \leq$ 6.0 cm, hence A_{cosmic} = 48 cm^2. In table 3.11 the values of N_{cosmic} are listed for the various centre-of-mass energies together with those of $N_{\mathrm{obs,cosmic}}$ and $N_{\mathrm{obs,muon}}$.

Table 3.11: *Number of cosmics N_{cosmic} determined from the number of data that satisfy the muon selection criteria $N_{\mathrm{obs,muon}}$ and the number of data that satisfy the cosmic selection criteria $N_{\mathrm{obs,cosmic}}$ for the various centre-of-mass energies.*

$\sqrt{s}$ (GeV)	$N_{\mathrm{obs,muon}}$	$N_{\mathrm{obs,cosmic}}$	N_{cosmic}
189	9	14	0.008 ± 0.004
192	2	4	0.003 ± 0.002
196	5	6	0.002 ± 0.002
200	6	6	0.000 ± 0.002
202	4	6	0.003 ± 0.002
205	1	1	0.000 ± 0.002
206.7	4	8	0.007 ± 0.003
189 - 206.7	31	45	0.023 ± 0.006

Table 3.12 contains the final number of selected events per contributing process and the number of observed events for the centre-of-mass energies ranging from 189 to 206.7 GeV, while table 3.13 consists of the efficiencies for these energies. The results for the non-Crete $\mu\nu_\mu e\nu_e$ final state are obtained by subtracting the results from the Crete $\mu\nu_\mu e\nu_e$ samples from the samples that include all $\mu\nu_\mu e\nu_e$ final states. The GRC4F sample $l\nu_l\bar{l}\bar{\nu}_l$ comprises the final states $\mu\nu_\mu\bar{\mu}\bar{\nu}_\mu$, $\tau\nu_\tau\bar{\tau}\bar{\nu}_\tau$, $\mu\nu_\mu\tau\nu_\tau$, $\mu\bar{\mu}\nu_e\bar{\nu}_e$, $\tau\bar{\tau}\nu_e\bar{\nu}_e$, $\mu\bar{\mu}\nu_\tau\bar{\nu}_\tau$ and $\tau\bar{\tau}\nu_\mu\bar{\nu}_\mu$. The final state $e\bar{e}l\bar{l}$ ($l \neq e$) is a remnant of the WPHACT $\gamma\gamma$-like $e\bar{e}f\bar{f}$ (wphactncgg) sample.

Table 3.12: *Number of selected events per contributing process and number of observed events for the various centre-of-mass energies for the muon analysis.*

	$\sqrt{s}$ (GeV)							
number of events	189	192	196	200	202	205	206.7	189 - 206.7
$N_{\mu\nu_\mu e\nu_e,\mathrm{Crete}}$	6.02 ± 0.09	1.00 ± 0.01	3.20 ± 0.04	3.83 ± 0.05	1.91 ± 0.03	3.44 ± 0.05	4.08 ± 0.06	23.48 ± 0.14
$N_{\mu\nu_\mu e\nu_e,\mathrm{non-Crete}}$	0.83 ± 0.33	0.16 ± 0.05	0.18 ± 0.17	0.29 ± 0.20	0.34 ± 0.10	0.53 ± 0.18	0.36 ± 0.21	2.69 ± 0.52
$N_{\tau\nu_\tau e\nu_e}$	0.47 ± 0.09	0.07 ± 0.01	0.19 ± 0.04	0.27 ± 0.05	0.12 ± 0.02	0.22 ± 0.05	0.29 ± 0.06	1.63 ± 0.14
$N_{l\nu_l\bar{l}\bar{\nu}_l}$	1.15 ± 0.16	0.18 ± 0.03	0.52 ± 0.08	0.55 ± 0.08	0.38 ± 0.05	0.52 ± 0.08	0.73 ± 0.10	4.03 ± 0.24
$N_{\mu^+\mu^-}$	0.60 ± 0.13	0.11 ± 0.02	0.29 ± 0.04	0.28 ± 0.04	0.15 ± 0.02	0.31 ± 0.04	0.27 ± 0.04	2.00 ± 0.16
$N_{\tau^+\tau^-}$	0.07 ± 0.05	0.00 ± 0.00	0.00 ± 0.00	0.03 ± 0.02	0.02 ± 0.01	0.00 ± 0.00	0.00 ± 0.00	0.11 ± 0.05
$N_{e\bar{e}l\bar{l}}$ $(l \neq e)$	0.06 ± 0.02	0.01 ± 0.01	0.03 ± 0.01	0.02 ± 0.01	0.02 ± 0.01	0.18 ± 0.06	0.02 ± 0.02	0.34 ± 0.07
N_{cosmic}	0.01 ± 0.00	0.00 ± 0.00	0.00 ± 0.00	0.00 ± 0.00	0.00 ± 0.00	0.00 ± 0.00	0.01 ± 0.00	0.02 ± 0.01
N_{expected}	9.21 ± 0.41	1.52 ± 0.06	4.40 ± 0.20	5.28 ± 0.23	2.93 ± 0.12	5.20 ± 0.22	5.77 ± 0.25	34.31 ± 0.63
N_{observed}	9	2	5	6	4	1	4	31

Table 3.13: *Efficiencies for the muon analysis for the various centre-of-mass energies.*

$\sqrt{s}$ (GeV)	efficiency $\varepsilon_{\mu\nu_\mu e\nu_e}$ (%)
189	50.4 ± 0.6
192	50.3 ± 0.6
196	50.5 ± 0.6
200	50.6 ± 0.6
202	49.9 ± 0.6
205	49.2 ± 0.6
206.7	49.2 ± 0.6
189 - 206.7	50.0 ± 0.2

3.5.2 Selected electron sample

Table 3.14 contains the final number of selected events per contributing process and the number of observed events for the centre-of-mass energies ranging from 189 to 206.7 GeV. The results for the final state $e\bar{e}\nu_l\bar{\nu}_l$ ($l \neq e$) are obtained by subtracting the GRC4F samples which include all $e\nu_e e\nu_e$ states from the GRC4F samples which include the final states $e\bar{e}\nu_l\bar{\nu}_l$ ($l = e, \mu$ or τ). The results for the non-Crete $e\nu_e e\nu_e$ final state are obtained by subtracting the results from the Crete $e\nu_e e\nu_e$ samples from the samples that include all $e\nu_e e\nu_e$ final states.
The efficiencies for the barrel and endcaps corresponding to the numbers in tables 3.14 and 3.15 are listed in table 3.16.

Table 3.16: *Efficiencies for the electron analysis in the barrel and endcaps and their combined efficiencies for the various centre-of-mass energies.*

$\sqrt{s}$ (GeV)	efficiency $\varepsilon^{\mathrm{barrel}}_{e\nu_e e\nu_e}$ (%)	efficiency $\varepsilon^{\mathrm{endcaps}}_{e\nu_e e\nu_e}$ (%)	efficiency $\varepsilon^{\mathrm{total}}_{e\nu_e e\nu_e}$ (%)
189	35.8 ± 0.7	1.1 ± 0.2	37.0 ± 0.7
192	35.8 ± 0.7	1.3 ± 0.2	37.1 ± 0.7
196	36.6 ± 0.7	1.1 ± 0.2	37.7 ± 0.7
200	35.6 ± 0.7	1.2 ± 0.2	36.8 ± 0.7
202	36.1 ± 0.7	1.3 ± 0.2	37.4 ± 0.7
205	34.5 ± 0.7	1.2 ± 0.2	35.6 ± 0.7
206.7	34.7 ± 0.7	1.2 ± 0.2	35.9 ± 0.7
189 - 206.7	35.5 ± 0.3	1.2 ± 0.1	36.7 ± 0.3

3.5.3 Selected hadronic sample

Table 3.17 contains the final number of selected events per contributing process and the number of observed events for the centre-of-mass energies ranging from 189 to 206.7 GeV and table 3.18 shows the corresponding efficiencies.

Table 3.14: *Number of selected events per contributing process and number of observed events for the various centre-of-mass energies in the barrel for the electron analysis.*

number of events	$\sqrt{s}$ (GeV) 189	192	196	200	202	205	206.7	189 - 206.7
$N_{e\nu_e e\nu_e,\mathrm{Crete}}$	4.31 $\pm$ 0.09	0.69 $\pm$ 0.02	2.27 $\pm$ 0.05	2.70 $\pm$ 0.06	1.35 $\pm$ 0.03	2.32 $\pm$ 0.05	2.82 $\pm$ 0.06	16.45 $\pm$ 0.15
$N_{e\nu_e e\nu_e,\mathrm{non-Crete}}$	0.37 $\pm$ 0.32	0.01 $\pm$ 0.05	-0.05 $\pm$ 0.15	0.21 $\pm$ 0.19	-0.02 $\pm$ 0.09	0.27 $\pm$ 0.17	0.06 $\pm$ 0.19	0.84 $\pm$ 0.49
$N_{\tau\nu_\tau e\nu_e}$	0.24 $\pm$ 0.06	0.04 $\pm$ 0.01	0.11 $\pm$ 0.03	0.18 $\pm$ 0.04	0.08 $\pm$ 0.02	0.15 $\pm$ 0.04	0.19 $\pm$ 0.05	0.99 $\pm$ 0.10
$N_{\mu\nu_\mu e\nu_e}$	0.03 $\pm$ 0.02	0.01 $\pm$ 0.01	0.04 $\pm$ 0.02	0.10 $\pm$ 0.03	0.03 $\pm$ 0.01	0.05 $\pm$ 0.02	0.01 $\pm$ 0.01	0.26 $\pm$ 0.05
$N_{e\bar{e}\nu_l\bar{\nu}_l}$ $(l \neq e)$	1.69 $\pm$ 0.53	0.34 $\pm$ 0.09	1.10 $\pm$ 0.27	1.10 $\pm$ 0.32	0.50 $\pm$ 0.15	1.11 $\pm$ 0.28	1.21 $\pm$ 0.32	7.05 $\pm$ 0.82
N_{Compton}	0.15 $\pm$ 0.11	0.00 $\pm$ 0.00	0.03 $\pm$ 0.03	0.08 $\pm$ 0.05	0.04 $\pm$ 0.04	0.06 $\pm$ 0.06	0.06 $\pm$ 0.04	0.42 $\pm$ 0.15
$N_{\nu_l\bar{\nu}_l(\gamma)}$	0.75 $\pm$ 0.23	0.08 $\pm$ 0.04	0.36 $\pm$ 0.06	0.34 $\pm$ 0.09	0.16 $\pm$ 0.06	0.28 $\pm$ 0.07	0.33 $\pm$ 0.09	2.29 $\pm$ 0.29
$N_{\tau^+\tau^-}$	0.00 $\pm$ 0.00	0.00 $\pm$ 0.00	0.00 $\pm$ 0.00	0.02 $\pm$ 0.02	0.01 $\pm$ 0.01	0.01 $\pm$ 0.01	0.01 $\pm$ 0.01	0.05 $\pm$ 0.03
N_{expected}	7.55 $\pm$ 0.68	1.16 $\pm$ 0.11	3.86 $\pm$ 0.32	4.72 $\pm$ 0.39	2.14 $\pm$ 0.20	4.25 $\pm$ 0.35	4.69 $\pm$ 0.40	28.36 $\pm$ 1.03
N_{observed}	6	1	2	4	0	4	5	22

Table 3.15: *Number of selected events per contributing process and number of observed events for the various centre-of-mass energies in the endcaps for the electron analysis.*

number of events	$\sqrt{s}$ (GeV) 189	192	196	200	202	205	206.7	189 - 206.7
$N_{e\nu_e e\nu_e,\mathrm{Crete}}$	0.13 $\pm$ 0.02	0.02 $\pm$ 0.01	0.07 $\pm$ 0.01	0.09 $\pm$ 0.01	0.05 $\pm$ 0.01	0.08 $\pm$ 0.01	0.10 $\pm$ 0.01	0.54 $\pm$ 0.03
$N_{e\nu_e e\nu_e,\mathrm{non-Crete}}$	0.04 $\pm$ 0.06	0.00 $\pm$ 0.01	-0.01 $\pm$ 0.02	-0.02 $\pm$ 0.03	0.00 $\pm$ 0.02	-0.02 $\pm$ 0.03	0.05 $\pm$ 0.04	0.03 $\pm$ 0.09
$N_{\tau\nu_\tau e\nu_e}$	0.01 $\pm$ 0.01	0.00 $\pm$ 0.00	0.00 $\pm$ 0.00	0.00 $\pm$ 0.00	0.00 $\pm$ 0.00	0.01 $\pm$ 0.01	0.01 $\pm$ 0.01	0.04 $\pm$ 0.02
$N_{\mu\nu_\mu e\nu_e}$	0.00 $\pm$ 0.00	0.00 $\pm$ 0.00	0.00 $\pm$ 0.00	0.00 $\pm$ 0.00	0.00 $\pm$ 0.00	0.00 $\pm$ 0.00	0.00 $\pm$ 0.00	0.00 $\pm$ 0.00
$N_{e\bar{e}\nu_l\bar{\nu}_l}$ $(l \neq e)$	0.18 $\pm$ 0.12	0.02 $\pm$ 0.02	0.04 $\pm$ 0.04	0.15 $\pm$ 0.07	0.04 $\pm$ 0.03	0.05 $\pm$ 0.05	0.00 $\pm$ 0.00	0.48 $\pm$ 0.16
N_{Compton}	0.00 $\pm$ 0.00	0.00 $\pm$ 0.00	0.00 $\pm$ 0.00	0.00 $\pm$ 0.00	0.00 $\pm$ 0.00	0.00 $\pm$ 0.00	0.02 $\pm$ 0.02	0.02 $\pm$ 0.02
$N_{\nu_l\bar{\nu}_l(\gamma)}$	0.05 $\pm$ 0.04	0.03 $\pm$ 0.02	0.04 $\pm$ 0.02	0.02 $\pm$ 0.02	0.03 $\pm$ 0.03	0.01 $\pm$ 0.01	0.00 $\pm$ 0.00	0.18 $\pm$ 0.06
$N_{\tau^+\tau^-}$	0.00 $\pm$ 0.00	0.00 $\pm$ 0.00	0.00 $\pm$ 0.00	0.00 $\pm$ 0.00	0.00 $\pm$ 0.00	0.00 $\pm$ 0.00	0.00 $\pm$ 0.00	0.00 $\pm$ 0.00
N_{expected}	0.41 $\pm$ 0.16	0.08 $\pm$ 0.03	0.14 $\pm$ 0.05	0.24 $\pm$ 0.08	0.12 $\pm$ 0.05	0.14 $\pm$ 0.06	0.17 $\pm$ 0.08	1.29 $\pm$ 0.21
N_{observed}	0	0	1	0	0	0	0	1

Table 3.17: *Number of selected events per contributing process and number of observed events for the various centre-of-mass energies for the hadronic analysis.*

number of events	$\sqrt{s}$ (GeV) 189	192	196	200	202	205	206.7	189 - 206.7
$N_{q\bar{q}e\nu_e,\mathrm{Crete}}$	15.79 ± 0.45	2.69 ± 0.08	8.39 ± 0.25	9.99 ± 0.29	4.86 ± 0.14	9.28 ± 0.28	11.52 ± 0.33	62.52 ± 0.75
$N_{q\bar{q}e\nu_e,\mathrm{non-Crete}}$	3.92 ± 1.56	0.91 ± 0.27	2.76 ± 0.85	2.63 ± 0.95	0.72 ± 0.45	3.26 ± 0.94	1.64 ± 1.01	15.84 ± 2.50
$N_{q\bar{q}l\nu_l}$ $(l \neq e)$	18.01 ± 1.73	3.12 ± 0.29	8.30 ± 0.84	10.83 ± 1.01	4.37 ± 0.45	8.56 ± 0.87	9.40 ± 0.96	62.60 ± 2.59
$N_{\mathrm{rest\ 4-fermion}}$	7.88 ± 1.73	1.62 ± 0.30	5.84 ± 0.85	6.98 ± 1.02	3.60 ± 0.45	7.06 ± 0.87	7.95 ± 0.96	40.95 ± 2.59
$N_{e\bar{e}f\bar{f}}$	0.10 ± 0.03	0.02 ± 0.01	0.65 ± 0.60	0.68 ± 0.66	0.35 ± 0.32	0.05 ± 0.02	0.07 ± 0.02	1.92 ± 0.95
$N_{q\bar{q}}$	10.38 ± 0.57	1.38 ± 0.08	3.91 ± 0.23	4.00 ± 0.24	1.77 ± 0.11	2.95 ± 0.19	3.53 ± 0.22	27.91 ± 0.73
$N_{\tau^+\tau^-}$	0.00 ± 0.00	0.00 ± 0.00	0.00 ± 0.00	0.02 ± 0.02	0.01 ± 0.01	0.02 ± 0.01	0.00 ± 0.00	0.04 ± 0.03
N_{expected}	56.10 ± 2.99	9.73 ± 0.51	29.85 ± 1.62	35.12 ± 1.88	15.68 ± 0.87	31.18 ± 1.58	34.11 ± 1.74	211.78 ± 4.65
N_{observed}	60	5	40	26	14	27	35	207

Table 3.18: *Efficiencies for the hadronic analysis for the various centre-of-mass energies.*

$\sqrt{s}$ (GeV)	efficiency $\varepsilon_{q\bar{q}e\nu_e}$ (%)
189	21.0 ± 0.6
192	20.8 ± 0.6
196	20.0 ± 0.6
200	20.5 ± 0.6
202	19.8 ± 0.6
205	19.1 ± 0.6
206.7	20.8 ± 0.6
189 - 206.7	20.3 ± 0.2

CHAPTER 4

Cross section analysis

This chapter presents the results for the single W cross section measurement for the muon, electron and hadronic final states that are obtained from the leptonic and hadronic event selections shown in the previous chapter.

4.1 Maximum Likelihood Technique

The maximum likelihood method is generally considered as an important technique of parameter estimation. This method consists of finding the best set of estimations $\hat{\vec{\alpha}}$ for the true values $\vec{\alpha}$, which maximises the joint probability density functions $f(x_i|\vec{\alpha})$ for the independently measured quantities x_i, given by:

$$\mathcal{L}(\vec{\alpha}) = \prod_i f(x_i|\vec{\alpha}), \tag{4.1}$$

where $\mathcal{L}$ is called the likelihood. In most cases it is more convenient to work with its natural logarithm ln$\mathcal{L}$. To find the maximum likelihood estimate of $\vec{\alpha}$, one has to solve the likelihood equation

$$\frac{\partial \ln\mathcal{L}}{\partial \alpha_n} = 0, \tag{4.2}$$

where the index n runs over all parameters to be estimated.
For the cross section analysis presented in this chapter, Poisson distributions are needed for the probability density functions in equation (4.1), which in general are given by:

$$P(n|\mu) = \frac{e^{-\mu}\mu^n}{n!} \quad ; \quad n \in \mathbb{N}\,; \;\; \mu \in \mathbb{R} \;\; \wedge \;\; \mu \geq 0, \tag{4.3}$$

which define the probability to observe n when μ is expected.
The goal of the cross section analysis is to find the best value for the cross section σ from the total number of observed events $N_{\text{obs},i}$ and the cross section dependent total number of expected events $N_{\text{exp},i}(\sigma)$, where the index i ranges over all performed measurements. Hence, the Poisson distribution in equation (4.3) can be written as:

$$P(N_{\text{obs},i}|N_{\text{exp},i}(\sigma)) = \frac{e^{-N_{\text{exp},i}(\sigma)}N_{\text{exp},i}(\sigma)^{N_{\text{obs},i}}}{N_{\text{obs},i}!}. \tag{4.4}$$

It is usually more convenient to work with the negative natural logarithm -ln$\mathcal{L}$. Therefore, determining the measured cross section σ corresponds to finding the minimum of:

$$\text{-ln}\mathcal{L}(\sigma) = \sum_i N_{\text{exp},i}(\sigma) - N_{\text{obs},i}\ln N_{\text{exp},i}(\sigma) + \ln N_{\text{obs},i}!. \tag{4.5}$$

4.2 Cross section analysis

In order to get an idea how well one has measured a certain quantity q, one can introduce the so-called "R-factor", which is defined as follows:

$$R = \frac{q^{\text{exp}}}{q^{\text{theor}}} \quad ; \quad q^{\text{theor}} \neq 0, \tag{4.6}$$

where q^{exp} and q^{theor} are the experimental and theoretical values of the quantity q.
This R-factor can be used for the single W cross section analysis, in which case equation (4.6) can be written as:

$$R_{We\nu_e} = \frac{\sigma^{\text{exp}}_{We\nu_e}}{\sigma^{\text{theor}}_{We\nu_e}}. \tag{4.7}$$

The measurement of this factor can be performed by determining the probability $P(N_{\text{obs},i}|R_{We\nu_e})$ that $N_{\text{obs},i}$ events are observed, while $N_{\text{exp},i}(R_{We\nu_e})$ are expected:

$$P(N_{\text{obs},i}|R_{We\nu_e}) = \frac{e^{-N_{\text{exp},i}(R_{We\nu_e})} N_{\text{exp},i}(R_{We\nu_e})^{N_{\text{obs},i}}}{N_{\text{obs},i}!}. \tag{4.8}$$

The corresponding likelihood is thus given by:

$$\mathcal{L}(R_{We\nu_e}) = \prod_i P(N_{\text{obs},i}|R_{We\nu_e}), \tag{4.9}$$

where the index i runs over the number of measurements.
What really is needed to determine $R_{We\nu_e}$, is a probability density function (pdf) $P(R_{We\nu_e}|N_{\text{obs},i})$, since $N_{\text{obs},i}$ is given and $R_{We\nu_e}$ is *not*! This function can be constructed using Bayes' theorem [50]:

$$P(R_{We\nu_e}|N_{\text{obs},i}) = N_0 P(N_{\text{obs},i}|R_{We\nu_e}) P(R_{We\nu_e}), \tag{4.10}$$

where N_0 is a normalisation factor and $P(R_{We\nu_e})$ is the Bayesian prior function of the possible values of $R_{We\nu_e}$. Since the single W cross section is supposed to be positive definite, this normalised prior function can be described as follows:

$$P(R_{We\nu_e}) = \begin{cases} 0 & R_{We\nu_e} < 0 \\ 1/R_{\text{max}} & 0 \leq R_{We\nu_e} \leq R_{\text{max}}. \end{cases} \tag{4.11}$$

The total normalised probability density function, obtained from the probability density functions $P(R_{We\nu_e}|N_{\text{obs},i})$, provides information to answer the question what the best value of $R_{We\nu_e}$ is. The following approach has been applied ([51]):

- **central value:** the median of the normalised pdf $R^{\mathrm{med}}_{We\nu_e}$ defines the central value.
- **upper and lower value:** the upper(lower) value of the confidence level (CL) interval is defined by the value of $R_{We\nu_e}$ for which 15.87% of the normalised pdf lies above(below) this value.
- **upper limit:** if less than 31.74% of the normalised pdf lies below the value of $R_{We\nu_e}$ for which this pdf is maximal ($R^{\mathrm{max}}_{We\nu_e}$), an upper limit is given, which is defined as the value for which 5% of the normalised pdf lies above this limit (95% CL).

It should be pointed out that the median $R^{\mathrm{med}}_{We\nu_e}$ is *always* larger than $R^{\mathrm{max}}_{We\nu_e}$, which results from the fact that Poisson distributions satisfy the following criteria, when μ is expected and n is given:

$$\begin{aligned} \text{most likely value of } \mu : \quad \mu^{\max} =& \ n \\ \text{expectation value of } \mu : \quad <\mu>=& \ n+1. \end{aligned} \tag{4.12}$$

In the next subsections the results from the single W measurements for the different decay channels are given.

4.2.1 Muon analysis

As an example of the approach explained in the previous section, figure 4.1 shows the -Δ2ln$\mathcal{L}$ distribution and the pdf as a function of $R_{\mu\nu_\mu e\nu_e}$ at $\sqrt{s}$ = 189 GeV and at $\sqrt{s}$ = 205 GeV. For the first centre-of-mass energy, a central value and upper and lower errors can be obtained, while for the second centre-of-mass energy only an upper limit can be deduced. The -Δ2ln$\mathcal{L}$ distribution is obtained from the "standard" -ln$\mathcal{L}$ distribution by multiplying the latter distribution by 2 and applying such a bias that the minimum of the distribution coincides with 0.
The -Δ2ln$\mathcal{L}$ distributions and the corresponding probability density distributions as a function of $R_{\mu\nu_\mu e\nu_e}$ for all energies ranging from 189 to 206.7 GeV and their combined distribution for $\sqrt{s}$ = 189 - 206.7 GeV can be found in appendix A.1. The latter distribution is, of course, obtained by adding the -Δ2ln$\mathcal{L}$ distributions from the seven centre-of-mass energies. In table 4.1 the medians and upper and lower values are shown for these pdfs together with the experimental cross sections and their statistical and systematic errors and the theoretical cross sections. These theoretical cross sections have been obtained using the generator GRC4F, which has also been used to determine the theoretical cross sections for the other two final states. At $\sqrt{s}$ = 205 GeV only an upper limit has been listed for these quantities. The systematic errors of this final state and the other two final states are discussed in more detail in section 4.3.

4.2.2 Electron analysis

Since the selection of electron events has been split into one for the barrel and one for the endcaps, the cross section analysis is also separated for these two regions. In table 4.2 the medians and upper and lower values are shown for the pdfs for all energies ranging from 189 to 206.7 GeV and their combined distribution for $\sqrt{s}$ = 189 - 206.7 GeV together with the experimental cross sections and their statistical and systematic errors for the barrel. The statistics for the endcaps is too low, giving rise to very large upper limits (several hundreds of fb), which are not very meaningful. Therefore, no numbers are listed in table 4.2 for the endcaps.

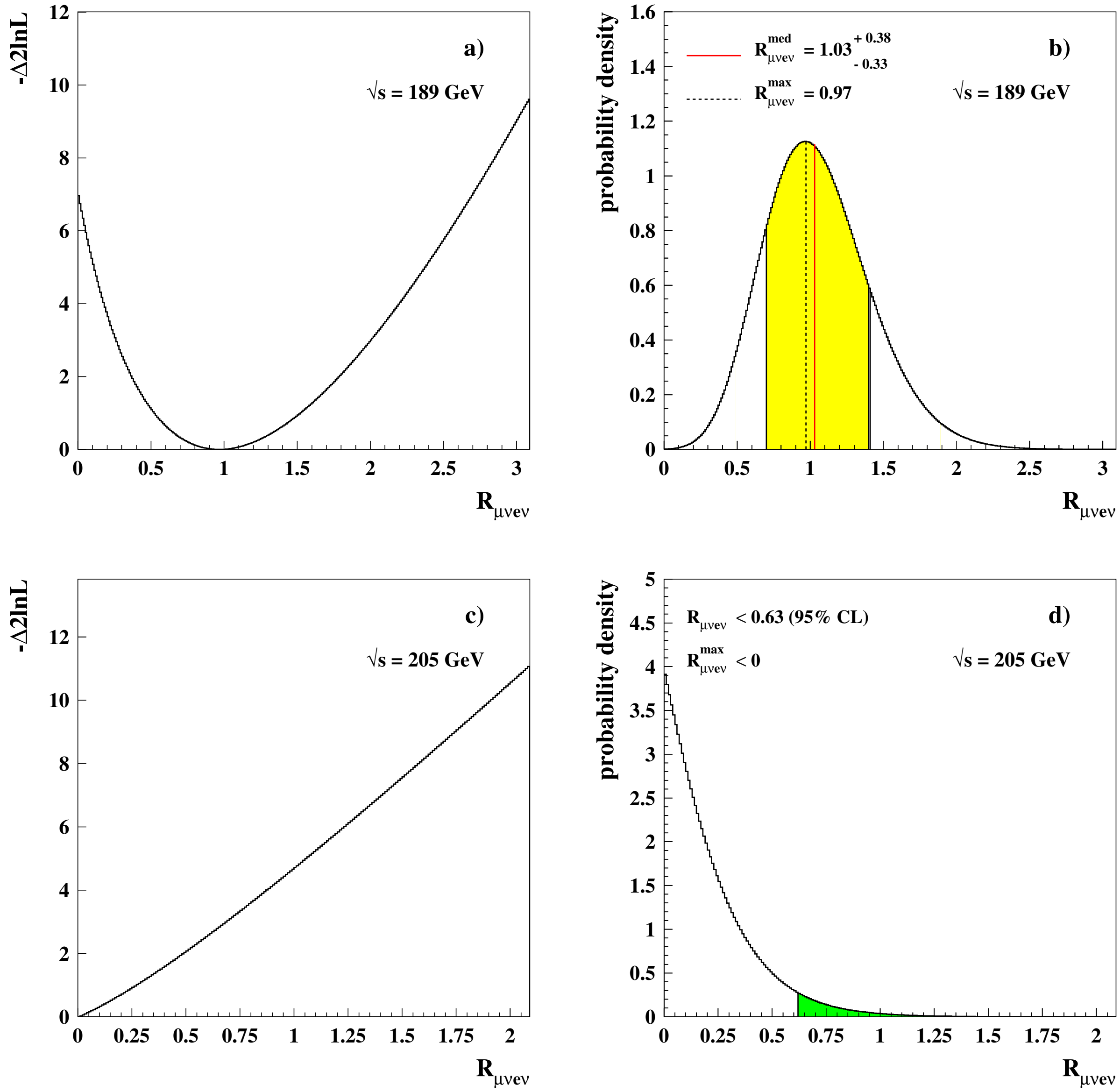

Figure 4.1: *Figure a) shows the -Δ2ln$\mathcal{L}$ distribution as a function of $R_{\mu\nu_\mu e\nu_e}$ for the muon analysis at $\sqrt{s}$ = 189 GeV and figure b) indicates the corresponding probability density function. The dotted line in figure b) indicates the most likely value of the pdf $R^{\max}_{\mu\nu_\mu e\nu_e}$, thus the minimum of the -Δ2ln$\mathcal{L}$ distribution, which is clearly smaller than the median of the pdf $R^{\mathrm{med}}_{\mu\nu_\mu e\nu_e}$ being represented by the solid line in the light shaded area. The two white areas below the pdf each account for 15.87% of the pdf. Figure c) and d) show the same distributions at $\sqrt{s}$ = 205 GeV for which energy point only an upper limit can be deduced. The grey area below the pdf accounts for 5% of the pdf.*

Table 4.1: *Values for $R_{\mu\nu_\mu e\nu_e}$ and $\sigma^{\mathrm{exp}}_{\mu\nu_\mu e\nu_e}$ including the upper and lower errors and systematic errors and theoretical cross sections $\sigma^{\mathrm{theor}}_{\mu\nu_\mu e\nu_e}$ for the various centre-of-mass energies. At $\sqrt{s}$ = 205 GeV only an upper limit is listed.*

$\sqrt{s}$ (GeV)	$R_{\mu\nu_\mu e\nu_e}$	$\sigma^{\mathrm{exp}}_{\mu\nu_\mu e\nu_e}$ (fb)	$\sigma^{\mathrm{theor}}_{\mu\nu_\mu e\nu_e}$ (fb)
189	$1.03^{+0.38}_{-0.33}\pm0.06$	$80^{+29}_{-26}\pm4$	77.6
192	$1.82^{+1.25}_{-0.91}\pm0.05$	$148^{+101}_{-74}\pm4$	81.1
196	$1.30^{+0.56}_{-0.46}\pm0.04$	$114^{+49}_{-40}\pm4$	87.8
200	$1.28^{+0.51}_{-0.42}\pm0.04$	$119^{+47}_{-39}\pm4$	92.6
202	$1.74^{+0.86}_{-0.68}\pm0.06$	$168^{+83}_{-66}\pm6$	96.4
205	$<0.63\pm0.05$	$<64\pm5$	101.0
206.7	$0.66^{+0.40}_{-0.32}\pm0.04$	$69^{+42}_{-33}\pm4$	103.9
189 - 206.7	$0.88^{+0.18}_{-0.16}\pm0.05$		

By adding the number of observed events and the number of expected signal and background events for the barrel and endcaps, corresponding values can be obtained for the total electron analysis, resulting in the -Δ2ln$\mathcal{L}$ distributions and the corresponding probability density distributions as a function of $R^{\mathrm{total}}_{e\nu_e e\nu_e}$ that can be found in appendix A.2. The values for the median $R^{\mathrm{total}}_{e\nu_e e\nu_e}$ and cross section $\sigma^{\mathrm{exp,total}}_{e\nu_e e\nu_e}$ for the different centre-of-mass energies are listed in table 4.2.

4.2.3 Hadronic analysis

The R-factor definition has also been applied to the hadronic analysis. The -Δ2ln$\mathcal{L}$ distributions and the corresponding probability density distributions as a function of $R_{q\bar{q}e\nu_e}$ for all energies ranging from 189 to 206.7 GeV and their combined distribution for $\sqrt{s}$ = 189 - 206.7 GeV can be found in appendix A.3. In table 4.3 the medians and upper and lower values are shown for these pdfs together with the experimental cross sections and their statistical and systematic errors and the theoretical cross sections.
From the distributions of the acceptance probabilities P_{acc} for the data, signal and background as described in section 3.4, one can construct the ratio r defined by:

$$r = \frac{N_{\mathrm{obs}} - N_{\mathrm{bkgr}}}{N_{\mathrm{sig}}}, \tag{4.13}$$

where N_{sig}, N_{bkgr} and N_{obs} are the number of expected signal and background events and the number of observed events respectively. This ratio r gives an indication of the discrepancy between the measurement and the expectation of the R-factor. Figure 4.2 shows this ratio for the years 1998 - 2000 combined, where the shaded area takes into account the 5% systematic error on the background cross section as will be explained in section 4.3.

Table 4.2: *Values for* $R^{\text{barrel}}_{e\nu_e e\nu_e}$, $\sigma^{\text{exp,barrel}}_{e\nu_e e\nu_e}$, $R^{\text{total}}_{e\nu_e e\nu_e}$ *and* $\sigma^{\text{exp,total}}_{e\nu_e e\nu_e}$ *including the upper and lower errors or upper limits and systematic errors and theoretical cross sections for the various centre-of-mass energies.*

$\sqrt{s}$ (GeV)	$R^{\text{barrel}}_{e\nu_e e\nu_e}$	$\sigma^{\text{exp,barrel}}_{e\nu_e e\nu_e}$ (fb)	$\sigma^{\text{theor,barrel}}_{e\nu_e e\nu_e}$ (fb)
189	$0.73^{+0.45}_{-0.36}\pm0.16$	$43^{+26}_{-21}\pm9$	58.4
192	$<3.96\pm0.14$	$<238\pm9$	60.0
196	$<1.41\pm0.14$	$<90\pm9$	64.0
200	$0.88^{+0.60}_{-0.47}\pm0.15$	$60^{+41}_{-32}\pm10$	68.3
202	$<1.12\pm0.11$	$<79\pm8$	70.6
205	$1.06^{+0.70}_{-0.55}\pm0.17$	$77^{+51}_{-40}\pm12$	72.5
206.7	$1.23^{+0.64}_{-0.52}\pm0.14$	$93^{+48}_{-39}\pm10$	75.5
189 - 206.7	$0.63^{+0.21}_{-0.20}\pm0.15$		
$\sqrt{s}$ (GeV)	$R^{\text{total}}_{e\nu_e e\nu_e}$	$\sigma^{\text{exp,total}}_{e\nu_e e\nu_e}$ (fb)	$\sigma^{\text{theor,total}}_{e\nu_e e\nu_e}$ (fb)
189	$0.66^{+0.43}_{-0.35}\pm0.17$	$52^{+34}_{-27}\pm13$	78.2
192	$<3.77\pm0.16$	$<296\pm13$	78.4
196	$0.76^{+0.61}_{-0.45}\pm0.15$	$65^{+53}_{-39}\pm13$	86.1
200	$0.81^{+0.57}_{-0.45}\pm0.16$	$75^{+53}_{-42}\pm15$	92.4
202	$<1.08\pm0.12$	$<101\pm12$	93.9
205	$1.00^{+0.68}_{-0.53}\pm0.16$	$97^{+66}_{-52}\pm16$	97.4
206.7	$1.17^{+0.62}_{-0.50}\pm0.14$	$119^{+63}_{-51}\pm14$	101.7
189 - 206.7	$0.63^{+0.21}_{-0.20}\pm0.16$		

The measured R-factor at $P_{\text{acc}} = 0.80$, the chosen working point for the event selection as described in section 3.4, agrees well within 1 standard deviation (1σ) with the expected value of 1.

Table 4.3: *Values for $R_{q\bar{q}e\nu_e}$ and $\sigma^{\rm exp}_{q\bar{q}e\nu_e}$ including the upper and lower errors and systematic errors and theoretical cross sections $\sigma^{\rm theor}_{q\bar{q}e\nu_e}$ for the various centre-of-mass energies. At $\sqrt{s}$ = 192 and 200 GeV only an upper limit is quoted.*

$\sqrt{s}$ (GeV)	$R_{q\bar{q}e\nu_e}$	$\sigma^{\rm exp}_{q\bar{q}e\nu_e}$ (pb)	$\sigma^{\rm theor}_{q\bar{q}e\nu_e}$ (pb)
189	$1.28^{+0.35}_{-0.34}\pm0.14$	$0.62^{+0.17}_{-0.17}\pm0.07$	0.487
192	$<1.19\pm0.14$	$<0.61\pm0.07$	0.512
196	$2.25^{+0.56}_{-0.51}\pm0.15$	$1.24^{+0.31}_{-0.28}\pm0.08$	0.552
200	$<0.86\pm0.13$	$<0.51\pm0.12$	0.589
202	$0.78^{+0.56}_{-0.45}\pm0.12$	$0.47^{+0.34}_{-0.27}\pm0.07$	0.609
205	$0.62^{+0.40}_{-0.34}\pm0.13$	$0.40^{+0.26}_{-0.22}\pm0.08$	0.638
206.7	$1.11^{+0.38}_{-0.35}\pm0.11$	$0.73^{+0.25}_{-0.23}\pm0.07$	0.655
189 - 206.7	$0.93^{+0.17}_{-0.16}\pm0.13$		

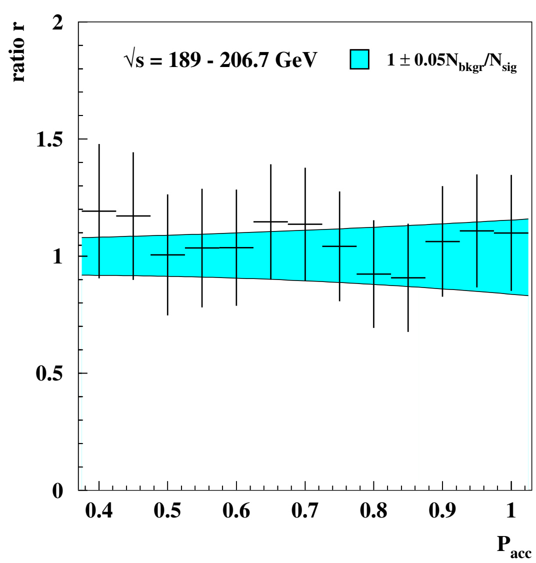

Figure 4.2: *Ratio r for the energies $\sqrt{s}$ = 189 - 206.7 GeV after having applied all selection criteria defined in the previous chapter. The shaded area, ranging from $1-\frac{0.05N_{\rm bkgr}}{N_{\rm sig}}$ to $1+\frac{0.05N_{\rm bkgr}}{N_{\rm sig}}$, takes into account the total systematic error on the background cross section, which is equal to 5$\%$.*

4.3 Systematic uncertainties

One of the contributions to the systematic uncertainty is due to the limited MC statistics for the signal and the background. The signal cross sections are known with a theoretical accuracy of 5$\%$, computed with WPHACT and GRC4F. The cross sections of the main background processes for both the hadronic and the leptonic analysis, the 4-fermion final states coming from WW and ZZ, are known with theoretical accuracies of respectively 0.5$\%$ from RacoonWW [52] and YFSWW [53] and 1$\%$ from YFSZZ [54].

Compton events and $\nu\bar{\nu}(\gamma)$ form the most important 2-fermion contribution for the electron analysis, while $\mu^+\mu^-(\gamma)$ are the most significant 2-fermion background for the muon analysis. All corresponding cross sections have typical theoretical uncertainties of the order of 1%.
For the hadronic analysis, $q\bar{q}(\gamma)$ produce the largest contribution after the beforementioned 4-fermion final states. Uncertainties due to fragmentation modelling are accounted for by assuming a 5% error on this QCD background [55].
The total systematic error on the background cross section due to the effects listed before amounts conservatively to 10% for the muon analysis, 20% and 30% for the barrel and endcaps electron analyses and 5% for the hadronic analysis.
As has been mentioned in section 3.1, the integrated luminosities after the run quality selection are known with an error of $6‰$, which causes a small systematic effect on the cross sections.
For the leptonic analyses, the corresponding muon and electron identification efficiencies ε_μ and ε_e contribute to the total systematic error.
The muon identification efficiency ε_μ can be determined by making use of the two independent muon tags for the muon identification in the hadron calorimeter and the muon chambers, which give rise to muon identification efficiencies $\varepsilon_\mu^{\mathrm{HCAL}}$ and $\varepsilon_\mu^{\mathrm{MUC}}$ respectively. These last two efficiencies are defined in the following way:

$$\varepsilon_\mu^{\mathrm{HCAL}} = \frac{N_\mu^{\mathrm{HCAL*MUC}}}{N_\mu^{\mathrm{MUC}}} \quad \text{and} \quad \varepsilon_\mu^{\mathrm{MUC}} = \frac{N_\mu^{\mathrm{HCAL*MUC}}}{N_\mu^{\mathrm{HCAL}}}, \tag{4.14}$$

where N_μ^{MUC} is the number of tight and standard muons in the MUC, N_μ^{HCAL} is the number of muons in the HCAL and $N_\mu^{\mathrm{HCAL*MUC}}$ is the number of tight and standard muons in both the HCAL and the MUC. These efficiencies can be obtained from figure 4.3, which shows the muon identification tag for the years 1998 - 2000 combined after having applied all selection criteria as defined in the previous chapter. The data are shown in the upper part and the combined contribution from the $\mu\nu_\mu e\nu_e$ sample that includes all diagrams and the $\mu^+\mu^-$ sample is indicated in the lower part of the figure, giving rise to the following results:
$\varepsilon_{\mu,\mathrm{data}}^{\mathrm{HCAL}}$ = 87.1 $\pm$ 6.0%, $\varepsilon_{\mu,\mathrm{MC}}^{\mathrm{HCAL}}$ = 79.5 $\pm$ 7.6%, $\varepsilon_{\mu,\mathrm{data}}^{\mathrm{MUC}}$ = 77.1 $\pm$ 7.1% and $\varepsilon_{\mu,\mathrm{MC}}^{\mathrm{MUC}}$ = 86.0 $\pm$ 6.8%.
The muon identification efficiency ε_μ can be constructed from these muon identification efficiencies via:

$$\varepsilon_\mu = 1 - (1 - \varepsilon_\mu^{\mathrm{MUC}})(1 - \varepsilon_\mu^{\mathrm{HCAL}}). \tag{4.15}$$

Therefore, the following results for the data and MC are obtained using the abovequoted results: $\varepsilon_{\mu,\mathrm{data}}$ = 97.1 $\pm$ 1.8% and $\varepsilon_{\mu,\mathrm{MC}}$ = 97.1 $\pm$ 1.9%, within errors nicely in agreement with each other. A systematic error of 2.6% for the muon identification efficiency is therefore being assigned.
The electron identification efficiency is deduced from events that have passed the complete track selection as described in section 3.3 and whose single charged track has deposited more than 10 GeV in the HPC or EMF and with a total energy deposition in the electromagnetic calorimeters not related to the charged track smaller than 5 GeV. This sample contains especially Comptons and therefore, it is a pure electron sample on which no electron identification has been applied. Two separate efficiencies are defined for the barrel and endcaps:

$$\varepsilon_{e,\mathrm{region}} = \frac{N_{\mathrm{tight,region}}}{N_{\mathrm{tot,region}}}, \tag{4.16}$$

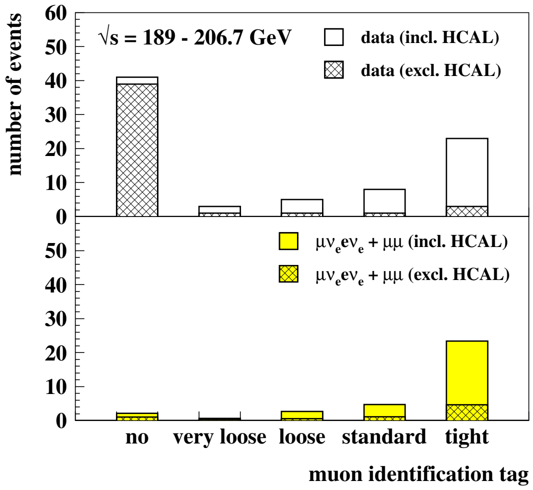

Figure 4.3: *Muon identification tag for the data (top) and the combined contribution from the $\mu\nu_\mu e\nu_e$ sample that includes all diagrams and the $\mu^+\mu^-$ sample (bottom) for the years 1998 - 2000 combined after having applied all selection criteria as defined in the previous chapter.*

where $N_{\mathrm{tight,region}}$ is the number of tight electrons in a certain region out of the total number $N_{\mathrm{tot,region}}$, where "region" represents either "barrel" or "endcaps".
Figure 4.4 shows the distributions of the electron identification tag for events from this sample for the barrel and endcaps for the years 1998 - 2000 combined.
The following efficiencies can be deduced from figure 4.4:
$\varepsilon^{\mathrm{barrel}}_{e,\mathrm{data}}$ = 92.3 $\pm$ 0.8%, $\varepsilon^{\mathrm{barrel}}_{e,\mathrm{MC}}$ = 93.8 $\pm$ 0.7%, $\varepsilon^{\mathrm{endcaps}}_{e,\mathrm{data}}$ = 95.2 $\pm$ 1.2% and $\varepsilon^{\mathrm{endcaps}}_{e,\mathrm{MC}}$ = 88.7 $\pm$ 1.4%, which results in a systematic error of 2.0% for the barrel and 7.5% for the endcaps.

This sample has also been used in determining the relative tracking efficiency for electrons (see section 3.3.2). This relative tracking efficiency also gives rise to a systematic uncertainty and corresponds with 3% for the barrel and 10% for the endcaps.

For the hadronic analysis, it is important to know precisely the energies of the jets and other related quantities. The resolution on the invariant mass of two jets, applying a no constrained fit, $\frac{\sigma_E}{E}$ = 11% ([56]). In order to compensate for the mismatch between data and MC in this distribution of about 10%, a smearing of 5% is applied to the abovementioned quantities, which makes the efficiency ε change from 20.35% to 20.03% and the purity p change from 29.52 to 29.48, considering the years 1998 - 2000 combined.
The effect of all uncertainties mentioned before on the measurement of the muon, electron and hadronic cross sections and their R-factors at $\sqrt{s}$ = 189 GeV are listed in tables 4.4, 4.5 and 4.6 respectively. The superscript "exp" for the indication of the experimental cross sections that appeared in the previous section will be left out from now on for convenience. The total systematic errors for this centre-of-mass energy and the other centre-of-mass energies can be found in tables 4.1, 4.2 and 4.3. Figures 4.5, 4.6 and 4.7 show the dependence of the R-factor and the cross section on the centre-of-mass energies for the years 1998 - 2000 combined, including both the statistical and systematic errors, for the muon, electron and hadronic analyses respectively.

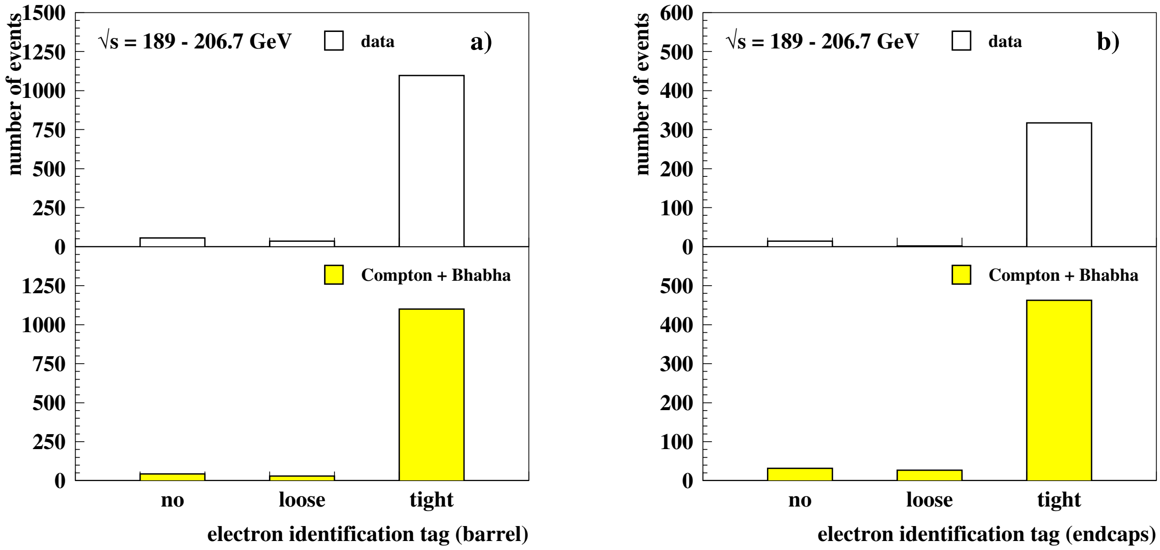

Figure 4.4: *Electron identification tag for the barrel (a)) and endcaps (b)) for the data and Compton and Bhabha events for the years 1998 - 2000 combined. Events in these distributions have passed the complete track selection with a single charged track that has deposited more than 10 GeV in the HPC or EMF and with a total energy deposition in the electromagnetic calorimeters not related to the charged track smaller than 5 GeV.*

In case of a central value, the total error in these plots is obtained from the sum in quadrature of the statistical and systematic components. In case of an upper limit, the starting point of the arrow in these plots is obtained from the sum in quadrature of the upper limit and the systematic error.

Table 4.4: *Contributions of the uncertainties described in the text to the systematic error on the R-factor and cross section for the muon analysis at $\sqrt{s}$ = 189 GeV.*

systematic effect	$\Delta R_{\mu\nu_\mu e\nu_e}$	$\Delta\sigma_{\mu\nu_\mu e\nu_e}$ (fb)
$\Delta\sigma_{\mathrm{bkgr},\mu\nu_\mu e\nu_e}$ $\pm10\%$	±0.06	±4
luminosity $\mathcal{L}$ $\pm6‰$	±0.01	±1
identification efficiency $\Delta\varepsilon_\mu$ $\pm2.6\%$	±0.02	±1
total	±0.06	±4

Table 4.5: *Contributions of the uncertainties described in the text to the systematic error on the R-factor and cross section for the barrel and total electron analyses at $\sqrt{s}$ = 189 GeV.*

systematic effect	$\Delta R^{\rm barrel}_{e\nu_e e\nu_e}$	$\Delta\sigma^{\rm barrel}_{e\nu_e e\nu_e}$ (fb)	$\Delta R^{\rm total}_{e\nu_e e\nu_e}$	$\Delta\sigma^{\rm total}_{e\nu_e e\nu_e}$ (fb)
$\Delta\sigma^{\rm barrel}_{{\rm bkgr},e\nu_e e\nu_e}$ $\pm 20\%$ / $\Delta\sigma^{\rm endcaps}_{{\rm bkgr},e\nu_e e\nu_e}$ $\pm 30\%$	± 0.16	± 9	± 0.17	± 13
luminosity $\mathcal{L}$ $\pm 6‰$	± 0.01	0	± 0.01	± 1
identif. effic. $\Delta\varepsilon_{e,\rm barrel}$ $\pm 2.0\%$ / identif. effic. $\Delta\varepsilon_{e,\rm endcaps}$ $\pm 7.5\%$	± 0.02	± 1	± 0.02	± 2
track. effic. $\Delta\varepsilon_{{\rm track},e,\rm barrel}$ $\pm 3\%$ / track. effic. $\Delta\varepsilon_{{\rm track},e,\rm endcaps}$ $\pm 10\%$	± 0.03	± 1	± 0.03	± 2
total	± 0.16	± 9	± 0.17	± 13

Table 4.6: *Contributions of the uncertainties described in the text to the systematic error on the R-factor and cross section for the hadronic analysis at $\sqrt{s}$ = 189 GeV.*

systematic effect	$\Delta R_{q\bar{q}e\nu_e}$	$\Delta\sigma_{q\bar{q}e\nu_e}$ (pb)
$\Delta\sigma_{{\rm bkgr},q\bar{q}e\nu_e}$ $\pm 5\%$	± 0.13	± 0.06
luminosity $\mathcal{L}$ $\pm 6‰$	± 0.03	± 0.01
smearing $+5\%$	$+0.05$	$+0.02$
total	± 0.14	± 0.07

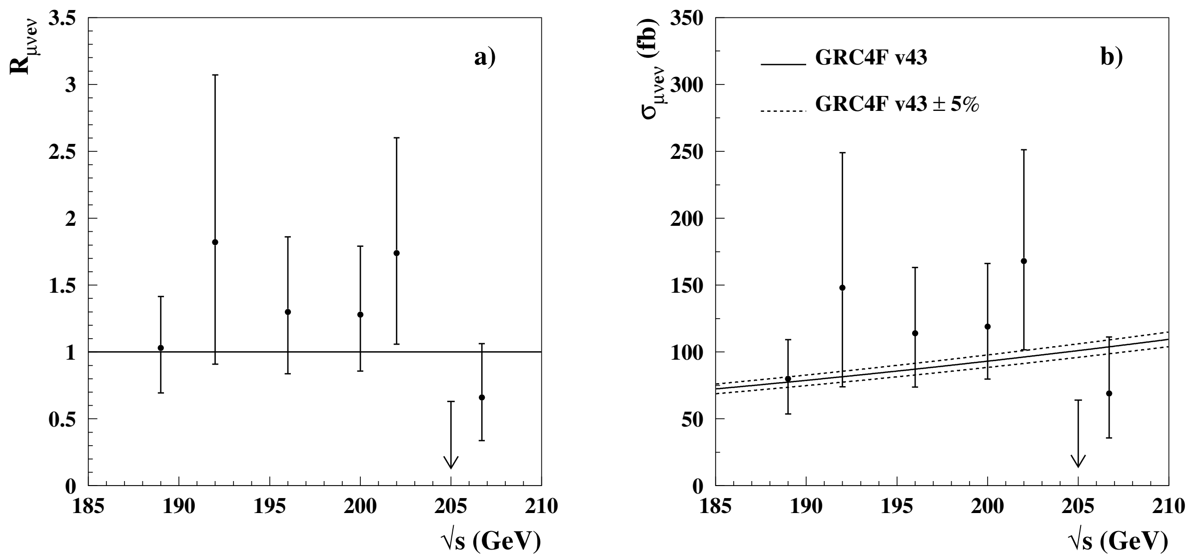

Figure 4.5: *Dependence of the R-factor (a)) and the cross section (b)) of the Crete final state $\mu\nu_\mu e\nu_e$ on the centre-of-mass energies for the years 1998 - 2000 combined.*

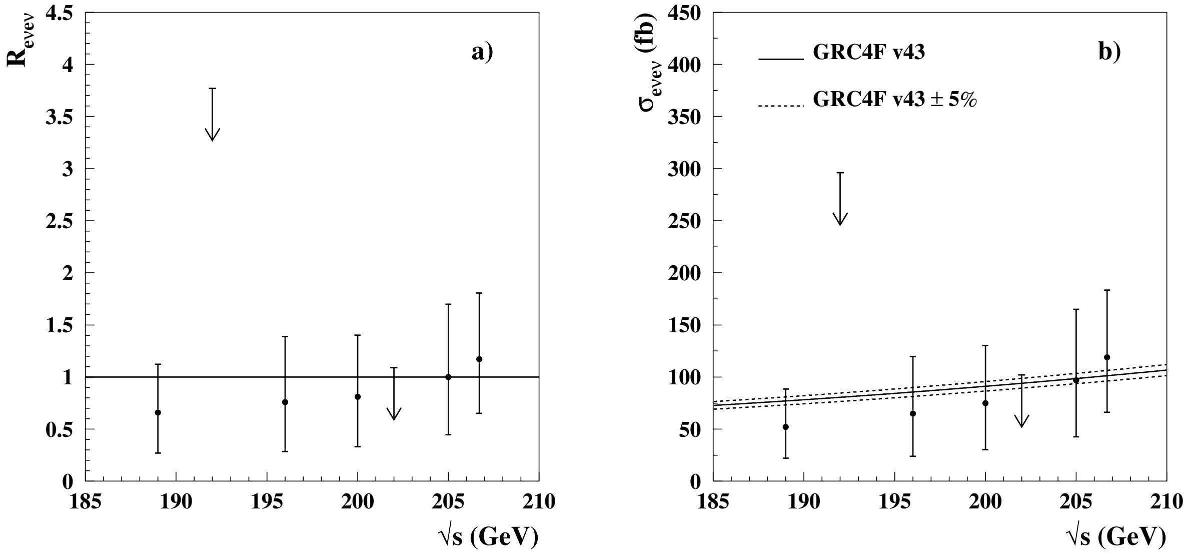

Figure 4.6: *Dependence of the R-factor (a)) and the cross section (b)) of the Crete final state $e\nu_e e\nu_e$ on the centre-of-mass energies for the years 1998 - 2000 combined.*

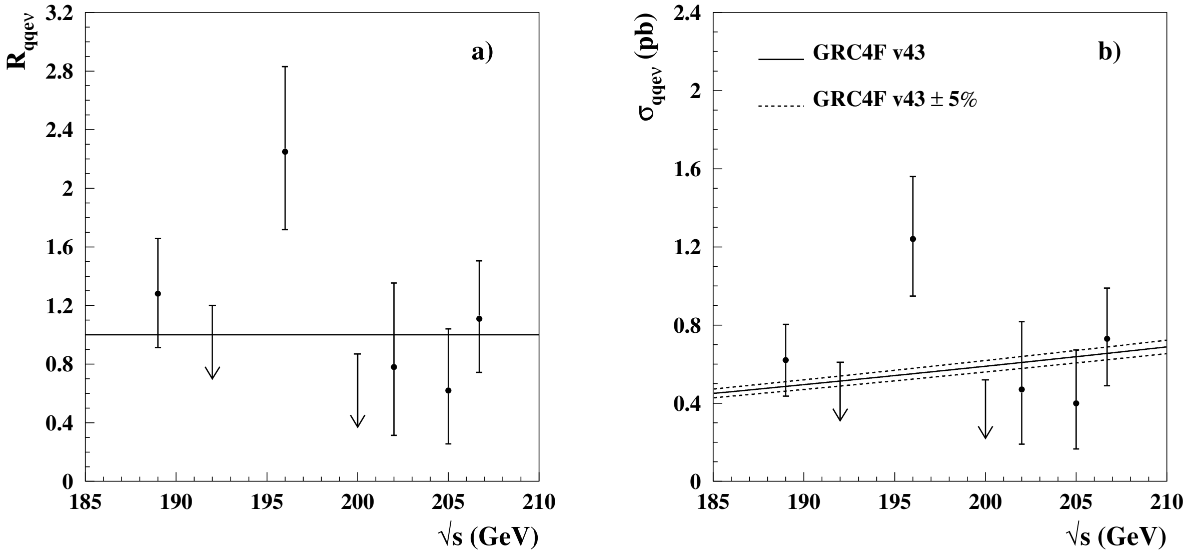

Figure 4.7: *Dependence of the R-factor (a)) and the cross section (b)) of the Crete final state $q\bar{q}e\nu_e$ on the centre-of-mass energies for the years 1998 - 2000 combined.*

4.4 Single W cross section

The single W cross section $\sigma_{We\nu_e}$ is obtained by adding the contributions from the electron, muon and hadronic analyses in the following way, assuming $\mu - \tau$ universality:

$$\sigma_{We\nu_e} = \sigma_{e\nu_e e\nu_e} + 2\sigma_{\mu\nu_\mu e\nu_e} + \sigma_{q\bar{q}e\nu_e}. \tag{4.17}$$

The factor 2 from equation (4.17) is taken into account by broadening the -Δ2ln$\mathcal{L}$ distribution from the muon analysis with respect to the minimum by a factor 2. Adding this distribution with the ones from the electron and hadronic analyses results in values of the R-factor $R_{We\nu_e}$ and the experimental cross section $\sigma_{We\nu_e}$ of the single W final state for the various centre-of-mass energies that are listed in table 4.7, which includes their statistical and systematic errors and theoretical cross sections. The corresponding -Δ2ln$\mathcal{L}$ distributions and pdfs can be seen in appendix A.4. For the calculation of the systematic errors, the uncertainty from the luminosity is treated as correlated error between the muon, the electron and hadronic analyses, while all other discussed systematic effects are taken as uncorrelated. The R-factor and cross section results are represented in graphical form in figure 4.8.
This method is model-dependent, since it is assumed that the branching ratios of the electron, the muon and the hadrons follow the SM values, which makes it possible to add the -Δ2ln$\mathcal{L}$ distributions of the three analyses as explained just before.

Table 4.7: *Values for $R_{We\nu_e}$ and $\sigma_{We\nu_e}$ including the upper and lower errors and systematic errors and theoretical cross sections $\sigma^{\rm theor}_{We\nu_e}$ for the various centre-of-mass energies for the single W final state. At $\sqrt{s}$ = 192 and 202 GeV only an upper limit is quoted.*

$\sqrt{s}$ (GeV)	$R_{We\nu_e}$	$\sigma_{We\nu_e}$ (pb)	$\sigma^{\rm theor}_{We\nu_e}$ (pb)
189	$1.02^{+0.26}_{-0.25}\pm0.04$	$0.73^{+0.19}_{-0.18}\pm0.03$	0.720
192	$<1.20\pm0.04$	$<0.90\pm0.03$	0.753
196	$1.64^{+0.40}_{-0.38}\pm0.03$	$1.33^{+0.33}_{-0.31}\pm0.02$	0.813
200	$0.47^{+0.28}_{-0.24}\pm0.03$	$0.41^{+0.24}_{-0.21}\pm0.02$	0.866
202	$<1.07\pm0.04$	$<0.96\pm0.03$	0.895
205	$0.51^{+0.30}_{-0.25}\pm0.04$	$0.48^{+0.28}_{-0.23}\pm0.03$	0.937
206.7	$1.03^{+0.28}_{-0.27}\pm0.03$	$0.99^{+0.27}_{-0.26}\pm0.02$	0.964
189 - 206.7	$0.83^{+0.12}_{-0.12}\pm0.03$		

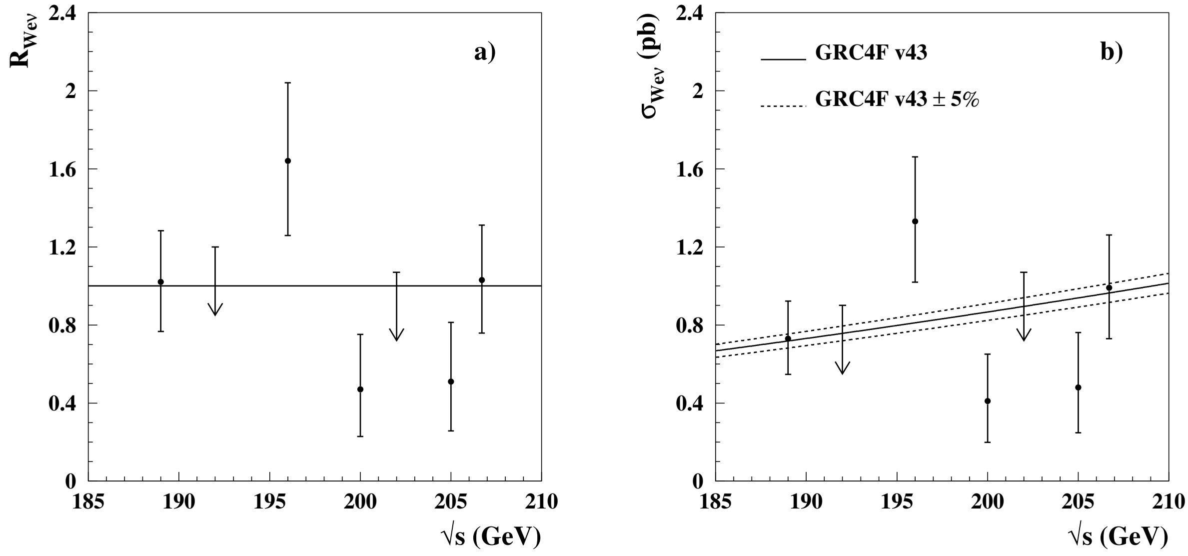

Figure 4.8: *Dependence of the R-factor (a)) and the cross section (b)) of the Crete single W final state on the centre-of-mass energies for the years 1998 - 2000 combined.*

4.5 Forward-backward asymmetry

For the leptonic case, it is interesting to investigate in which direction the leptons tend to traverse the detector in view of the TGC analysis that is discussed in the next chapter: is there a preference for the forward direction ($\theta_l \leq 90°$; ($l = e$ or μ)), for the backward direction ($\theta_l > 90°$) or is there no preferred direction?
The distribution of -$Q_l\cos\theta_l$, where Q_l is the charge of the lepton, is used to examine this behaviour.

4.5.1 Muon analysis

Figure 4.9 shows the distribution of $\frac{\mathrm{d}\sigma}{\mathrm{d}(-Q_\mu\cos\theta_\mu)}$ coming from the $\mu\nu_\mu e\nu_e$ final state, both for all diagrams and the Crete subset, at generator level at $\sqrt{s}$ = 189 GeV. It is clear from the figure that the muons that satisfy the Crete definition have a small preference for going in the forward direction, while this behaviour is much more visible for the other muons.

The final number of events in the forward direction that have passed the muon selection criteria that have been explained in the previous chapter are listed in table 4.8, while the results for the backward direction can be found in table 4.9. The efficiencies for the forward and backward direction are the same within the statistical error for the various centre-of-mass energies.

The abovelisted results give rise to the R-factors and cross sections for the forward and backward directions that are summarised in table 4.10 and depicted in figure 4.10.

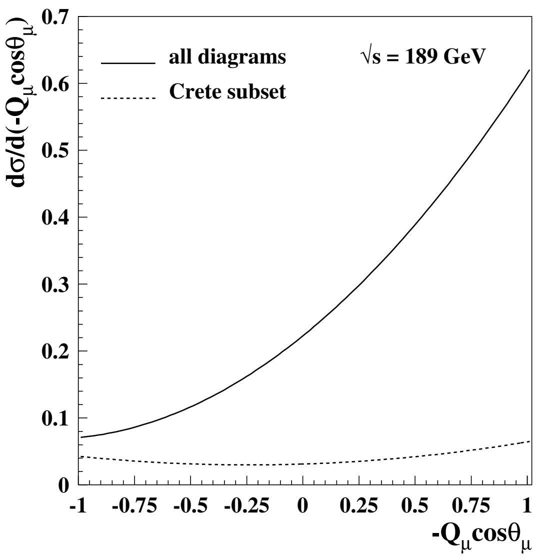

Figure 4.9: *Distributions of* $\frac{\mathrm{d}\sigma}{\mathrm{d}(-Q_{\mu}\cos\theta_{\mu})}$ *coming from the* $\mu\nu_{\mu}e\nu_{e}$ *final state, both for all diagrams and the Crete subset, at generator level at* $\sqrt{s}$ *= 189 GeV.*

Table 4.8: *Number of selected events in the forward direction per contributing process and number of observed events for the various centre-of-mass energies for the muon analysis.*

	$\sqrt{s}$ (GeV)							
number of events	189	192	196	200	202	205	206.7	189 - 206.7
$N_{\mu\nu_\mu e\nu_e,\mathrm{Crete}}$	3.42 ± 0.07	0.56 ± 0.01	1.72 ± 0.04	1.99 ± 0.04	1.01 ± 0.02	1.82 ± 0.04	2.18 ± 0.05	12.69 ± 0.11
$N_{\mu\nu_\mu e\nu_e,\mathrm{non-Crete}}$	0.44 ± 0.25	0.14 ± 0.04	0.31 ± 0.13	0.32 ± 0.15	0.24 ± 0.08	0.50 ± 0.14	0.47 ± 0.17	2.42 ± 0.40
$N_{\tau\nu_\tau e\nu_e}$	0.28 ± 0.07	0.03 ± 0.01	0.10 ± 0.03	0.14 ± 0.04	0.06 ± 0.02	0.12 ± 0.03	0.16 ± 0.04	0.89 ± 0.10
$N_{l\nu_l\bar{l}\bar{\nu}_l}$	1.01 ± 0.15	0.13 ± 0.02	0.40 ± 0.07	0.48 ± 0.08	0.33 ± 0.05	0.46 ± 0.07	0.54 ± 0.08	3.35 ± 0.22
$N_{\mu^+\mu^-}$	0.37 ± 0.10	0.06 ± 0.01	0.17 ± 0.03	0.17 ± 0.03	0.10 ± 0.02	0.19 ± 0.03	0.13 ± 0.03	1.20 ± 0.12
$N_{\tau^+\tau^-}$	0.03 ± 0.03	0.00 ± 0.00	0.00 ± 0.00	0.03 ± 0.02	0.02 ± 0.01	0.00 ± 0.00	0.00 ± 0.00	0.08 ± 0.04
$N_{e\bar{e}l\bar{l}}\ (l \neq e)$	0.05 ± 0.02	0.00 ± 0.00	0.01 ± 0.01	0.01 ± 0.01	0.01 ± 0.01	0.10 ± 0.05	0.00 ± 0.00	0.18 ± 0.06
N_{cosmic}	0.00 ± 0.00	0.00 ± 0.00	0.00 ± 0.00	0.00 ± 0.00	0.00 ± 0.00	0.00 ± 0.00	0.00 ± 0.00	0.01 ± 0.01
N_{expected}	5.61 ± 0.33	0.93 ± 0.05	2.71 ± 0.16	3.14 ± 0.19	1.76 ± 0.10	3.19 ± 0.18	3.47 ± 0.20	20.82 ± 0.50
N_{observed}	5	0	3	3	3	1	1	16

Table 4.9: *Number of selected events in the backward direction per contributing process and number of observed events for the various centre-of-mass energies for the muon analysis.*

	$\sqrt{s}$ (GeV)							
number of events	189	192	196	200	202	205	206.7	189 - 206.7
$N_{\mu\nu_\mu e\nu_e,\mathrm{Crete}}$	2.60 ± 0.07	0.44 ± 0.01	1.47 ± 0.04	1.84 ± 0.04	0.90 ± 0.02	1.62 ± 0.04	1.91 ± 0.05	10.79 ± 0.11
$N_{\mu\nu_\mu e\nu_e,\mathrm{non-Crete}}$	0.39 ± 0.22	0.02 ± 0.04	-0.13 ± 0.13	-0.03 ± 0.14	0.10 ± 0.07	0.03 ± 0.12	-0.11 ± 0.14	0.27 ± 0.35
$N_{\tau\nu_\tau e\nu_e}$	0.19 ± 0.06	0.03 ± 0.01	0.09 ± 0.03	0.14 ± 0.04	0.05 ± 0.02	0.10 ± 0.03	0.13 ± 0.04	0.74 ± 0.10
$N_{l\nu_l\bar{l}\bar{\nu}_l}$	0.14 ± 0.06	0.04 ± 0.01	0.12 ± 0.04	0.08 ± 0.03	0.05 ± 0.02	0.06 ± 0.02	0.19 ± 0.05	0.68 ± 0.10
$N_{\mu^+\mu^-}$	0.23 ± 0.08	0.05 ± 0.01	0.12 ± 0.03	0.11 ± 0.03	0.05 ± 0.01	0.12 ± 0.02	0.14 ± 0.03	0.81 ± 0.10
$N_{\tau^+\tau^-}$	0.03 ± 0.03	0.00 ± 0.00	0.00 ± 0.00	0.00 ± 0.00	0.00 ± 0.00	0.00 ± 0.00	0.00 ± 0.00	0.03 ± 0.03
$N_{e\bar{e}l\bar{l}}\ (l \neq e)$	0.01 ± 0.01	0.01 ± 0.01	0.02 ± 0.01	0.01 ± 0.01	0.02 ± 0.01	0.08 ± 0.04	0.02 ± 0.02	0.16 ± 0.05
N_{cosmic}	0.00 ± 0.00	0.00 ± 0.00	0.00 ± 0.00	0.00 ± 0.00	0.00 ± 0.00	0.00 ± 0.00	0.00 ± 0.00	0.01 ± 0.01
N_{expected}	3.59 ± 0.26	0.59 ± 0.04	1.69 ± 0.15	2.14 ± 0.15	1.17 ± 0.08	2.01 ± 0.14	2.29 ± 0.16	13.49 ± 0.41
N_{observed}	4	2	2	3	1	0	3	15

Table 4.10: *Values for* $R^{\mathrm{forw}}_{\mu\nu_\mu e\nu_e}$, $\sigma^{\mathrm{forw}}_{\mu\nu_\mu e\nu_e}$, $R^{\mathrm{backw}}_{\mu\nu_\mu e\nu_e}$ *and* $\sigma^{\mathrm{backw}}_{\mu\nu_\mu e\nu_e}$ *including the upper and lower errors or upper limits and systematic errors and theoretical cross sections for the various centre-of-mass energies.*

$\sqrt{s}$ (GeV)	$R^{\mathrm{forw}}_{\mu\nu_\mu e\nu_e}$	$\sigma^{\mathrm{forw}}_{\mu\nu_\mu e\nu_e}$ (fb)	$\sigma^{\mathrm{theor,forw}}_{\mu\nu_\mu e\nu_e}$ (fb)
189	$0.93^{+0.52}_{-0.43}\pm0.07$	$41^{+23}_{-19}\pm3$	44.0
192	$<2.68\pm0.06$	$<122\pm3$	45.7
196	$1.37^{+0.84}_{-0.65}\pm0.06$	$67^{+41}_{-32}\pm3$	49.1
200	$1.11^{+0.73}_{-0.56}\pm0.06$	$56^{+37}_{-28}\pm3$	50.6
202	$2.57^{+1.45}_{-1.12}\pm0.09$	$137^{+77}_{-60}\pm5$	53.4
205	$<1.25\pm0.08$	$<69\pm4$	55.5
206.7	$<1.06\pm0.06$	$<60\pm3$	56.4
189 - 206.7	$0.66^{+0.23}_{-0.22}\pm0.07$		
$\sqrt{s}$ (GeV)	$R^{\mathrm{backw}}_{\mu\nu_\mu e\nu_e}$	$\sigma^{\mathrm{backw}}_{\mu\nu_\mu e\nu_e}$ (fb)	$\sigma^{\mathrm{theor,backw}}_{\mu\nu_\mu e\nu_e}$ (fb)
189	$1.29^{+0.63}_{-0.50}\pm0.04$	$43^{+21}_{-17}\pm1$	33.6
192	$4.95^{+2.83}_{-2.06}\pm0.05$	$175^{+100}_{-73}\pm2$	35.4
196	$1.44^{+0.85}_{-0.62}\pm0.02$	$56^{+33}_{-24}\pm1$	38.7
200	$1.65^{+0.79}_{-0.61}\pm0.02$	$69^{+33}_{-26}\pm1$	42.0
202	$<3.20\pm0.03$	$<138\pm1$	43.0
205	$<0.93\pm0.02$	$<42\pm1$	45.5
206.7	$1.55^{+0.77}_{-0.59}\pm0.03$	$74^{+37}_{-28}\pm1$	47.5
189 - 206.7	$1.17^{+0.28}_{-0.24}\pm0.03$		

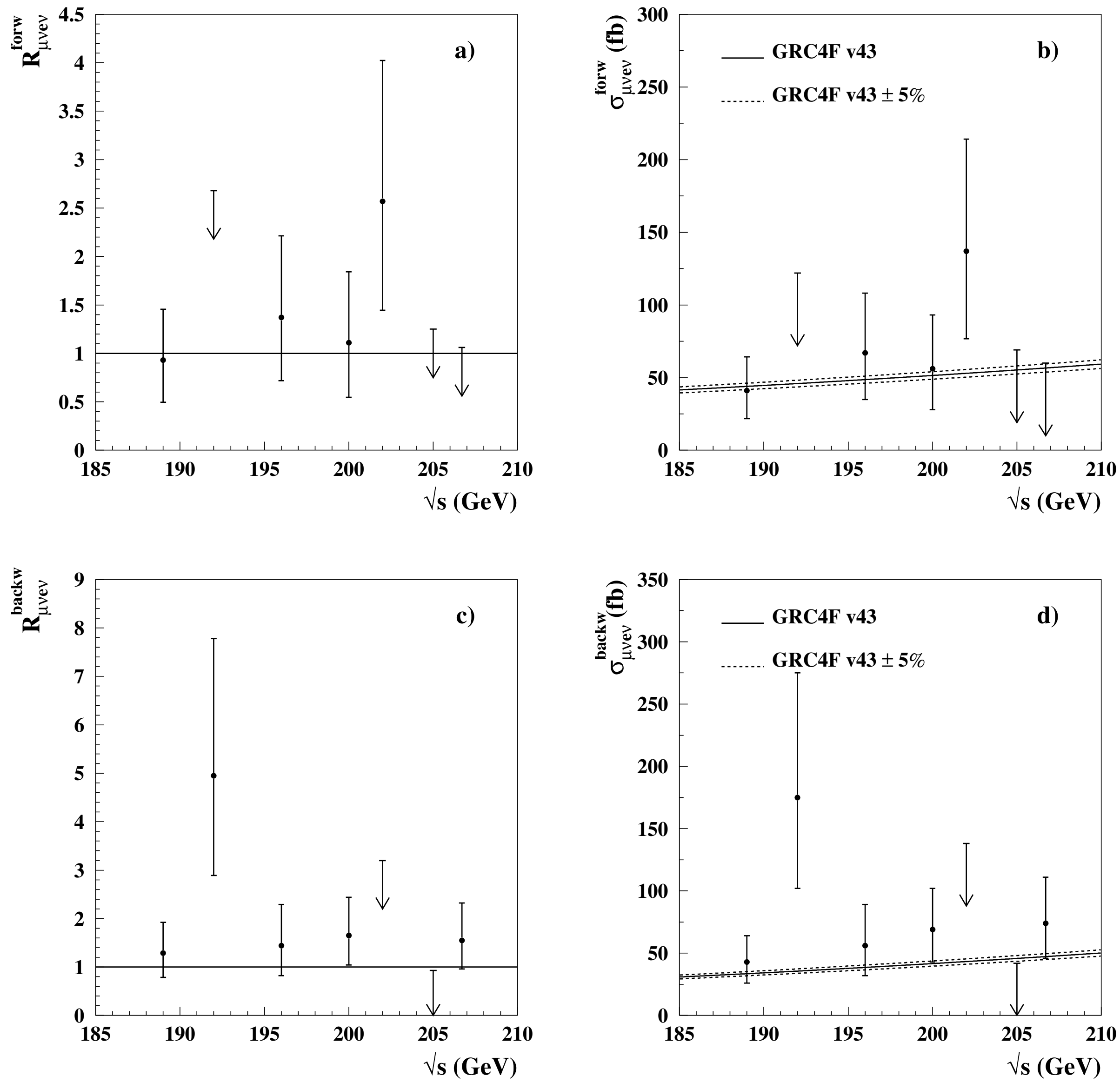

Figure 4.10: *Dependence of the R-factor and the cross section of the Crete final state $\mu\nu_\mu e\nu_e$ on the centre-of-mass energies for the years 1998 - 2000 combined for the forward and backward directions.*

4.5.2 Electron analysis

Figure 4.11 indicates the distribution of $\frac{d\sigma}{d(-Q_e\cos\theta_e)}$ coming from the $e\nu_e e\nu_e$ final state, both for all diagrams and the Crete subset, at generator level at $\sqrt{s}$ = 189 GeV. One can conclude from the figure that electrons that satisfy the Crete definition have a small preference for going in the forward direction, while the other electrons prefer more to go into this direction.

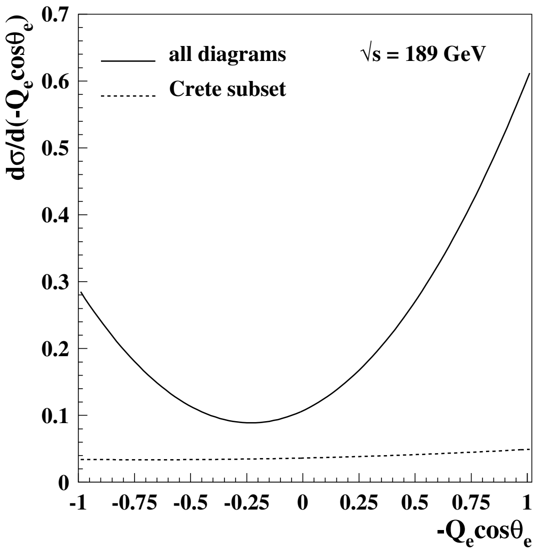

Figure 4.11: *Distributions of* $\frac{d\sigma}{d(-Q_e\cos\theta_e)}$ *coming from the* $e\nu_e e\nu_e$ *final state, both for all diagrams and the Crete subset, at generator level at* $\sqrt{s}$ *= 189 GeV.*

The same procedure as for the muons is repeated for the electron analysis, which results in the number of events that are represented in tables 4.11 and 4.12.

Table 4.11: *Number of selected events in the forward direction per contributing process and number of observed events for the various centre-of-mass energies for the electron analysis.*

number of events	$\sqrt{s}$ (GeV) 189	192	196	200	202	205	206.7	189 - 206.7
$N_{e\nu_e e\nu_e,\mathrm{Crete}}$	2.42 $\pm$ 0.07	0.38 $\pm$ 0.01	1.26 $\pm$ 0.04	1.54 $\pm$ 0.05	0.75 $\pm$ 0.02	1.30 $\pm$ 0.04	1.59 $\pm$ 0.05	9.25 $\pm$ 0.12
$N_{e\nu_e e\nu_e,\mathrm{non-Crete}}$	0.28 $\pm$ 0.24	0.05 $\pm$ 0.04	0.04 $\pm$ 0.12	0.01 $\pm$ 0.14	-0.03 $\pm$ 0.07	0.07 $\pm$ 0.12	-0.07 $\pm$ 0.14	0.31 $\pm$ 0.36
$N_{\tau\nu_\tau e\nu_e}$	0.10 $\pm$ 0.04	0.03 $\pm$ 0.01	0.06 $\pm$ 0.02	0.09 $\pm$ 0.03	0.04 $\pm$ 0.01	0.04 $\pm$ 0.02	0.09 $\pm$ 0.03	0.44 $\pm$ 0.07
$N_{\mu\nu_\mu e\nu_e}$	0.03 $\pm$ 0.02	0.01 $\pm$ 0.01	0.04 $\pm$ 0.02	0.09 $\pm$ 0.03	0.02 $\pm$ 0.01	0.03 $\pm$ 0.02	0.01 $\pm$ 0.01	0.23 $\pm$ 0.05
$N_{e\bar{e}\nu_l\bar{\nu}_l}$ $(l \neq e)$	0.90 $\pm$ 0.40	0.17 $\pm$ 0.07	0.44 $\pm$ 0.19	0.69 $\pm$ 0.24	0.36 $\pm$ 0.12	0.65 $\pm$ 0.21	0.56 $\pm$ 0.23	3.76 $\pm$ 0.61
N_{Compton}	0.15 $\pm$ 0.11	0.00 $\pm$ 0.00	0.03 $\pm$ 0.03	0.04 $\pm$ 0.04	0.04 $\pm$ 0.04	0.06 $\pm$ 0.06	0.08 $\pm$ 0.05	0.41 $\pm$ 0.15
$N_{\nu_l\bar{\nu}_l(\gamma)}$	0.20 $\pm$ 0.12	0.06 $\pm$ 0.03	0.25 $\pm$ 0.05	0.26 $\pm$ 0.08	0.13 $\pm$ 0.05	0.19 $\pm$ 0.06	0.18 $\pm$ 0.07	1.26 $\pm$ 0.19
$N_{\tau^+\tau^-}$	0.00 $\pm$ 0.00	0.00 $\pm$ 0.00	0.00 $\pm$ 0.00	0.02 $\pm$ 0.02	0.01 $\pm$ 0.01	0.01 $\pm$ 0.01	0.01 $\pm$ 0.01	0.04 $\pm$ 0.03
N_{expected}	4.10 $\pm$ 0.50	0.70 $\pm$ 0.09	2.08 $\pm$ 0.24	2.74 $\pm$ 0.30	1.31 $\pm$ 0.15	2.35 $\pm$ 0.26	2.45 $\pm$ 0.29	15.72 $\pm$ 0.76
N_{observed}	4	1	1	2	0	3	2	13

Table 4.12: *Number of selected events in the backward direction per contributing process and number of observed events for the various centre-of-mass energies for the electron analysis.*

number of events	$\sqrt{s}$ (GeV) 189	192	196	200	202	205	206.7	189 - 206.7
$N_{e\nu_e e\nu_e,\mathrm{Crete}}$	2.02 $\pm$ 0.07	0.33 $\pm$ 0.01	1.08 $\pm$ 0.04	1.24 $\pm$ 0.04	0.65 $\pm$ 0.02	1.10 $\pm$ 0.04	1.32 $\pm$ 0.05	7.73 $\pm$ 0.11
$N_{e\nu_e e\nu_e,\mathrm{non-Crete}}$	0.13 $\pm$ 0.22	-0.04 $\pm$ 0.04	-0.06 $\pm$ 0.11	0.18 $\pm$ 0.13	0.01 $\pm$ 0.07	0.18 $\pm$ 0.12	0.18 $\pm$ 0.14	0.57 $\pm$ 0.34
$N_{\tau\nu_\tau e\nu_e}$	0.16 $\pm$ 0.05	0.02 $\pm$ 0.01	0.04 $\pm$ 0.02	0.08 $\pm$ 0.03	0.04 $\pm$ 0.01	0.13 $\pm$ 0.03	0.11 $\pm$ 0.03	0.58 $\pm$ 0.08
$N_{\mu\nu_\mu e\nu_e}$	0.00 $\pm$ 0.00	0.00 $\pm$ 0.00	0.00 $\pm$ 0.00	0.01 $\pm$ 0.01	0.00 $\pm$ 0.00	0.02 $\pm$ 0.01	0.00 $\pm$ 0.00	0.03 $\pm$ 0.01
$N_{e\bar{e}\nu_l\bar{\nu}_l}$ $(l \neq e)$	0.97 $\pm$ 0.37	0.19 $\pm$ 0.06	0.70 $\pm$ 0.19	0.57 $\pm$ 0.23	0.19 $\pm$ 0.11	0.51 $\pm$ 0.20	0.64 $\pm$ 0.23	3.77 $\pm$ 0.58
N_{Compton}	0.00 $\pm$ 0.00	0.00 $\pm$ 0.00	0.00 $\pm$ 0.00	0.04 $\pm$ 0.04	0.00 $\pm$ 0.00	0.00 $\pm$ 0.00	0.00 $\pm$ 0.00	0.04 $\pm$ 0.04
$N_{\nu_l\bar{\nu}_l(\gamma)}$	0.59 $\pm$ 0.20	0.05 $\pm$ 0.03	0.16 $\pm$ 0.04	0.10 $\pm$ 0.05	0.06 $\pm$ 0.04	0.11 $\pm$ 0.04	0.15 $\pm$ 0.06	1.21 $\pm$ 0.23
$N_{\tau^+\tau^-}$	0.00 $\pm$ 0.00	0.00 $\pm$ 0.00	0.00 $\pm$ 0.00	0.00 $\pm$ 0.00	0.00 $\pm$ 0.00	0.00 $\pm$ 0.00	0.01 $\pm$ 0.01	0.01 $\pm$ 0.01
N_{expected}	3.87 $\pm$ 0.48	0.54 $\pm$ 0.08	1.92 $\pm$ 0.22	2.21 $\pm$ 0.27	0.95 $\pm$ 0.13	2.04 $\pm$ 0.24	2.41 $\pm$ 0.28	13.94 $\pm$ 0.72
N_{observed}	2	0	2	2	0	1	3	10

These number of events and efficiencies lead to the R-factors and cross sections for the forward and backward directions that are listed in table 4.13 and depicted in figure 4.12. In determining the systematic errors, it is assumed that the total systematic error on the background cross section $\Delta\sigma_{\mathrm{bkgr},e\nu_e e\nu_e}$ = 22%, the electron identification efficiency $\Delta\varepsilon_e$ = 3.5% and the tracking efficiency $\Delta\varepsilon_{\mathrm{track},e}$ = 5%.

Table 4.13: *Values for $R^{\mathrm{forw}}_{e\nu_e e\nu_e}$, $\sigma^{\mathrm{forw}}_{e\nu_e e\nu_e}$, $R^{\mathrm{backw}}_{e\nu_e e\nu_e}$ and $\sigma^{\mathrm{backw}}_{e\nu_e e\nu_e}$ including the upper and lower errors or upper limits and systematic errors and theoretical cross sections for the various centre-of-mass energies.*

$\sqrt{s}$ (GeV)	$R^{\mathrm{forw}}_{e\nu_e e\nu_e}$	$\sigma^{\mathrm{forw}}_{e\nu_e e\nu_e}$ (fb)	$\sigma^{\mathrm{theor,forw}}_{e\nu_e e\nu_e}$ (fb)
189	$1.10^{+0.68}_{-0.53}\pm0.16$	$48^{+30}_{-23}\pm7$	43.8
192	$<7.46\pm0.19$	$<322\pm8$	43.1
196	$<1.99\pm0.14$	$<95\pm7$	47.7
200	$<2.25\pm0.19$	$<114\pm9$	50.6
202	$<2.01\pm0.16$	$<104\pm8$	51.8
205	$1.76^{+1.12}_{-0.85}\pm0.18$	$93^{+59}_{-45}\pm10$	52.8
206.7	$0.96^{+0.78}_{-0.55}\pm0.12$	$53^{+43}_{-30}\pm7$	55.4
189 - 206.7	$0.74^{+0.30}_{-0.26}\pm0.16$		
$\sqrt{s}$ (GeV)	$R^{\mathrm{backw}}_{e\nu_e e\nu_e}$	$\sigma^{\mathrm{backw}}_{e\nu_e e\nu_e}$ (fb)	$\sigma^{\mathrm{theor,backw}}_{e\nu_e e\nu_e}$ (fb)
189	$<1.50\pm0.21$	$<52\pm7$	34.4
192	$<4.54\pm0.19$	$<160\pm7$	35.3
196	$1.42^{+1.13}_{-0.82}\pm0.18$	$55^{+43}_{-31}\pm7$	38.4
200	$1.15^{+0.99}_{-0.70}\pm0.18$	$48^{+41}_{-29}\pm8$	41.8
202	$<2.31\pm0.20$	$<97\pm8$	42.1
205	$<2.23\pm0.20$	$<99\pm9$	44.6
206.7	$1.72^{+1.10}_{-0.85}\pm0.19$	$80^{+51}_{-39}\pm9$	46.3
189 - 206.7	$0.52^{+0.31}_{-0.26}\pm0.19$		

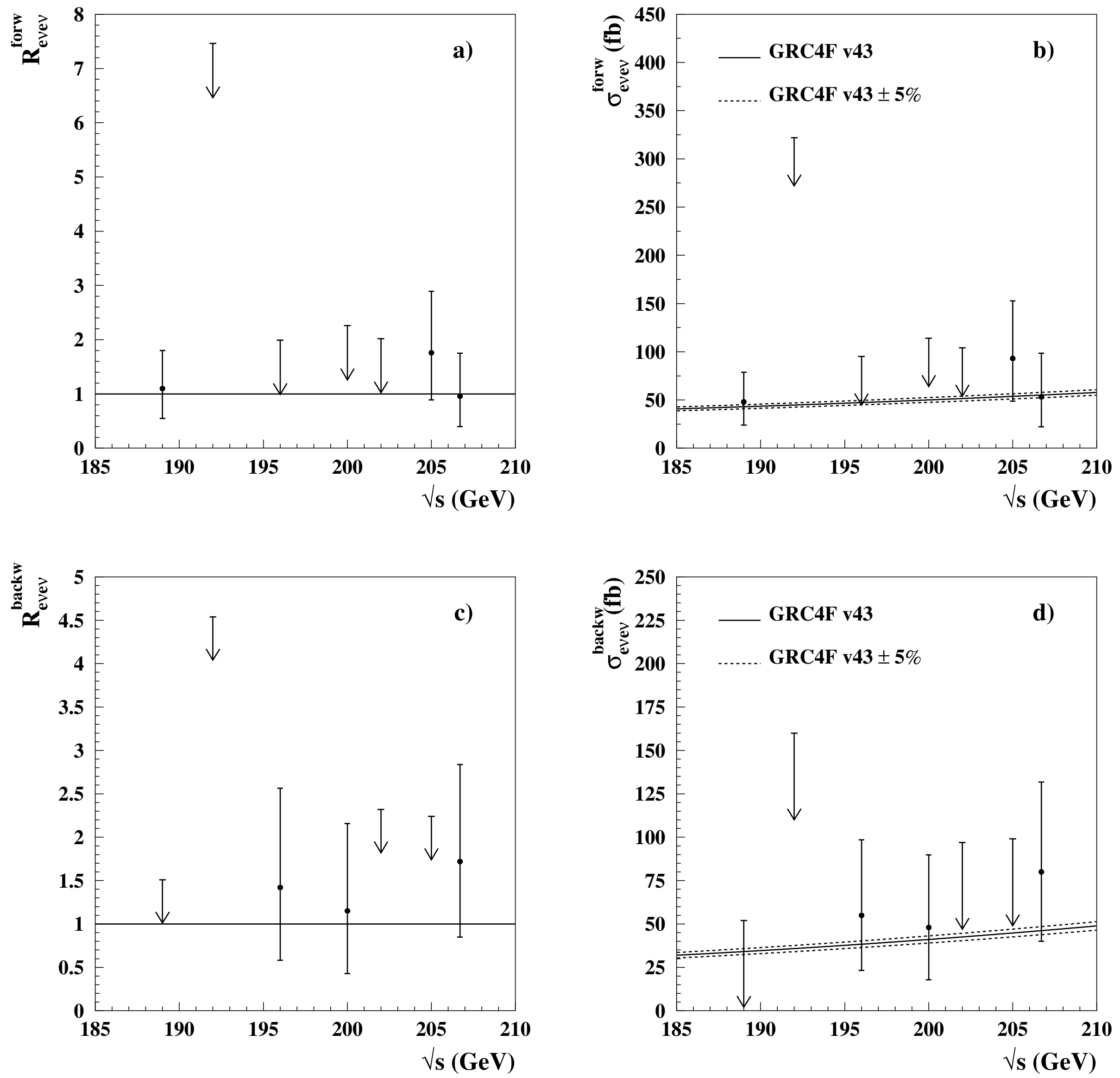

Figure 4.12: *Dependence of the R-factor and the cross section of the Crete final state $e\nu_e e\nu_e$ on the centre-of-mass energies for the years 1998 - 2000 combined for the forward and backward directions.*

4.6 Conclusions

From the different analyses, the conclusion can be drawn that the R-factor values and cross section results are generally in good agreement with their SM expectations. In case of upper limits, these SM values are usually not excluded.
For the calculation of the R-factor from the single W analysis for the years 1998 - 2000 combined, the following result is obtained:

$$R_{We\nu_e} = 0.83 \pm 0.12(\text{stat}) \pm 0.03(\text{syst}).$$

CHAPTER 5

TGC analysis

This chapter presents the results of the TGC measurements for the muon, electron and hadronic final states that are obtained from the leptonic and hadronic event selections as described in chapter 3.

5.1 TGC analysis

The TGC analysis follows the same procedure in finding the best value for the coupling α (α = $\Delta\kappa_\gamma$, λ_γ or Δg_1^Z) as the cross section analysis described in section 4.1, but in this case the cross section σ gets a dependence on the coupling α: $\sigma = \sigma(\alpha)$.
The best measured coupling α is thus obtained by finding the minimum of:

$$\text{-ln}\mathcal{L}(\alpha) = \sum_i N_{\text{exp},i}(\alpha) - N_{\text{obs},i}\text{ln}N_{\text{exp},i}(\alpha) + \text{ln}N_{\text{obs},i}!. \tag{5.1}$$

The value of the coupling α can obtain $a\ priori$ any real number, contrary to the value of the cross section σ. The prior function $P(\alpha)$ is a constant function over the whole parameter space and it is therefore completely justified to obtain from the -Δ2ln$\mathcal{L}$ distribution the best value and its errors for α. In such a distribution, the horizontal line of the 1σ error cuts the vertical axis at 1, interpreting the distribution as a χ^2-distribution. In case of a distribution with most likely value $\alpha^{\max}$, the probability that the coupling α lies in the interval [$\alpha^{\max}$ - $\delta_{1,1\sigma}$, $\alpha^{\max}$ + $\delta_{2,1\sigma}$], with -Δ2ln$\mathcal{L}$($\alpha^{\max}$ - $\delta_{1,1\sigma}$) = -Δ2ln$\mathcal{L}$($\alpha^{\max}$ + $\delta_{2,1\sigma}$) = 1, equals 68.27$\%$; the confidence level CL = 68.27$\%$. For convenience, this confidence level will be referred to as "CL = 68$\%$" in the rest of this thesis. The horizontal line of the 2σ error intersects the vertical axis at 4: the probability that the coupling α lies in the interval [$\alpha^{\max}$ - $\delta_{3,2\sigma}$, $\alpha^{\max}$ + $\delta_{4,2\sigma}$], with -Δ2ln$\mathcal{L}$($\alpha^{\max}$ - $\delta_{3,2\sigma}$) = -Δ2ln$\mathcal{L}$($\alpha^{\max}$ + $\delta_{4,2\sigma}$) = 4, corresponds with the case "CL = 95$\%$".
In some cases the -Δ2ln$\mathcal{L}$ distribution shows the appearance of two minima, which can become clearly visible for the coupling $\Delta\kappa_\gamma$. For this coupling, the minima of the t-channel cross sections of the $e\nu_e e\nu_e$, $\mu\nu_\mu e\nu_e$ and $q\bar{q}e\nu_e$ final states are located around -1 (see figures 1.4a), 1.5a) and 1.6a) respectively), while a measurement that favours the SM value, i.e. N_{obs} = N_{exp}($\Delta\kappa_\gamma$ = 0.0), introduces two minima in the -Δ2ln$\mathcal{L}$ distribution: one minimum around $\Delta\kappa_\gamma$ = -2.0 and one minimum at $\Delta\kappa_\gamma$ = 0.0. In general, this shape of the -Δ2ln$\mathcal{L}$ distribution is not observed for the couplings λ_γ and Δg_1^Z, since for these couplings the minima of the t-channel cross sections of the $e\nu_e e\nu_e$, $\mu\nu_\mu e\nu_e$ and $q\bar{q}e\nu_e$ final states are situated at their SM values (see figures 1.4b), 1.4c),

1.5b), 1.5c), 1.6b) and 1.6c)).

The expressions for $N_{\text{exp},i}(\alpha)$ from equation (5.1) for the different TGC analyses are obtained by simulating events for the TGC dependent contributions at the values α = -2.0, -1.0, 0.0, 1.0 and 2.0. Contrary to the single W cross section analysis, one does not make use of a signal sample that satisfies the Crete definition. The simulated samples contain not only the diagrams corresponding to this definition, but also all other diagrams. The corresponding number of events that pass one of the event selections presented in chapter 3 is given by:

$$N_{\text{proc}}(\alpha) = \mathcal{L}\varepsilon_{\text{proc}}(\alpha)\sigma_{\text{proc}}(\alpha), \tag{5.2}$$

where $\mathcal{L}$ is the total integrated luminosity for a certain year after having applied the run selection, $\varepsilon_{\text{proc}}(\alpha)$ is the efficiency and $\sigma_{\text{proc}}(\alpha)$ is the cross section of the process under consideration. The selection criteria cause the contributions from the TGC dependent s-channel diagrams nearly to be excluded. Hence, $N_{\text{proc}}(\alpha)$ gets its TGC dependence almost only from the single W fusion diagrams, which are t-channel diagrams. The SM results $N_{\text{proc}}(0.0)$ have already been quoted in chapter 3 for the different contributing processes. The final expression for $N_{\text{exp},i}(\alpha)$ in equation (5.1) is acquired by fitting second order polynomials to these TGC dependent contributions $N_{\text{proc}}(\alpha)$ and adding these parametrisations to the possible TGC independent contributions.
In the following three subsections, the results from the muon, electron and hadronic analyses are presented respectively.

5.1.1 Muon analysis

As has been described in chapter 3, the following final states contribute to the total number of expected events: $\mu\nu_\mu e\nu_e$, $\tau\nu_\tau e\nu_e$, $l\nu_l\bar{l}\bar{\nu}_l$, $\mu^+\mu^-$, $\tau^+\tau^-$, $e\bar{e}l\bar{l}$ ($l \neq e$) and cosmics. The first three contributions are TGC dependent: they get TGC contributions from the s-channel and t-channel. The $\mu\nu_\mu e\nu_e$ and $\tau\nu_\tau e\nu_e$ final states contain TGC dependent single W diagrams, while the $l\nu_l\bar{l}\bar{\nu}_l$ final state gets its t-channel TGC dependence via the production of a single Z and single γ from the final states $\mu\bar{\mu}\nu_e\bar{\nu}_e$ and $\tau\bar{\tau}\nu_e\bar{\nu}_e$. The diagrams for the production of a single Z and single γ can be obtained from the single W fusion diagram as depicted in figure 1.3 by reversing the outgoing W and virtual Z/γ, leading to a $Z\nu_e\bar{\nu}_e$ and $\gamma\nu_e\bar{\nu}_e$ final state.
The cross sections and the number of selected events per contribution at $\sqrt{s}$ = 189 GeV as a function of the couplings $\Delta\kappa_\gamma$, λ_γ and Δg_1^Z are listed in tables 5.1, 5.2 and 5.3 respectively. The SM values are the same as the ones quoted in table 3.12.
The second order polynomial fits to the TGC dependent contributions from tables 5.1, 5.2 and 5.3 are listed in figures 5.1, 5.3 and 5.5 respectively, together with the TGC independent backgrounds $\mu^+\mu^-$, $\tau^+\tau^-$, $e\bar{e}l\bar{l}$ ($l \neq e$) and cosmics. The total number of expected events and the corresponding -Δ2ln$\mathcal{L}$ distributions are represented in figures 5.2, 5.4 and 5.6 for the couplings $\Delta\kappa_\gamma$, λ_γ and Δg_1^Z respectively. Note that the ranges along the horizontal axes differ for the -Δ2ln$\mathcal{L}$ distributions.

Differential distributions

Until now, only the TGC dependence of the cross section has been included in the analysis. The influence of the possible TGC dependence of differential distributions has not been investigated

Table 5.1: *Cross sections and number of selected events per contributing process at $\sqrt{s}$ = 189 GeV as a function of $\Delta\kappa_\gamma$ for the muon analysis.*

process	value of $\Delta\kappa_\gamma$ -2.0	-1.0	0.0	1.0	2.0
$\sigma_{\mu\nu_\mu e\nu_e}$ (pb)	0.700	0.535	0.526	0.671	0.955
$N_{\mu\nu_\mu e\nu_e}$	5.86 ± 0.35	2.60 ± 0.20	6.85 ± 0.32	18.08 ± 0.54	36.20 ± 0.88
$\sigma_{\tau\nu_\tau e\nu_e}$ (pb)	0.621	0.476	0.472	0.606	0.872
$N_{\tau\nu_\tau e\nu_e}$	0.26 ± 0.08	0.18 ± 0.06	0.47 ± 0.09	1.19 ± 0.16	2.18 ± 0.25
$\sigma_{l\nu_l\bar{l}\bar{\nu}_l}$ (pb)	1.209	1.003	0.899	0.905	1.014
$N_{l\nu_l\bar{l}\bar{\nu}_l}$	1.67 ± 0.23	1.26 ± 0.18	1.15 ± 0.16	1.28 ± 0.17	1.35 ± 0.19
$\sigma_{\mu^+\mu^-}$ (pb)	9.2	9.2	9.2	9.2	9.2
$N_{\mu^+\mu^-}$	0.60 ± 0.13	0.60 ± 0.13	0.60 ± 0.13	0.60 ± 0.13	0.60 ± 0.13
$\sigma_{\tau^+\tau^-}$ (pb)	8.2	8.2	8.2	8.2	8.2
$N_{\tau^+\tau^-}$	0.07 ± 0.05	0.07 ± 0.05	0.07 ± 0.05	0.07 ± 0.05	0.07 ± 0.05
$\sigma_{e\bar{e}l\bar{l}}$ (pb)	58.50	58.50	58.50	58.50	58.50
$N_{e\bar{e}l\bar{l}}$ ($l \neq e$)	0.06 ± 0.02	0.06 ± 0.02	0.06 ± 0.02	0.06 ± 0.02	0.06 ± 0.02
N_{cosmic}	0.01 ± 0.00	0.01 ± 0.00	0.01 ± 0.00	0.01 ± 0.00	0.01 ± 0.00
N_{expected}	8.53 ± 0.45	4.78 ± 0.27	9.21 ± 0.39	21.29 ± 0.60	40.47 ± 0.94

Table 5.2: *Cross sections and number of selected events per contributing process at $\sqrt{s}$ = 189 GeV as a function of λ_γ for the muon analysis.*

process	value of λ_γ -2.0	-1.0	0.0	1.0	2.0
$\sigma_{\mu\nu_\mu e\nu_e}$ (pb)	1.230	0.706	0.526	0.687	1.182
$N_{\mu\nu_\mu e\nu_e}$	16.15 ± 0.73	8.45 ± 0.40	6.85 ± 0.32	9.91 ± 0.43	16.66 ± 0.73
$\sigma_{\tau\nu_\tau e\nu_e}$ (pb)	1.098	0.633	0.472	0.608	1.059
$N_{\tau\nu_\tau e\nu_e}$	0.77 ± 0.17	0.46 ± 0.10	0.47 ± 0.09	0.45 ± 0.10	1.15 ± 0.21
$\sigma_{l\nu_l\bar{l}\bar{\nu}_l}$ (pb)	1.946	1.174	0.899	1.126	1.851
$N_{l\nu_l\bar{l}\bar{\nu}_l}$	2.10 ± 0.32	1.36 ± 0.20	1.15 ± 0.16	1.21 ± 0.19	2.56 ± 0.35
$\sigma_{\mu^+\mu^-}$ (pb)	9.2	9.2	9.2	9.2	9.2
$N_{\mu^+\mu^-}$	0.60 ± 0.13	0.60 ± 0.13	0.60 ± 0.13	0.60 ± 0.13	0.60 ± 0.13
$\sigma_{\tau^+\tau^-}$ (pb)	8.2	8.2	8.2	8.2	8.2
$N_{\tau^+\tau^-}$	0.07 ± 0.05	0.07 ± 0.05	0.07 ± 0.05	0.07 ± 0.05	0.07 ± 0.05
$\sigma_{e\bar{e}l\bar{l}}$ (pb)	58.50	58.50	58.50	58.50	58.50
$N_{e\bar{e}l\bar{l}}$ ($l \neq e$)	0.06 ± 0.02	0.06 ± 0.02	0.06 ± 0.02	0.06 ± 0.02	0.06 ± 0.02
N_{cosmic}	0.01 ± 0.00	0.01 ± 0.00	0.01 ± 0.00	0.01 ± 0.00	0.01 ± 0.00
N_{expected}	19.76 ± 0.82	11.01 ± 0.47	9.21 ± 0.39	12.31 ± 0.50	21.11 ± 0.85

Table 5.3: *Cross sections and number of selected events per contributing process at* $\sqrt{s}$ *= 189 GeV as a function of* Δg_1^Z *for the muon analysis.*

process	value of Δg_1^Z -2.0	-1.0	0.0	1.0	2.0
$\sigma_{\mu\nu_\mu e\nu_e}$ (pb)	1.239	0.713	0.526	0.701	1.199
$N_{\mu\nu_\mu e\nu_e}$	7.87 ± 0.53	6.77 ± 0.37	6.85 ± 0.32	6.71 ± 0.37	8.74 ± 0.56
$\sigma_{\tau\nu_\tau e\nu_e}$ (pb)	1.094	0.627	0.472	0.614	1.076
$N_{\tau\nu_\tau e\nu_e}$	0.44 ± 0.13	0.44 ± 0.10	0.47 ± 0.09	0.41 ± 0.10	0.36 ± 0.12
$\sigma_{l\nu_l\bar{l}\bar{\nu}_l}$ (pb)	2.149	1.222	0.899	1.183	2.073
$N_{l\nu_l\bar{l}\bar{\nu}_l}$	2.09 ± 0.34	1.60 ± 0.22	1.15 ± 0.16	1.94 ± 0.24	3.30 ± 0.42
$\sigma_{\mu^+\mu^-}$ (pb)	9.2	9.2	9.2	9.2	9.2
$N_{\mu^+\mu^-}$	0.60 ± 0.13	0.60 ± 0.13	0.60 ± 0.13	0.60 ± 0.13	0.60 ± 0.13
$\sigma_{\tau^+\tau^-}$ (pb)	8.2	8.2	8.2	8.2	8.2
$N_{\tau^+\tau^-}$	0.07 ± 0.05	0.07 ± 0.05	0.07 ± 0.05	0.07 ± 0.05	0.07 ± 0.05
$\sigma_{e\bar{e}l\bar{l}}$ (pb)	58.50	58.50	58.50	58.50	58.50
$N_{e\bar{e}l\bar{l}}$ ($l \neq e$)	0.06 ± 0.02	0.06 ± 0.02	0.06 ± 0.02	0.06 ± 0.02	0.06 ± 0.02
N_{cosmic}	0.01 ± 0.00	0.01 ± 0.00	0.01 ± 0.00	0.01 ± 0.00	0.01 ± 0.00
N_{expected}	11.14 ± 0.65	9.55 ± 0.46	9.21 ± 0.39	9.80 ± 0.47	13.14 ± 0.72

yet. Since the signal is characterised by the presence of one charged track, the muon track, in the detector, the most logical distribution to consider is that of $\frac{\mathrm{d}\sigma}{\mathrm{dcos}\theta_\mu}$, where $\cos\theta_\mu$ is the cosine of the polar angle of the muon. In order to avoid possible differences in this distribution due to the charge of the muon, the distribution of $\frac{\mathrm{d}\sigma}{\mathrm{d}(-Q_\mu\cos\theta_\mu)}$ is investigated, where Q_μ represents the charge of the muon. Figure 5.7 shows these normalised distributions coming from the $\mu\nu_\mu e\nu_e$ final state for the couplings $\Delta\kappa_\gamma$, λ_γ and Δg_1^Z for the values 0.0, -1.0 and -2.0 at generator level at $\sqrt{s}$ = 189 GeV, without having applied any selection criterium. Only the diagrams that satisfy the Crete definition are taken into account in these plots. One can clearly conclude from this figure that the muons tend to go in the forward direction and that the value of a coupling influences this behaviour.

Using this information, the minimum of the following equation determines the best value of the coupling:

$$\begin{aligned} -\Delta 2\ln\mathcal{L}(\alpha) &= 2\sum_i (N_{\text{exp},F,i}(\alpha) - N_{\text{obs},F,i}\ln N_{\text{exp},F,i}(\alpha) + \\ &\quad N_{\text{exp},B,i}(\alpha) - N_{\text{obs},B,i}\ln N_{\text{exp},B,i}(\alpha)) + C, \end{aligned} \tag{5.3}$$

where the subscripts F and B refer to "forward" and "backward" and the factor C is the bias needed to let the minimum of this -Δ2ln$\mathcal{L}$ distribution coincide with 0.

In tables 4.8 and 4.9, the SM values of the expected and observed number of events in the forward and backward directions are listed.

The -Δ2ln$\mathcal{L}$ distributions at $\sqrt{s}$ = 189 GeV after having included this forward-backward information for all contributing final states are shown in figure 5.8.

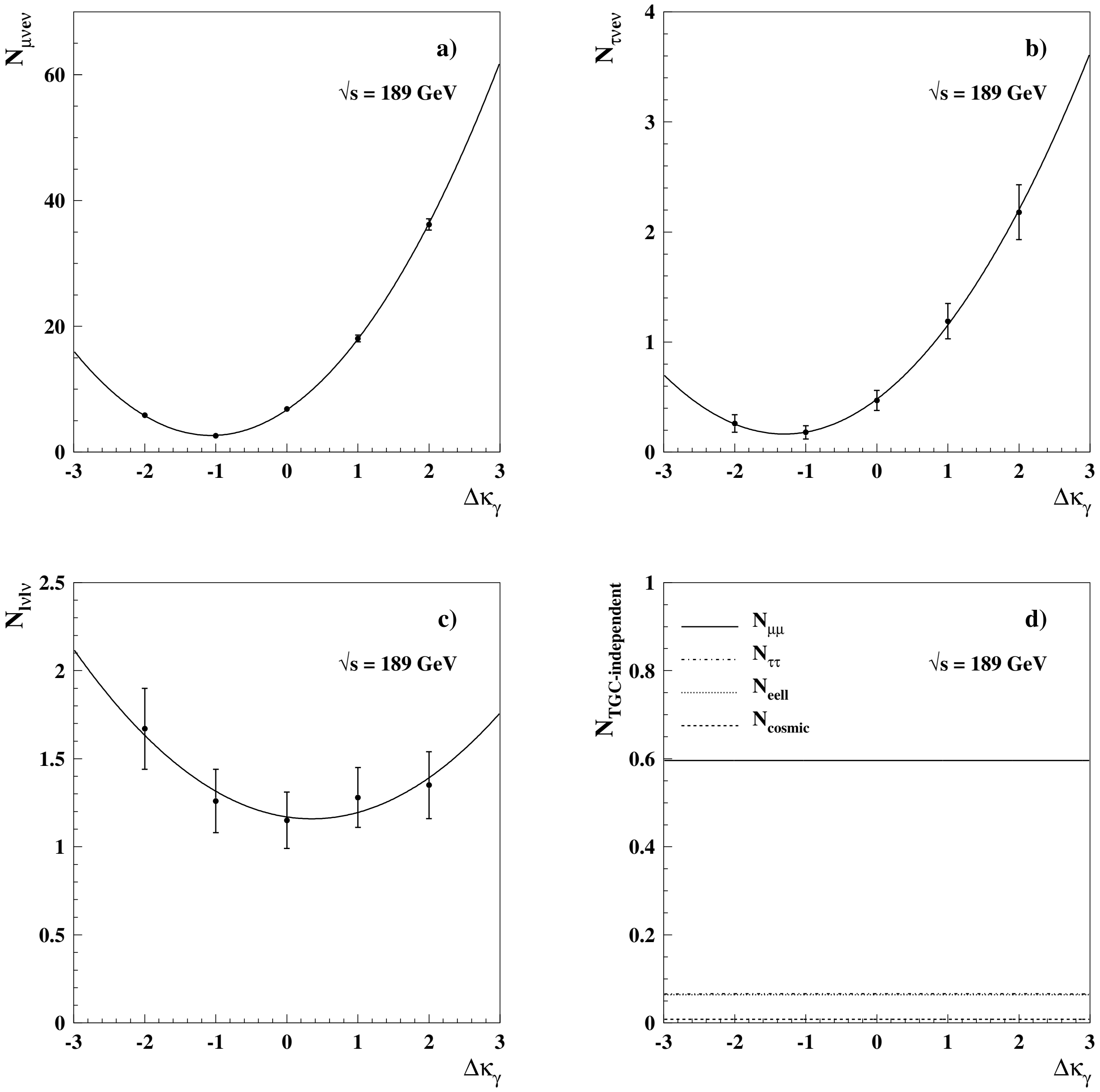

Figure 5.1: *Dependence of the different contributions to the total number of expected events on the coupling $\Delta\kappa_\gamma$ at $\sqrt{s}$ = 189 GeV for the muon analysis: figure a) shows this dependence for the final state $\mu\nu_\mu e\nu_e$, which includes the signal, figure b) represents the $\tau\nu_\tau e\nu_e$ background, figure c) indicates the $l\nu_l\bar{l}\bar{\nu}_l$ background and figure d) shows the TGC independent backgrounds: $\mu^+\mu^-$, $\tau^+\tau^-$, $e\bar{e}l\bar{l}$ ($l \neq e$) and cosmics.*

Including this forward-backward information results in -Δ2ln$\mathcal{L}$ distributions that do not have to be symmetric with respect to the absolute minimum in case of one minimum or with respect to the relative maximum between two minima in case of two minima, contrary to the distributions that lack this information. This behaviour can already be observed, comparing the distributions of

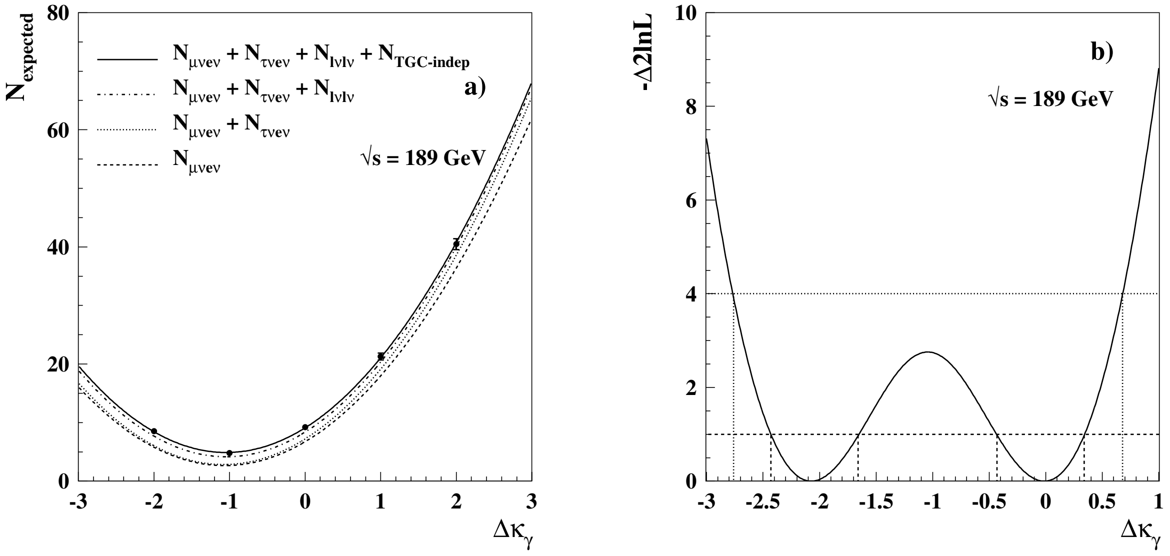

Figure 5.2: *Figure a) shows the dependence of the total number of expected events on the coupling $\Delta\kappa_\gamma$ at $\sqrt{s}$ = 189 GeV for the muon analysis, containing the seven contributions that are represented in figure 5.1 individually. Figure b) indicates the corresponding -Δ2ln$\mathcal{L}$ distribution. The horizontal dashed line represents the 68% error band, while the horizontal dotted line indicates the 95% error band.*

λ_γ and Δg_1^Z in figures 5.4, 5.6 and 5.8. It is possible that the asymmetry in the -Δ2ln$\mathcal{L}$ distribution of $\Delta\kappa_\gamma$ becomes so apparent that the first minimum still coincides with 0, while the second relative minimum has shifted above 1 and the difference between this minimum and the local maximum, located around $\Delta\kappa_\gamma$ = -1.0, has a value above 1 or even above 4. Quoting 68% CL and 95% CL errors by finding the intersection points of the distribution with the horizontal lines at 1 and 4 is then not correct. The errors are deduced from the values +1 and +4 of the likelihood with respect to the (local) minima. Hence, it is very important to show a -Δ2ln$\mathcal{L}$ distribution and deduce from it the corresponding errors instead of just listing errors in order to avoid confusion.

Table 5.4 gives an overview of the measured values of the couplings $\Delta\kappa_\gamma$, λ_γ and Δg_1^Z including the 68% CL errors and 95% CL intervals at $\sqrt{s}$ = 189 GeV for the cases that the forward-backward information is used and is not taken into account.
As already explained before, there can appear two minima in the -Δ2ln$\mathcal{L}$ distribution of $\Delta\kappa_\gamma$, which is indeed the case here: one minimum around $\Delta\kappa_\gamma$ = -2.0, being far away from the SM expectation and one minimum close to the SM value $\Delta\kappa_\gamma$ = 0.0.
In case of two minima, 68% CL errors are quoted with respect to both minima, but the minimum close to the SM expectation is considered as *the* result of the measurement. The listed results of the 95% CL intervals are determined with respect to the absolute minimum. This is not only the case for table 5.4, but this idea is also carried out throughout the rest of this chapter.

The same procedure has been repeated for the centre-of-mass energies ranging from 192 to

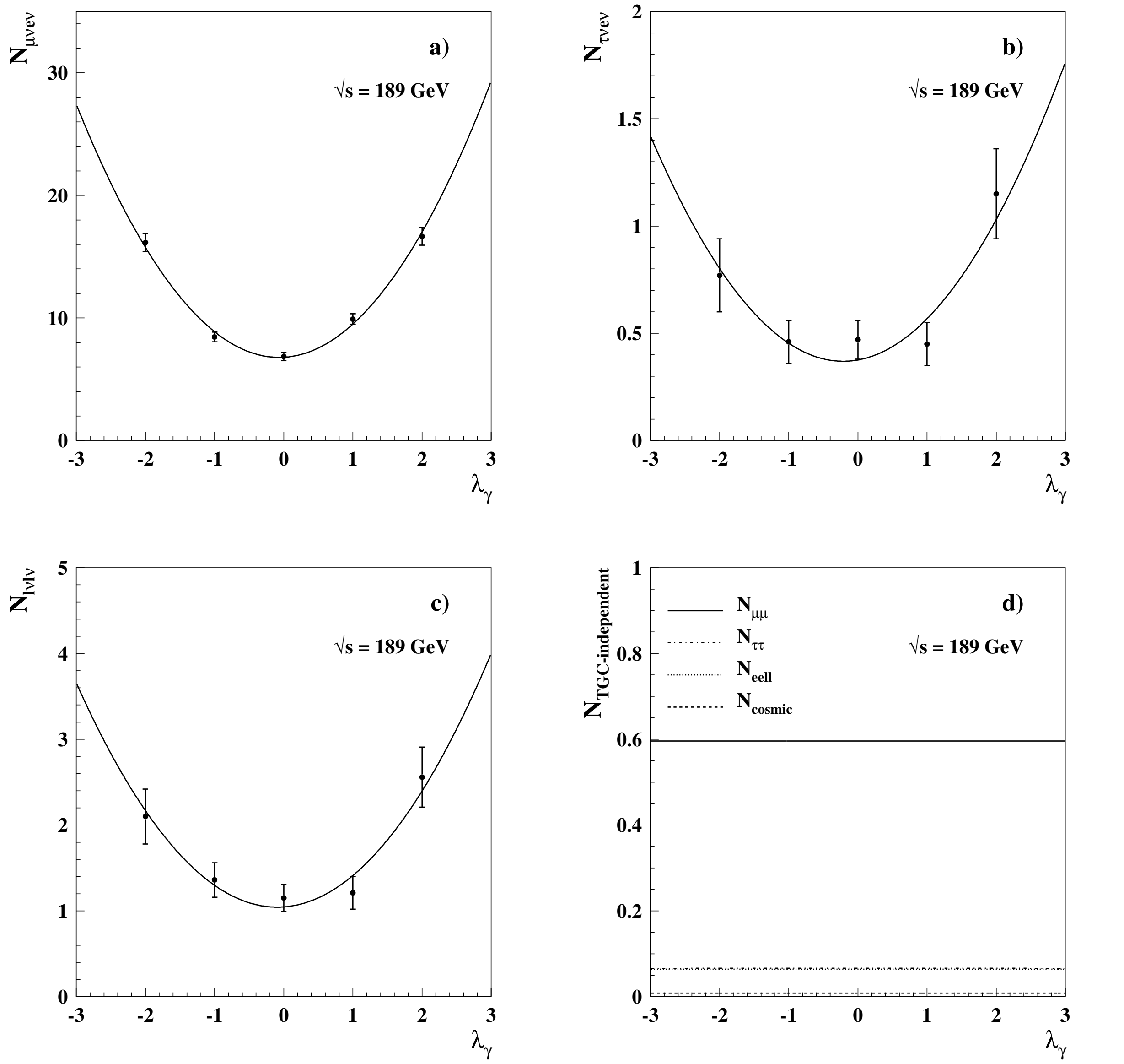

Figure 5.3: *Dependence of the different contributions to the total number of expected events on the coupling λ_γ at $\sqrt{s}$ = 189 GeV for the muon analysis: figure a) shows this dependence for the final state $\mu\nu_\mu e\nu_e$, which includes the signal, figure b) represents the $\tau\nu_\tau e\nu_e$ background, figure c) indicates the $l\nu_l\bar{l}\bar{\nu}_l$ background and figure d) shows the TGC independent backgrounds: $\mu^+\mu^-$, $\tau^+\tau^-$, $e\bar{e}l\bar{l}$ ($l \neq e$) and cosmics.*

206.7 GeV, thus including and excluding the forward-backward information. It turns out that the 68% CL errors and 95% CL intervals tend to be slightly smaller for the case where the forward-backward information has been included. The -$\Delta 2\ln\mathcal{L}$ distributions that have included the forward-backward information corresponding to the centre-of-mass energies ranging from

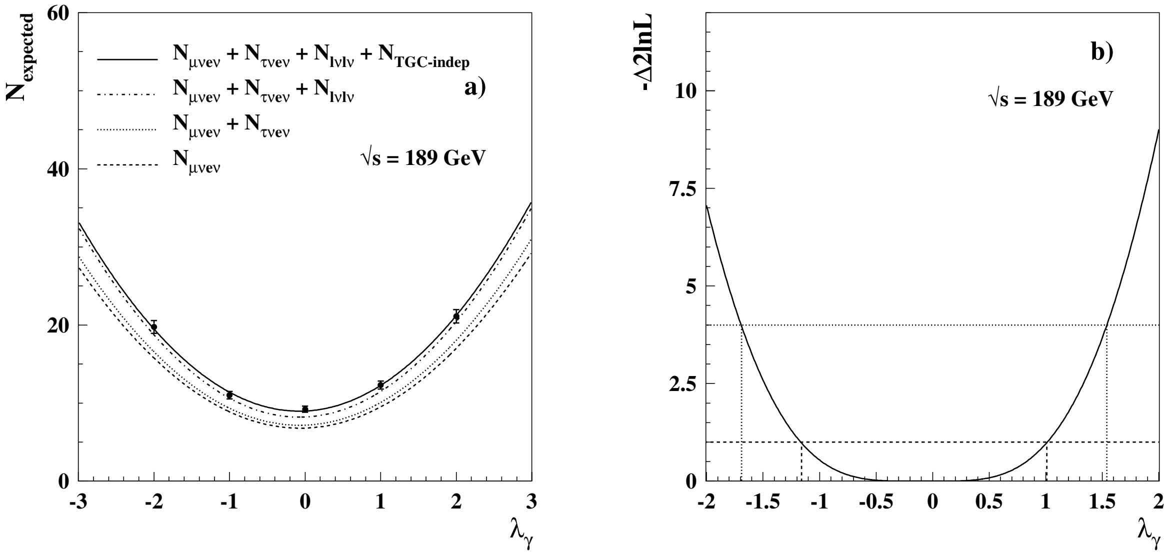

Figure 5.4: *Figure a) shows the dependence of the total number of expected events on the coupling λ_γ at $\sqrt{s}$ = 189 GeV for the muon analysis, containing the seven contributions that are represented in figure 5.3 individually. Figure b) indicates the corresponding -Δ2ln$\mathcal{L}$ distribution.*

Table 5.4: *Measured values for the TGC parameters $\Delta\kappa_\gamma$, λ_γ and Δg_1^Z including the 68% CL errors (first and third rows) and 95% CL intervals (second and fourth rows) at $\sqrt{s}$ = 189 GeV for the muon analysis for the cases that the forward-backward information is used and is not taken into account.*

	$\Delta\kappa_\gamma$	λ_γ	Δg_1^Z
forward-backward info is not used	$-2.07^{+0.41}_{-0.36}$ $-0.01^{+0.35}_{-0.42}$	$-0.19^{+1.20}_{-0.97}$	$-0.45^{+2.28}_{-1.91}$
	[-2.76, +0.68]	[-1.69, +1.54]	[-3.38, +2.85]
forward-backward info is used	$-2.09^{+0.39}_{-0.34}$ $0.00^{+0.35}_{-0.39}$	$+0.20^{+0.82}_{-1.32}$	$+0.48^{+1.39}_{-2.88}$
	[-2.77, +0.68]	[-1.67, +1.54]	[-3.40, +2.85]

189 to 206.7 GeV are presented in appendix B.1.
The -Δ2ln$\mathcal{L}$ distributions of the seven centre-of-mass energies are added for every coupling separately, giving rise to a value for $\Delta\kappa_\gamma$, λ_γ and Δg_1^Z for the years 1998 - 2000 combined. These distributions are shown both in figure 5.9 and in appendix B.1.
The measured values for the TGC parameters $\Delta\kappa_\gamma$, λ_γ and Δg_1^Z including the 68% CL errors and 95% CL intervals that are deduced from the figures in appendix B.1 are listed in table 5.5.

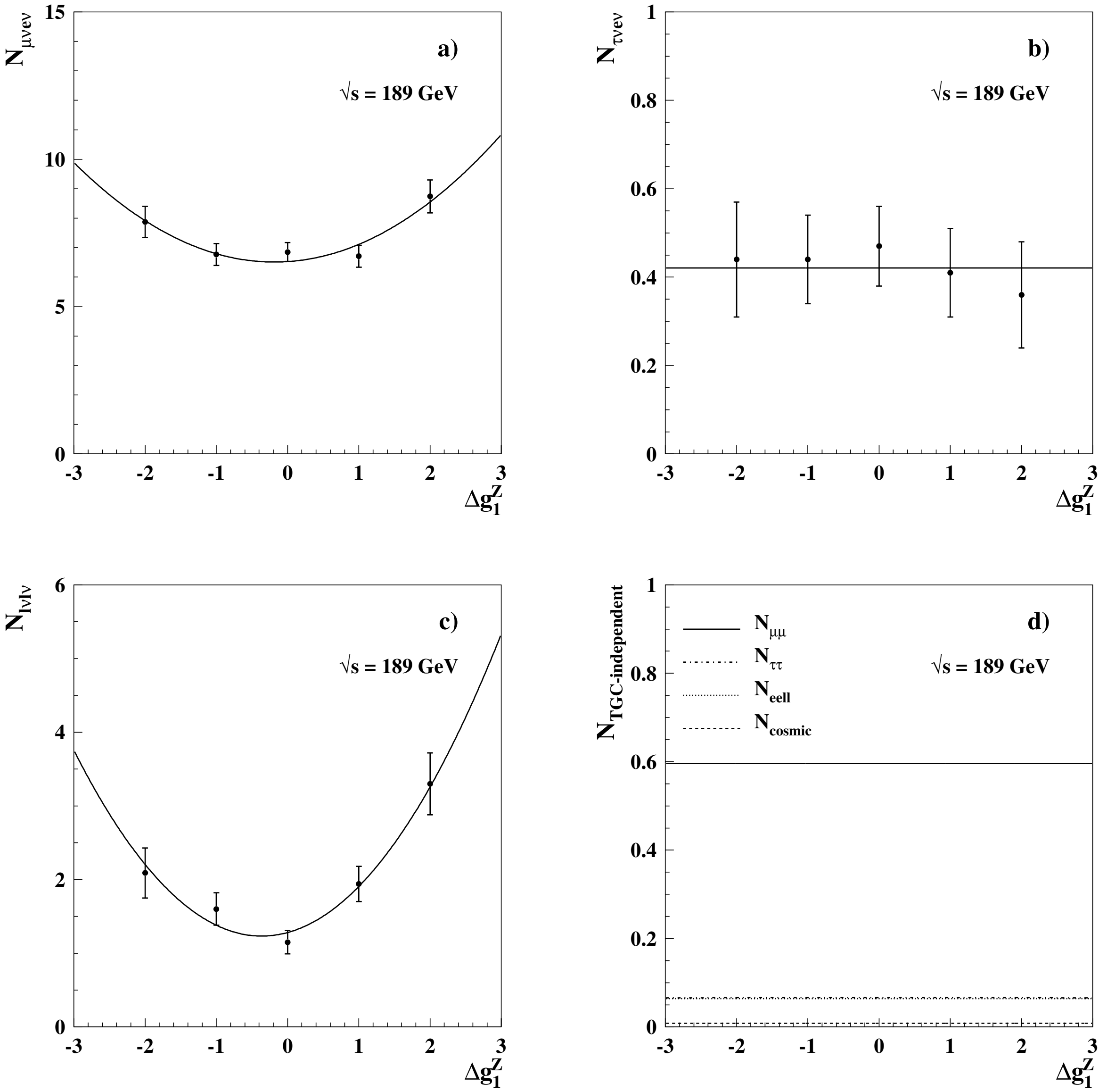

Figure 5.5: *Dependence of the different contributions to the total number of expected events on the coupling Δg_1^Z at $\sqrt{s}$ = 189 GeV for the muon analysis: figure a) shows this dependence for the final state $\mu\nu_\mu e\nu_e$, which includes the signal, figure b) represents the $\tau\nu_\tau e\nu_e$ background, figure c) indicates the $l\nu_l\bar{l}\bar{\nu}_l$ background and figure d) shows the TGC independent backgrounds: $\mu^+\mu^-$, $\tau^+\tau^-$, $e\bar{e}l\bar{l}$ ($l \neq e$) and cosmics. Note that to the distribution of the $\tau\nu_\tau e\nu_e$ background a constant has been fitted, since it lacks a clear dependence on Δg_1^Z.*

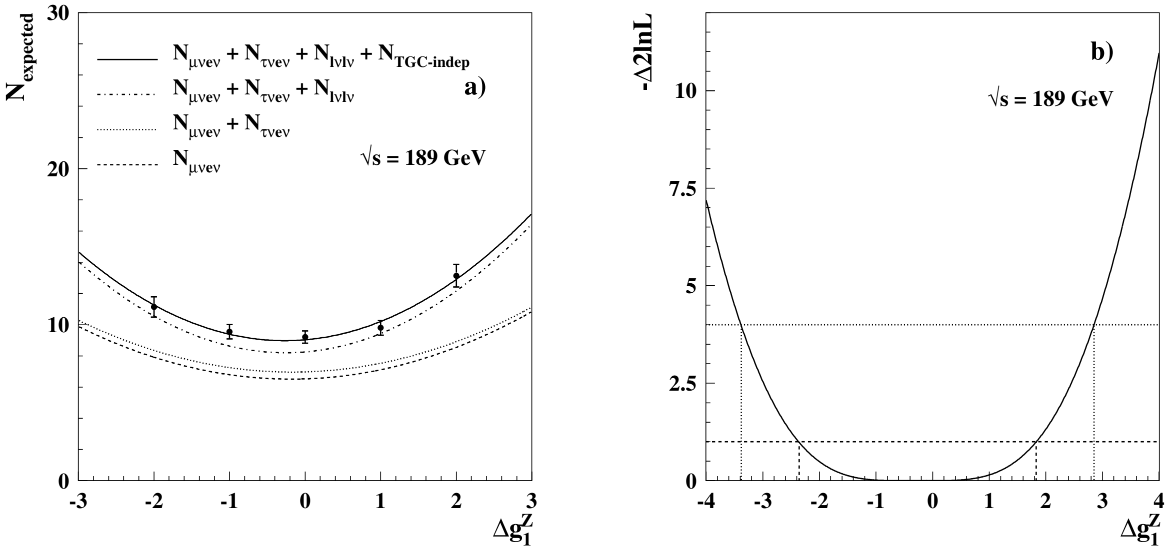

Figure 5.6: *Figure a) shows the dependence of the total number of expected events on the coupling* Δg_1^Z *at* $\sqrt{s}$ *= 189 GeV for the muon analysis, containing the seven contributions that are represented in figure 5.5 individually. Figure b) indicates the corresponding -*$\Delta 2\ln\mathcal{L}$ *distribution.*

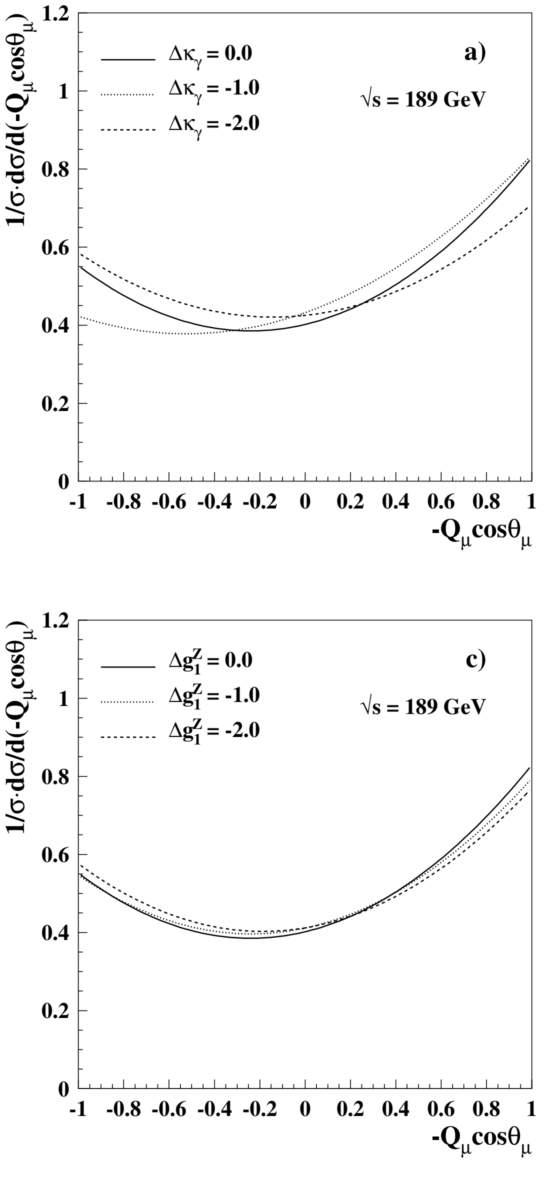

Figure 5.7: *Normalised distributions of $\frac{\mathrm{d}\sigma}{\mathrm{d}(-Q_\mu \cos\theta_\mu)}$ coming from the $\mu\nu_\mu e\nu_e$ final state for the couplings $\Delta\kappa_\gamma$ (a)), λ_γ (b)) and Δg_1^Z (c)) for the values 0.0, -1.0 and -2.0 at generator level at $\sqrt{s}$ = 189 GeV. The diagrams that contribute to this final state satisfy the Crete definition.*

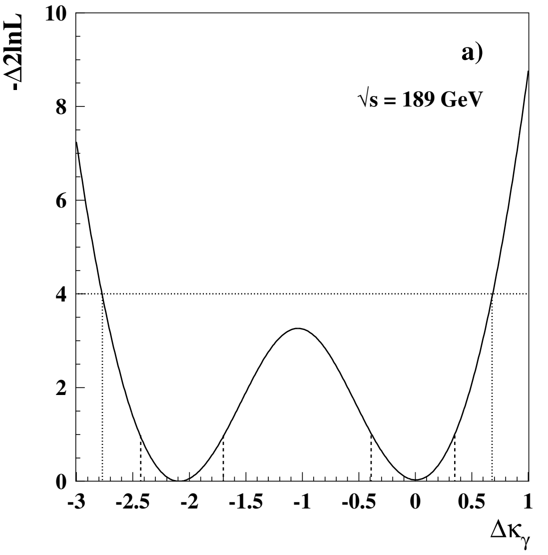

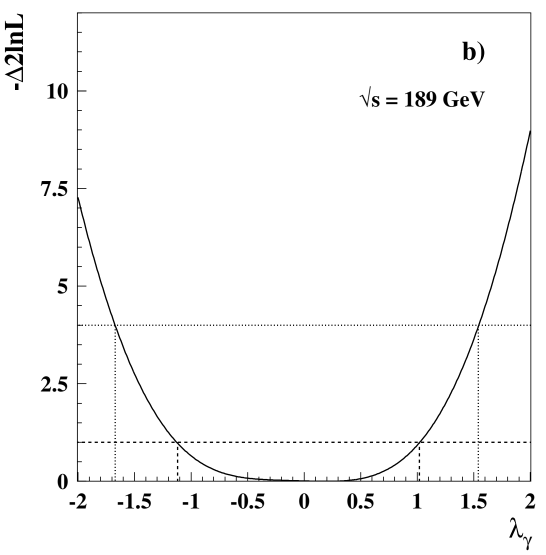

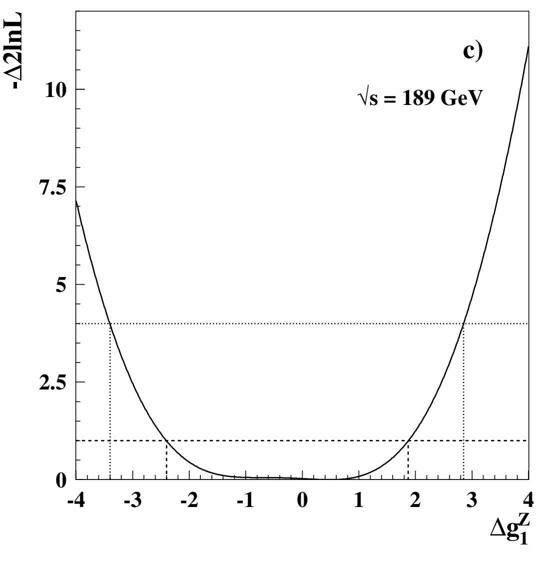

Figure 5.8: *-$\Delta 2ln\mathcal{L}$ distributions for the muon analysis for the couplings $\Delta\kappa_\gamma$ (a)), λ_γ (b)) and Δg_1^Z (c)) at $\sqrt{s}$ = 189 GeV after having included the forward-backward information for all contributing final states.*

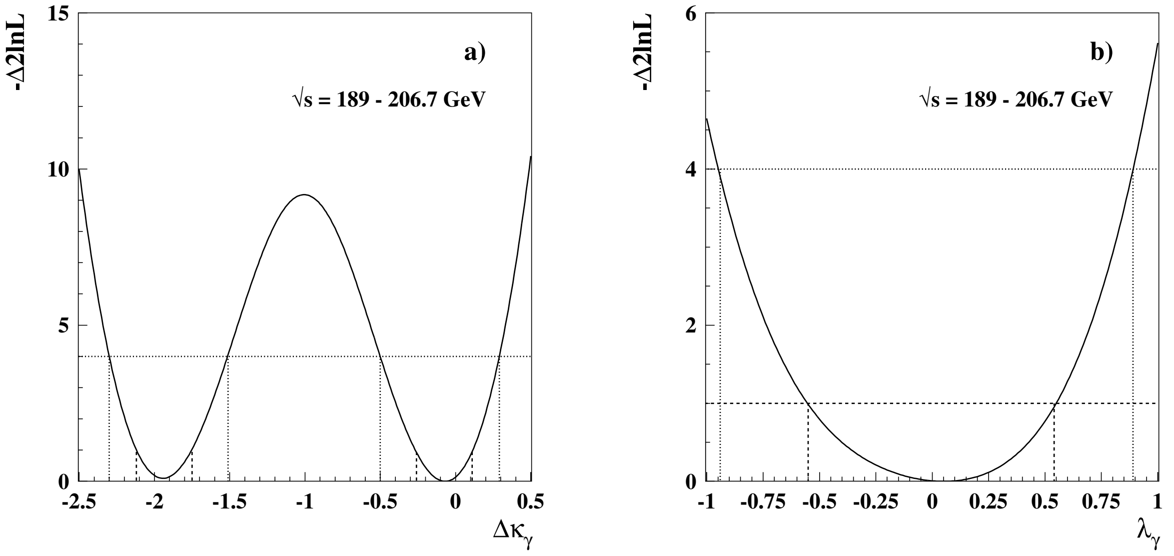

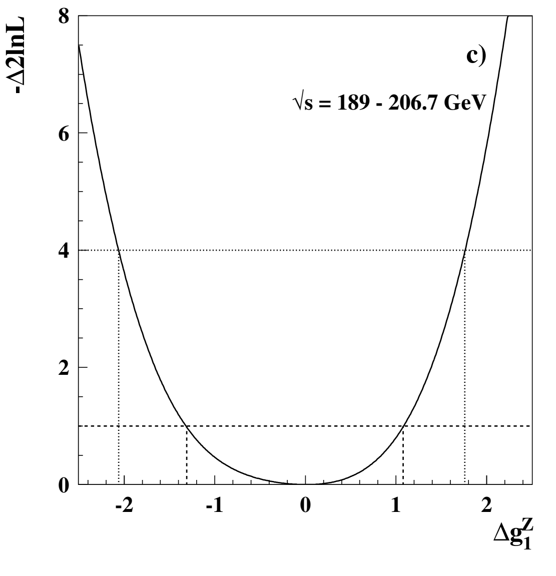

Figure 5.9: *-Δ2ln$\mathcal{L}$ distributions for the years 1998 - 2000 combined for the muon analysis as a function of $\Delta\kappa_\gamma$ (a)), λ_γ (b)) and Δg_1^Z (c)).*

Table 5.5: *Measured values for the TGC parameters $\Delta\kappa_\gamma$, λ_γ and Δg_1^Z including the 68% CL errors (first row per energy point) and 95% CL intervals (second row per energy point) for the centre-of-mass energies ranging from 189 to 206.7 GeV and 189 - 206.7 GeV for the muon analysis. In case of two minima, the 68% CL errors are determined with respect to both local minima, while the 95% CL intervals are measured with respect to the absolute minimum.*

$\sqrt{s}$ (GeV)	$\Delta\kappa_\gamma$	λ_γ	Δg_1^Z
189	$-2.09^{+0.39}_{-0.34}$ $\quad 0.00^{+0.35}_{-0.39}$	$+0.20^{+0.82}_{-1.32}$	$+0.48^{+1.39}_{-2.88}$
	[-2.77, +0.68]	[-1.67, +1.54]	[-3.40, +2.85]
192	$-2.43^{+0.73}_{-0.70}$ $\quad +0.48^{+0.70}_{-0.74}$	$+0.93^{+1.05}_{-2.71}$	$+2.82^{+2.04}_{-7.28}$
	[-3.85, +1.89]	[-2.94, +2.93]	[-6.45, +6.77]
196	$-2.05^{+0.55}_{-0.45}$ $\quad +0.10^{+0.46}_{-0.54}$	$+0.51^{+1.44}_{-2.48}$	$+0.89^{+1.36}_{-3.60}$
	[-2.94, +1.00]	[-1.97, +1.95]	[-3.77, +3.30]
200	$-2.10^{+0.45}_{-0.40}$ $\quad +0.17^{+0.40}_{-0.45}$	$+0.56^{+0.71}_{-1.81}$	$-1.59^{+3.83}_{-1.41}$
	[-2.88, +0.97]	[-1.86, +1.82]	[-4.13, +3.48]
202	$-2.52^{+0.66}_{-0.58}$ $\quad +0.32^{+0.59}_{-0.64}$	$-1.33^{+3.10}_{-0.79}$	$+1.70^{+1.85}_{-4.09}$
	[-3.67, +1.49]	[-2.84, +2.55]	[-4.74, +5.14]
205	$-1.06^{+0.55}_{-0.55}$	$-0.14^{+0.62}_{-0.60}$	$-0.08^{+1.24}_{-1.24}$
	[-2.14, +0.01]	[-1.33, +1.08]	[-2.55, +2.39]
206.7	$-0.23^{+0.44}_{-1.82}$	$+0.09^{+0.73}_{-0.82}$	$-0.42^{+2.01}_{-1.73}$
	[-2.50, +0.61]	[-1.41, +1.42]	[-3.57, +3.24]
189 - 206.7	$-1.94^{+0.19}_{-0.18}$ $\quad -0.07^{+0.18}_{-0.19}$	$+0.05^{+0.49}_{-0.60}$	$+0.01^{+1.07}_{-1.32}$
	[-2.30, -1.51] [-0.50, +0.29]	[-0.94, +0.89]	[-2.06, +1.76]

5.1.2 Electron analysis

The procedure that is followed is analogous to the one presented in the previous section. The TGC dependent final states $e\nu_e e\nu_e$, $\tau\nu_\tau e\nu_e$, $\mu\nu_\mu e\nu_e$ contribute to the total number of expected events, while in this case the final state $e\bar{e}\nu_l\bar{\nu}_l$ ($l \neq e$), Compton events, $\nu_l\bar{\nu}_l(\gamma)$ and $\tau^+\tau^-$ form the TGC independent part.
The cross sections and the number of selected events per contribution at $\sqrt{s}$ = 189 GeV as a function of the couplings $\Delta\kappa_\gamma$, λ_γ and Δg_1^Z are listed in tables 5.6, 5.7 and 5.8 respectively. In these tables the l in $\sigma_{e\bar{e}\nu_l\bar{\nu}_l}$ represents all leptons, while the l in $N_{e\bar{e}\nu_l\bar{\nu}_l}$ only includes μ and τ. The SM values equal the sum of the values presented in tables 3.14 and 3.15.

Table 5.6: *Cross sections and number of selected events per contributing process at $\sqrt{s}$ = 189 GeV as a function of $\Delta\kappa_\gamma$ for the electron analysis.*

process	value of $\Delta\kappa_\gamma$ -2.0	-1.0	0.0	1.0	2.0
$\sigma_{e\nu_e e\nu_e}$ (pb)	0.726	0.591	0.637	0.780	1.026
$N_{e\nu_e e\nu_e}$	4.24 ± 0.31	2.19 ± 0.20	4.86 ± 0.31	15.95 ± 0.75	25.45 ± 0.88
$\sigma_{\tau\nu_\tau e\nu_e}$ (pb)	0.621	0.476	0.472	0.606	0.872
$N_{\tau\nu_\tau e\nu_e}$	0.21 ± 0.07	0.09 ± 0.04	0.26 ± 0.07	0.54 ± 0.11	0.93 ± 0.16
$\sigma_{\mu\nu_\mu e\nu_e}$ (pb)	0.700	0.535	0.526	0.671	0.955
$N_{\mu\nu_\mu e\nu_e}$	0.06 ± 0.04	0.07 ± 0.03	0.03 ± 0.02	0.10 ± 0.04	0.20 ± 0.07
$\sigma_{e\bar{e}\nu_l\bar{\nu}_l}$ (pb)	1.153	1.153	1.153	1.153	1.153
$N_{e\bar{e}\nu_l\bar{\nu}_l}$ ($l \neq e$)	1.87 ± 0.54	1.87 ± 0.54	1.87 ± 0.54	1.87 ± 0.54	1.87 ± 0.54
σ_{Compton} (pb)	53.4	53.4	53.4	53.4	53.4
N_{Compton}	0.15 ± 0.11	0.15 ± 0.11	0.15 ± 0.11	0.15 ± 0.11	0.15 ± 0.11
$\sigma_{\nu_l\bar{\nu}_l(\gamma)}$ (pb)	11.1	11.1	11.1	11.1	11.1
$N_{\nu_l\bar{\nu}_l(\gamma)}$	0.80 ± 0.23	0.80 ± 0.23	0.80 ± 0.23	0.80 ± 0.23	0.80 ± 0.23
$\sigma_{\tau^+\tau^-}$ (pb)	8.2	8.2	8.2	8.2	8.2
$N_{\tau^+\tau^-}$	0.00 ± 0.00	0.00 ± 0.00	0.00 ± 0.00	0.00 ± 0.00	0.00 ± 0.00
N_{expected}	7.33 ± 0.68	5.17 ± 0.63	7.97 ± 0.68	19.41 ± 0.97	29.40 ± 1.08

The second order polynomial fits to the TGC dependent contributions from tables 5.6, 5.7 and 5.8 are shown in figures 5.10, 5.12 and 5.14 respectively, together with the TGC independent contributions from the final state $e\bar{e}\nu_l\bar{\nu}_l$ ($l \neq e$), the Compton events and $\nu_l\bar{\nu}_l(\gamma)$. The $\tau^+\tau^-$ events do not contribute at $\sqrt{s}$ = 189 GeV. The total number of expected events and the corresponding -Δ2ln$\mathcal{L}$ distributions are represented in figures 5.11, 5.13 and 5.15 for the couplings $\Delta\kappa_\gamma$, λ_γ and Δg_1^Z respectively. For the coupling Δg_1^Z, it is not possible to obtain a -Δ2ln$\mathcal{L}$ distribution, since the distribution of the total number of events is a flat one. One can conclude from figure 5.14 that the only TGC dependence is coming from the background, not from the signal! Therefore, no results are quoted for the coupling Δg_1^Z for the electron analysis. The other centre-of-mass energies deal with the same problem.

Table 5.7: *Cross sections and number of selected events per contributing process at $\sqrt{s}$ = 189 GeV as a function of λ_γ for the electron analysis.*

process	value of λ_γ -2.0	-1.0	0.0	1.0	2.0
$\sigma_{e\nu_e e\nu_e}$ (pb)	0.977	0.672	0.637	0.656	0.928
$N_{e\nu_e e\nu_e}$	9.99 ± 0.57	5.07 ± 0.33	4.86 ± 0.31	6.21 ± 0.37	9.37 ± 0.56
$\sigma_{\tau\nu_\tau e\nu_e}$ (pb)	1.098	0.633	0.472	0.608	1.059
$N_{\tau\nu_\tau e\nu_e}$	0.35 ± 0.12	0.25 ± 0.08	0.26 ± 0.07	0.47 ± 0.10	0.63 ± 0.15
$\sigma_{\mu\nu_\mu e\nu_e}$ (pb)	1.230	0.706	0.526	0.687	1.182
$N_{\mu\nu_\mu e\nu_e}$	0.14 ± 0.07	0.10 ± 0.05	0.03 ± 0.02	0.20 ± 0.06	0.09 ± 0.06
$\sigma_{e\bar{e}\nu_l\bar{\nu}_l}$ (pb)	1.153	1.153	1.153	1.153	1.153
$N_{e\bar{e}\nu_l\bar{\nu}_l}$ ($l \neq e$)	1.87 ± 0.54	1.87 ± 0.54	1.87 ± 0.54	1.87 ± 0.54	1.87 ± 0.54
σ_{Compton} (pb)	53.4	53.4	53.4	53.4	53.4
N_{Compton}	0.15 ± 0.11	0.15 ± 0.11	0.15 ± 0.11	0.15 ± 0.11	0.15 ± 0.11
$\sigma_{\nu_l\bar{\nu}_l(\gamma)}$ (pb)	11.1	11.1	11.1	11.1	11.1
$N_{\nu_l\bar{\nu}_l(\gamma)}$	0.80 ± 0.23	0.80 ± 0.23	0.80 ± 0.23	0.80 ± 0.23	0.80 ± 0.23
$\sigma_{\tau^+\tau^-}$ (pb)	8.2	8.2	8.2	8.2	8.2
$N_{\tau^+\tau^-}$	0.00 ± 0.00	0.00 ± 0.00	0.00 ± 0.00	0.00 ± 0.00	0.00 ± 0.00
N_{expected}	13.30 ± 0.84	8.24 ± 0.69	7.97 ± 0.68	9.70 ± 0.71	12.91 ± 0.84

Table 5.8: *Cross sections and number of selected events per contributing process at $\sqrt{s}$ = 189 GeV as a function of Δg_1^Z for the electron analysis.*

process	value of Δg_1^Z -2.0	-1.0	0.0	1.0	2.0
$\sigma_{e\nu_e e\nu_e}$ (pb)	0.930	0.730	0.637	0.696	0.929
$N_{e\nu_e e\nu_e}$	4.28 ± 0.37	4.73 ± 0.35	4.86 ± 0.31	4.44 ± 0.31	4.43 ± 0.37
$\sigma_{\tau\nu_\tau e\nu_e}$ (pb)	1.094	0.627	0.472	0.614	1.076
$N_{\tau\nu_\tau e\nu_e}$	0.40 ± 0.13	0.32 ± 0.09	0.26 ± 0.07	0.23 ± 0.07	0.40 ± 0.13
$\sigma_{\mu\nu_\mu e\nu_e}$ (pb)	1.239	0.713	0.526	0.701	1.199
$N_{\mu\nu_\mu e\nu_e}$	0.15 ± 0.08	0.08 ± 0.04	0.03 ± 0.02	0.14 ± 0.06	0.26 ± 0.10
$\sigma_{e\bar{e}\nu_l\bar{\nu}_l}$ (pb)	1.153	1.153	1.153	1.153	1.153
$N_{e\bar{e}\nu_l\bar{\nu}_l}$ ($l \neq e$)	1.87 ± 0.54	1.87 ± 0.54	1.87 ± 0.54	1.87 ± 0.54	1.87 ± 0.54
σ_{Compton} (pb)	53.4	53.4	53.4	53.4	53.4
N_{Compton}	0.15 ± 0.11	0.15 ± 0.11	0.15 ± 0.11	0.15 ± 0.11	0.15 ± 0.11
$\sigma_{\nu_l\bar{\nu}_l(\gamma)}$ (pb)	11.1	11.1	11.1	11.1	11.1
$N_{\nu_l\bar{\nu}_l(\gamma)}$	0.80 ± 0.23	0.80 ± 0.23	0.80 ± 0.23	0.80 ± 0.23	0.80 ± 0.23
$\sigma_{\tau^+\tau^-}$ (pb)	8.2	8.2	8.2	8.2	8.2
$N_{\tau^+\tau^-}$	0.00 ± 0.00	0.00 ± 0.00	0.00 ± 0.00	0.00 ± 0.00	0.00 ± 0.00
N_{expected}	7.65 ± 0.72	7.95 ± 0.70	7.97 ± 0.68	7.63 ± 0.68	7.91 ± 0.72

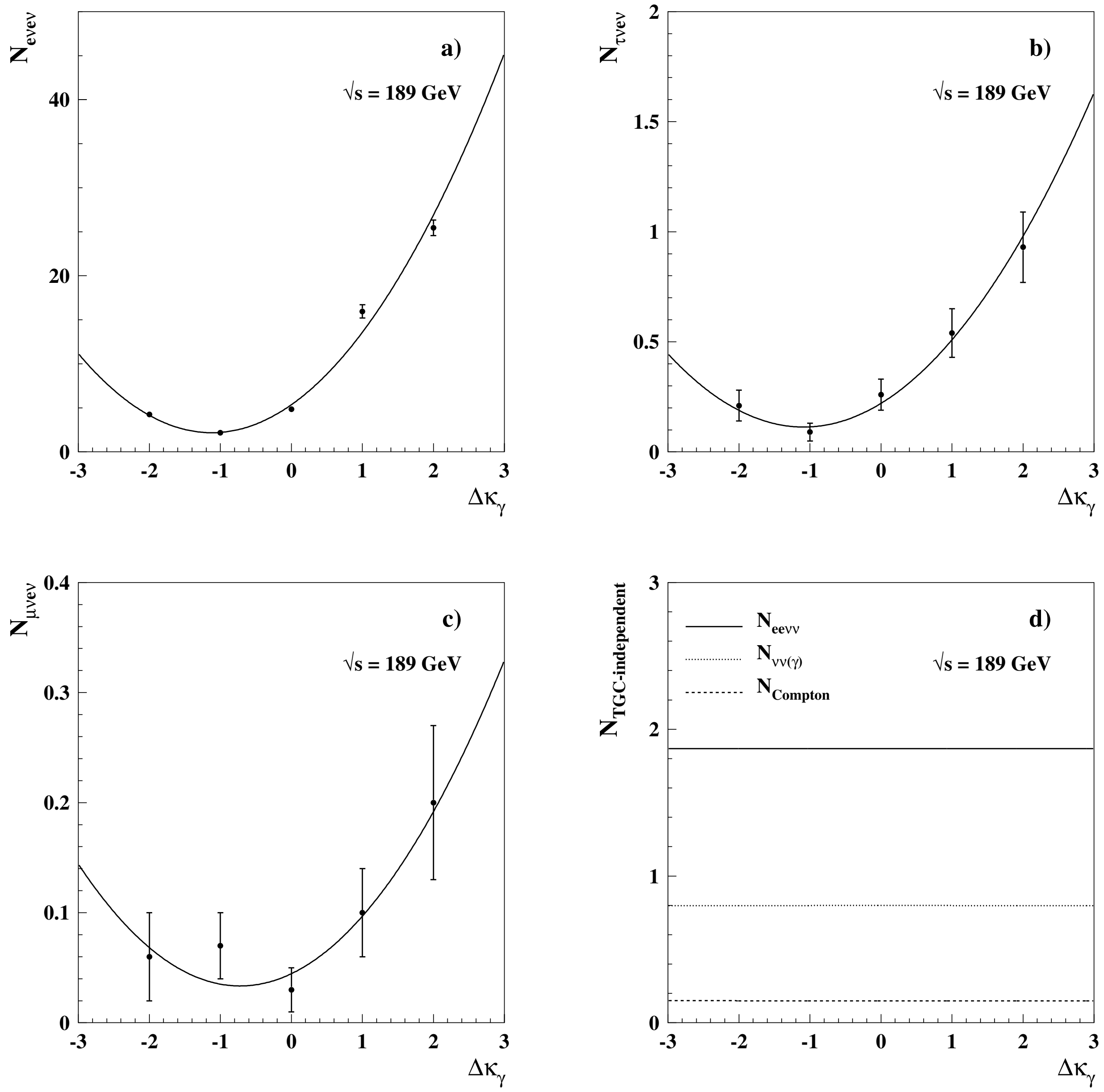

Figure 5.10: *Dependence of the different contributions to the total number of expected events on the coupling $\Delta\kappa_\gamma$ at $\sqrt{s}$ = 189 GeV for the electron analysis: figure a) shows this dependence for the final state $e\nu_e e\nu_e$, which includes the signal, figure b) represents the $\tau\nu_\tau e\nu_e$ background, figure c) indicates the $\mu\nu_\mu e\nu_e$ background and figure d) shows the TGC independent backgrounds: $e\bar{e}\nu_l\bar{\nu}_l$ ($l \neq e$), $\nu_l\bar{\nu}_l(\gamma)$ and Compton events.*

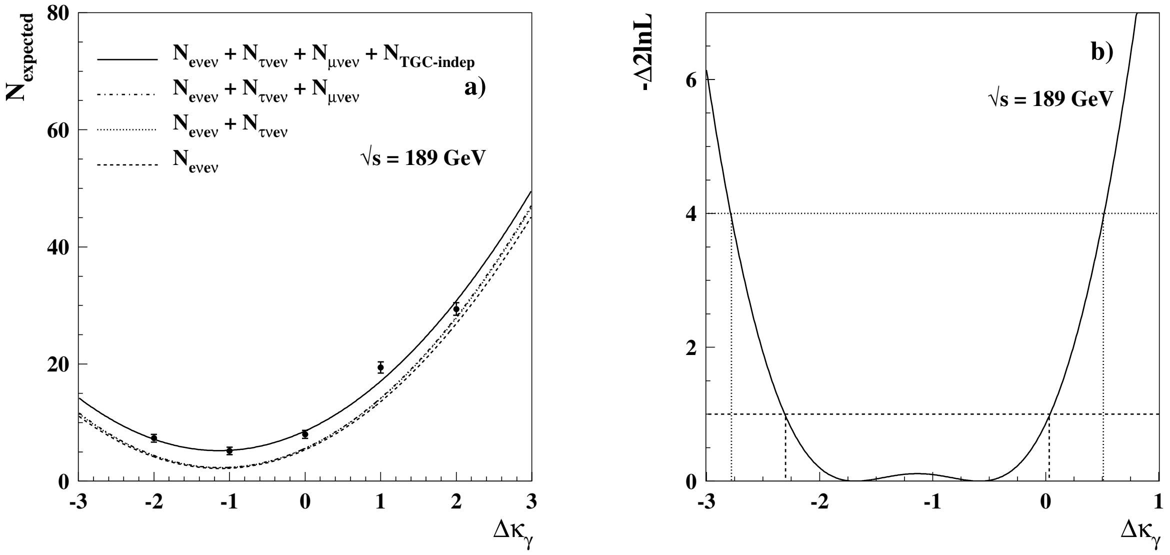

Figure 5.11: *Figure a) shows the dependence of the total number of expected events on the coupling $\Delta\kappa_\gamma$ at $\sqrt{s}$ = 189 GeV for the electron analysis, containing the six contributions that are represented in figure 5.10 individually. Figure b) indicates the corresponding -$\Delta 2\ln\mathcal{L}$ distribution.*

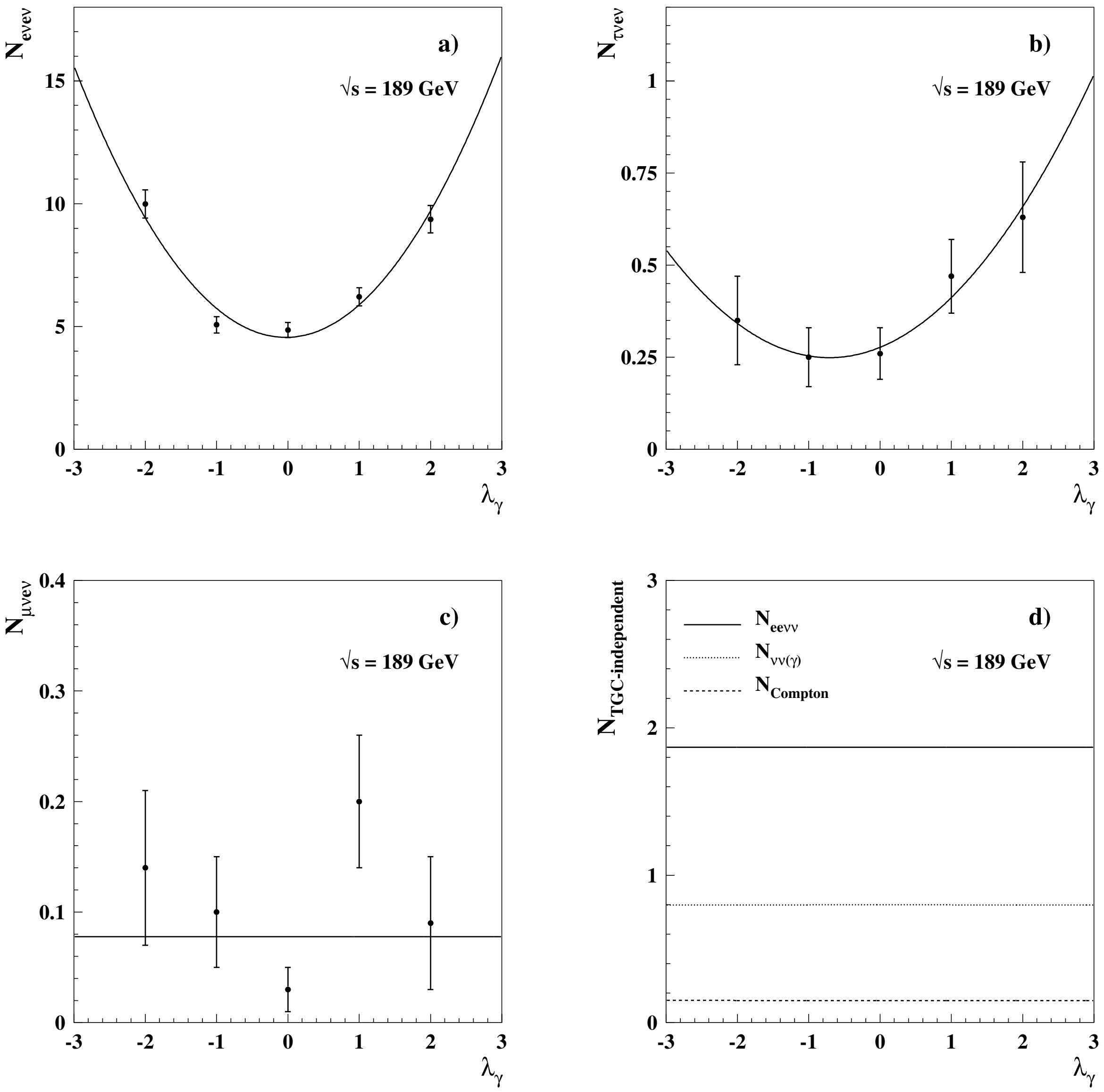

Figure 5.12: *Dependence of the different contributions to the total number of expected events on the coupling λ_γ at $\sqrt{s}$ = 189 GeV for the electron analysis: figure a) shows this dependence for the final state $e\nu_e e\nu_e$, which includes the signal, figure b) represents the $\tau\nu_\tau e\nu_e$ background, figure c) indicates the $\mu\nu_\mu e\nu_e$ background and figure d) shows the TGC independent backgrounds: $e\bar{e}\nu_l\bar{\nu}_l$ ($l \neq e$), $\nu_l\bar{\nu}_l(\gamma)$ and Compton events. Note that to the distribution of the $\mu\nu_\mu e\nu_e$ background a constant has been fitted, since it lacks a clear dependence on λ_γ.*

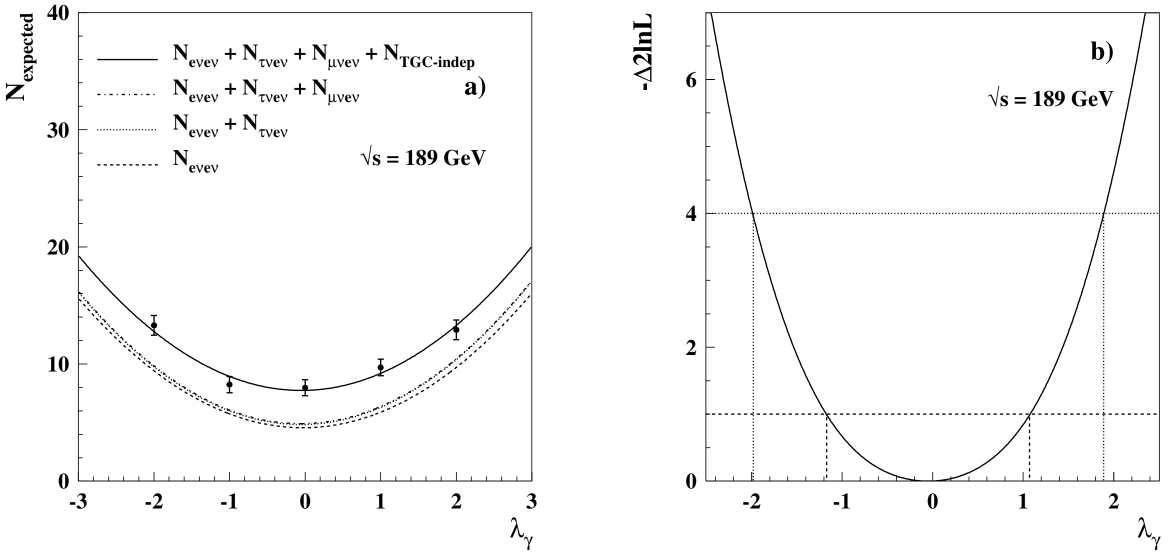

Figure 5.13: *Figure a) shows the dependence of the total number of expected events on the coupling λ_γ at $\sqrt{s}$ = 189 GeV for the electron analysis, containing the six contributions that are represented in figure 5.12 individually. Figure b) indicates the corresponding -$\Delta 2\ln\mathcal{L}$ distribution.*

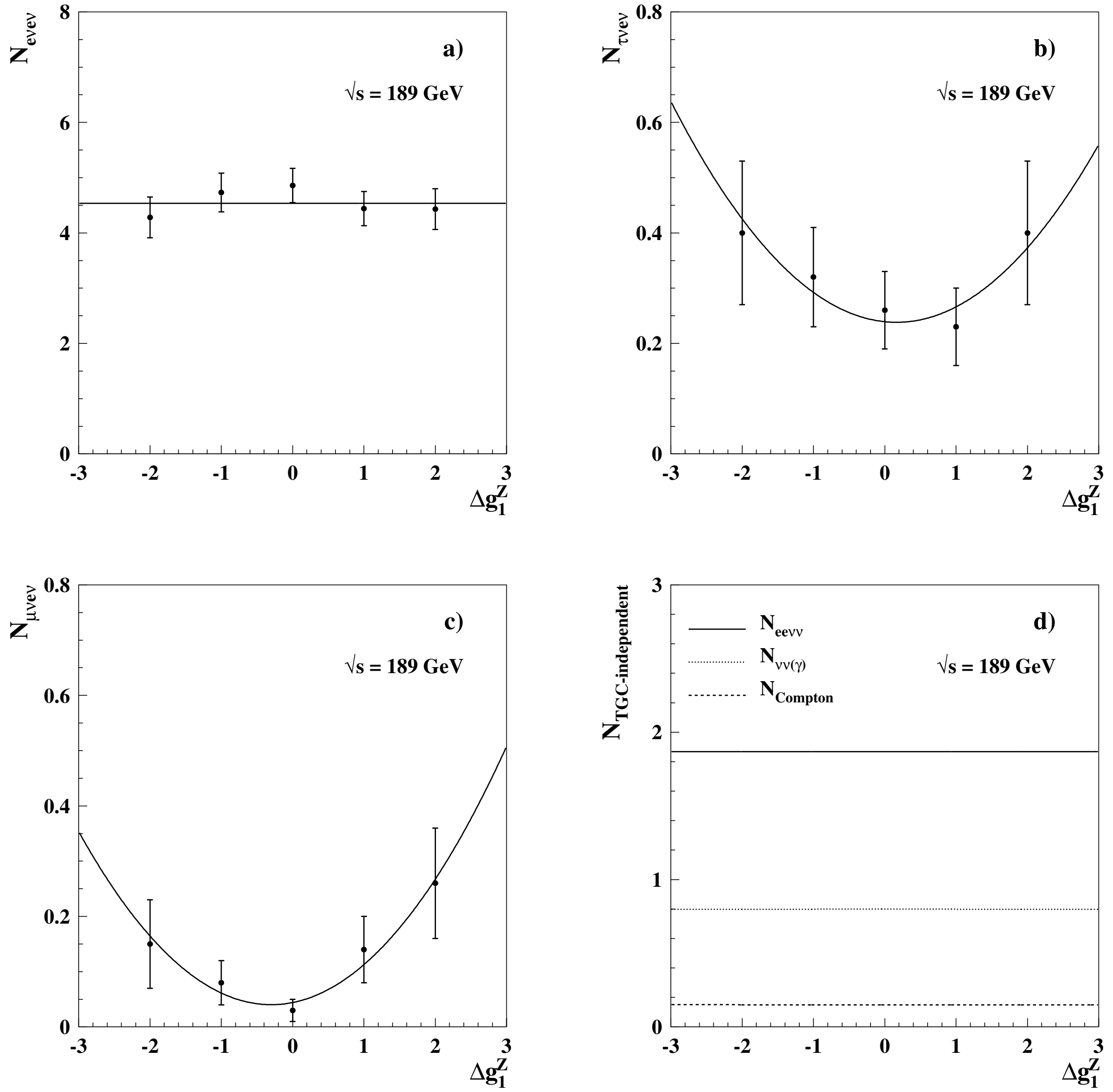

Figure 5.14: *Dependence of the different contributions to the total number of expected events on the coupling Δg_1^Z at $\sqrt{s}$ = 189 GeV for the electron analysis: figure a) shows this dependence for the final state $e\nu_e e\nu_e$, which includes the signal, figure b) represents the $\tau\nu_\tau e\nu_e$ background, figure c) indicates the $\mu\nu_\mu e\nu_e$ background and figure d) shows the TGC independent backgrounds: $e\bar{e}\nu_l\bar{\nu}_l$ ($l \neq e$), $\nu_l\bar{\nu}_l(\gamma)$ and Compton events. Note that to the distribution of the $e\nu_e e\nu_e$ final state a constant has been fitted, since it lacks a clear dependence on Δg_1^Z.*

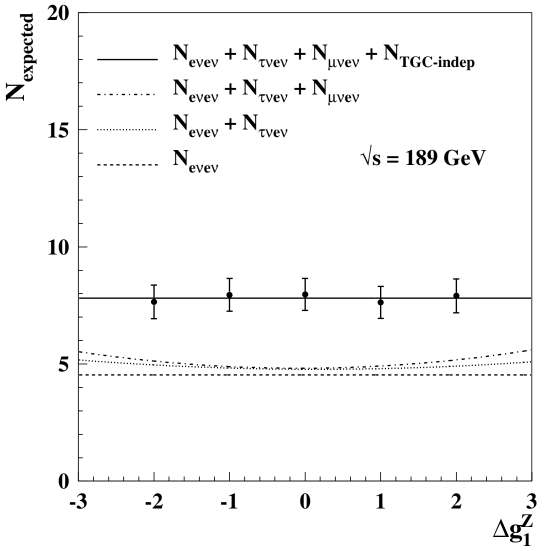

Figure 5.15: *Dependence of the total number of expected events on the coupling Δg_1^Z at $\sqrt{s}$ = 189 GeV for the electron analysis, containing the six contributions that are represented in figure 5.14 individually. Since this distribution is flat, no useful -$\Delta 2\ln\mathcal{L}$ distribution can be obtained from it.*

Differential distributions

In this case, the influence of the distributions of $\frac{d\sigma}{d(-Q_e \cos\theta_e)}$ is inquired, where Q_e and $\cos\theta_e$ represent the charge and the cosine of the polar angle of the detected electron or positron. These normalised distributions coming from the $e\nu_e e\nu_e$ final state are shown in figure 5.16 for the couplings $\Delta\kappa_\gamma$ and λ_γ for the values 0.0, -1.0 and -2.0 at generator level at $\sqrt{s}$ = 189 GeV, without having applied any selection criterium. Only the diagrams that satisfy the Crete definition are taken into account in these plots.
In tables 4.11 and 4.12, the SM values of the expected and observed number of events in the forward and backward directions are listed.
The -$\Delta 2\ln\mathcal{L}$ distributions at $\sqrt{s}$ = 189 GeV after having included the forward-backward information for all contributing final states are given in figure 5.17.
Table 5.9 gives an overview of the measured values of the couplings $\Delta\kappa_\gamma$ and λ_γ including the 68% CL errors and 95% CL intervals at $\sqrt{s}$ = 189 GeV for the cases that the forward-backward information is used and is not taken into account.
This procedure has been repeated for the centre-of-mass energies ranging from 192 to 206.7 GeV, thus including and excluding the forward-backward information. It turns out that the 68% CL errors and 95% CL intervals tend to be slightly smaller for the case where the forward-backward information has been included, although this is clearly not the case for 189 GeV. The -$\Delta 2\ln\mathcal{L}$ distributions for $\Delta\kappa_\gamma$ and λ_γ that have included the forward-backward information corresponding to the centre-of-mass energies ranging from 189 to 206.7 GeV are presented in appendix B.2, while these distributions for the years 1998 - 2000 combined are given in figure 5.18 and in this appendix.
The measured values for the TGC parameters $\Delta\kappa_\gamma$ and λ_γ including the 68% CL errors and 95% CL intervals that are deduced from the figures in appendix B.2 are listed in table 5.10.

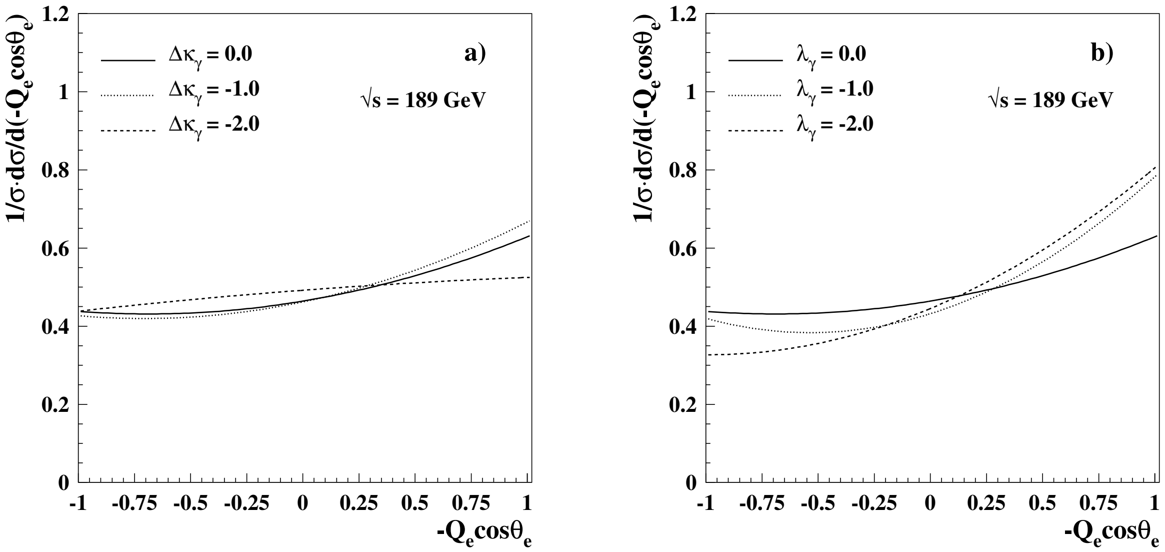

Figure 5.16: *Normalised distributions of* $\frac{\mathrm{d}\sigma}{\mathrm{d}(-Q_e \cos\theta_e)}$ *coming from the* $e\nu_e e\nu_e$ *final state for the couplings* $\Delta\kappa_\gamma$ *(a)) and* λ_γ *(b)) for the values 0.0, -1.0 and -2.0 at generator level at* $\sqrt{s}$ *= 189 GeV. The diagrams that contribute to this final state satisfy the Crete definition.*

Table 5.9: *Measured values for the TGC parameters* $\Delta\kappa_\gamma$ *and* λ_γ *including the 68% CL errors (first and third rows) and 95% CL intervals (second and fourth rows) at* $\sqrt{s}$ *= 189 GeV for the electron analysis for the cases that the forward-backward information is used and is not taken into account.*

	$\Delta\kappa_\gamma$	λ_γ
forward-backward info is not used	$-1.68^{+1.71}_{-0.62}$	$-0.05^{+1.12}_{-1.12}$
	[-2.78, +0.51]	[-1.98, +1.89]
forward-backward info is used	$-0.55^{+0.59}_{-1.73}$	$-0.26^{+1.39}_{-1.08}$
	[-2.77, +0.52]	[-2.10, +1.95]

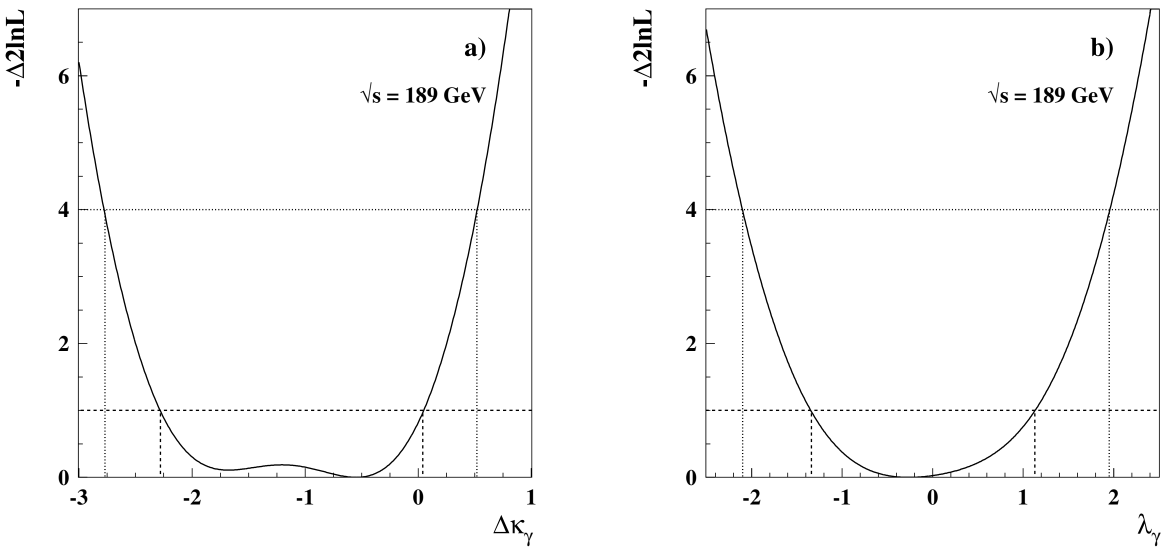

Figure 5.17: -Δ*2ln*$\mathcal{L}$ *distributions for the electron analysis for the couplings* $\Delta\kappa_\gamma$ *(a)) and* λ_γ *(b)) at* $\sqrt{s}$ *= 189 GeV after having included the forward-backward information for all contributing final states.*

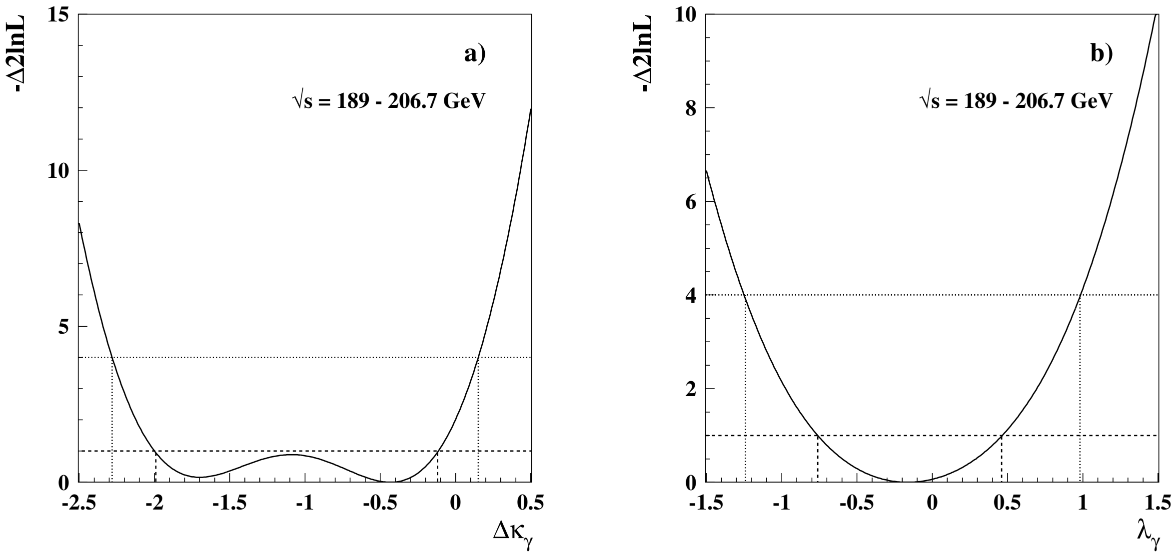

Figure 5.18: -Δ*2ln*$\mathcal{L}$ *distributions for the years 1998 - 2000 combined for the electron analysis as a function of* $\Delta\kappa_\gamma$ *(a)) and* λ_γ *(b)).*

Table 5.10: *Measured values for the TGC parameters $\Delta\kappa_\gamma$ and λ_γ including the 68% CL errors (first row per energy point) and 95% CL intervals (second row per energy point) for the centre-of-mass energies ranging from 189 to 206.7 GeV and 189 - 206.7 GeV for the electron analysis. At $\sqrt{s}$ = 206.7 GeV for the coupling $\Delta\kappa_\gamma$, the 68% CL errors are determined with respect to both local minima, while the 95% CL interval is measured with respect to the absolute minimum.*

$\sqrt{s}$ (GeV)	$\Delta\kappa_\gamma$	λ_γ
189	$-0.55^{+0.59}_{-1.73}$	$-0.26^{+1.39}_{-1.08}$
	[-2.77, +0.52]	[-2.10, +1.95]
192	$-0.39^{+1.19}_{-2.29}$	$-0.69^{+2.61}_{-1.75}$
	[-3.82, +1.83]	[-3.85, +3.44]
196	$-1.57^{+1.80}_{-0.78}$	$-0.06^{+1.16}_{-1.19}$
	[-2.96, +0.84]	[-2.16, +1.99]
200	$-0.20^{+0.63}_{-2.21}$	$-0.01^{+1.55}_{-1.56}$
	[-2.97, +0.99]	[-2.71, +2.68]
202	$-1.08^{+0.78}_{-0.78}$	$-0.15^{+1.10}_{-1.10}$
	[-2.65, +0.49]	[-2.36, +2.06]
205	$-2.03^{+2.42}_{-0.64}$	$-1.02^{+2.23}_{-1.29}$
	[-3.24, +1.00]	[-3.29, +2.37]
206.7	$-2.13^{+0.91}_{-0.55}$ $+0.07^{+0.55}_{-0.82}$	$+0.27^{+1.10}_{-1.62}$
	[-3.18, +1.14]	[-2.27, +2.16]
189 - 206.7	$-0.43^{+0.31}_{-1.56}$	$-0.16^{+0.62}_{-0.60}$
	[-2.28, +0.15]	[-1.24, +0.98]

5.1.3 Hadronic analysis

The hadronic analysis contains the same ingredients as those for the leptonic analyses. The TGC dependent final states $q\bar{q}e\nu_e$and $q\bar{q}l\nu_l$ contribute to the total number of expected events, while in this case the final states $q\bar{q}$, "rest 4-fermion", $e\bar{e}f\bar{f}$ and $\tau^+\tau^-$ form the TGC independent part.
The production of a single Z and γ (see muon analysis) supplement also to the TGC dependent background, producing a $q\bar{q}\nu_e\bar{\nu}_e$ final state, but for simplicity this contribution is considered as TGC independent and it is taken into account by the "rest 4-fermion" part. Furthermore, their contribution is negligibly small.
The cross sections and the number of selected events per contribution at $\sqrt{s}$ = 189 GeV as a function of the couplings $\Delta\kappa_\gamma$, λ_γ and Δg_1^Z are listed in tables 5.11, 5.12 and 5.13 respectively. The SM values are the same as the ones presented in table 3.17.

Table 5.11: *Cross sections and number of selected events per contributing process at $\sqrt{s}$ = 189 GeV as a function of $\Delta\kappa_\gamma$ for the hadronic analysis.*

process	value of $\Delta\kappa_\gamma$ -2.0	-1.0	0.0	1.0	2.0
$\sigma_{q\bar{q}e\nu_e}$ (pb)	4.353	3.344	3.311	4.153	5.940
$N_{q\bar{q}e\nu_e}$	16.63 ± 1.58	9.18 ± 1.04	19.72 ± 1.49	50.63 ± 2.61	103.87 ± 4.34
$\sigma_{q\bar{q}l\nu_l}$ (pb) $(l \neq e)$	6.712	5.422	4.795	4.823	5.519
$N_{q\bar{q}l\nu_l}$ $(l \neq e)$	29.25 ± 2.60	27.79 ± 2.26	18.01 ± 1.73	17.82 ± 1.73	18.13 ± 1.86
$\sigma_{\text{rest 4-fermion}}$ (pb)	18.78	18.78	18.78	18.78	18.78
$N_{\text{rest 4-fermion}}$	7.88 ± 1.73	7.88 ± 1.73	7.88 ± 1.73	7.88 ± 1.73	7.88 ± 1.73
$\sigma_{e\bar{e}f\bar{f}}$ (pb)	58.50	58.50	58.50	58.50	58.50
$N_{e\bar{e}f\bar{f}}$	0.10 ± 0.03	0.10 ± 0.03	0.10 ± 0.03	0.10 ± 0.03	0.10 ± 0.03
$\sigma_{q\bar{q}}$ (pb)	100.1	100.1	100.1	100.1	100.1
$N_{q\bar{q}}$	10.38 ± 0.57	10.38 ± 0.57	10.38 ± 0.57	10.38 ± 0.57	10.38 ± 0.57
$\sigma_{\tau^+\tau^-}$ (pb)	8.2	8.2	8.2	8.2	8.2
$N_{\tau^+\tau^-}$	0.00 ± 0.00	0.00 ± 0.00	0.00 ± 0.00	0.00 ± 0.00	0.00 ± 0.00
N_{expected}	64.24 ± 3.55	55.33 ± 3.08	56.10 ± 2.92	86.81 ± 3.62	140.36 ± 5.06

The second order polynomial fits to the TGC dependent contributions from tables 5.11, 5.12 and 5.13 are shown in figures 5.19, 5.21 and 5.23 respectively, together with the TGC independent contributions from the final states $q\bar{q}$, "rest 4-fermion" and $e\bar{e}f\bar{f}$. The $\tau^+\tau^-$ events do not contribute at $\sqrt{s}$ = 189 GeV. The total number of expected events and the corresponding -Δ2ln$\mathcal{L}$ distributions are represented in figures 5.20, 5.22 and 5.24 for the couplings $\Delta\kappa_\gamma$, λ_γ and Δg_1^Z respectively.

Table 5.12: *Cross sections and number of selected events per contributing process at $\sqrt{s}$ = 189 GeV as a function of λ_γ for the hadronic analysis.*

process	value of λ_γ -2.0	-1.0	0.0	1.0	2.0
$\sigma_{q\bar{q}e\nu_e}$ (pb)	7.583	4.373	3.311	4.286	7.345
$N_{q\bar{q}e\nu_e}$	51.04 $\pm$ 3.60	26.52 $\pm$ 1.97	19.72 $\pm$ 1.49	33.53 $\pm$ 2.19	61.88 $\pm$ 3.88
$\sigma_{q\bar{q}l\nu_l}$ (pb) ($l \neq e$)	11.281	6.492	4.795	6.192	10.675
$N_{q\bar{q}l\nu_l}$ ($l \neq e$)	59.46 $\pm$ 4.77	33.69 $\pm$ 2.73	18.01 $\pm$ 1.73	26.24 $\pm$ 2.35	43.24 $\pm$ 3.98
$\sigma_{\mathrm{rest\ 4-fermion}}$ (pb)	18.78	18.78	18.78	18.78	18.78
$N_{\mathrm{rest\ 4-fermion}}$	7.88 $\pm$ 1.73	7.88 $\pm$ 1.73	7.88 $\pm$ 1.73	7.88 $\pm$ 1.73	7.88 $\pm$ 1.73
$\sigma_{e\bar{e}f\bar{f}}$ (pb)	58.50	58.50	58.50	58.50	58.50
$N_{e\bar{e}f\bar{f}}$	0.10 $\pm$ 0.03	0.10 $\pm$ 0.03	0.10 $\pm$ 0.03	0.10 $\pm$ 0.03	0.10 $\pm$ 0.03
$\sigma_{q\bar{q}}$ (pb)	100.1	100.1	100.1	100.1	100.1
$N_{q\bar{q}}$	10.38 $\pm$ 0.57	10.38 $\pm$ 0.57	10.38 $\pm$ 0.57	10.38 $\pm$ 0.57	10.38 $\pm$ 0.57
$\sigma_{\tau^+\tau^-}$ (pb)	8.2	8.2	8.2	8.2	8.2
$N_{\tau^+\tau^-}$	0.00 $\pm$ 0.00	0.00 $\pm$ 0.00	0.00 $\pm$ 0.00	0.00 $\pm$ 0.00	0.00 $\pm$ 0.00
N_{expected}	128.86 $\pm$ 6.25	78.57 $\pm$ 3.83	56.10 $\pm$ 2.92	78.13 $\pm$ 3.69	123.48 $\pm$ 5.85

Table 5.13: *Cross sections and number of selected events per contributing process at $\sqrt{s}$ = 189 GeV as a function of Δg_1^Z for the hadronic analysis.*

process	value of Δg_1^Z -2.0	-1.0	0.0	1.0	2.0
$\sigma_{q\bar{q}e\nu_e}$ (pb)	7.695	4.417	3.311	4.335	7.512
$N_{q\bar{q}e\nu_e}$	24.83 $\pm$ 2.58	24.68 $\pm$ 1.92	19.72 $\pm$ 1.49	23.85 $\pm$ 1.89	26.87 $\pm$ 2.64
$\sigma_{q\bar{q}l\nu_l}$ (pb) ($l \neq e$)	12.507	6.790	4.795	6.536	12.051
$N_{q\bar{q}l\nu_l}$ ($l \neq e$)	57.47 $\pm$ 4.96	27.34 $\pm$ 2.53	18.01 $\pm$ 1.73	25.87 $\pm$ 2.41	62.53 $\pm$ 5.07
$\sigma_{\mathrm{rest\ 4-fermion}}$ (pb)	18.78	18.78	18.78	18.78	18.78
$N_{\mathrm{rest\ 4-fermion}}$	7.88 $\pm$ 1.73	7.88 $\pm$ 1.73	7.88 $\pm$ 1.73	7.88 $\pm$ 1.73	7.88 $\pm$ 1.73
$\sigma_{e\bar{e}f\bar{f}}$ (pb)	58.50	58.50	58.50	58.50	58.50
$N_{e\bar{e}f\bar{f}}$	0.10 $\pm$ 0.03	0.10 $\pm$ 0.03	0.10 $\pm$ 0.03	0.10 $\pm$ 0.03	0.10 $\pm$ 0.03
$\sigma_{q\bar{q}}$ (pb)	100.1	100.1	100.1	100.1	100.1
$N_{q\bar{q}}$	10.38 $\pm$ 0.57	10.38 $\pm$ 0.57	10.38 $\pm$ 0.57	10.38 $\pm$ 0.57	10.38 $\pm$ 0.57
$\sigma_{\tau^+\tau^-}$ (pb)	8.2	8.2	8.2	8.2	8.2
$N_{\tau^+\tau^-}$	0.00 $\pm$ 0.00	0.00 $\pm$ 0.00	0.00 $\pm$ 0.00	0.00 $\pm$ 0.00	0.00 $\pm$ 0.00
N_{expected}	100.66 $\pm$ 5.88	70.38 $\pm$ 3.66	56.10 $\pm$ 2.92	68.08 $\pm$ 3.56	107.76 $\pm$ 6.00

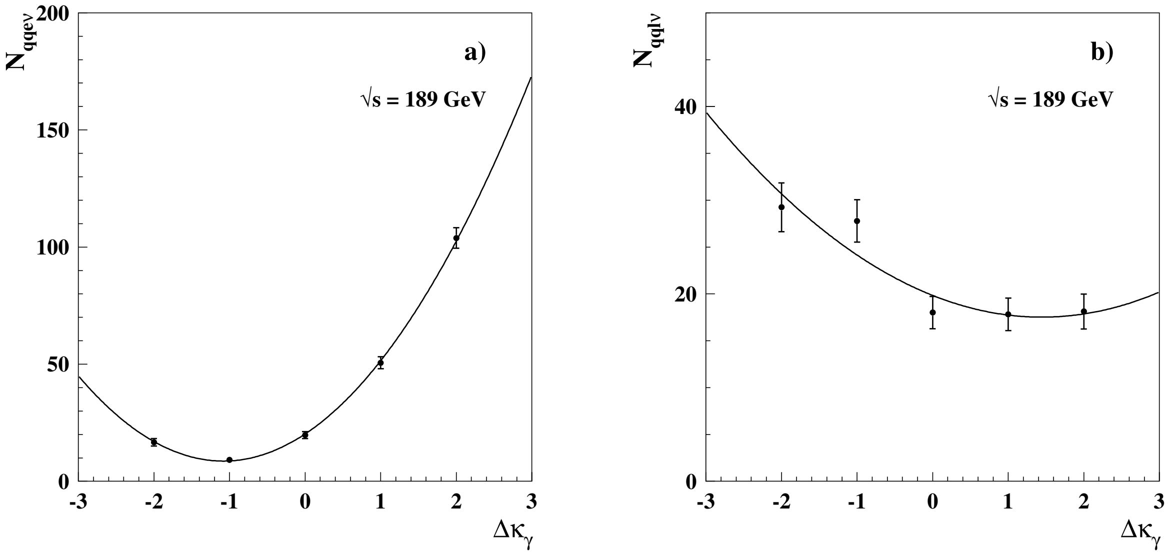

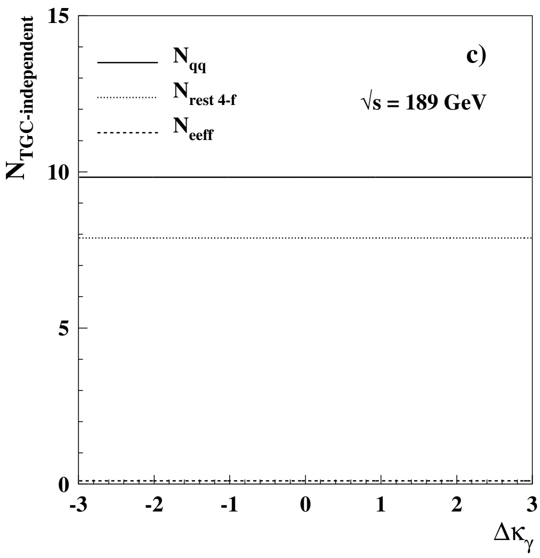

Figure 5.19: *Dependence of the different contributions to the total number of expected events on the coupling $\Delta\kappa_\gamma$ at $\sqrt{s}$ = 189 GeV for the hadronic analysis: figure a) shows this dependence for the final state $q\bar{q}e\nu_e$, which includes the signal, figure b) represents the $q\bar{q}l\nu_l$ background and figure c) shows the TGC independent backgrounds: $q\bar{q}$, "rest 4-fermion" and $e\bar{e}f\bar{f}$.*

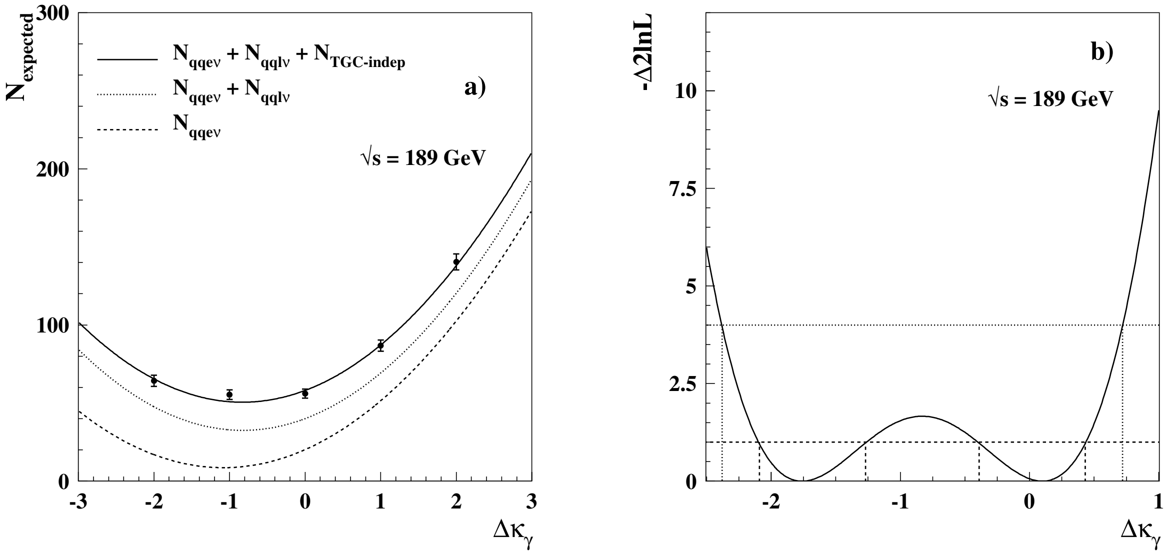

Figure 5.20: *Figure a) shows the dependence of the total number of expected events on the coupling $\Delta\kappa_\gamma$ at $\sqrt{s}$ = 189 GeV for the hadronic analysis, containing the five contributions that are represented in figure 5.19 individually. Figure b) indicates the corresponding -$\Delta 2\ln\mathcal{L}$ distribution.*

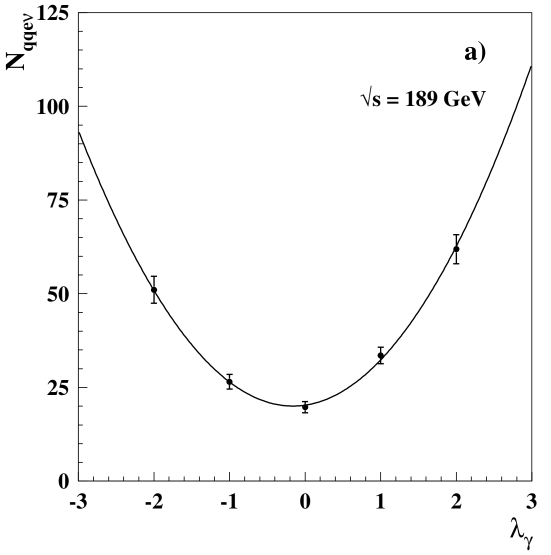

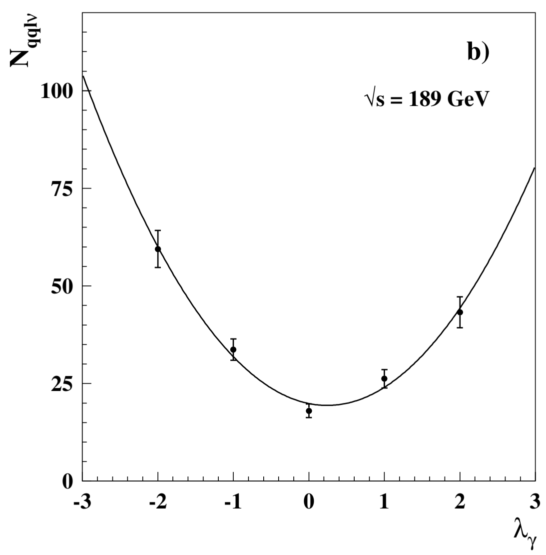

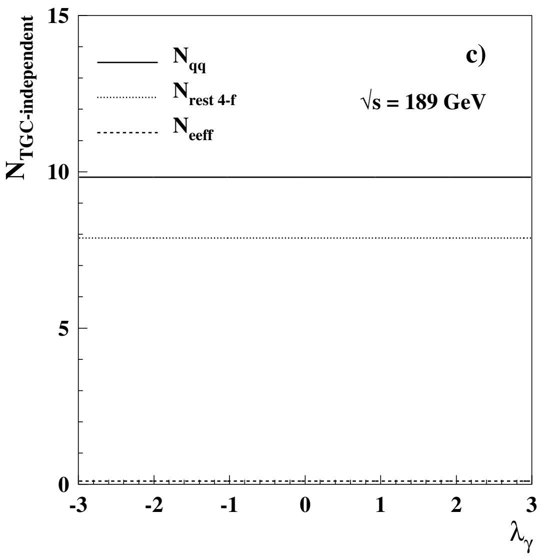

Figure 5.21: *Dependence of the different contributions to the total number of expected events on the coupling λ_γ at $\sqrt{s}$ = 189 GeV for the hadronic analysis: figure a) shows this dependence for the final state $q\bar{q}e\nu_e$, which includes the signal, figure b) represents the $q\bar{q}l\nu_l$ background and figure c) shows the TGC independent backgrounds: $q\bar{q}$, "rest 4-fermion" and $e\bar{e}f\bar{f}$.*

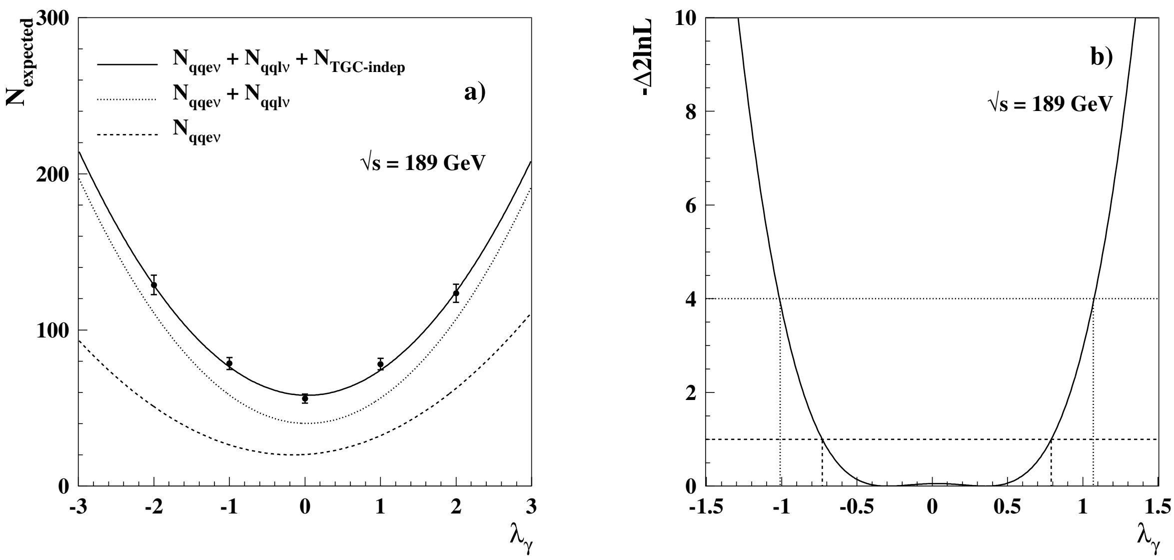

Figure 5.22: *Figure a) shows the dependence of the total number of expected events on the coupling λ_γ at $\sqrt{s}$ = 189 GeV for the hadronic analysis, containing the five contributions that are represented in figure 5.21 individually. Figure b) indicates the corresponding -$\Delta 2\ln\mathcal{L}$ distribution.*

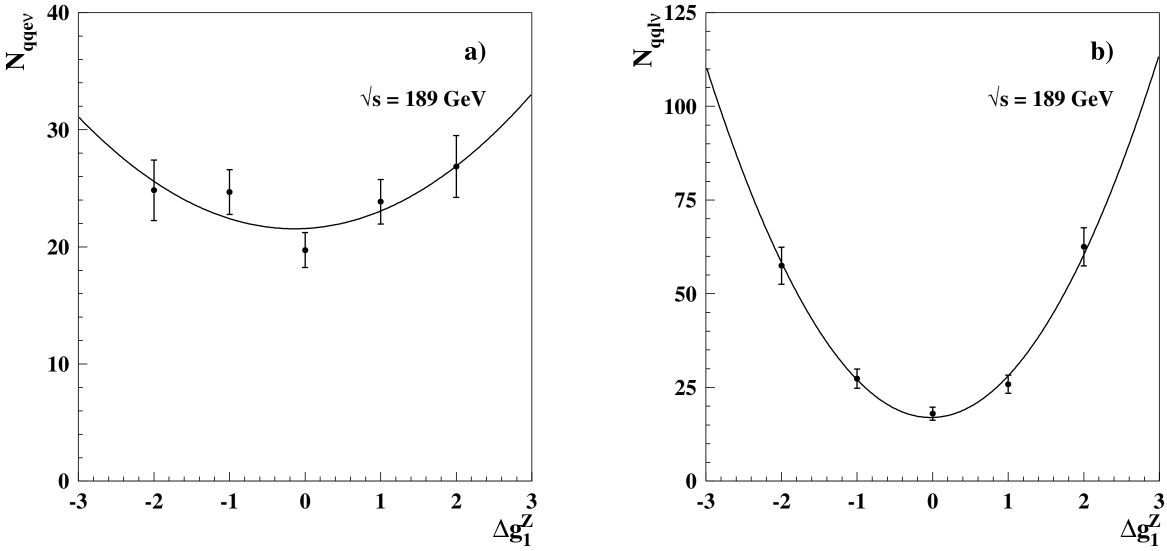

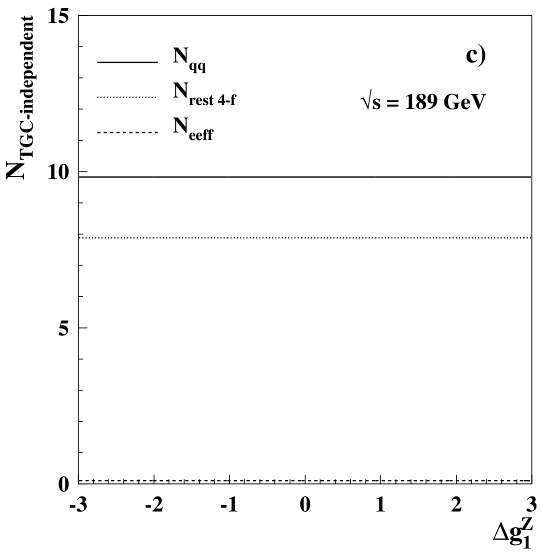

Figure 5.23: *Dependence of the different contributions to the total number of expected events on the coupling Δg_1^Z at $\sqrt{s}$ = 189 GeV for the hadronic analysis: figure a) shows this dependence for the final state $q\bar{q}e\nu_e$, which includes the signal, figure b) represents the $q\bar{q}l\nu_l$ background and figure c) shows the TGC independent backgrounds: $q\bar{q}$, "rest 4-fermion" and $e\bar{e}f\bar{f}$.*

For the hadronic analysis, the impact of the possible TGC dependence of differential distributions has not been taken into account. The most reasonable distribution to study would be that of $\frac{\mathrm{d}\sigma}{\mathrm{d}(-Q_W \cos\theta_W)}$, where Q_W and $\cos\theta_W$ indicate the charge and the cosine of the polar angle of the W from which its two jets are reconstructed. Due to the absence of a clear charge signature of the W, it is complicated to consider this distribution. The potential gain in resolution by taking into account the effect of differential distributions is very small, judging from the leptonic analyses.

This whole procedure has been repeated for the centre-of-mass energies ranging from 192 to 206.7 GeV, resulting in the -$\Delta 2\ln\mathcal{L}$ distributions that are given in appendix B.3, while the -$\Delta 2\ln\mathcal{L}$ distributions for $\Delta\kappa_\gamma$, λ_γ and Δg_1^Z for the years 1998 - 2000 combined are shown in figure 5.25 and in this appendix.

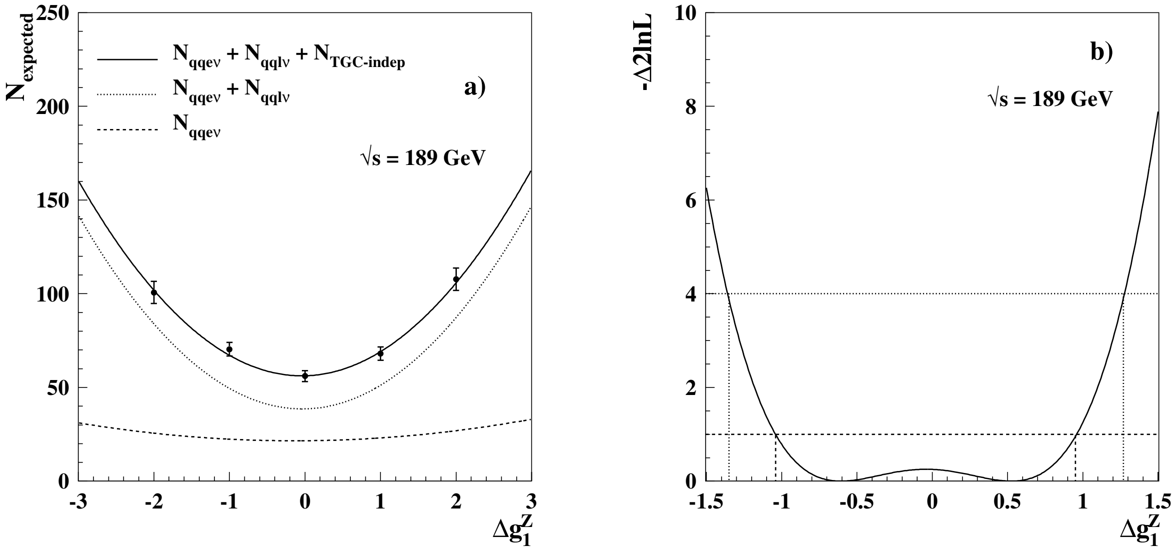

Figure 5.24: *Figure a) shows the dependence of the total number of expected events on the coupling Δg_1^Z at $\sqrt{s}$ = 189 GeV for the hadronic analysis, containing the five contributions that are represented in figure 5.23 individually. Figure b) indicates the corresponding -$\Delta 2\ln\mathcal{L}$ distribution.*

The measured values for the TGC parameters $\Delta\kappa_\gamma$, λ_γ and Δg_1^Z including the 68% CL errors and 95% CL intervals that are deduced from the figures in appendix B.3 are listed in table 5.14.

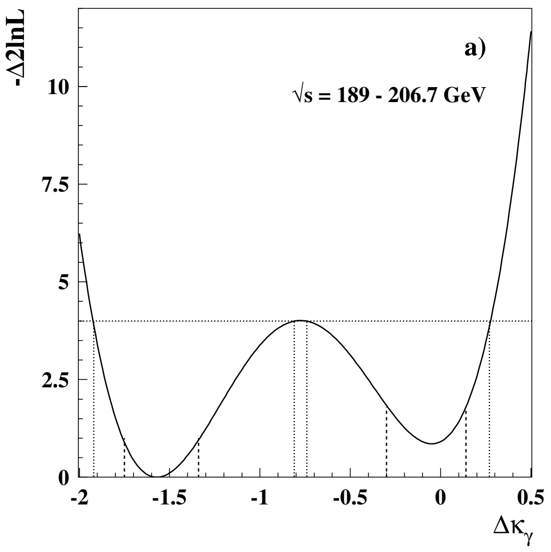

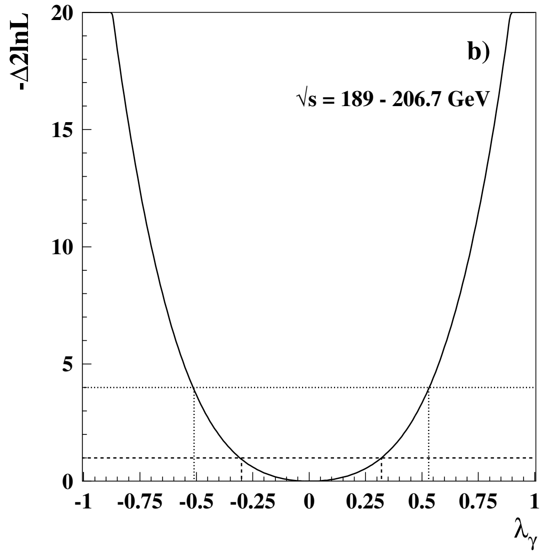

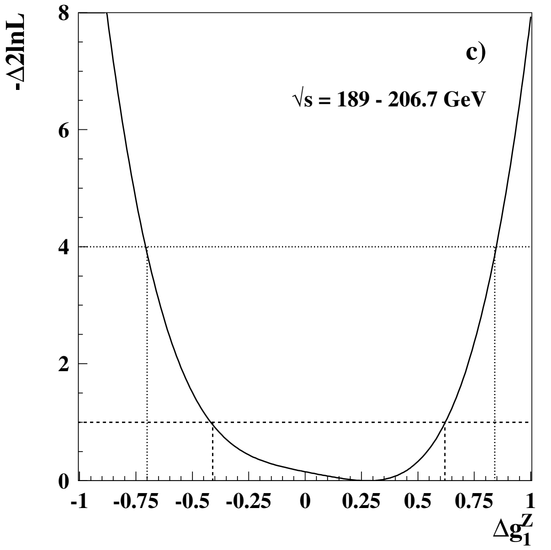

Figure 5.25: *-$\Delta 2ln\mathcal{L}$ distributions for the years 1998 - 2000 combined for the hadronic analysis as a function of $\Delta\kappa_\gamma$ (a)), λ_γ (b)) and Δg_1^Z (c)).*

Table 5.14: *Measured values for the TGC parameters $\Delta\kappa_\gamma$, λ_γ and Δg_1^Z including the 68% CL errors (first row per energy point) and 95% CL intervals (second row per energy point) for the centre-of-mass energies ranging from 189 to 206.7 GeV and 189 - 206.7 GeV for the hadronic analysis. In case of two minima, the 68% CL errors are determined with respect to both local minima, while the 95% CL intervals are measured with respect to the absolute minimum.*

$\sqrt{s}$ (GeV)	$\Delta\kappa_\gamma$	λ_γ	Δg_1^Z
189	$-1.76^{+0.49}_{-0.33}$ $+0.10^{+0.33}_{-0.49}$	$+0.35^{+0.44}_{-1.08}$	$-0.61^{+1.56}_{-0.43}$
	[-2.38, +0.72]	[-1.01, +1.07]	[-1.35, +1.27]
192	$-0.84^{+0.77}_{-0.77}$	$-0.06^{+0.56}_{-0.56}$	$+0.07^{+0.74}_{-0.74}$
	[-2.29, +0.61]	[-1.13, +1.02]	[-1.33, +1.48]
196	$-2.19^{+0.34}_{-0.31}$ $+0.73^{+0.30}_{-0.35}$	$-0.97^{+0.38}_{-0.28}$ $+0.88^{+0.29}_{-0.37}$	$-1.24^{+0.43}_{-0.35}$ $+1.34^{+0.34}_{-0.43}$
	[-2.78, -1.39] [-0.08, +1.32]	[-1.51, +1.42]	[-1.91, +2.00]
200	$-0.83^{+0.71}_{-0.70}$	$-0.01^{+0.37}_{-0.37}$	$+0.05^{+0.53}_{-0.53}$
	[-1.99, +0.34]	[-0.71, +0.68]	[-0.91, +1.01]
202	$-0.32^{+0.72}_{-1.61}$	$+0.01^{+0.64}_{-0.65}$	$+0.02^{+0.87}_{-0.86}$
	[-2.41, +0.88]	[-1.06, +1.07]	[-1.33, +1.38]
205	$-0.30^{+0.54}_{-1.43}$	$0.00^{+0.46}_{-0.45}$	$+0.15^{+0.65}_{-0.64}$
	[-2.10, +0.61]	[-0.79, +0.79]	[-0.91, +1.22]
206.7	$-1.74^{+0.61}_{-0.36}$ $+0.02^{+0.36}_{-0.61}$	$-0.02^{+0.72}_{-0.55}$	$-0.41^{+1.45}_{-0.57}$
	[-2.41, +0.69]	[-0.86, +0.98]	[-1.37, +1.42]
189 - 206.7	$-1.57^{+0.23}_{-0.18}$ $-0.05^{+0.19}_{-0.25}$	$0.00^{+0.32}_{-0.30}$	$+0.28^{+0.34}_{-0.69}$
	[-1.92, -0.81] [-0.74, +0.27]	[-0.51, +0.53]	[-0.70, +0.84]

5.2 Single *W* analysis

The TGC results from the $We\nu_e$ final state are deduced from the -Δ2ln$\mathcal{L}$ distributions that are obtained by adding the -Δ2ln$\mathcal{L}$ distributions from the three decay channels. These -Δ2ln$\mathcal{L}$ distributions corresponding to the $We\nu_e$ final state can be viewed in appendix B.4. Table 5.15 shows the measured values for the TGC parameters $\Delta\kappa_\gamma$, λ_γ and Δg_1^Z including the 68% CL errors and 95% CL intervals. The -Δ2ln$\mathcal{L}$ distributions for the years 1998 - 2000 combined are shown in figure 5.26.

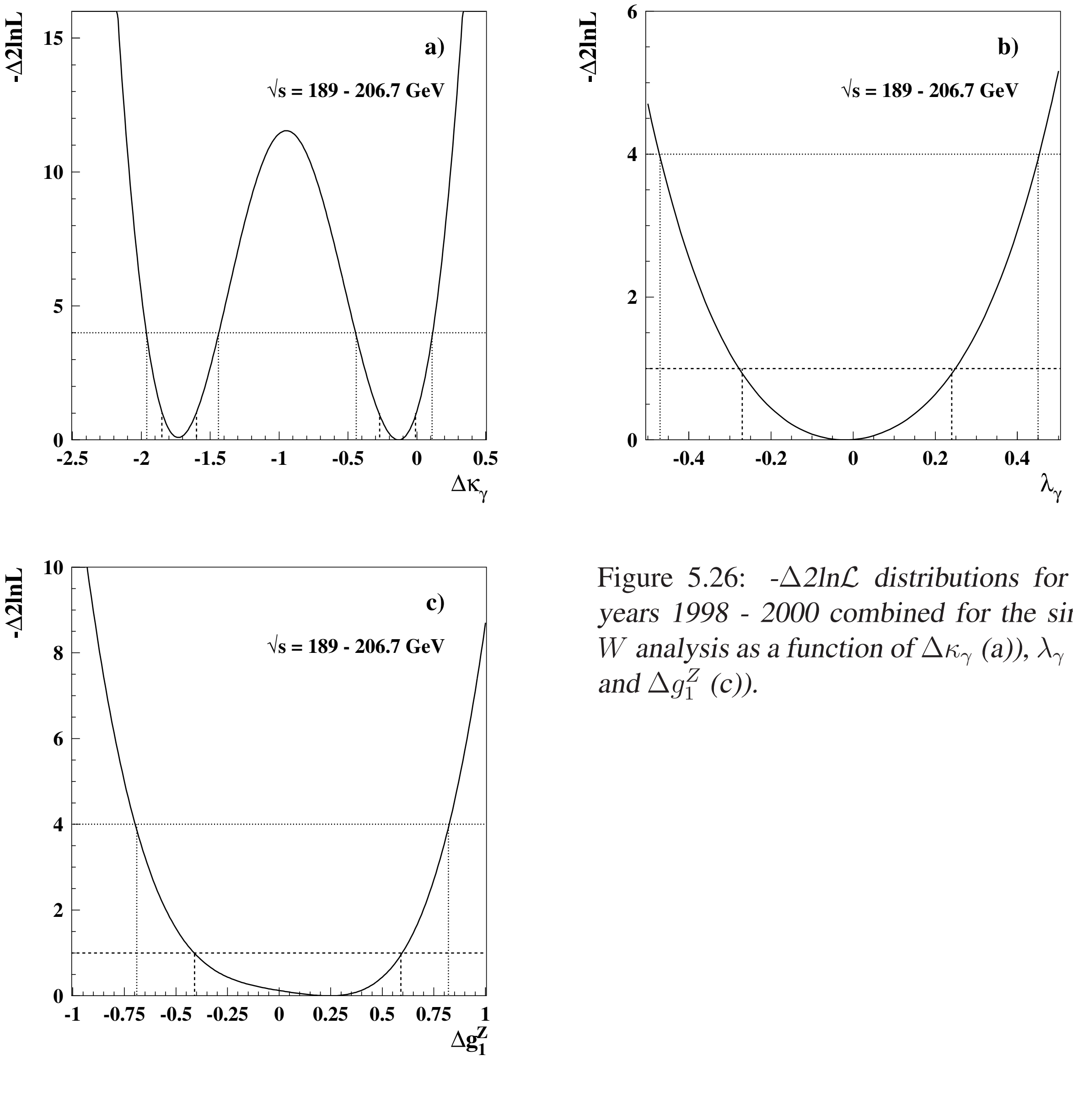

Figure 5.26: *-Δ2ln$\mathcal{L}$ distributions for the years 1998 - 2000 combined for the single W analysis as a function of $\Delta\kappa_\gamma$ (a)), λ_γ (b)) and Δg_1^Z (c)).*

Table 5.15: *Measured values for the TGC parameters $\Delta\kappa_\gamma$, λ_γ and Δg_1^Z including the 68% CL errors (first row per energy point) and 95% CL intervals (second row per energy point) for the centre-of-mass energies ranging from 189 to 206.7 GeV and 189 - 206.7 GeV for the single W analysis. In case of two minima, the 68% CL errors are determined with respect to both local minima, while the 95% CL intervals are measured with respect to the absolute minimum.*

$\sqrt{s}$ (GeV)	$\Delta\kappa_\gamma$	λ_γ	Δg_1^Z
189	$-1.88^{+0.26}_{-0.22}$ $-0.07^{+0.24}_{-0.28}$	$-0.26^{+0.93}_{-0.42}$	$+0.52^{+0.42}_{-1.55}$
	[-2.31, -1.17] [-0.80, +0.37]†	[-0.95, +0.96]	[-1.35, +1.25]
192	$-0.21^{+0.48}_{-1.60}$	$-0.02^{+0.56}_{-0.58}$	$+0.08^{+0.77}_{-0.77}$
	[-2.43, +0.70]	[-1.11, +1.02]	[-1.37, +1.53]
196	$-2.08^{+0.27}_{-0.24}$ $+0.33^{+0.26}_{-0.31}$	$-0.86^{+0.40}_{-0.28}$ $+0.78^{+0.28}_{-0.39}$	$-1.25^{+0.42}_{-0.34}$ $+1.31^{+0.34}_{-0.42}$
	[-2.56, -1.48] [-0.08, +0.66]†	[-1.38, +1.30]	[-1.90, +1.96]
200	$-1.62^{+0.61}_{-0.30}$ $-0.17^{+0.28}_{-0.37}$	$0.00^{+0.37}_{-0.37}$	$+0.04^{+0.54}_{-0.53}$
	[-2.08, +0.37]	[-0.69, +0.68]	[-0.93, +1.01]
202	$-0.29^{+0.45}_{-1.59}$	$-0.06^{+0.66}_{-0.60}$	$+0.19^{+0.74}_{-0.98}$
	[-2.32, +0.53]	[-1.05, +1.01]	[-1.30, +1.40]
205	$-1.12^{+0.68}_{-0.46}$	$-0.07^{+0.37}_{-0.36}$	$+0.09^{+0.60}_{-0.56}$
	[-1.91, +0.01]	[-0.73, +0.63]	[-0.87, +1.12]
206.7	$-1.78^{+0.34}_{-0.26}$ $-0.07^{+0.26}_{-0.33}$	$+0.12^{+0.48}_{-0.57}$	$-0.41^{+1.33}_{-0.55}$
	[-2.24, +0.43]	[-0.76, +0.88]	[-1.35, +1.35]
189 - 206.7	$-1.73^{+0.13}_{-0.12}$ $-0.13^{+0.12}_{-0.14}$	$-0.02^{+0.26}_{-0.25}$	$+0.25^{+0.34}_{-0.66}$
	[-1.96, -1.44] [-0.44, +0.11]	[-0.47, +0.45]	[-0.69, +0.82]

† At $\sqrt{s}$ = 189 and 196 GeV, the absolute minimum of the -$\Delta 2\ln\mathcal{L}$ distribution for the coupling $\Delta\kappa_\gamma$ does not coincide with the minimum close to the SM value and the difference between this local minimum and the local maximum close to $\Delta\kappa_\gamma$ = -1.0 is larger than 4. Considering only this local minimum close to the SM prediction, the 95% CL interval is deduced from the values +4 of the distribution with respect to this minimum. These points are indicated by the dashed-dotted lines in the corresponding -$\Delta 2\ln\mathcal{L}$ distributions of appendix B.4, resulting in the following 95% CL intervals: $\sqrt{s}$ = 189 GeV: [-0.88, +0.38] and $\sqrt{s}$ = 196 GeV: [-0.40, +0.84].

5.3 Systematic uncertainties

The systematic effects for the three decay channels that are discussed in section 4.3 for the cross section analyses are also treated for the TGC analyses. The influence of these systematic uncertainties have only been studied for the -Δ2ln$\mathcal{L}$ distributions that take into account all centre-of-mass energies. Tables 5.16, 5.17 and 5.18 show the impact of the various systematic effects on the couplings $\Delta\kappa_\gamma$, λ_γ and Δg_1^Z for the muon, electron and hadronic analyses respectively.

Table 5.16: *Contributions to the systematic error on the couplings $\Delta\kappa_\gamma$, λ_γ and Δg_1^Z for the muon analysis for $\sqrt{s}$ = 189 - 206.7 GeV.*

systematic effect	$\Delta(\Delta\kappa_\gamma)$	$\Delta(\lambda_\gamma)$	$\Delta(\Delta g_1^Z)$
$\Delta\sigma_{\mathrm{bkgr},\mu\nu_\mu e\nu_e}$ $\pm10\%$	$\pm$0.05	$\pm$0.01	$\pm$0.05
luminosity $\mathcal{L}$ $\pm6‰$	$\pm$0.01	<0.01	<0.01
identification efficiency $\Delta\varepsilon_\mu$ $\pm2.6\%$	$\pm$0.04	$\pm$0.01	$\pm$0.03
total	$\pm$0.06	$\pm$0.01	$\pm$0.05

Table 5.17: *Contributions to the systematic error on the couplings $\Delta\kappa_\gamma$ and λ_γ for the electron analysis for $\sqrt{s}$ = 189 - 206.7 GeV.*

systematic effect	$\Delta(\Delta\kappa_\gamma)$	$\Delta(\lambda_\gamma)$
$\Delta\sigma_{\mathrm{bkgr},e\nu_e e\nu_e}$ $\pm22\%$	$\pm$0.21	$\pm$0.03
luminosity $\mathcal{L}$ $\pm6‰$	<0.01	<0.01
identification efficiency $\Delta\varepsilon_e$ $\pm3.5\%$	$\pm$0.07	$\pm$0.04
tracking efficiency $\Delta\varepsilon_{\mathrm{track},e}$ $\pm5\%$	$\pm$0.10	$\pm$0.06
total	$\pm$0.24	$\pm$0.08

Table 5.18: *Contributions to the systematic error on the couplings $\Delta\kappa_\gamma$, λ_γ and Δg_1^Z for the hadronic analysis for $\sqrt{s}$ = 189 - 206.7 GeV.*

systematic effect	$\Delta(\Delta\kappa_\gamma)$	$\Delta(\lambda_\gamma)$	$\Delta(\Delta g_1^Z)$
$\Delta\sigma_{\mathrm{bkgr},q\bar{q}e\nu_e}$ $\pm5\%$	$\pm$0.15	$\pm$0.03	$\pm$0.16
luminosity $\mathcal{L}$ $\pm6‰$	$\pm$0.02	<0.01	$\pm$0.03
smearing $+5\%$	+0.06	+0.01	$\pm$0.08
total	$\pm$0.16	$\pm$0.03	$\pm$0.18

The results of these three decay channels give rise to the following systematic errors for the single W analysis:
$\Delta(\Delta\kappa_\gamma)$: $\pm$0.05, $\Delta(\lambda_\gamma)$: $\pm$0.01 and $\Delta(\Delta g_1^Z)$: $\pm$0.05.

The results for the total systematic error $\sigma_{\rm syst}$ can be used in determining the 95% CL intervals that take this systematic error into account from the likelihood $\mathcal{L}_{\rm stat+syst}$ that is defined in the following way:

$$\mathcal{L}_{\rm stat+syst} = \frac{\sigma^2_{\rm stat}}{\sigma^2_{\rm stat} + \sigma^2_{\rm syst}} \mathcal{L}_{\rm stat}, \tag{5.4}$$

where $\sigma_{\rm stat}$ represents the total statistical error and $\mathcal{L}_{\rm stat}$ is the "original" likelihood from which this statistical error is deduced. Table 5.19 shows the 95% CL intervals that include both the statistical and the systematic errors for the muon, electron, hadronic and single W analyses for the years 1998 - 2000 combined for the couplings $\Delta\kappa_\gamma$, λ_γ and Δg_1^Z.

Table 5.19: *Measured values of the 95% CL intervals that include both the statistical and the systematic errors for the muon, electron, hadronic and single W analyses for the years 1998 - 2000 combined for the couplings $\Delta\kappa_\gamma$, λ_γ and Δg_1^Z.*

analysis	$\Delta\kappa_\gamma$	λ_γ	Δg_1^Z
muon	[-2.31, -1.49] [-0.52, +0.30]	[-0.94, +0.89]	[-2.06, +1.76]
electron	[-2.29, +0.16]	[-1.25, +0.99]	–
hadronic	[-1.99, +0.35]	[-0.51, +0.53]	[-0.73, +0.87]
single W	[-1.97, -1.42] [-0.47, +0.13]	[-0.47, +0.45]	[-0.69, +0.82]

Including the systematic error hardly influences the results for the 95% CL intervals that only take the statistical error into account.

5.4 Conclusions

Considering the muon, electron, hadronic and single W analyses for the years 1998 - 2000 combined, the obtained results for the couplings $\Delta\kappa_\gamma$, λ_γ and Δg_1^Z are in agreement with SM expectations. As can already be concluded from figures 1.4, 1.5 and 1.6, the sensitivity to the coupling $\Delta\kappa_\gamma$ turns out to be the strongest, while the sensitivity to the coupling Δg_1^Z is the weakest. Because of the fact that the minimum of the signal cross section for the coupling $\Delta\kappa_\gamma$ is located around -1, while this minimum is close to the SM value for the couplings λ_γ and Δg_1^Z, two apparent minima can be distinguished in the -Δ2ln$\mathcal{L}$ distribution for the former coupling, which is not the case for the latter two couplings. Except for the electron analysis, the other three analyses give clearly rise to this behaviour: one minimum located around -2 and one minimum close to 0, the SM expectation.
The single W analysis for the years 1998 - 2000 combined gives rise to the measurements of the anomalous couplings, that are listed in table 5.20, abandoning the $\Delta\kappa_\gamma$ result around -2.0. Both statistical and systematic errors are included in these quoted results.

Table 5.20: *Single W results for the centre-of-mass energies $\sqrt{s}$ = 189 - 206.7 GeV for the TGC parameters $\Delta\kappa_\gamma$, λ_γ and Δg_1^Z including the 68% CL errors and 95% CL intervals. Both statistical and systematic errors are included.*

coupling	68% CL	95% CL
$\Delta\kappa_\gamma$	$-0.13^{+0.12}_{-0.14}$(stat) $\pm$ 0.05(syst)	[-0.47, +0.13]
λ_γ	$-0.02^{+0.26}_{-0.25}$(stat) $\pm$ 0.01(syst)	[-0.47, +0.45]
Δg_1^Z	$+0.25^{+0.34}_{-0.66}$(stat) $\pm$ 0.05(syst)	[-0.69, +0.82]

CHAPTER 6

Discussion and Conclusions

In this chapter, the single W cross section and TGC results presented in the previous two chapters are compared with other analyses. The single W TGC results are also considered in view of other measurements of the couplings at the WWV vertex ($V = \gamma$ or Z), which comprehend LEP results, measurements performed at currently running experiments and expectations for these couplings at future colliders.

6.1 LEP results

Cross section results

The cross section measurements as described in chapter 4 are in good agreement with an alternative DELPHI analysis, presented in [57]. The single W analysis results presented in this paper are listed in table 6.1 and take into account the S-period (see section 2.1). The efficiencies and purities from the muon, electron and hadronic analyses from this paper correspond well with the results presented in this thesis. In general, the statistical and systematic errors from this thesis are smaller.
A combined measurement of the four LEP experiments results in the plot of the single W cross section as depicted in figure 6.1. The results of the individual experiments can be retrieved from [58]. The eight measurements are clearly in agreement with the SM expectations.

TGC results

The analysis of the TGCs as discussed in chapter 5 gives rise to anomalous couplings that are in concordance with another DELPHI analysis, presented in [59], with the following values for the years 1998 - 2000 combined:

$$\begin{aligned}
\Delta\kappa_\gamma &= 0.05^{+0.12}_{-0.14}(\text{stat}) \pm 0.13(\text{syst}),\\
\lambda_\gamma &= 0.06^{+0.24}_{-0.31}(\text{stat}) \pm 0.07(\text{syst}),\\
\Delta g_1^Z &= 0.04^{+0.28}_{-0.28}(\text{stat}) \pm 0.03(\text{syst}).
\end{aligned}$$

Table 6.1: *Values for the total single W cross section as measured in [57] for the centre-of-mass energies ranging from $\sqrt{s}$ = 189 to 206.7 GeV, including the statistical and systematic errors.*

$\sqrt{s}$ (GeV)	$\sigma_{We\nu_e}$ (pb)
189	$0.70^{+0.29}_{-0.25}\pm0.08$
192	$0.12^{+0.29}_{-0.12}\pm0.01$
196	$0.90^{+0.39}_{-0.34}\pm0.10$
200	$0.45^{+0.31}_{-0.19}\pm0.05$
202	$1.09^{+0.52}_{-0.43}\pm0.11$
205	$0.56^{+0.36}_{-0.30}\pm0.06$
206.7	$0.58^{+0.25}_{-0.22}\pm0.06$

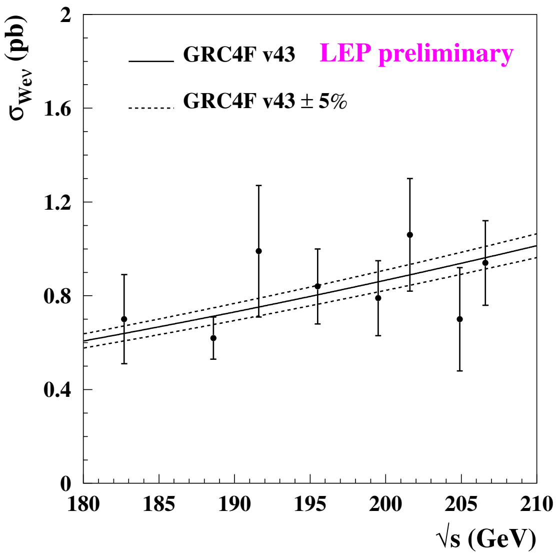

Figure 6.1: *Preliminary LEP-combined measurements of the single W cross section, compared to the predictions of GRC4F. The dotted lines represent the $\pm5\%$ uncertainty on the predictions.*

In order to obtain values for these couplings the generator DELTGC [60] has been used for this analysis. This generator has been designed with a special attention to the anomalous gauge boson couplings.

As already shown before, the non-Abelian classes of diagrams, i.e. fusion and annihilation diagrams (see figure 1.2), contain TGCs. The former type of diagram gives rise to the final state $We\nu_e$, while the latter type results in a W-pair. Studies are performed to determine the couplings $\Delta\kappa_\gamma$, λ_γ and Δg_1^Z from the semi-leptonic and fully hadronic decay of this W-pair, resulting in the final states $q\bar{q}l\nu_l$ (l = e, μ or τ) and $q\bar{q}q\bar{q}$ respectively. Analysing the leptonic final state $l\nu_l l\nu_l$ is difficult, because of the two non-detectable neutrinos. Furthermore, the cross section of this process is about a factor 4 smaller than each of the other two final states. Figure 1.6 shows that the sensitivity of the s-channel $q\bar{q}e\nu_e$ cross section on the couplings λ_γ and Δg_1^Z is much stronger than that of the t-channel $q\bar{q}e\nu_e$ cross section, while these sensitivities on the coupling $\Delta\kappa_\gamma$ are of the same magnitude. Hence, the TGC analysis of the W^+W^- final state should result in much stronger limits on the couplings $\Delta\kappa_\gamma$, λ_γ and Δg_1^Z than those from the $We\nu_e$ final state, taking into account only the cross section information. Including the information coming from angular distributions from W-pairs turns out to be much more fruitful than in case of the single W analysis. The W^+W^- final state can be characterised in terms of the following five angular variables:

- the W^- production angle Θ_{W^-}, which is defined as the angle between the incoming electron and the outgoing W^-,
- the decay angles (θ_1, ϕ_1) of the fermion in the rest frame of the W^-,
- the decay angles (θ_2, ϕ_2) of the anti-fermion in the rest frame of the W^+.

Especially the distribution of cosΘ_{W^-} appears to be sensitive to anomalous couplings. The couplings obtained from the semi-leptonic and fully hadronic analyses result in accuracies that are about twice as high for all three couplings for the semi-leptonic analysis compared to the fully hadronic analysis. The reason why the fully hadronic analysis produces results that are weaker than the ones from the semi-leptonic analysis is caused by the difficulty to distinguish quarks from anti-quarks and to determine which (anti-)quark belongs to which W-boson. The precisions of the semi-leptonic analysis and the single W analysis on the coupling $\Delta\kappa_\gamma$ are of the same size. Combining the measurements from the four LEP experiments for the complete LEP2 data set ($\sqrt{s}$ = 161 - 209 GeV, which corresponds to integrated luminosities of about 700 pb^{-1} per experiment) gives rise to the 68% CL errors and 95% CL intervals that are quoted in table 6.2 [61], indicating that these measurements are in good agreement with SM predictions.

Table 6.2: *Combined results from the four LEP experiments for the centre-of-mass energies $\sqrt{s}$ = 161 - 209 GeV for the TGC parameters $\Delta\kappa_\gamma$, λ_γ and Δg_1^Z including the 68% CL errors and 95% CL intervals. Both statistical and systematic errors are included.*

coupling	68% CL	95% CL
$\Delta\kappa_\gamma$	$-0.057^{+0.055}_{-0.055}$	[-0.165, +0.052]
λ_γ	$-0.020^{+0.024}_{-0.024}$	[-0.067, +0.028]
Δg_1^Z	$-0.002^{+0.023}_{-0.025}$	[-0.049, +0.043]

6.2 Beyond LEP2 energies

At centre-of-mass energies much higher than the ones available at LEP2, it is interesting to observe that the single W cross section rises with the energy, while the W-pair cross section drops like $\frac{1}{s}$ as can be seen from figure 6.2. Hence, the impact of the single W final state becomes much more important in determining the couplings at the WWV vertex at such centre-of-mass energies than at LEP2 energies.

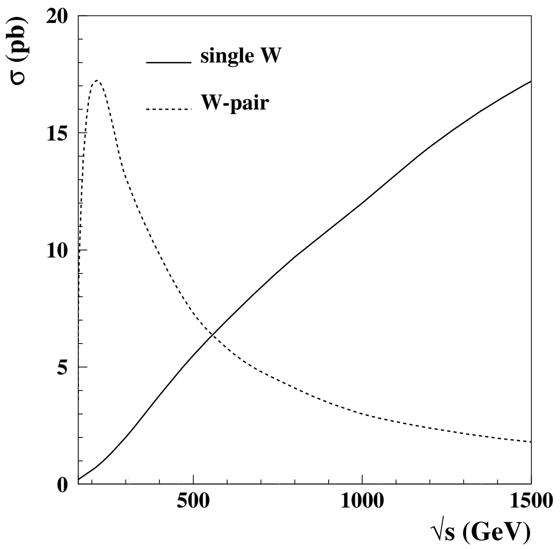

Figure 6.2: *Total cross section for single W and W-pair production as a function of the centre-of-mass energy.*

Other TGC measurements

The rest of this section is focused on the TGC measurements that are performed currently elsewhere in the world and on measurements that will be performed in the future.

The ZEUS collaboration has reported results on the measurement of the anomalous couplings at the $WW\gamma$ vertex from single W production in positron-proton collisions at HERA in Hamburg via the reaction $e^+p \rightarrow e^+W^\pm X$ [62]. The 95% CL results are obtained at a centre-of-mass energy $\sqrt{s}$ = 300 GeV and correspond to an integrated luminosity $\mathcal{L}$ = 47.7 pb^{-1}:

$$-4.7 < \Delta\kappa_\gamma < 1.5 \;\text{ and }\; -3.2 < \lambda_\gamma < 3.2.$$

At the currently running Tevatron $p\bar{p}$ collider ($\sqrt{s}$ = 1.96 TeV) near Chicago, the WWV vertex is especially probed via the production of one of the following vector boson pairs: $W\gamma$, WW and WZ. The production of these gauge boson pairs will be studied at the LHC pp collider for the same reasons. This collider will become active in 2007 and will reach a centre-of-mass energy $\sqrt{s}$ = 14 TeV. The signature of events with anomalous couplings is an excess of these vector boson pairs, particularly for large values of the invariant mass of the gauge boson pair and for large values of the gauge boson transverse momentum p_{T}. With non-SM couplings, the cross sections for vector boson pair production grow with the centre-of-mass energy, eventually violating tree-level unitarity. This can be avoided by parametrising any coupling α ($\alpha = \Delta\kappa_\gamma$, λ_γ or Δg_1^Z) in the following way:

$$\alpha(\hat{s}) = \frac{\alpha}{(1+\frac{\hat{s}}{\Lambda^2})^2}, \tag{6.1}$$

where $\hat{s}$ is the invariant mass of the gauge boson pair and α is the coupling value at the low energy limit. Λ is related to the energy scale at which new physics becomes important. The sensitivity of the couplings is dependent on the value of this cut-off scale Λ: the higher the value of Λ, the more accurate coupling results can be obtained. The value of the form factor Λ needs to be chosen such that the coupling limit is less than the unitarity limit. The Tevatron experiments DØ and CDF usually quote coupling results for a scale Λ = 1.5 TeV or 2.0 TeV [63, 64], while LHC will be able to produce couplings for a form factor Λ = 10 TeV [65].

One of the possible options for a future collider after LHC is the construction of the linear collider TESLA, which is to be built near Hamburg. The proposal is to create a linear e^+e^- collider, which should be running at centre-of-mass energies $\sqrt{s}$ = 0.09 - 1.0 TeV. Due to the higher centre-of-mass energies possible at TESLA, the produced Ws get a larger boost, assuming that a W-pair has been created, which makes it possible to measure the production angle Θ_{W^-} with significantly higher accuracy than at LEP2. At LEP2, the single W production is mainly sensitive to $WW\gamma$ couplings, while the WWZ and the $WW\gamma$ vertex contribute roughly equally to W-pair production. Hence, only a linear combination of the two types of couplings is effectively measured. Since TESLA will run with polarised beams, these types can be disentangled. A W-pair can be produced by means of the conversion diagram and the non-Abelian annihilation diagrams as depicted in figure 1.2. The contribution of the first diagram vanishes for right-handed electrons or left-handed positrons. Therefore, this diagram can be excluded completely by polarising one of the incoming beams appropriately, leaving only TGC dependent diagrams. The WW cross section for left-handed electrons $\sigma_{WW,L}$ is at least a factor 10 larger than the one for right-handed electrons $\sigma_{WW,R}$ for all polar angles Θ_{W^-} at TESLA energies. Also the left-right asymmetry A_{LR} for W-pair production is very useful in disentangling couplings at the WWZ and the $WW\gamma$ vertex [66].

To summarise, figure 6.3 shows the obtained or obtainable precisions of the couplings $\Delta\kappa_\gamma$ and λ_γ at LEP, Tevatron, LHC and TESLA [66]. Tevatron will run until 2008, resulting in data samples of up to $\mathcal{L}_{\mathrm{Tevatron}}$ = 30 fb^{-1}. If an integrated luminosity $\mathcal{L}$ = 10 fb^{-1} can be achieved, limits on anomalous couplings are expected to improve the current results by a factor of about 5. Each additional factor 10 in integrated luminosity leads to roughly another factor 2 improvement in the accuracies that can be achieved [67].
For LHC and TESLA three years of running are assumed with the following specifications: $\mathcal{L}_{\mathrm{LHC}}$ = 300 fb^{-1} and $\sqrt{s}_{\mathrm{TESLA}}$ = 800 GeV and $\mathcal{L}_{\mathrm{TESLA}}$ = 1500 fb^{-1}. Especially for the coupling $\Delta\kappa_\gamma$ TESLA can reach a much higher sensitivity than LHC.

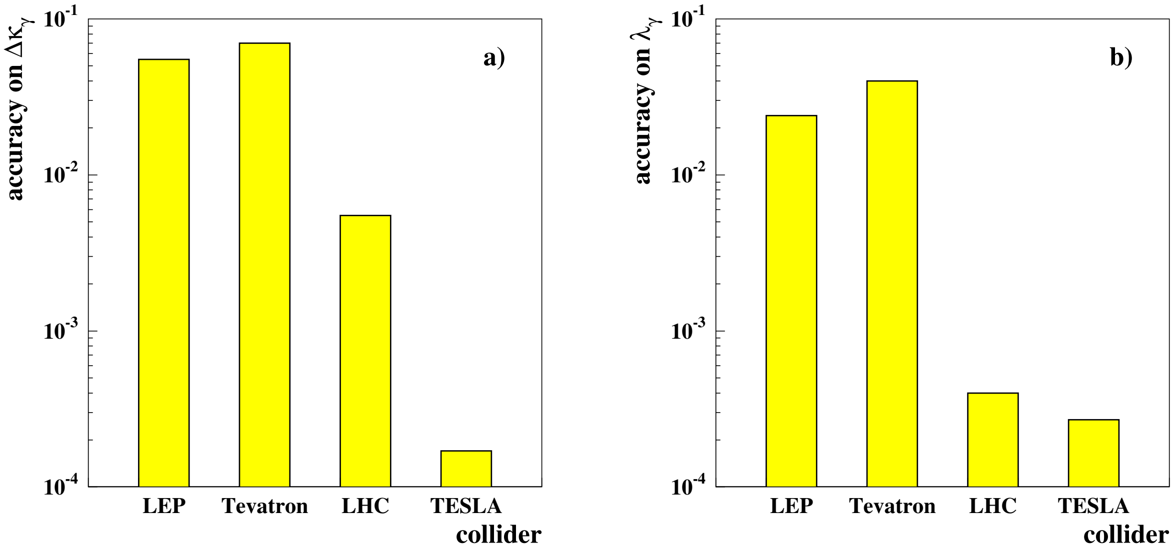

Figure 6.3: *Obtained or expected accuracy on the couplings $\Delta\kappa_\gamma$ (a)) and λ_γ (b)) from the colliders LEP, Tevatron, LHC and TESLA.*

APPENDIX A

R-factor distributions from the cross section analyses

The following sections contain the -$\Delta 2\ln\mathcal{L}$ distributions and the probability density distributions for the R-factor from the cross section analyses for the various centre-of-mass energies.

A.1 Muon analysis

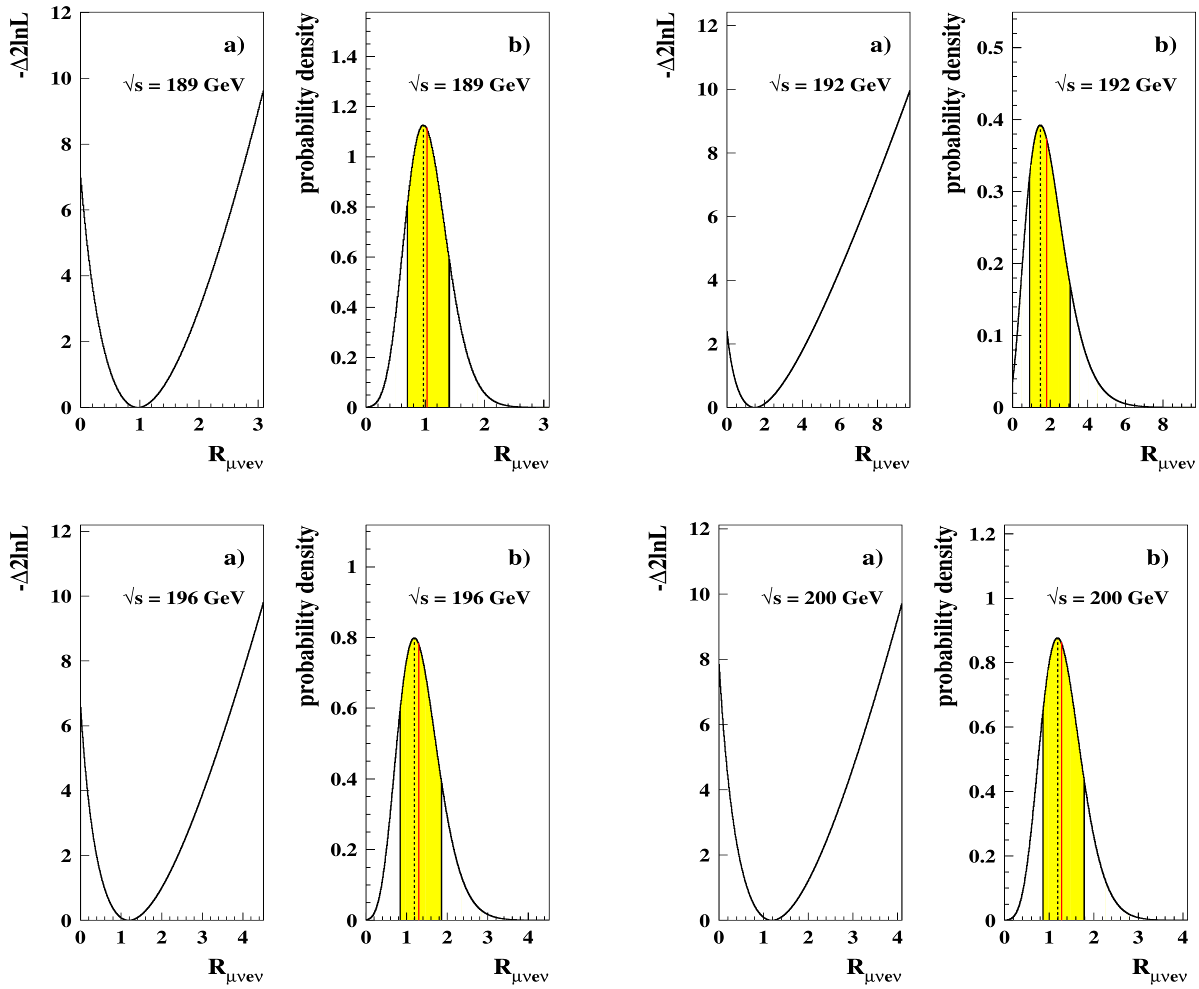

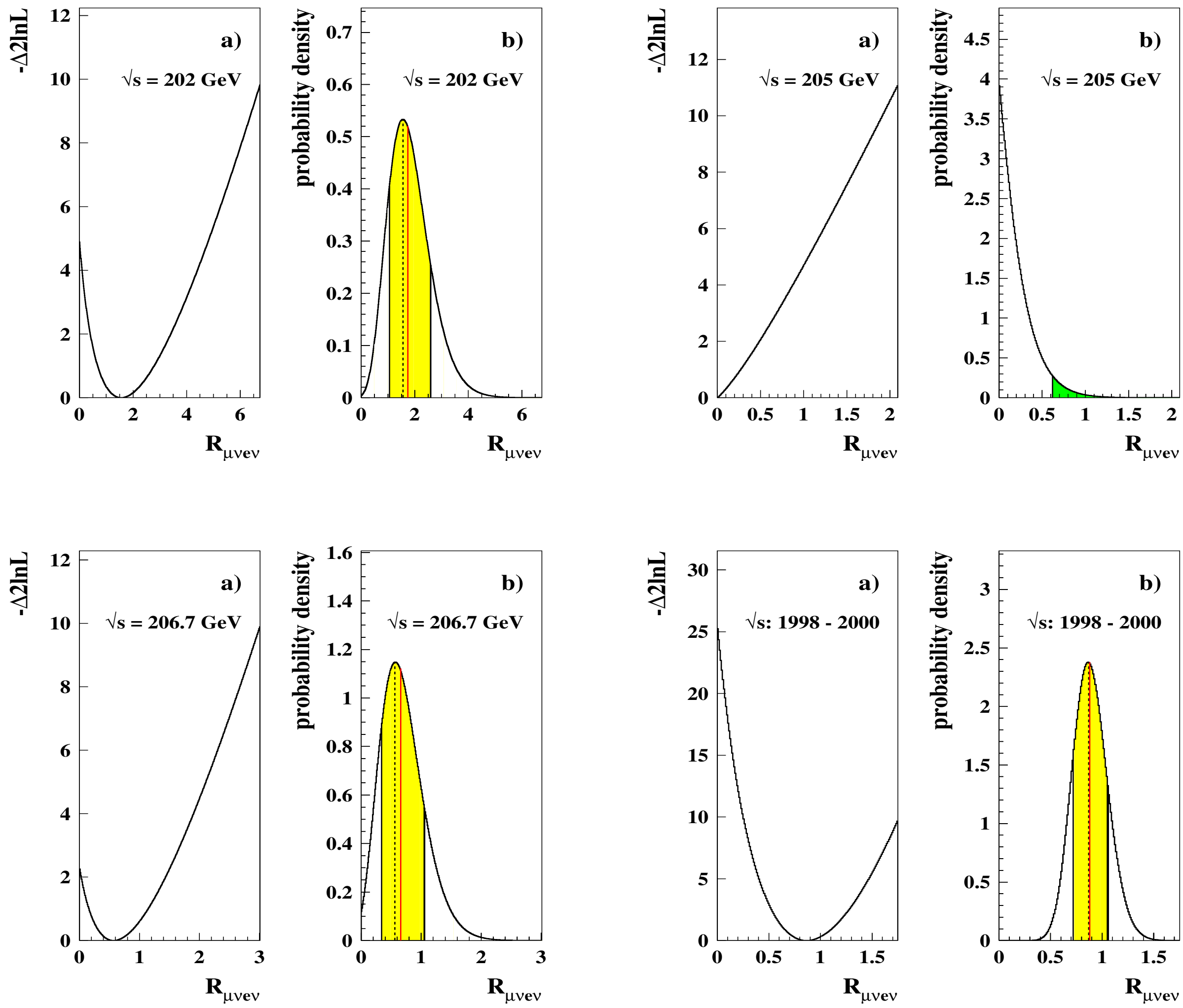

A.2 Electron analysis

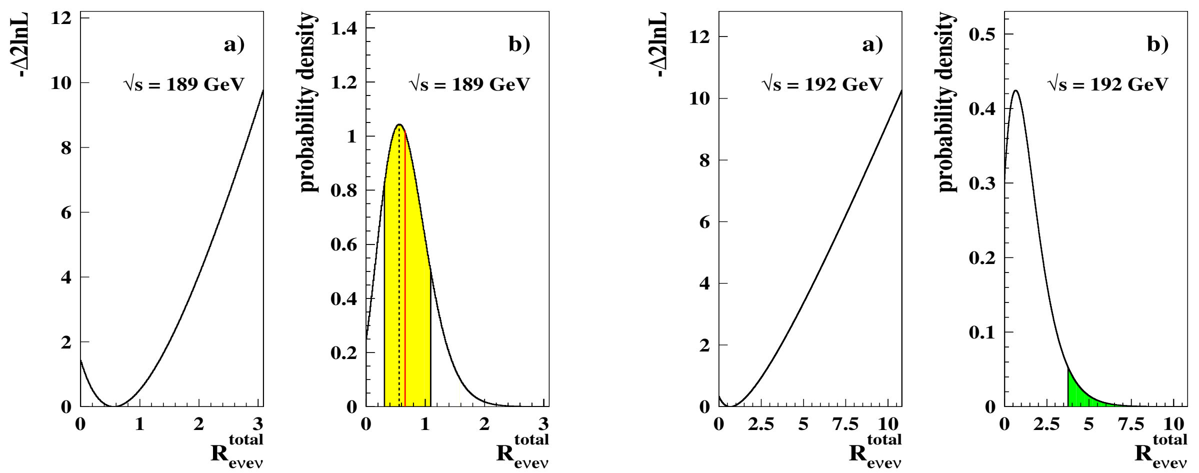

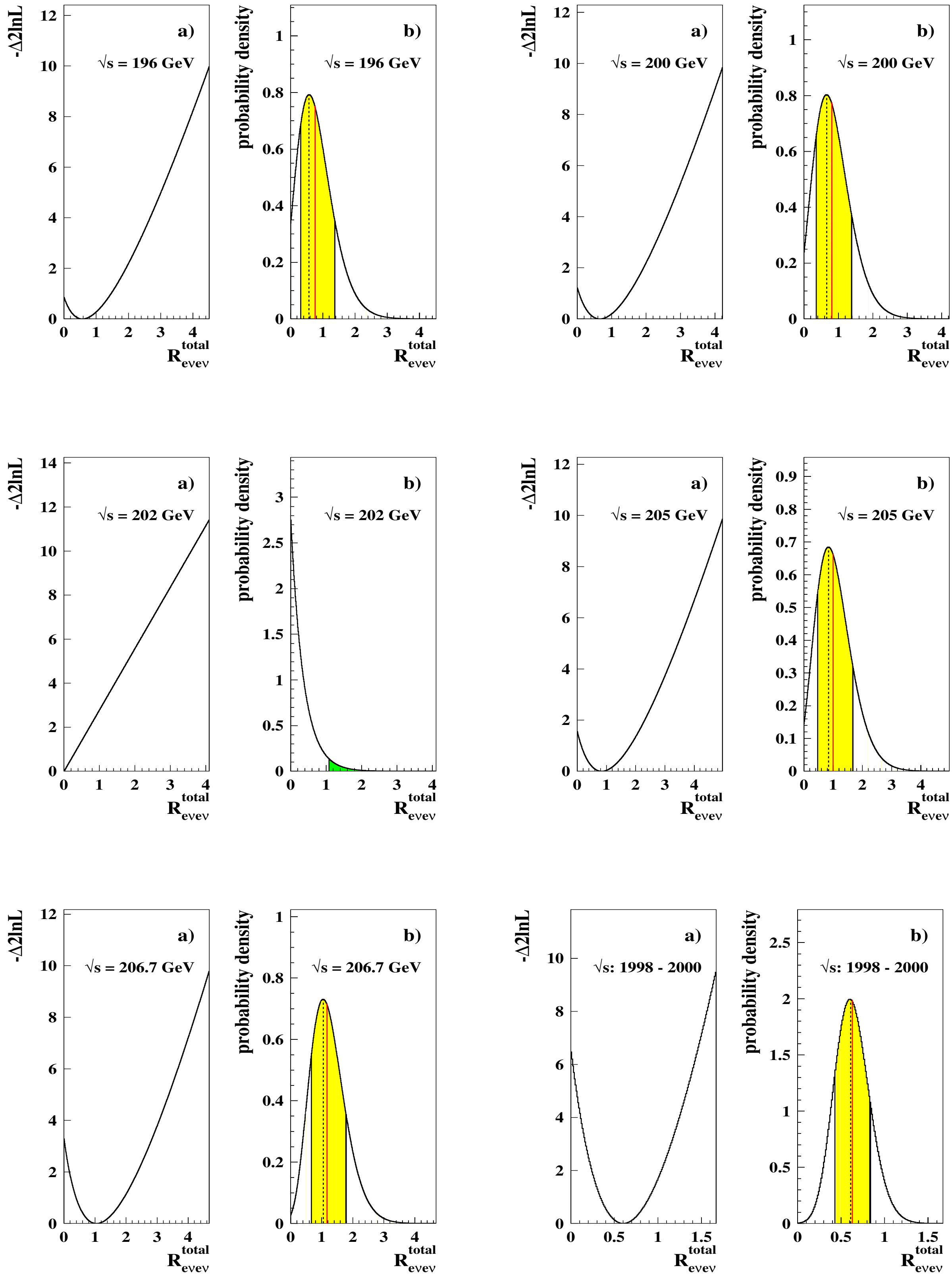

-Δ2lnL
a)
√s = 196 GeV
probability density
b)
√s = 196 GeV
-Δ2lnL
a)
√s = 200 GeV
probability density
b)
√s = 200 GeV
-Δ2lnL
a)
√s = 202 GeV
probability density
b)
√s = 202 GeV
-Δ2lnL
a)
√s = 205 GeV
probability density
b)
√s = 205 GeV
-Δ2lnL
a)
√s = 206.7 GeV
probability density
b)
√s = 206.7 GeV
-Δ2lnL
a)
√s: 1998 - 2000
probability density
b)
√s: 1998 - 2000
$R_{e\nu e\nu}^{total}$

A.3 Hadronic analysis

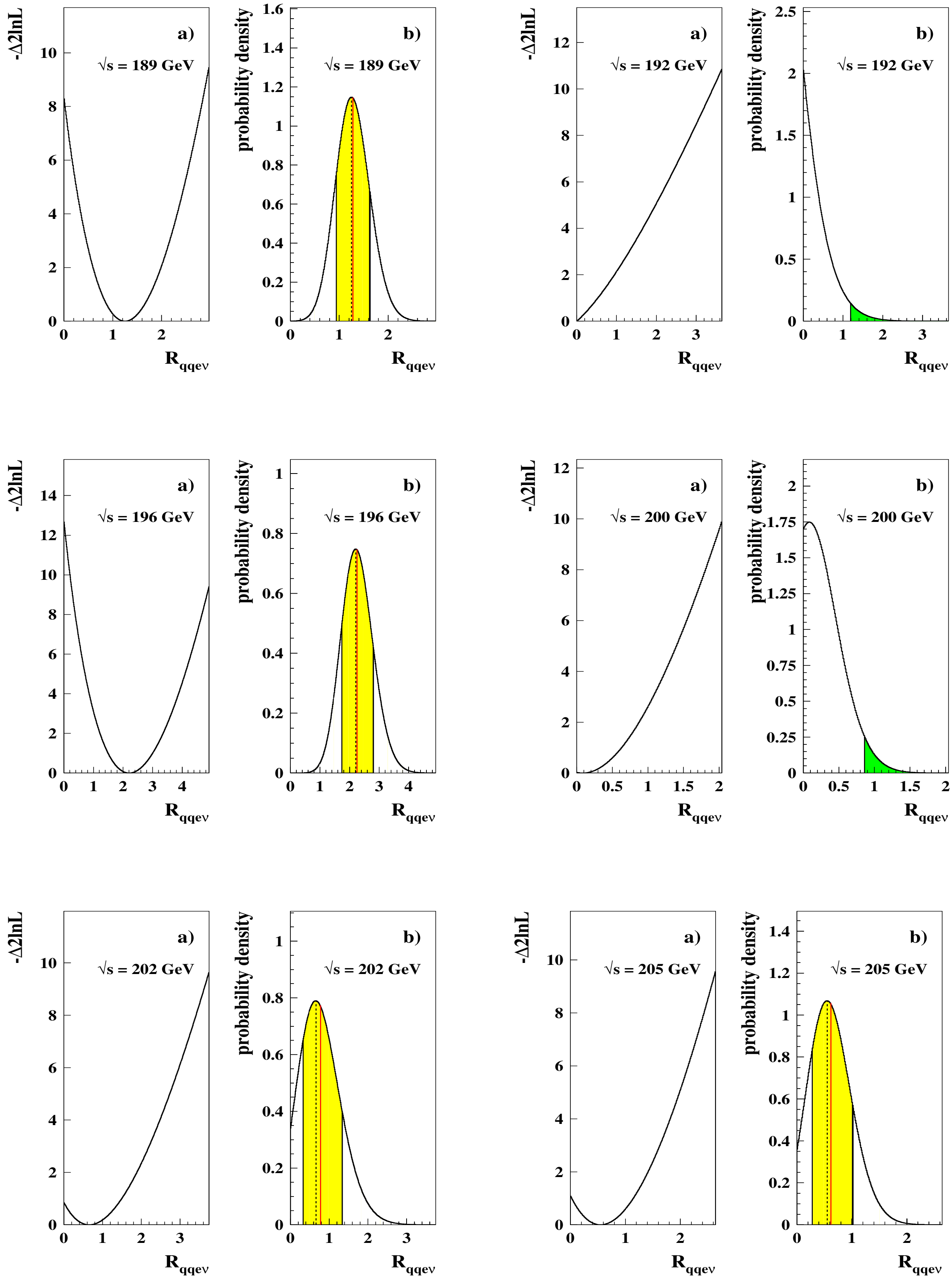

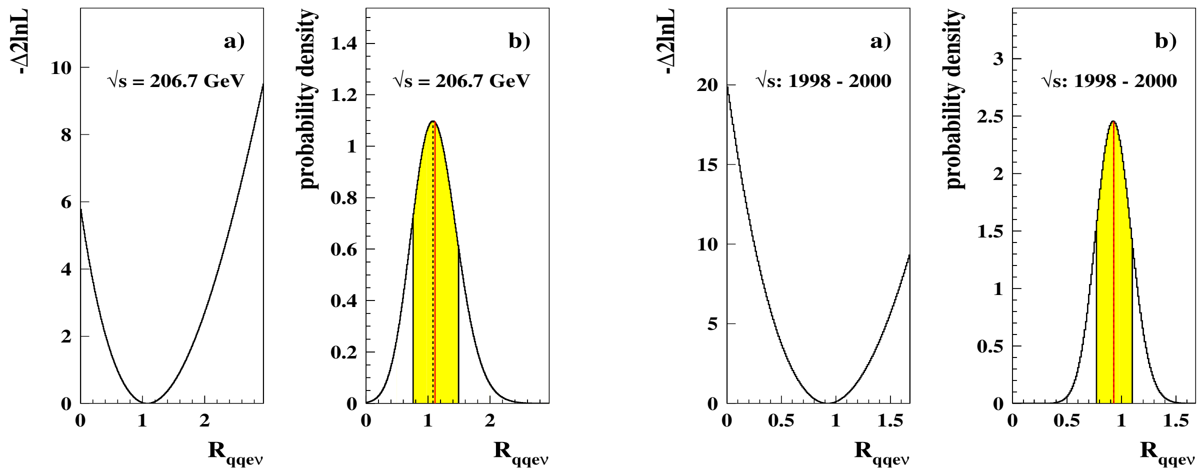

A.4 Single W analysis

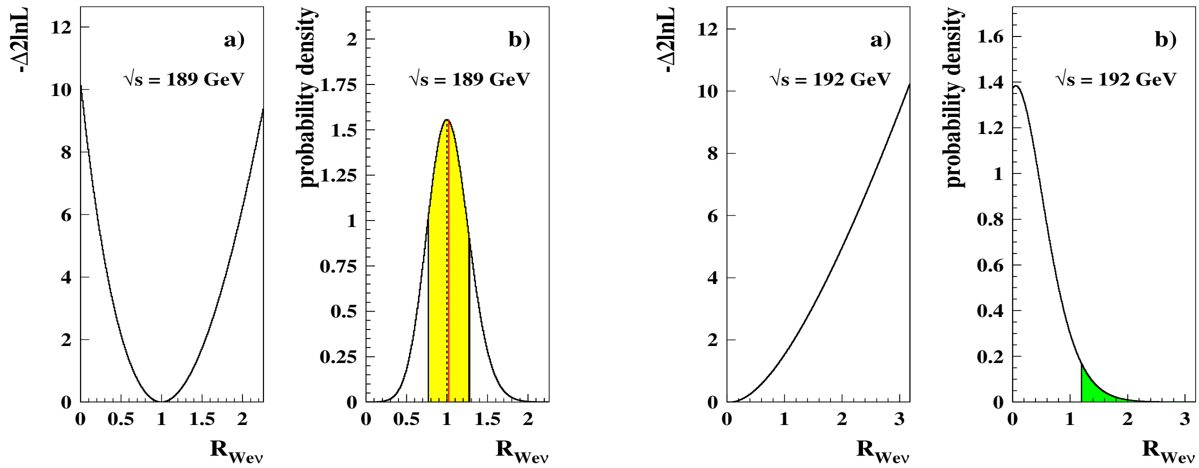

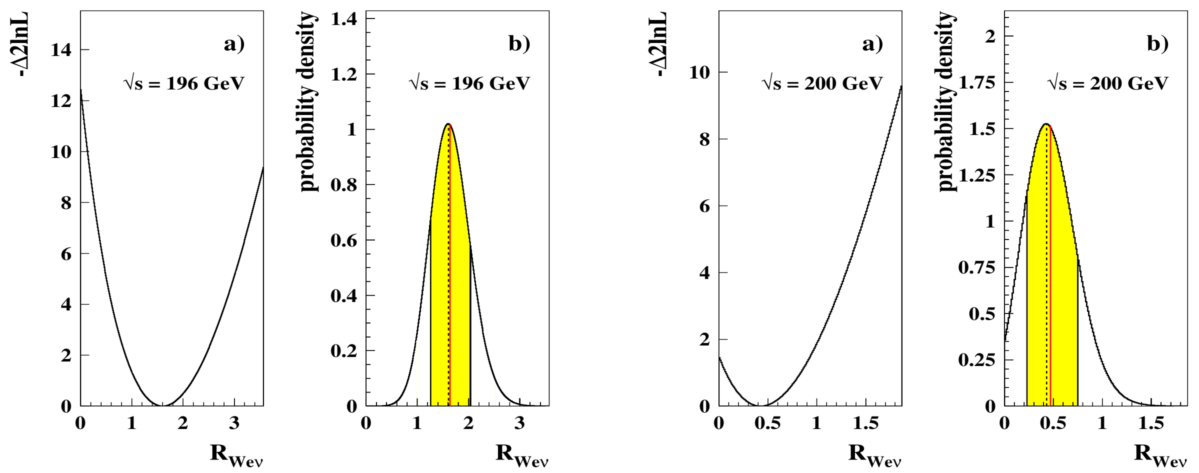

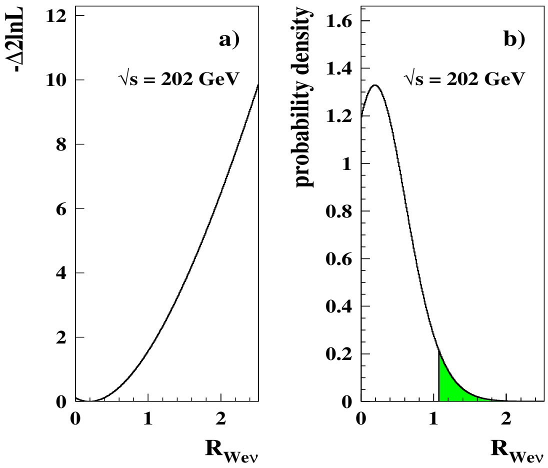
-Δ2lnL
a)
√s = 202 GeV
R_Weν
probability density
b)
√s = 202 GeV
R_Weν

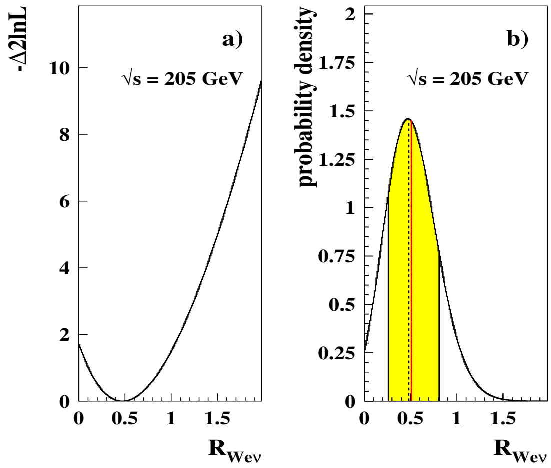
-Δ2lnL
a)
√s = 205 GeV
R_Weν
probability density
b)
√s = 205 GeV
R_Weν

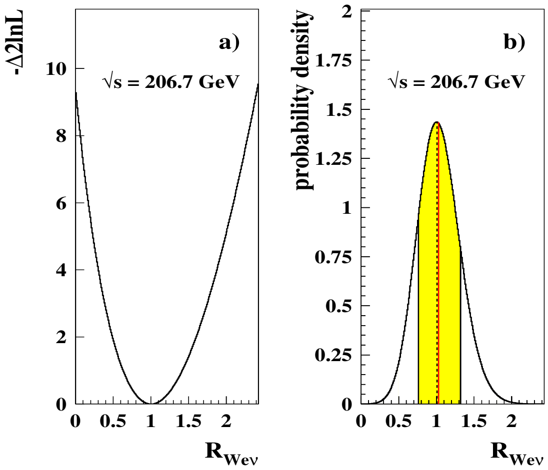
-Δ2lnL
a)
√s = 206.7 GeV
R_Weν
probability density
b)
√s = 206.7 GeV
R_Weν

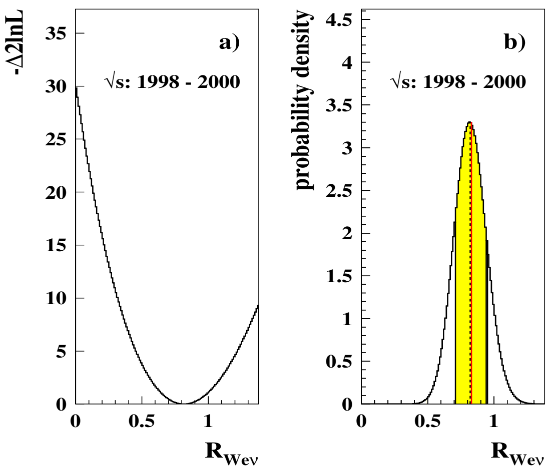
-Δ2lnL
a)
√s: 1998 - 2000
R_Weν
probability density
b)
√s: 1998 - 2000
R_Weν

APPENDIX B

-Δ2ln$\mathcal{L}$ distributions from the TGC analyses

The following sections contain the -Δ2ln$\mathcal{L}$ distributions from the TGC analyses for the various centre-of-mass energies.

B.1 Muon analysis

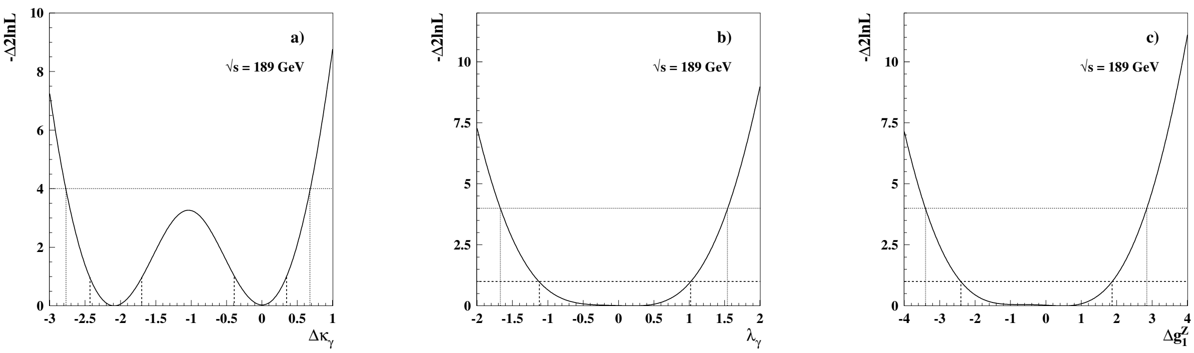

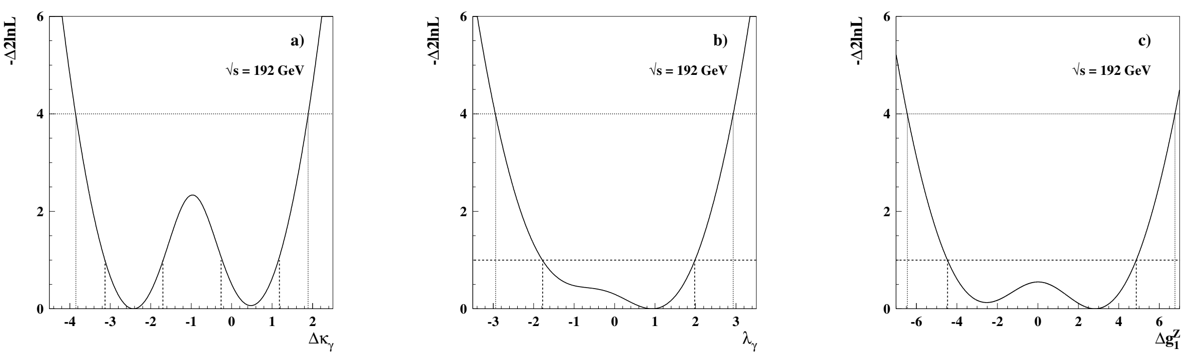

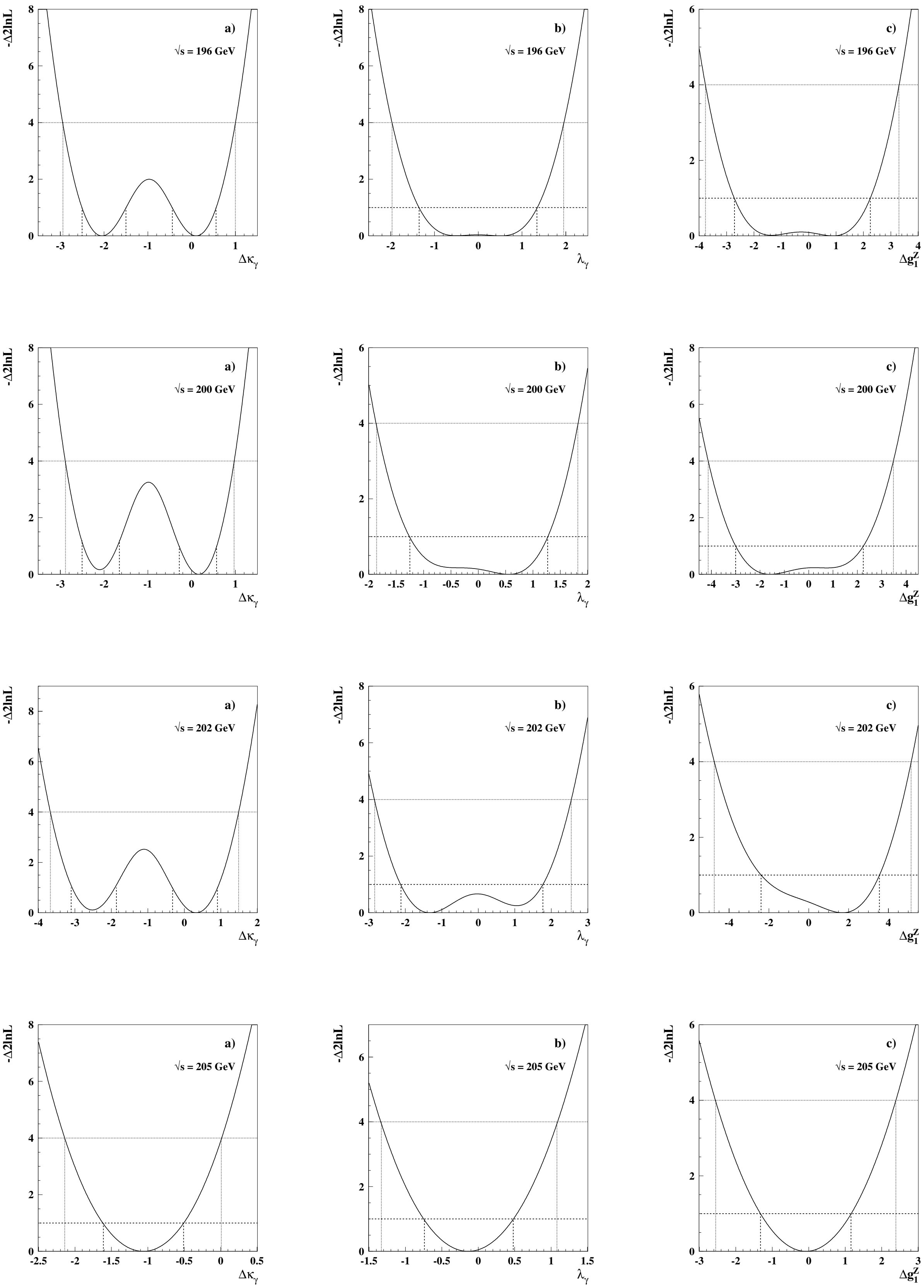
-Δ2lnL
a)
√s = 196 GeV
Δκγ
b)
√s = 196 GeV
λγ
c)
√s = 196 GeV
Δg1Z
a)
√s = 200 GeV
b)
√s = 200 GeV
c)
√s = 200 GeV
a)
√s = 202 GeV
b)
√s = 202 GeV
c)
√s = 202 GeV
a)
√s = 205 GeV
b)
√s = 205 GeV
c)
√s = 205 GeV

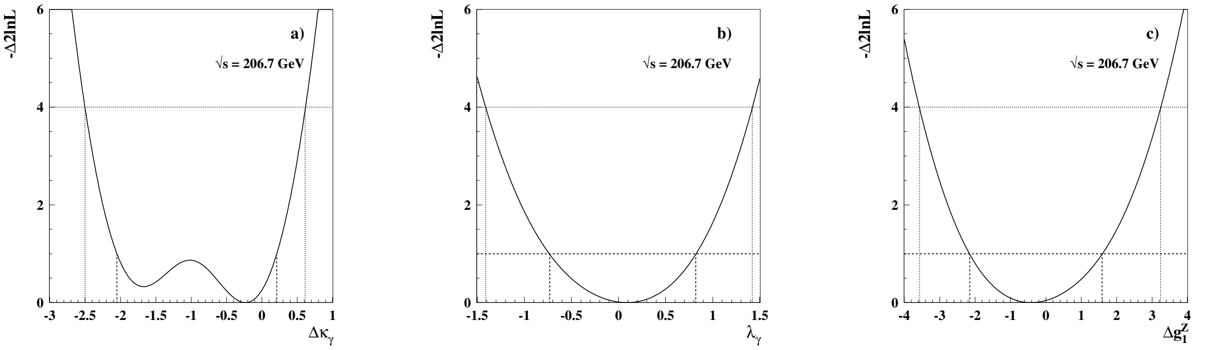

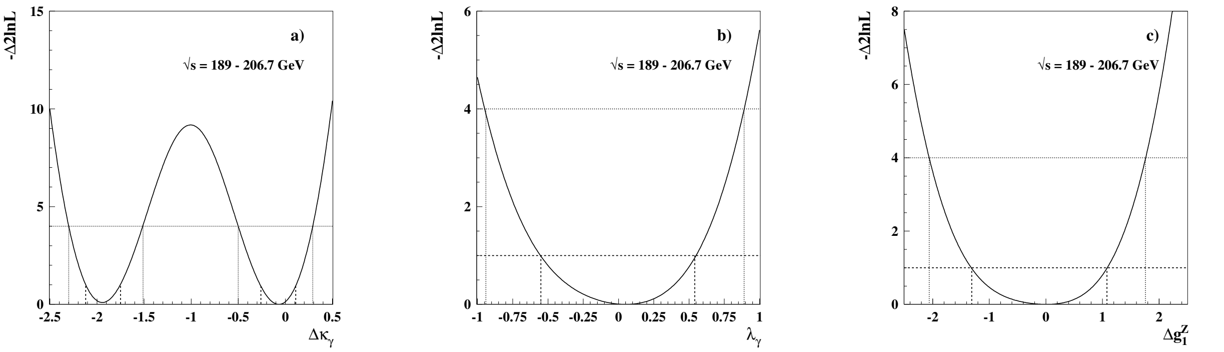

B.2 Electron analysis

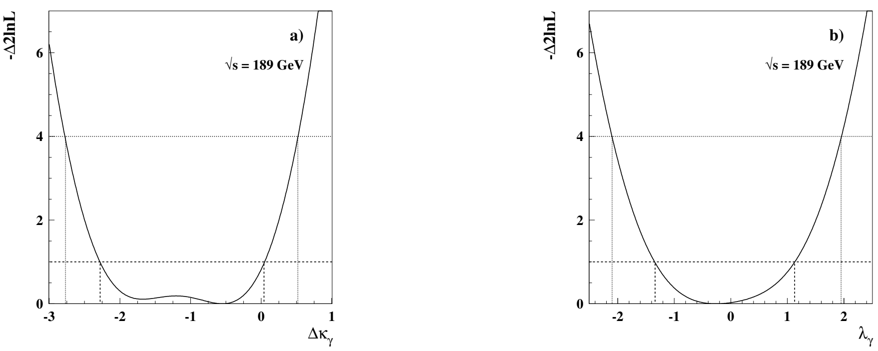

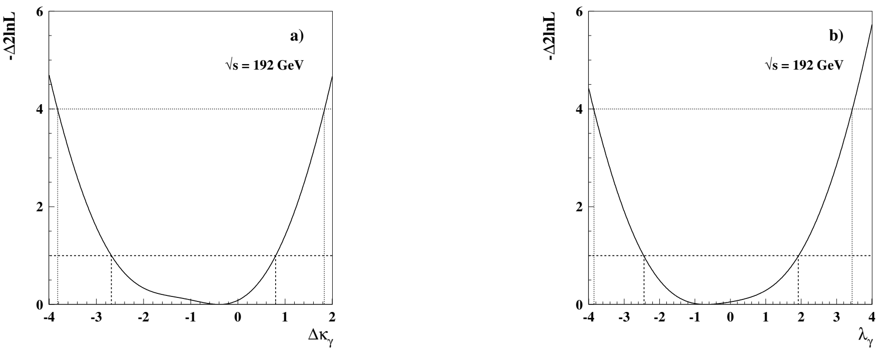

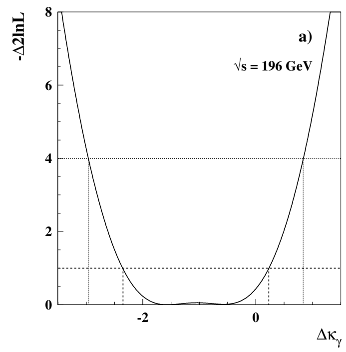
a)
√s = 196 GeV
-Δ2lnL
Δκγ

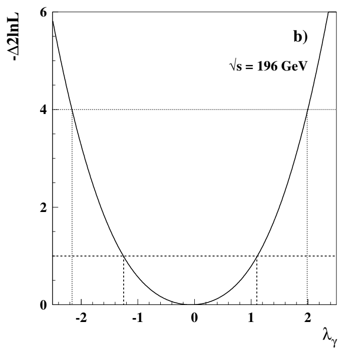
b)
√s = 196 GeV
-Δ2lnL
λγ

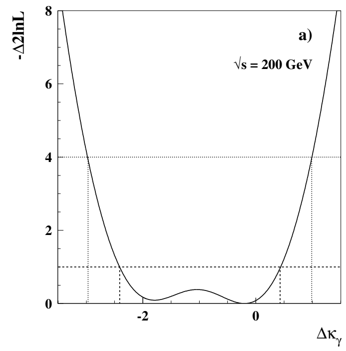
a)
√s = 200 GeV
-Δ2lnL
Δκγ

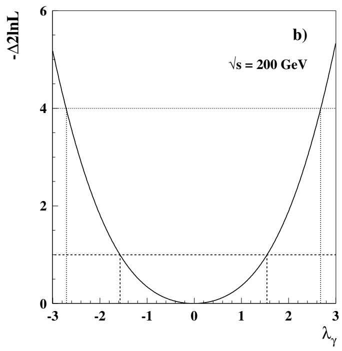
b)
√s = 200 GeV
-Δ2lnL
λγ

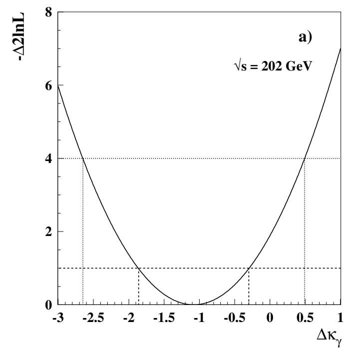
a)
√s = 202 GeV
-Δ2lnL
Δκγ

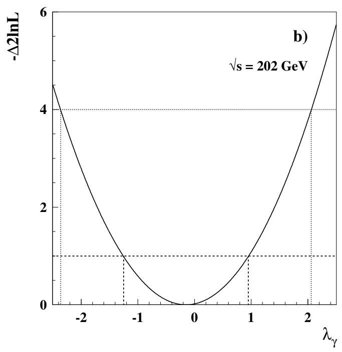
b)
√s = 202 GeV
-Δ2lnL
λγ

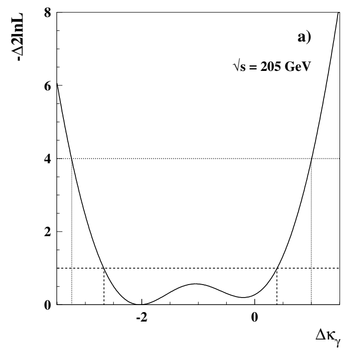
a)
√s = 205 GeV
-Δ2lnL
Δκγ

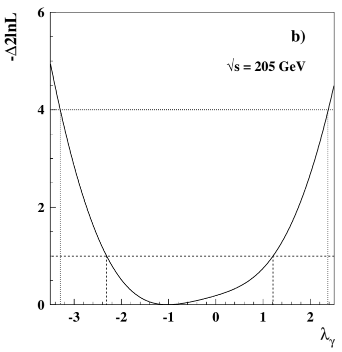
b)
√s = 205 GeV
-Δ2lnL
λγ

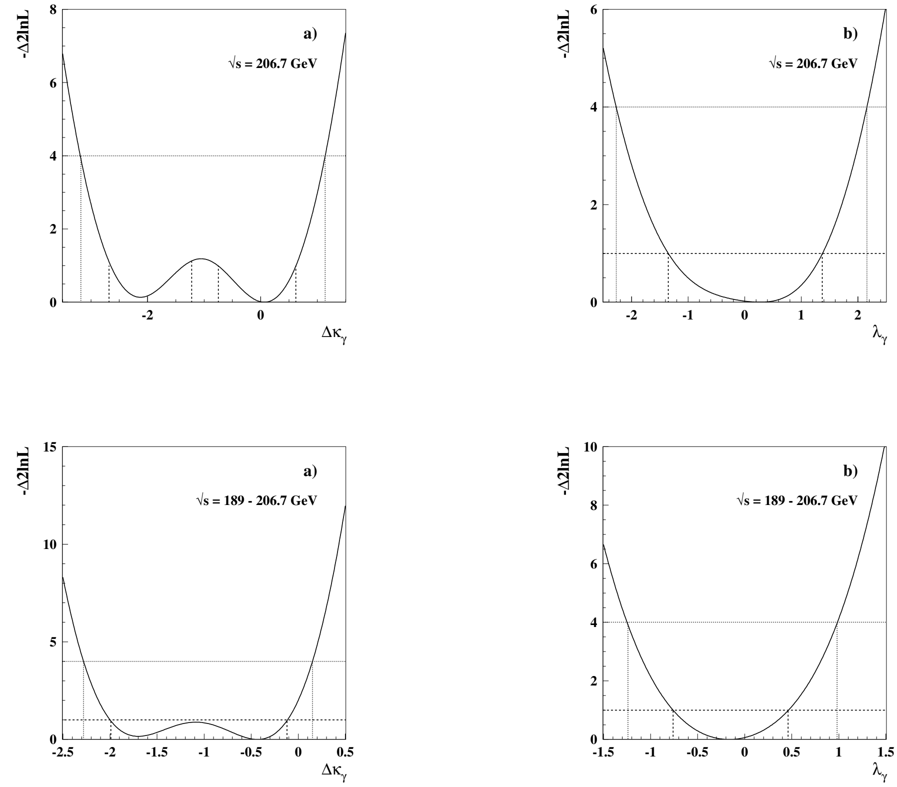

B.3 Hadronic analysis

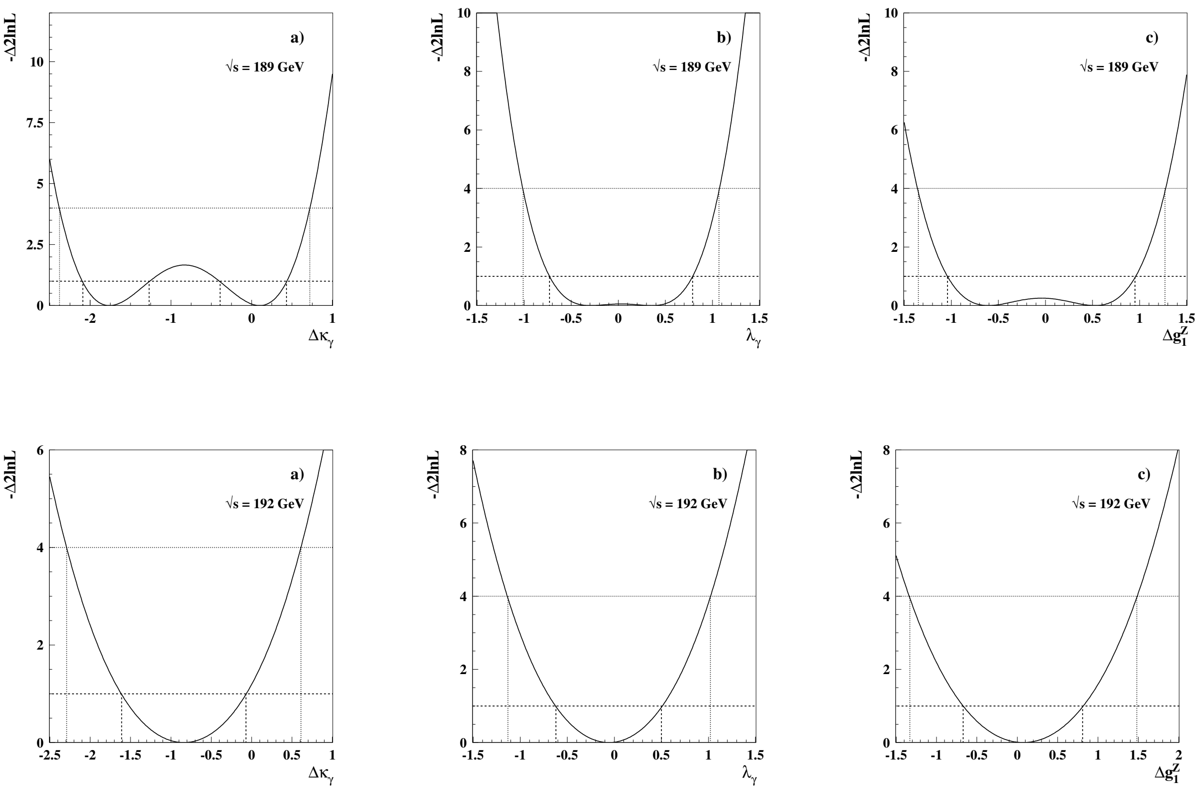

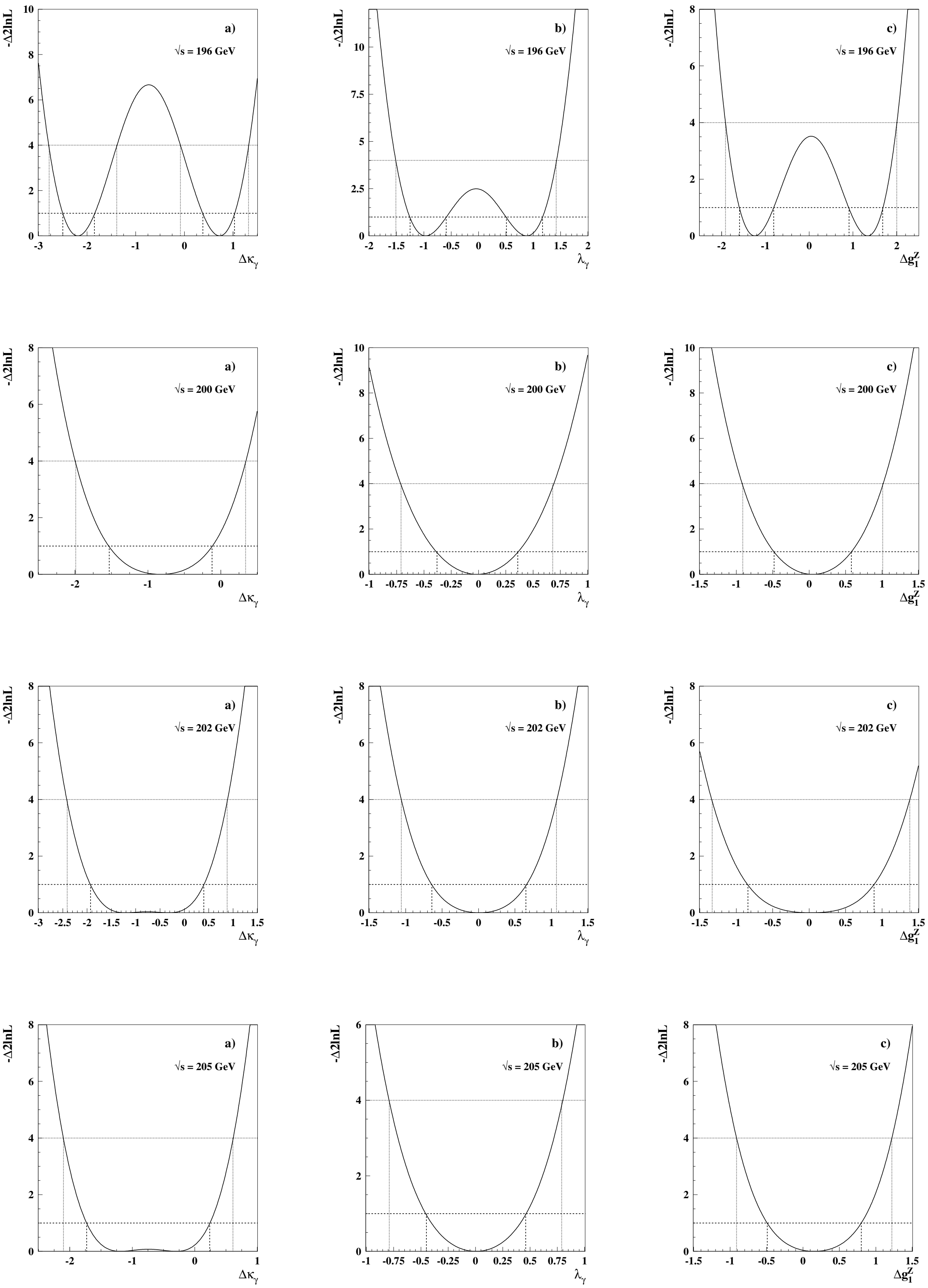
-Δ2lnL
a)
√s = 196 GeV
Δκ_γ
b)
√s = 196 GeV
λ_γ
c)
√s = 196 GeV
Δg_1^Z
a)
√s = 200 GeV
b)
√s = 200 GeV
c)
√s = 200 GeV
a)
√s = 202 GeV
b)
√s = 202 GeV
c)
√s = 202 GeV
a)
√s = 205 GeV
b)
√s = 205 GeV
c)
√s = 205 GeV

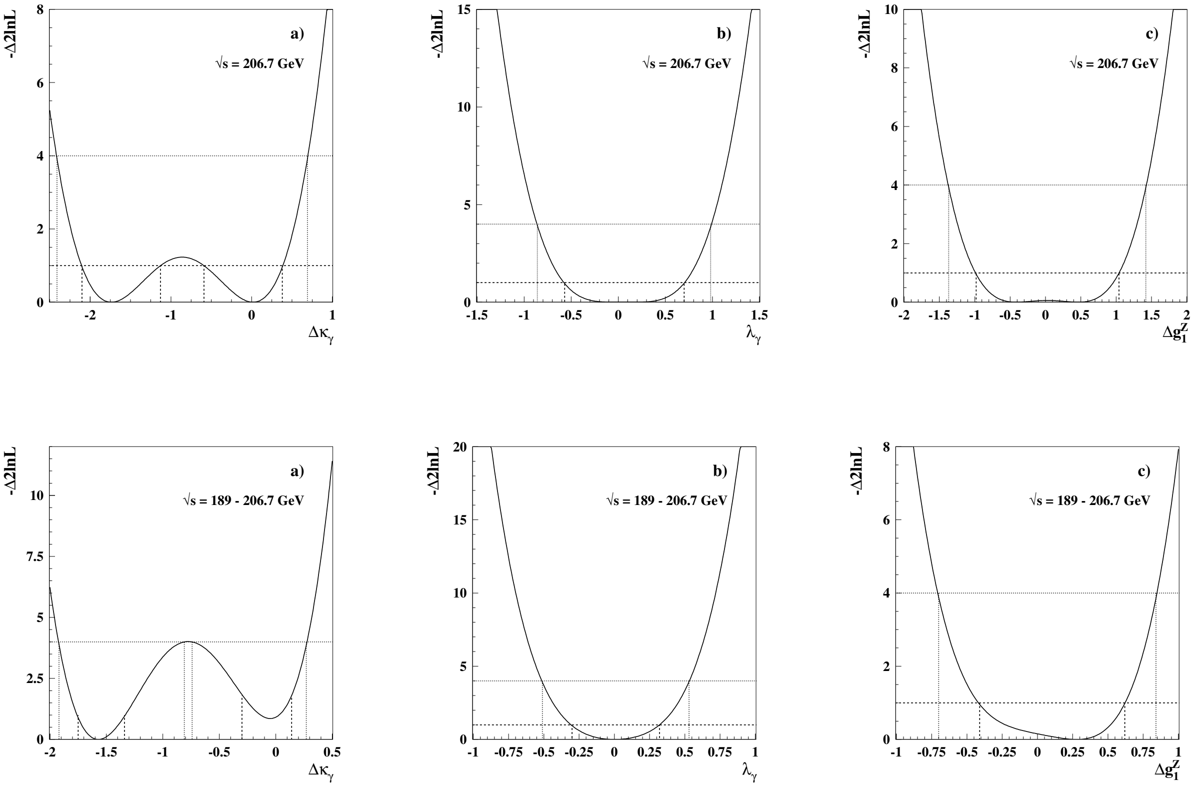

B.4 Single W analysis

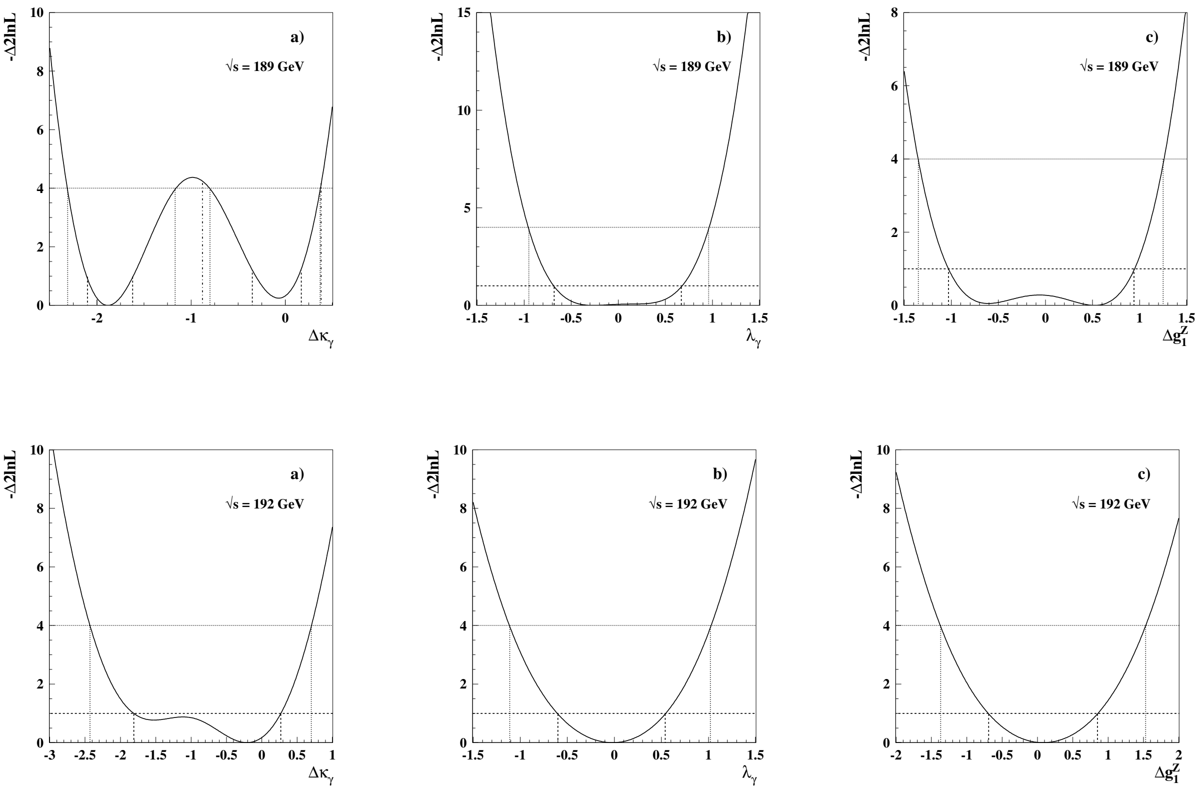

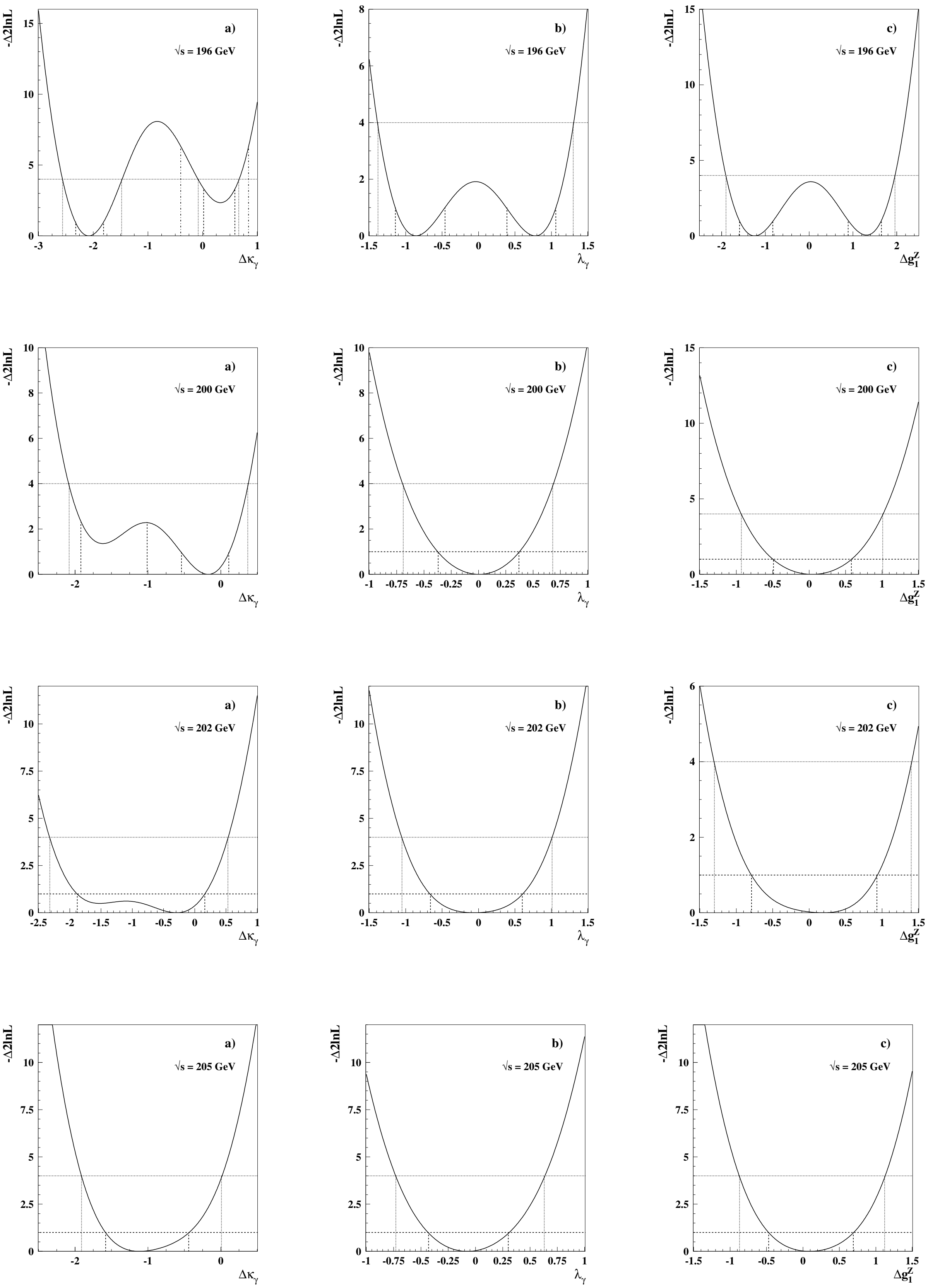
-Δ2lnL
a)
√s = 196 GeV
Δκγ
b)
√s = 196 GeV
λγ
c)
√s = 196 GeV
Δg1Z
a)
√s = 200 GeV
b)
√s = 200 GeV
c)
√s = 200 GeV
a)
√s = 202 GeV
b)
√s = 202 GeV
c)
√s = 202 GeV
a)
√s = 205 GeV
b)
√s = 205 GeV
c)
√s = 205 GeV

-$\triangle 2\ln\mathcal{L}$ distributions from the TGC analyses

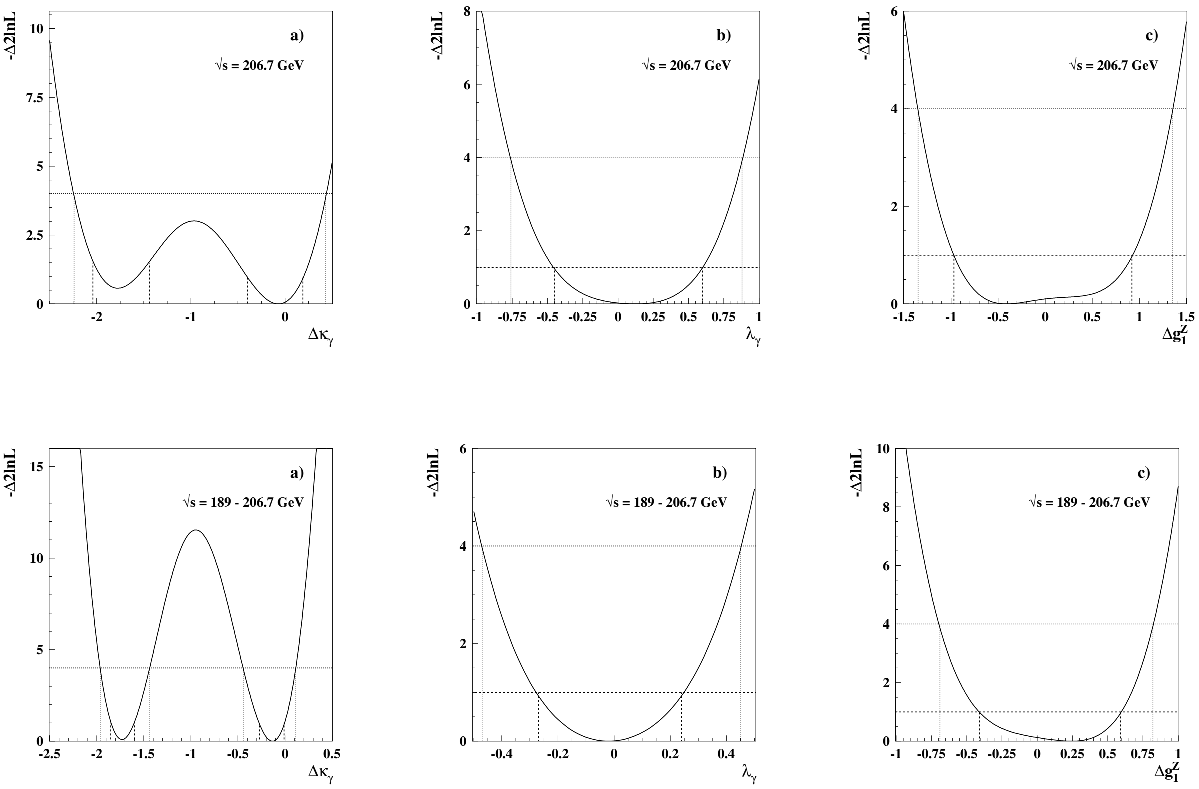

References

[1] M. de Roo, *Elementaire deeltjes fysica*, Collegedictaat Rijksuniversiteit Groningen, 1991.

[2] E. Fermi, *An attempt of a theory of beta radiation*, Z. Phys. **88**, 161 (1934).

[3] R.P. Feynman and M. Gell-Mann, *Theory of the Fermi interaction*, Phys. Rev. **109**, 193 (1958).

[4] T.D. Lee and C.N. Yang, *Question of parity conservation in weak interactions*, Phys. Rev. **104**, 254 (1956).

[5] C.S. Wu *et al.*, *Experimental test of parity conservation in beta decay*, Phys. Rev. **105**, 1413 (1957).

[6] S. Glashow, *Partial symmetries of weak interactions*, Nucl. Phys. **22**, 579 (1961).

[7] S. Weinberg, *A model of leptons*, Phys. Rev. Lett. **19**, 1264 (1967).

[8] A. Salam, *Weak and electromagnetic interactions*, In: Elementary Particle Theory, Proceedings Of The Nobel Symposium Held 1968 At Lerum, Sweden, Stockholm 1968, 367-377.

[9] G. 't Hooft, *Renormalization of massless Yang-Mills fields*, Nucl. Phys. **B33**, 173 (1971).

[10] G. 't Hooft and M. Veltman, *Regularization and renormalization of gauge fields*, Nucl. Phys. **B44**, 189 (1972).

[11] F. Englert and R. Brout, *Broken symmetry and the mass of gauge vector mesons*, Phys. Rev. Lett. **13**, 321 (1964).

[12] P. Higgs, *Broken symmetries, massless particles and gauge fields*, Phys. Lett. **12**, 132 (1964).

[13] G. Guralnik, C. Hagen and T. Kibble, *Global conservation laws and massless particles*, Phys. Rev. Lett. **13**, 585 (1964).

[14] J. Goldstone, *Field theories with 'superconductor' solutions*, Nuovo Cimento **19**, 154 (1961).

[15] N. Cabibbo, *Unitary symmetry and leptonic decays*, Phys. Rev. Lett. **10**, 531 (1963).

[16] M. Kobayashi and M. Maskawa, *CP-violation in the renormalizable theory of weak interactions*, Prog. Theor. Phys. **49**, 652 (1973).

[17] Particle Data Group (K. Hagiwara *et al.*), *Review of Particle Physics*, Phys. Rev. **D66**, 010001 (2002).

[18] K.J.F. Gaemers and G.J. Gounaris, *Polarization amplitudes for $e^+e^- \to W^+W^-$ and $e^+e^- \to ZZ$*, Z. Phys. **C1**, 259 (1979).

[19] K. Hagiwara, R.D. Peccei, D. Zeppenfeld and K. Hikasa, *Probing the weak boson sector in $e^+e^- \to W^+W^-$*, Nucl. Phys. **B282**, 253 (1987).

[20] Minami-Tateya collaboration, *GRACE manual version 1.0*, KEK Report **92-19** (1993).

[21] J. Fujimoto *et al.*, *grc4f v1.1: a four-fermion event generator for e^+e^- collisions*, Comp. Phys. Comm. **100**, 128 (1997), hep-ph/9605312.

[22] E. Accomando *et al.*, *Four-fermion production in electron-positron collisions*, hep-ph/0005309, Contribution to the LEP2 Monte Carlo workshop: *Report of the Working Groups on Precision Calculations for LEP2 Physics*, CERN Yellow Report, CERN-2000-009.

[23] S. Myers, E. Picasso, *The design, construction and commissioning of the CERN large electron positron collider*, Contemp. Phys. **31**, 387 (1990).

[24] ALEPH Collaboration (D. Decamp *et al.*), *ALEPH: a detector for electron - positron annihilations at LEP*, Nucl. Instr. Meth. **A294**, 121 (1990).

[25] DELPHI Collaboration (P. Aarnio *et al.*), *The DELPHI detector at LEP*, Nucl. Instr. Meth. **A303**, 233 (1991).

[26] L3 Collaboration, *The construction of the L3 experiment*, Nucl. Instr. Meth. **A289**, 35 (1990).

[27] OPAL Collaboration (K. Ahmet *et al.*), *The OPAL detector at LEP*, Nucl. Instr. Meth. **A305**, 275 (1991).

[28] UA1 Collaboration (G. Arnison *et al.*), *Experimental observation of isolated large transverse energy electrons with associated missing energy at $\sqrt{s}$ = 540 GeV*, Phys. Lett. **B122**, 103 (1983).

[29] UA2 Collaboration (M. Banner *et al.*), *Observation of single isolated electrons of high transverse momentum in events with missing transverse energy at the CERN $\bar{p}p$ collider*, Phys. Lett. **B122**, 476 (1983).

[30] UA1 Collaboration (G. Arnison *et al.*), *Experimental observation of lepton pairs of invariant mass around 95 GeV/c^2 at the CERN SPS collider*, Phys. Lett. **B126**, 398 (1983).

[31] UA2 Collaboration (P. Bagnaia *et al.*), *Evidence for $Z^0 \to e^+e^-$ at the CERN $\bar{p}p$ collider*, Phys. Lett. **B129**, 130 (1983).

[32] DELPHI Collaboration (P. Abreu *et al.*), *Performance of the DELPHI detector*, Nucl. Instr. Meth. **A378**, 57 (1996).

[33] V. Bocci *et al.* (The DELPHI Trigger Group), *Architecture and performance of the DELPHI trigger system*, Nucl. Instr. Meth. **A362**, 361 (1995).

[34] A. Augustinus *et al.* (The DELPHI Trigger Group), *The DELPHI trigger system at LEP2 energies*, CERN-EP/2002-086 (Accepted by Nucl. Instr. Meth. A).

[35] *DELPHI Data Analysis Program (DELANA) User's Guide* , DELPHI-89-44.

[36] F. Cossutti *et al.*, *Improvements to SKELANA for version 2.0* , DELPHI-99-175.

[37] *DELSIM, DELPHI event generation and detector simulation - reference manual* , DELPHI-89-68.

[38] E. Accomando, A. Ballestrero and E. Maina, *WPHACT2.0: A fully massive Monte Carlo generator for four-fermion physics at e^+e^- colliders,*hep-ph/0204052.

[39] F.A. Berends, P.H. Daverveldt and R. Kleiss, *Monte Carlo simulation of two-photon processes II: Complete lowest order calculations for four-lepton production processes in electron-positron collisions*, Comp. Phys. Comm. **40**, 285 (1986).

[40] F.A. Berends, P.H. Daverveldt and R. Kleiss, *Monte Carlo simulation of two-photon processes I: Radiative corrections to multiperipheral $e^+e^-\mu^+\mu^-$ production*, Comp. Phys. Comm. **40**, 238 (1986).

[41] T. Sjöstrand, L. Lönnblad and S. Mrenna, *PYTHIA 6.2: Physics and Manual*, Comp. Phys. Comm. **135**, 238 (2001), hep-ph/0108264.

[42] S. Jadach, W. Placzek and B.F.L. Ward, *BHWIDE 1.00: $\mathcal{O}(\alpha)$ YFS exponentiated Monte Carlo for Bhabha scattering at wide angles for LEP1/SLC and LEP2*, Phys. Lett. **B390**, 298 (1997), hep-ph/9608412.

[43] D. Karlen, *Radiative Bhabha scattering for singly tagged and untagged configurations*, Nucl. Phys. **B289**, 23 (1987).

[44] S. Jadach, B.F.L. Ward and Z. Wąs, *The precision Monte Carlo event generator $\mathcal{KK}$ for two-fermion final states in e^+e^-collisions*, Comp. Phys. Comm. **130**, 260 (2000), hep-ph/9912214.

[45] S. Jadach, B.F.L. Ward and Z. Wąs, *The Monte Carlo program KORALZ for the lepton or quark pair production at LEP/SLC energies - from version 4.0 to version 4.04*, Comp. Phys. Comm. **124**, 233 (2000), hep-ph/9905205.

[46] F.A. Berends and R. Kleiss, *Distributions for electron - positron annihilation into two and three photons*, Nucl. Phys. **B186**, 22 (1981).

[47] F. Cossutti, A. Tonazzo, F. Mazzucato, *REMCLU: a package for the Reconstruction of ElectroMagnetic CLUsters at LEP200* , DELPHI-2000-164.

[48] S. Catani, Yu. L. Dokshitzer, M. Olsson, G. Turnock and B. R. Webber, *New clustering algorithm for multi-jet cross-sections in e^+e^-annihilation*, Phys. Lett. **B269**, 432 (1991).

[49] P. Abreu *et al.*, *The estimation of the effective centre-of-mass energy in $q\bar{q}\gamma$ events from DELPHI*, Nucl. Instr. Meth. **A427**, 487 (1999), hep-ex/9809008.

[50] T. Bayes, *An Essay Toward Solving a Problem in the Doctrine of Chances*, Philos. Trans. R. Soc. London 53, page 370-418 (1763).

[51] I. van Vulpen, *Measurement of Z boson pair production and a search for the Higgs boson in e^+e^-collisions at LEP*, Ph.D. Thesis, University of Amsterdam, 2002.

[52] A. Denner *et al.*, *Precise predictions for W-pair production at LEP2 with RacoonWW* (2000), hep-ph/0005074.

[53] S. Jadach *et al.*, *The Monte Carlo program KoralW version 1.51 and the concurrent Monte Carlo KoralW&YFSWW3 with all background graphs and first order corrections to W-pair production*, Comp. Phys. Comm. **140**, 475 (2001), hep-ph/0104049.

[54] S. Jadach, W. Placzek and B. F. L. Ward, *Gauge invariant YFS exponentiation of (un)stable Z-pair production at and beyond LEP2 energies*, Phys. Rev. **D56**, 6939 (1997), hep-ph/9705430.

[55] P. Abreu *et al.*, *W-pair production cross section and W branching fractions in e^+e^- interactions at 189 GeV*, Phys. Lett. **B479**, 89 (2000).

[56] M. Mulders, *Direct measurement of the W boson mass in e^+e^- collisions at LEP*, Ph.D. Thesis, University of Amsterdam, 2001.

[57] H.M. Blom *et al.*, *Single intermediate vector boson production at $\sqrt{s}$ = 183 - 209 GeV*, XXXIth International Conference on High Energy Physics, Amsterdam, The Netherlands, 2002, DELPHI-2002-057-CONF-591.

[58] ALEPH, DELPHI, L3 and OPAL collaborations, *LEP W-pair, Z-pair and single W cross section results for the summer 2001 conferences*, LEPEWWG/XSEC note 2001-03.

[59] S. Andringa *et al.*, *Measurement of trilinear gauge boson couplings in e^+e^- collisions at $\sqrt{s}$ = 189 - 209 GeV*, XXXIth International Conference on High Energy Physics, Amsterdam, The Netherlands, 2002, DELPHI-2002-034-CONF-568.

[60] O.P. Yushchenko and V.V. Kostyukhin, *DELTGC: a program for four-fermion calculations* , DELPHI-99-4 PHYS 816.

[61] ALEPH, DELPHI, L3 and OPAL collaborations, *A combination of preliminary results on gauge boson couplings measured by the LEP experiments for the summer 2002 conferences*, LEPEWWG/TGC note 2002-02.

[62] J. Breitweg *et al.*, *W production and the search for events with an isolated high-energy lepton and missing transverse momentum at HERA*, Phys. Lett. **B471**, 411 (2000).

[63] B. Abbott *et al.*, *Studies of WW and WZ production and limits on anomalous $WW\gamma$ and WWZ couplings*, Phys. Rev. **D60**, 072002 (1999).

[64] F. Abe *et al.*, *Measurement of W-photon couplings in $p\bar{p}$ collisions at $\sqrt{s}$ = 1.8 TeV*, Phys. Rev. Lett. **74**, 1936 (1995).

[65] G. Altarelli and M.L. Mangano (editors), *Proceedings on the workshop on Standard Model physics (and more) at the LHC*, CERN 2000-004.

[66] R.-D. Heuer, D. Miller, F. Richard and P.M. Zerwas (editors), *Part III: Physics at an e^+e^- linear collider*, 2001, TESLA Technical Design Report.

[67] D. Amidei *et al.*, *Future electroweak physics at the Fermilab Tevatron*, 1996, Fermilab-Pub-96/082.

Summary

This thesis describes the study of the single W final state that is produced from collisions between electrons and positrons at the Large Electron Positron collider (LEP) at CERN near Geneva.
The collisions that have been produced by LEP during the years 1998 - 2000, at centre-of-mass energies ranging from 189 to 209 GeV and with a total integrated luminosity of about 600 pb^{-1}, are analysed by studying the reaction products that have been recorded by one of the four LEP experiments: the DELPHI detector.

The reason why the single W final state is studied has been born out of the curiosity to verify the predictions of the Standard Model that describes our current understanding of fundamental matter and its interactions. This final state offers a unique possibility to satisfy this curiosity.
The model, constructed in the 1960s and 1970s, describes the electroweak and strong interactions. The emphasis of this thesis is focused on the electroweak part of the Standard Model, which is described by a non-Abelian gauge theory, resulting in the existence of interactions between the gauge fields corresponding to the gauge bosons W, Z and γ. The self-couplings between three gauge bosons, "trilinear gauge boson couplings" (TGCs) at the $WW\gamma$ and WWZ vertices, are studied by measuring the couplings $\Delta\kappa_\gamma$, λ_γ and Δg_1^Z, optimised to reveal possible deviations from the Standard Model values, since these parameters are all equal to zero in this model.

The single W final state $We\nu_e$ is analysed in order to deduce these TGC parameters, since this final state can contain a $WW\gamma$ or WWZ vertex when it is produced via a fusion diagram. Besides by this process the single W final state can also be created by means of bremsstrahlung diagrams that lack these vertices.
The four LEP experiments have agreed on a common signal definition for the cross section of the single W final state, which is defined by the complete t-channel subset of diagrams contributing to $e^+e^- \rightarrow We\nu_e$; $W \rightarrow f\bar{f}'$, with additional cuts on kinematical variables at generator level.

For the cross section and TGC analyses, the final states $We\nu_e$; $W \rightarrow l\nu_l$ with $l = e$ or μ and $W \rightarrow q\bar{q}$ are studied. The electron or positron in the final state (not coming from the W decay) usually escapes along the beam pipe. Since neutrinos cannot be detected, the topology of single W events is fully characterised by the decay products of the W. Therefore, the leptonic decay of the W results in the presence of only one highly energetic charged lepton accompanied by a large missing momentum without the appearance of another significant energy deposition in the detector. The hadronic decay of the W leads to the appearance of two acoplanar jets with a large amount of missing energy.

The maximum likelihood method is applied to the observed number of events in determining the best value for the cross section and TGC parameters.
The R-factor, defined as the ratio of the experimental and theoretical values of a certain quantity, is used for the cross section analysis to determine how well the cross section agrees with the Standard Model prediction. The value of this R-factor for the single W cross section $R_{We\nu_e}$ for the years 1998 - 2000 combined is calculated to be, including the 68% confidence level (CL) statistical error and systematic uncertainty:

$$R_{We\nu_e} = 0.83 \pm 0.12(\text{stat}) \pm 0.03(\text{syst}).$$

The theoretical single W cross sections vary from about 0.7 to 1.0 pb for the centre-of-mass energies available at LEP during these years of data-taking.

The single W TGC analysis for the years 1998 - 2000 combined gives rise to the following measurements of the anomalous couplings $\Delta\kappa_\gamma$, λ_γ and Δg_1^Z, indicating both the 68% CL statistical error and systematic uncertainty:

$$\begin{aligned}\Delta\kappa_\gamma &= -0.13^{+0.12}_{-0.14}(\text{stat}) \pm 0.05(\text{syst}),\\ \lambda_\gamma &= -0.02^{+0.26}_{-0.25}(\text{stat}) \pm 0.01(\text{syst}),\\ \Delta g_1^Z &= +0.25^{+0.34}_{-0.66}(\text{stat}) \pm 0.05(\text{syst}).\end{aligned}$$

Extending the CL region to 95% CL intervals leads to the following limiting values of the TGC parameters, where both statistical and systematic errors are taken into account:

$$\begin{aligned}\Delta\kappa_\gamma &\in [-0.47, +0.13],\\ \lambda_\gamma &\in [-0.47, +0.45],\\ \Delta g_1^Z &\in [-0.69, +0.82].\end{aligned}$$

In general, both the cross section and TGC measurements corresponding to the individual centre-of-mass energies during the years 1998 - 2000 and the combined results show no evidence for deviations from Standard Model predictions.
The Standard Model remains unchallenged at current energy scales.

Samenvatting

Dit proefschrift beschrijft de studie van de eindtoestand met één enkel W-deeltje, geproduceerd in botsingen tussen elektronen en positronen in de grote Europese deeltjesversneller LEP van CERN bij Genève. De botsingen die geproduceerd zijn door LEP gedurende de jaren 1998 - 2000, bij zwaartepuntsenergieën tussen 189 en 209 GeV en met een totale geïntegreerde luminositeit van ongeveer 600 pb^{-1}, worden geanalyseerd door de reactieproducten te bestuderen die gedetecteerd zijn door één van de vier LEP-experimenten: de DELPHI-detector.

De reden waarom de enkelvoudige W eindtoestand bestudeerd wordt, is gelegen in de nieuwsgierigheid om de voorspellingen van het Standaard Model te verifiëren. Dit model geeft een beschrijving van ons huidige begrip van fundamentele materie en haar interacties. Deze eindtoestand biedt een unieke mogelijkheid om die nieuwsgierigheid te bevredigen. Het model, dat in de jaren '60 en '70 geconstrueerd is, beschrijft de elektro-zwakke en sterke wisselwerkingen. In dit proefschrift wordt de nadruk gelegd op het elektro-zwakke gedeelte van het Standaard Model, dat beschreven wordt door een niet-Abelse ijktheorie, hetgeen resulteert in het bestaan van wisselwerkingen tussen de ijkvelden die corresponderen met de ijkbosonen, de zogenaamde W-, Z- en γ-deeltjes. De zelf-koppelingen tussen drie ijkbosonen, zogenaamde "TGCs" bij de $WW\gamma$- en WWZ-vertices, worden bestudeerd door de koppelingen $\Delta\kappa_\gamma$, λ_γ en Δg_1^Z te meten. Deze koppelingsparameters zijn een gevoelige maat voor mogelijke afwijkingen van de Standaard Model voorspellingen, aangezien deze parameters allemaal gelijk aan nul zijn in dit model.

De enkelvoudige W eindtoestand $We\nu_e$ wordt geanalyseerd met de bedoeling deze TGC-parameters te bepalen, aangezien deze eindtoestand een $WW\gamma$- of WWZ-vertex kan bevatten wanneer hij door een fusiediagram geproduceerd wordt. Behalve door dit proces kan de enkelvoudige W eindtoestand ook gecreëerd worden door middel van bremsstrahlung-diagrammen die deze vertices niet bevatten.
De vier LEP-experimenten zijn onderling een gemeenschappelijke definitie van het signaal voor de werkzame doorsnede van de enkelvoudige W eindtoestand overeengekomen, die bepaald wordt door de volledige deelverzameling van t-kanaal diagrammen die bijdragen aan $e^+e^- \to We\nu_e; W \to f\bar{f}'$, met daarnaast snedes op kinematische variabelen op generatorniveau.

Voor de analyses van de werkzame doorsnede en de TGCs worden de eindtoestanden $We\nu_e; W \to l\nu_l$ met $l = e$ of μ en $W \to q\bar{q}$ bestudeerd. Het elektron of positron in de eindtoestand (dat niet afkomstig is van het W-verval) ontsnapt meestal langs de bundelpijp. Aangezien neutrino's niet gedetecteerd kunnen worden, wordt de topologie van enkelvoudige W eindtoestanden volledig gekarakteriseerd door de vervalsproducten van de W. Het leptonische verval van de W resulteert

daarom in de aanwezigheid van één hoog-energetisch geladen lepton met daarnaast een grote hoeveelheid missende impuls zonder enig andere belangrijke energiedepositie in de detector.
Het hadronische verval van de W leidt tot de aanwezigheid van twee acoplanaire bundels van deeltjes ("jets") met een grote hoeveelheid missende energie.

De methode van de "meest aannnemelijke aanpassing" wordt toegepast op het aantal waargenomen gebeurtenissen om de beste waarde voor de werkzame doorsnede en de TGC-parameters te bepalen. De R-factor, die gedefiniëerd wordt als het quotiënt van de experimentele en theoretische waarden van een zekere grootheid, wordt gebruikt voor de analyse van de werkzame doorsnede om te bepalen hoe goed deze overeenkomt met de Standaard Model voorspelling.
De waarde van deze R-factor voor de werkzame doorsnede van de enkelvoudige W eindtoestand $R_{We\nu_e}$ voor de jaren 1998 - 2000 gecombineerd, is als volgt;

$$R_{We\nu_e} = 0.83 \pm 0.12(\text{stat}) \pm 0.03(\text{syst}),$$

waarbij zowel de statistische fout (68% betrouwbaarheidsinterval) en de systematische onzekerheid zijn weergegeven.
De theoretische waarden van de werkzame doorsnede voor de enkelvoudige W eindtoestand liggen tussen de 0.7 en 1.0 pb voor de de zwaartepuntsenergieën die beschikbaar waren gedurende de periode dat LEP gegevens leverde.

De TGC-analyse van de enkelvoudige W eindtoestand voor de jaren 1998 - 2000 gecombineerd levert de volgende metingen van de koppelingen $\Delta\kappa_\gamma$, λ_γ en Δg_1^Z;

$$\begin{aligned}
\Delta\kappa_\gamma &= -0.13^{+0.12}_{-0.14}(\text{stat}) \pm 0.05(\text{syst}),\\
\lambda_\gamma &= -0.02^{+0.26}_{-0.25}(\text{stat}) \pm 0.01(\text{syst}),\\
\Delta g_1^Z &= +0.25^{+0.34}_{-0.66}(\text{stat}) \pm 0.05(\text{syst}),
\end{aligned}$$

waarbij zowel de statistische fout (68% betrouwbaarheidsinterval) en de systematische fout zijn weergegeven.

Wanneer het betrouwbaarheidsgebied tot 95% waarschijnlijkheid wordt uitgebreid, worden de volgende intervalwaarden van de TGC-parameters verkregen;

$$\begin{aligned}
\Delta\kappa_\gamma &\in [-0.47, +0.13],\\
\lambda_\gamma &\in [-0.47, +0.45],\\
\Delta g_1^Z &\in [-0.69, +0.82],
\end{aligned}$$

waarbij zowel de statistische als systematische fout zijn inbegrepen.

In het algemeen geldt dat zowel de metingen van de werkzame doorsnede als die van de TGCs van de individuele zwaartepuntsenergieën gedurende de jaren 1998 - 2000 en de gecombineerde resultaten niet afwijken van de Standaard Model voorspellingen.
Het Standaard Model blijft bij de huidige energieschalen onbetwist overeind.

Acknowledgements

Na bijna vijf jaar is er een einde gekomen aan mijn aanstelling als promovendus. Ik prijs me gelukkig dat de weg naar de voltooiing van dit proefschrift, die gepaard ging met pieken en dalen, uiteindelijk een succesvolle is gebleken. De positieve invloed van vele mensen heeft bijgedragen tot de afronding van dit manuscript. Van hen ben ik de volgende mensen in het bijzonder dank verschuldigd.

Als eersten wil ik mijn promotor en co-promotores bedanken.
Jos Engelen wil ik bedanken voor zijn steun en vertrouwen. Jan Timmermans wil ik in de eerste plaats bedanken voor het feit dat hij me heeft aangenomen bij DELPHI en in de tweede plaats voor het meer dan secuur doorlezen van voorgaande versies van dit proefschrift. De uitdrukking "iets met een timmermansoog beoordelen" lijkt ontleend te zijn aan hem. Peter Kluit wil ik hulde brengen voor het feit dat hij me gedurende de laatste 1,5 jaar op het NIKHEF zeer nuttig geholpen heeft met de analyses.

Gedurende de ruim twee jaar dat ik gedetacheerd ben geweest op CERN, heb ik vele mensen leren kennen, die mij die periode als een bijzonder prettige doen ervaren.
I would like to thank Duncan Reid for being my supervisor during my stay at CERN. It was a pleasant thought that I could always call him when I was on-call for the inner detector. Thanks to him, I know, besides physics, a lot more about history and language.
Op Jan van Eldik schrijf ik credit voor de briljante scriptjes die hij voor me geschreven heeft, waardoor ik bij vlagen in een stroomversnelling kwam in mijn onderzoek.
Naast werken was er voldoende ruimte voor ontspanning die op uiteenlopende manieren gevonden werd met verschillende mensen. Hiervoor wil ik in het bijzonder Cathelijne Bal, Robert van Gulik, het huidige "L3m-team" Vinod Baldew en Mark Dierckxsens, Rutger Hierck, Karin Koopman, Nick Van Remortel en Katja Nummiaro bedanken.

Na mijn detachering op CERN was het verblijf op het NIKHEF ook een aangename periode.
Het regelmatig nuttigen van menig maaltijd en biertje en het ondernemen van andere activiteiten met mede-promovendi vormde een welkome afwisseling met het "stoempen" achter de computer. Hiervoor wil ik in het bijzonder Aart Heijboer, Marco van Leeuwen, Mark Dierckxsens en René Scholte bedanken.

Van mijn voorgangers bij het DELPHI-experiment wil ik naast de laatstvermelde Jan de heren Edik Boudinov, Martijn Mulders en Ivo van Vulpen bedanken. Dankzij "kumac-koning" Ivo is het maken van fraaie plaatjes een fluitje van een cent geworden. Zijn interesse en "mental coaching” heb ik altijd zeer op prijs gesteld.

Robert van Gulik, Vinod Baldew en Kees Huyser ben ik dankbaar voor hun bijdrage bij de tot stand koming van de kaft van dit proefschrift. Robert wil ik ook bedanken voor het doorlezen van delen van voorgaande versies van dit manuscript.

Peter Balke en Marc-Jan de Haas wil ik bedanken voor hun interesse in mijn onderzoek en voor het willen accepteren van het paranimfschap. Wat zullen zij ontspannen door de Oude Lutherse Kerk lopen, aangezien zij al in dit schuitje hebben gezeten!

Tot slot wil ik mijn ouders en broer bedanken voor het vertrouwen dat ze altijd in me gehad hebben. Hoewel ze de weg van a tot z niet met mij heeft meegemaakt en eigenlijk alleen de z heeft mogen ervaren, wil ik Anouk bedanken voor de bijzonder prettige invulling van de laatste letter van het alfabet.